Theory and Methods of Frequency-Dependent AVO Inversion

Adam Wilson

Thesis submitted in fulfilment of
the requirements for the degree of
Doctor of Philosophy

School of Geosciences
University of Edinburgh
2010

Declaration

I declare that this thesis has been composed solely by myself and that it has not been submitted, either in whole or in part, in any previous application for a degree. Except where otherwise acknowledged, the work presented is entirely my own.

Adam Wilson
September 2010

Abstract

Amplitude-versus-offset, AVO, approximations allow the estimation of various properties from pre-stack seismic gathers. Recently it has been suggested that fluid mobility is a controlling factor in pore pressure equalisation and can result in anomalous velocity dispersion in the seismic bandwidth. However, current approximations all assume an elastic subsurface and are unable to account for velocity dispersion. I have applied existing methodologies to a real dataset to qualitatively detect and interpret spectral amplitude anomalies. Three areas had AVO and spectral signature consistent with frequency-dependent AVO theory. The results suggest that it is feasible to measure such effects on real data in the presence of random noise. It would imply that the relaxation parameter, tau, is larger in the field than has been measured in water-saturated real and synthetic sandstones in the laboratory.

I extended a two-term AVO approximation by accounting for velocity dispersion and showed how the resultant reflection coefficient becomes frequency-dependent. I then used this to measure P- and S-wave reflectivity dispersion using spectrally-balanced amplitudes. The inversion was able to quantify the affect of the P-wave velocity dispersion as an instantaneous effect on the reflection. NMO stretch was an issue at the far offsets and I limited myself to the near offsets and effectively measured only the P-wave reflectivity dispersion. I showed how the P-wave reflectivity dispersion signs depend on the AVO classification of the reflection whilst the magnitude depends on the crack density of my model. I showed how the effect of noise and thin-bed tuning can enter uncertainties into the interpretation of spectral anomalies. Whilst it is possible to detect frequency-dependent AVO signatures on pre-stack gathers, the interpretation remains non-unique.

I have quantitatively measured a new physical property, reflectivity dispersion, from pre-stack seismic data. I have presented a method of detecting and measuring velocity dispersion in pre-stack gathers but there remain ambiguities in the interpretation of such results. The approach incorporates spectrally decomposed data in an extended AVO inversion scheme. Future work should investigate the application of the methodology to a real seismic dataset.

Acknowledgements

I am extremely grateful to Xiang-Yang Li, Mark Chapman, Andrew Curtis and Enru Liu for supporting and supervising me throughout my PhD. I would like to thank Xiang-Yang for his support of my work and to keep my focus not only on the small details but on the over-arching goal of my research. I owe a huge debt of gratitude to Mark for the many discussions on theoretical aspects covered within this thesis and his support and advice on progressing the work of frequency-dependent AVO. I would like to thank both Andrew and Enru who have supported and helped my transition into a researcher.

I am grateful to the sponsors of the Edinburgh Anisotropy Project (EAP) and the British Geological Survey University Funding Initiative (BUFI) for the funding that supported my research in Edinburgh. I would also like to thank the Marathon Oil Company for providing me with the marine dataset I used in this thesis.

I would like to thank those who have provided supplementary support that has helped me complete this thesis. I would like to thank Brian Bainbridge, Henchang Dai and Steve Love who provided various levels of computer assistance throughout my time within the British Geological Survey (BGS). I would like to thank Enru Liu and Jingha Zhang for the guidance on using both spectral decomposition and GeoView and also to Tieqiang Zhang for advice on using his matching pursuit method algorithm in this thesis.

I would like to thank friends with whom I've shared geophysics and work-based discussions during my time in Edinburgh; Tom S, Tom G, David H and Pete M.

I would like to thank the numerous officemates with whom I have worked in the BGS; Jinghua Z, Lifeng W, Zhongping Q, Isabel V, Anish V, Martin E, Yunghui X, Tieqiang Z, Chuntau Z, Heather N and Xiaoyang W. The coffee mornings, chats and discussions provided me with entertaining relief from my research.

I offer my heartfelt thanks to my family who have supported me throughout my time at the BGS. My mother and mother-in-law for their patience and support and

my father-in-law for acting as my proof reader. All remaining errors are mine alone. Finally I should like to thank my wife, Gina, for her perseverance and her love. She is the reason for the completion of this thesis.

Contents

List of Tables

List of Figures

Conventions and notations

Abbreviation	Meaning
AVO	amplitude-versus-offset
CMP	central mid-point
IL	inline
XL	crossline
STFT	short-time Fourier transform
HUP	Heisenberg Uncertainty Principle
CWT	continuous wavelet transform
MPM	matching pursuit method
NMO	normal moveout
Q	quality factor
η	fluid viscosity
ε	crack density
μ	shear modulus
k	permeability
Φ	porosity
τ	relaxation parameter
ρ	density
V_P and V_S	P- and S-wave velocity
q	V_P/V_S

θ_1 and θ_2	angle of incidence and transmission
ϕ	average of angle of incidence and transmission
$\frac{d}{df}\left(\frac{\Delta V}{V}\right)$	reflectivity dispersion

Chapter 1: Introduction

1.1 Motivation

Rock physics theories and empirical relationships are widely used to estimate rock properties from pre-stack reflection seismic amplitudes in an attempt to detect hydrocarbons. Fluid saturation, porosity and fractures are all of interest in exploration surveys to determine the location of recoverable oil and gas deposits. Amplitude-versus-offset, AVO, approximations to the exact reflection coefficients allow the estimation of various properties from pre-stack seismic gathers and are useful in mapping rock properties over their areal coverage. They provide the link between rock physics theories and recorded seismic amplitudes. With the continuing improvement in rock physics theories there is a growing chasm between them and their applicability through seismic data analyses and AVO techniques. There is growing consensus that, under certain conditions, fluid saturated rocks can have frequency-dependent properties within the seismic bandwidth (Batzle *et al*., 2006). Improvements in laboratory techniques have enabled the measurement of velocity dispersion at low frequencies within the seismic bandwidth. However, typical AVO approximations do not take into account the possibility of dispersion and assume a homogeneous elastic subsurface which is not necessarily correct. The progress made in rock physics has not been matched in AVO techniques and there is currently no way to include frequency-dependent velocities into the quantitative determination of rock properties from seismic amplitudes. It is the intention of this thesis to address the divide between frequency-dependent rock physics theory and the measurement of relevant properties from pre-stack seismic amplitudes. The approach I have taken is not to be constrained by details of the mechanisms that result in velocity dispersion but to construct an inversion methodology that can be applied to any seismic data and the results interpreted according to established theory.

Typically, geophysicists have used Gassmann theory (1951) to characterise rock properties during fluid substitution at seismic frequencies. Since then, several notable advancements have been made to extend the theory to higher frequencies and to replace some of the simplifications he made. Biot (1956a, b) introduced a method to produce formulations for frequency-dependent moduli and velocities by considering fluid viscosity and permeability but ignoring fluid motion on the pore scale. His theory underestimated velocities that were measured at ultrasonic frequencies. The squirt flow relationship (Mavko and Jizba, 1991), which described the local flow due to the build up of pore pressure gradients, accounted for this discrepancy between measured ultrasonic and predicted velocities. Dvorkin *et al*., (1995) derived expressions for calculating moduli and velocities at the intermediate frequencies between the high and low-frequency limits. Batzle *et al*., (2001 and 2006) argued that fluid mobility controlled the bandwidth of this dispersive region. They argued that for either high viscosity or low permeability reservoir systems, the fluid mobility will be low, resulting in dispersive moduli and velocities that may be within the seismic bandwidth. Hofmann *et al*., (2005) discussed the various relaxation mechanisms related to fluid motion in a saturated rock under a variable stress field at different frequency bandwidths and found it reasonable to conclude that in many reservoir systems the Biot-Gassmann assumptions are broken and their formulations could be invalid at seismic frequencies.

Current AVO approximations (Aki and Richards, 1980; Shuey, 1985; Smith and Gidlow, 1987; Fatti *et al*., 1994 and Verm and Hilterman, 1995) all assume an elastic homogeneous subsurface and are Gassmann consistent. Velocity dispersion within the seismic bandwidth results in the reflection coefficient becoming frequency-dependent whilst still satisfying the Zoeppritz equations. However, none of the AVO approximations are able to account for this and "lump" all frequencies together and ignore the potential of using this fluid sensitive rock property. Castagna *et al*., (2003) provided insight by suggesting that instantaneous spectral analysis (spectral decomposition) can be used to detect frequency-dependent AVO. More recently, Brown (2009) suggested that velocity dispersion is small for brine saturated rocks

and anomalously large for hydrocarbon-bearing formations and that frequency-dependent AVO could be exploited for reservoir detection and monitoring. Neither, though, has actually suggested a suitable approach to accurately measure and quantify frequency-dependent amplitude-versus-offsets.

Chapman *et al*., (2002) derived a microstructural poroelastic model that is consistent with key assumptions of both Gassmann and Biot theory. They insert penny-shaped cracks and spherical pore shapes into a background medium where fluid flow at the different scales reproduces either the low-frequency Gassman domain or the high-frequency squirt domain. They make no assumption on the exact mechanism resulting in the velocity dispersion between the high and low-frequency limits in their model but define a timescale parameter (tau) that describes the time to achieve pore pressure relaxation. The tau parameter determines the frequency range of the dispersion and acts in much the same way as the fluid mobility parameter; when tau is low and mobility is high, we are in the low-frequency, relaxed domain; when tau is high and mobility is low, we are in the high-frequency, unrelaxed domain. It is when both tau and mobility are in-between these limiting cases that strong P-wave velocity dispersion and attenuation can occur. However, it is the crack density, determining the ratio of the inclusions and fluid flow mechanisms, which controls the magnitude of the separation between the limits. Chapman *et al*., (2006) showed how P-wave velocity dispersion is sensitive to the saturating fluid and increases as the bulk fluid modulus decreases. They were able to model reflections from a dispersive medium and found that the reflection coefficient can be frequency dependent within the seismic bandwidth.

Spectral decomposition is able to resolve time-dependent spectra of non-stationary seismic signals and has recently been applied to mapping thin-bed sands and discontinuities (Partyka *et al*., 1999). Castagna *et al*., (2003) suggested using spectral decomposition to detect low-frequency shadows (Taner *et al*., 1979) observed below gas sands and oil reservoirs as a substantiating hydrocarbon indicator. Whilst Ebrom (2004) discussed how both stack and non-stack related effects could result in these

shadows, Castagna *et al*., (2003) suggested other uses of spectral decomposition in the detection of hydrocarbons including frequency-dependent AVO. Chapman *et al*., (2006) discuss the theoretical implications of frequency-dependent AVO and Odebeatu *et al*., (2006) discuss using spectral decomposition to detect fluid related spectral anomalies within the context of a classical AVO analysis.

Currently, spectral anomalies associated with dispersive reflections and materials are processed and analysed within an elastic AVO framework. There isn't a suitable frequency-dependent AVO approximation to fully investigate and interpret dispersion in seismic data. I initially investigated the possibility of detecting fluid related dispersion on a real dataset by merging a traditional reconnaissance AVO analysis with spectral decomposition. This highlighted the shortcomings of using an elastic AVO approximation to investigate frequency-dependent reflection coefficients. A new frequency-dependent AVO approximation that incorporates the velocity dispersion and allows it to be quantified using an inversion methodology is necessary. I have considered the effect of P- and S-wave velocity dispersion on an existing AVO approximation and examined how it can be extended to become frequency-dependent. Seismic data groups the amplitudes of all frequencies within the bandwidth together and I have used spectral decomposition to transform traditional seismic amplitudes into spectral amplitudes. I designed a weight function to remove the effects of the source wavelet and balanced the spectral amplitudes which contain the relevant frequency-dependent amplitude information that relates to the AVO approximation. The extra frequency dimension allows the dispersive nature of materials and reflections to be captured and measured by inverting for frequency-dependent reflectivities. The behaviour of P-wave reflectivities can be integrated into the common AVO classification system and provide additional interpretational value. I derived a new term called reflectivity dispersion that quantifies the inverted frequency-dependent reflectivities. I investigated the effect that various input and processing parameters have on this and showed how the inversion is sensitive to these changes.

This thesis will demonstrate that frequency-dependent rock properties can be quantitatively derived from pre-stack reflection seismic gathers and that advancement in rock physics theories can be incorporated into a new frequency-dependent AVO inversion methodology.

1.2 Objective and outline of the thesis

The main objectives of the thesis are: to qualitatively link a reconnaissance AVO analysis with any spectral anomalies observed on real seismic data; to develop a frequency-dependent AVO approximation and incorporate the frequency dimension into an AVO inversion to quantify P-wave velocity dispersion; and to investigate the key factors that affect the sensitivity of the frequency-dependent inversion.

In Chapter 2, I introduce fundamental rock physics theory which is used to quantitatively describe seismic rock properties of interest in hydrocarbon exploration. I describe recent advances to correct for discrepancies between scale lengths and present the growing body of evidence suggesting frequency-dependent moduli and velocity are relevant parameters within the seismic frequency band.

In Chapter 3, I show the development of P-wave AVO approximations to the exact Zoeppritz reflection coefficient and illustrate how pre-stack seismic gathers can be inverted for various parameters. I provide a thorough review of the AVO classification systems that are incorporated into analyses to help identify anomalies against a background trend due to either changes in the lithology or fluid saturation. I describe how careful acquisition and processing steps have led to the development of time-lapse AVO to aid in reservoir monitoring. Despite these advancements there remains an inability to characterise and measure fluid-related velocity dispersion within the context of an AVO analysis.

In Chapter 4, I characterise the two spectral decomposition algorithms that I use in this thesis. I test the continuous wavelet transform, CWT, and the matching pursuit

method, MPM, on a synthetic trace to optimise the parameterisation I use in this thesis. I describe the ways in which spectral decomposition is being applied to seismic data and define in detail my balancing processes to remove the overprint of the source wavelet to allow interpretation of the decomposed data. Finally, I demonstrate how tuning can be mistaken for dispersion when the thickness of a layer is such that either the seismic or decomposed spectral wavelets interfere with each other.

In Chapter 5, I present the combined results and interpretation from a reconnaissance AVO and spectral analysis of two intersecting seismic lines from a North Sea dataset. I invert the data, generate sub-stacks and crossplots using the intercept and gradient and identify and classify six anomalous areas. I perform spectral decomposition, balance the data and create spectral difference plots of the two lines using both the CWT and MPM. I qualitatively interpret both sets of results from the anomalous areas using frequency-dependent AVO theory and show how such a scheme aids interpretation of these areas.

In Chapter 6, I introduce a frequency-dependent AVO approximation by accounting for velocity dispersion. When applying this to central-midpoint gathers I show how balanced spectral amplitudes replace seismic amplitudes to invert for P- and S-wave reflectivity dispersion in a similar manner to elastic AVO inversions. I describe a methodology to follow when performing frequency-dependent AVO inversions and show that I can quantitatively measure reflectivity dispersion from a number of simple two-layer synthetic gathers.

In Chapter 7, I test the limitations and robustness of the inversion methodology by varying the parameters of the input synthetics. I establish that NMO stretch on far-offsets disrupts the balancing and reflectivity dispersion and show how I minimised this by adjusting the processing flow. I create several three-layer synthetic gathers with an additional elastic reflection to simplify the balancing of the decomposed amplitudes. I test the inversion on gathers with varying crack densities and different

AVO classifications and am able to quantify the P-wave reflectivity dispersion and explain how it can be used to aid interpretation of frequency-dependent AVO anomalies. Further, I show how the flexible MPM algorithm can minimise the problem of distinguishing between tuning and frequency-dependent reflections.

In Chapter 8, I present and discuss the key conclusions from this thesis and consider the implications these may have on subsequent research and on how the techniques may be advanced in the future.

1.3 Datasets and software used in this thesis

The synthetic seismograms in Chapters 4, 6 and 7 are generated using ANISEIS (David Taylor) and the frequency-dependent elastic constants used in Chapters 6 and 7 are generated in FORTRAN (EAP).

The inline, crossline and 3-D velocity cube used in Chapter 5 were supplied by Marathon Oil Corporation and the subsequent AVO analysis was carried out using GeoView (Hampson-Russell).

The processing of the synthetic gathers in Chapters 4, 6 and 7 was carried out using Seismic Unix (CWP, Colorado School of Mines); the spectral decomposition algorithms were coded in C+ (EAP) and integrated into the Seismic Unix package (EAP).

The reflection coefficient curves in Chapters 6 and 7 were generated using FORTRAN (EAP).

The frequency-dependent AVO inversions carried out in Chapters 6 and 7 were written by myself (MATLAB).

1.4 List of publications

1. **Wilson, A.,** Chapman, M. and Li, X.Y., 2009. *Use of frequency dependent AVO inversion to estimate P-wave dispersion properties from reflection data*, 71st Annual EAGE meeting.

2. **Wilson, A.,** Chapman, M. and Li, X.Y., 2009. *Frequency-dependent AVO inversion*, 79th Annual SEG meeting.

3. Wu, X., **Wilson, A.,** Chapman, M. and Li, X.Y., 2010. *Frequency-dependent AVO inversion using smoothed pseudo Wigner-Ville distribution*, 72nd Annual EAGE meeting.

Chapter 2: Rock physics theory

2.1 Introduction

In this Chapter I introduce equivalent medium theories, limited by bounds on their elastic moduli, used to predict rock properties and perform fluid substitution. I show how Gassmann's theory has been extended to be frequency-dependent when both local and squirt flow are considered. I introduce an inclusion-based theory which models velocity dispersion that I can use to create frequency-dependent fluid saturated synthetic materials. Recent research has shown that fluid mobility and viscosity can result in large velocity dispersion in the seismic bandwidth and empirical relationships provide the link between velocity and rock properties. I also review published measurements of the relaxation parameter, tau.

2.2 The Voigt and Reuss bounds

The Voigt and Reuss bounds place absolute upper and lower limits on the effective elastic modulus (bulk, shear, Young's etc.) of a material made up of constituent material phases, *N*, by calculating their volumetric average. The Voigt upper bound effectively states that nature cannot create an elastically stiffer material from its constituents and is

$$M_V = \sum_{i=1}^{N} f_i M_i \qquad (2\text{-}1)$$

where f_i and M_i are the volume fraction and elastic modulus of the *i*th constituent (Avseth *et al*., 2005). The Reuss lower bound effectively states the nature cannot create an elastically softer material from its constituents and is

$$\frac{1}{M_R} = \sum_{i=1}^{N} \frac{f_i}{M_i}. \qquad (2\text{-}2)$$

For any volumetric mixture of isotropic, linear, elastic constituent materials (Mavko *et al*., 1998) the effective elastic modulus will fall somewhere between the two bounds.

2.3 Equivalent medium theories

Seismic velocities are sensitive to critical reservoir parameters; porosity, lithofacies, pore fluid, saturation and pore pressure. Seismic amplitudes can be interpreted for hydrocarbon detection, reservoir characterisation and monitoring, and rock physics research and theories provide the link between the data and reservoir relationships. Equivalent medium theories make simplifications and approximations to allow insight into the interaction of the rock and saturating fluid properties and they play an important role in amplitude versus offset (AVO) analyses and in the construction of numerical synthetic models. I present and show the development of theoretical models that have developed from the elastic Gassmann theory into a frequency-dependent rock physics theory.

2.3.1 Gassmann theory

Gassmann (1951) derived expressions to predict how rock properties change when a fluid substitution takes place that alters both the rock bulk density and compressibility (Avseth *et al*., 2005). His expressions are for an elastic and homogeneous rock matrix and assume statistical isotropy of the pore space but make no further assumptions on pore geometry. There are a number of ways to express Gassmann's relationship but I have chosen the following from Mavko *et al*., 1998

$$\kappa_{sat} = \kappa_{dry} + \frac{\left(1-\frac{\kappa_{dry}}{\kappa_m}\right)^2}{\frac{\Phi}{\kappa_{fl}}+\frac{1-\Phi}{\kappa_m}-\frac{\kappa_{dry}}{\kappa_m^2}} \qquad (2\text{-}3)$$

where κ_{sat} is the effective bulk modulus of a saturated rock, κ_m is the bulk modulus of the mineral matrix, κ_{dry} it the effective bulk modulus of the dry rock frame, κ_{fl} is the effective bulk modulus of the pore fluid and Φ is the porosity. A conclusion of the theory is that the shear modulus is independent of fluid saturation (Berryman, 1999),

$$\frac{1}{\mu_{sat}} = \frac{1}{\mu_{dry}} \qquad (2\text{-}4)$$

where μ_{sat} is the shear modulus of the saturated rock and μ_{dry} is the shear modulus of the dry rock. This conclusion may be violated though when the pore spaces are not connected (Smith *et al*., 2003).

Gassmann theory assumes that the saturating fluid is frictionless, all pores are connected and that the wavelength is infinite, or zero frequency (Wang, 2001). These assumptions ensure full equilibrium of the pore fluid and prevent pore pressure gradients induced by the applied stress. Whilst this condition may be met for seismic frequencies, lab-measured velocities are often higher than those predicted due to local flow at ultrasonic frequencies (Winkler, 1986).

Avseth *et al*., (2005) present a common work-flow for applying the Gassmann equations which I repeat here. Firstly the bulk and shear moduli are extracted from the initial density and P- and S-wave velocities. Gassmann's relation is used to transform the bulk modulus whilst the shear modulus remains unchanged. Finally, the new P- and S-wave velocities can be recalculated using the updated bulk density.

2.3.2 Biot and squirt flow theory

Whilst Gassmann theory is only valid for low frequencies, Biot (1956 a, b) derived formulations for predicting frequency-dependent moduli and velocities in rocks saturated with a linear viscous fluid. Like Gassmann, no assumption is made on pore geometry or fluid flow within the rock; these terms are included in parameters that

average the solid and fluid motions on a scale larger than the pores. The Biot theory reduces to Gassmann for zero frequency, and is often referred to as Biot-Gassmann fluid substitution (Avseth *et al*., 2005).

One of the major elements of the Biot theory is that there exist two compressional waves, the commonly observed fast one and a slow one. The Biot slow wave is not easily observed in real rocks since it is highly dissipative and is scattered greatly by grains in porous rocks but it has been seen in artificial porous rocks (Plona, 1980 and Klimentos and McCann, 1988).

Biot theory predicts velocities much slower than those measured at ultrasonic frequencies (Winkler, 1986) and claims that velocity decreases with increasing viscosity, whilst Jones (1986) showed experimentally that velocity increases with increasing viscosity. Both of the discrepancies can be explained by incorporating the local grain-scale flow into the theory. At low frequencies the fluid can flow easily and the pore pressure can equalise. However, at high frequencies the viscous effects of the fluid cause pressure to build up in the pore space making them stiffer and increasing the bulk modulus of the dry rock frame. It is in this high frequency situation that the theory breaks Gassmann's assumption of relaxed pore pressure. They calculated the effect of this local flow on bulk and shear modulus by deriving formulae for calculating these high frequency moduli. It is this squirt flow that accounts for the discrepancy between the velocities predicted by the Biot theory and measured ultrasonic velocities.

Dvorkin *et al*. (1995) extended the squirt flow relationship to calculate moduli and velocities for the intermediate or dispersive frequencies between the low and high frequency limits. In their model the squirt flow is characterised by pore fluid being squeezed from thin, compliant cracks by the pressure gradient of a passing wave into larger, connected, stiff pores. They incorporate the effect of the pressure gradient on thin cracks into equations for calculating the moduli and velocities. An input parameter, Z, describes the viscoelastic behaviour of the rock. It is given by

$$Z = \sqrt{\frac{R^2}{\mathrm{K}}} \qquad (2\text{-}5)$$

where K is the diffusivity of the soft-pore space and *R* is a combination of constants that are hard to determine. They assumed that Z is a fundamental rock property which does not depend on frequency and can be found using V_P measurements. Fluid viscosity is incorporated in *R* and Batzle *et al*. (2001) showed how it plays an important part in determining the frequency band of the velocity dispersion described by Dvorkin *et al*. (1995).

2.3.3 Frequency-dependent inclusion model

Chapman *et al*. (2002) derived a microstructural poroelastic model by describing a linear elastic solid containing a system of connected uniformly-sized and shaped ellipsoidal cracks and uniformly-sized spherical pores. The model was extended by Chapman (2003) to describe the fluid motion on the grain scale size, reproducing high-frequency limits, and on the fracture scale, reproducing the low-frequency limits. The model is consistent with the Gassmann theory at zero-frequency and predicts two compressional P-waves in agreement with Biot theory.

The crack ratio, ε, controls the ratio of the number of cracks to pores and the different fluid motions in a material. A higher crack density increases the high frequency moduli and therefore the magnitude of the velocity dispersion. The timescale parameter, τ, describes the time to achieve pore pressure relaxation for the model and is given by

$$\tau = \frac{\eta c_v (1+\mathrm{K}_c)}{6k\zeta\sigma_c} \qquad (2\text{-}6)$$

where $c_v = \frac{4}{3}\pi a^3 r$ is the crack volume, ζ is the grain size, η is the fluid viscosity, k is the permeability,

$$\sigma_c = \frac{\pi \mu r}{2(1-v)} \qquad (2\text{-}7)$$

where μ is the shear modulus, r is the aspect ratio, v is the Poisson ratio and

$$\mathrm{K}_c = \frac{\pi}{2(1-v)} \mu c_{fl} r \qquad (2\text{-}8)$$

where $c_{fl} = \frac{1}{\kappa_{fl}}$ is the fluid compressibility.

Since it is extremely unlikely to know τ exactly, Chapman *et al*. (2002) gave an approximation that is valid for small aspect ratio ($r < 10^{-2}$),

$$\tau = \frac{4\eta a^3 (1-v)}{9k\zeta\mu} \qquad (2\text{-}9)$$

which is then independent of aspect ratio.

This model can be used to generate a frequency-dependent elastic tensor and the quality factor, *Q*, is given by

$$Q_P = \frac{-Re\left(\kappa_{\mathrm{eff}} + {}^4/_3 \mu_{\mathrm{eff}}\right)}{Im\left(\kappa_{\mathrm{eff}} + {}^4/_3 \mu_{\mathrm{eff}}\right)} \qquad (2\text{-}10)$$

and

$$Q_S = \frac{-Re(\mu_{\mathrm{eff}})}{Im(\mu_{\mathrm{eff}})} \qquad (2\text{-}11)$$

where κ_{eff} is the effective, frequency-dependent, bulk modulus and μ_{eff} is the effective shear modulus. The P- and S-wave velocities and attenuations are formally linked by the Kramers-Kronig integrals (Jones, 1986).

2.4 Fluid mobility and viscosity

Batzle *et al*. (2001) noted that seismic velocities are often not constant across the different frequency measurement bands. They argued that the dispersion is not just the result of the pore fluid properties but is also due to its mobility within the rock which they defined as

$$M = \frac{k}{\eta} \qquad (2\text{-}12)$$

where k is the permeability and η is the fluid viscosity. Fluid mobility affects the pore pressure equalisation between pores and cracks and if mobility is low then the pressure will not equilibrate no matter the frequency and the system is within the high frequency domain. For high fluid mobility the fluid is able to flow freely and the pore pressure is able to reach equilibrium and the system is within the low frequency domain where Biot-Gassmann theory is valid. Batzle *et al*., (2006) suggested that some sedimentary rocks have low permeability and therefore low fluid mobility and that, even within the seismic bandwidth, most rocks are not within the low-frequency Biot-Gassmann domain. It is quite clear from their arguments that fluid viscosity can play an important role in determining whether a saturated rock is in the low, high or dispersive domain. Whilst Gassmann theory assumes zero fluid viscosity Biot theory tied it through inertial coupling of the fluid with the rock frame and defined the fast compressional wave characteristic frequency, ω_c, as

$$\omega_c = \frac{\eta\phi}{k\rho_{fl}} \qquad (2\text{-}13)$$

where ϕ is the porosity and ρ_{fl} is the density of the saturating fluid. Mavko *et al*., (1998) interpreted the characteristic frequency as the point where the viscous forces (low-frequency) equal the inertial forces (high-frequency) acting on the fluid. Squirt flow mechanisms (Mavko and Jizba, 1991 and Dvorkin and Nur, 1993) define ω_c as

$$\omega_c = \frac{\kappa_{dry} r^3}{\eta} \qquad (2\text{-}14)$$

where κ_{dry} is the dry frame bulk modulus and r is the crack aspect ratio. These two competing theories define the characteristic frequency with the viscosity in the numerator and denominator respectively. Batzle *et al*., (2006) performed laboratory tests on dry and saturated rock samples at different frequencies and temperatures. Their results indicated that the dispersion zone between the low and high-frequency regimes is strongly influenced by the fluid viscosity and that it shifts to lower frequencies as fluid viscosity increases. The implication is that Biot's inertial coupling is not a dominant factor for velocity dispersion. Squirt flow and the inverse relationship between the characteristic frequency and viscosity, $\omega_c \propto \frac{1}{\eta}$, greatly affects velocity dispersion in rocks.

Hofmann *et al*., (2005) discussed various flow related relaxation mechanisms and how they affect the elastic tensor and velocity. In typical porous, permeable rocks there may be macroscopic fluid flow, inter-pore space pressure equalisation or intra-pore squirt flow depending on the frequency band of the applied stress field. They concluded that low mobility systems, due to either low permeability or high fluid viscosity, can result in strong velocity dispersion leading to frequency-dependent reflection coefficients. Brown (2009) recently argued that frequency-dependent AVO, proposed by Chapman *et al*., (2006), contains much information about reservoirs due to hydrocarbon bearing rocks having exaggerated velocity dispersion compared to brine saturated formations. An AVO analysis that accounts for and quantifies this dispersion could be a useful tool in the detection and monitoring of hydrocarbon reservoirs.

2.5 Dispersive synthetic modelling

Chapman (2003) theory describes the process of creating a frequency-dependent elastic tensor for a material that defines the P- and S-wave velocities. Estimates are made of the material properties under one fluid saturation (typically water) porosity, Φ, crack density, ε, aspect ratio, r, timescale parameter, τ, P-wave velocity, V_P, S-wave velocity, V_S, saturated density, ρ_{sat} and the bulk fluid modulus, κ_{fl}. When another fluid is substituted (typically oil or gas) then new estimates are also made of the changed fluid-dependent parameters; the new saturated density, ρ_{sat}, and bulk fluid modulus, κ_{fl}. To ensure an elastic material the timescale parameter can be set to $\tau_0 = 1e^{-6}s$ which ensures pore pressure equalisation and that the material is within the Biot-Gassmann domain.

In Chapter 6, I introduce a sandstone exhibiting frequency-dependent properties from Chapman *et al*. (2006). Its material properties are: $\Phi = 30\%$, $\varepsilon = 0.1$ and under water saturation, $V_P = 2790m.s^{-1}$, $V_S = 1463m.s^{-1}$, $K_{fl} = 2000MPa$ and $\rho_{sat} = 2.08g.cm^{-3}$. When the gas is substituted for water the bulk modulus is lowered to $\kappa_{fl} = 400MPa$ and the saturated density reduces to, $\rho_{sat} = 2.06g.cm^{-3}$, following the Gassmann theory. The new P- and S-wave velocities are calculated from the elastic matrix after the fluid replacement.

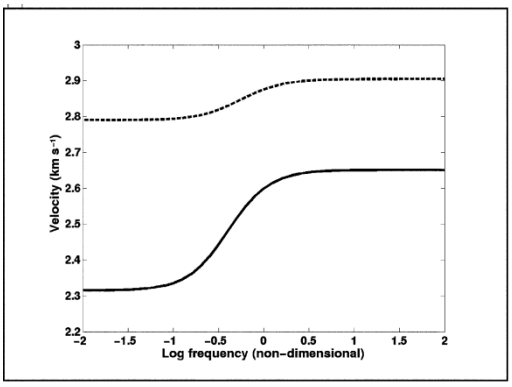

(a) P-wave velocity

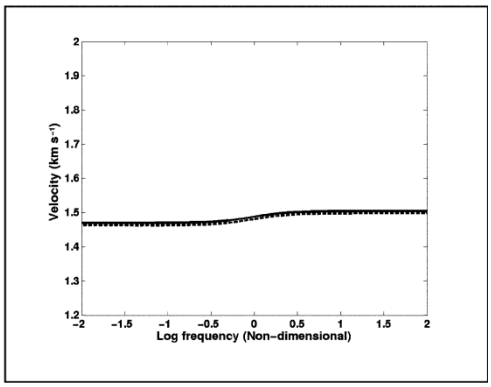

(b) S-wave velocity

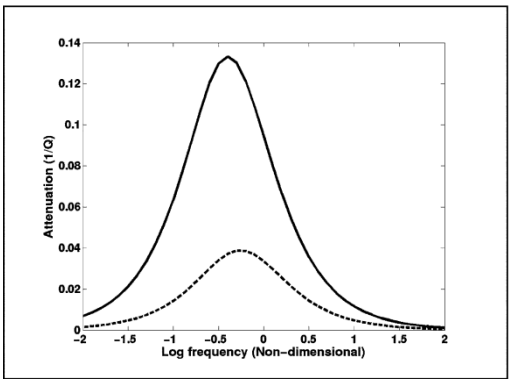

(c) P-wave attenuation

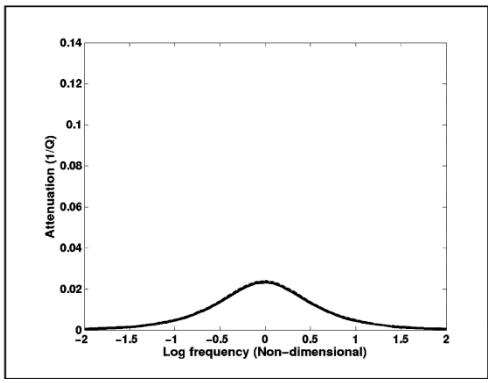

(d) S-wave attenuation

Figure 2.1: Predicted velocities and attenuation from a sandstone material with water and gas saturation (dashed and solid lines respectively) from Chapman *et al*. (2006).

I have reproduced Chapman *et al.*'s (2006) plots of predicted P- and S-wave velocities and attenuations versus dimensionless frequency ($\omega\tau$) under both water and gas saturation. When gas is substituted for water the P-wave velocity decreases and the dispersion between the high and low frequency limits increases due to the lower fluid bulk modulus. The velocity and attenuation are linked via the Kramers-Kronig relationship and the strong velocity dispersion under gas saturation is coupled with large attenuation. The peak of attenuation in figure 2.1c is at a slightly lower frequency for gas than water, suggesting that the dispersive region is at lower frequencies for gas saturation. This may be due to the increased fluid mobility in gas over water, shifting the dispersion curve to slightly lower frequencies.

The results of Chapman *et al*. (2006) show three regions on their velocity versus frequency plots; the low-frequency Gassmann limit, the high-frequency limit and the dispersive region. In this model it is the order of magnitude of the timescale parameter that determines the frequency range of the dispersive region and whether it is within the seismic bandwidth. As the timescale parameter increases the fluid mobility decreases and the dispersive region shifts to lower frequencies, potentially within the seismic bandwidth.

2.6 Common empirical relationships

Considering the numerous factors that affect velocity (e.g. porosity, pressure and clay content) empirical relationships, derived from either well-logs or laboratory measurements, allow for trends to be identified. Empirical rock physics relationships allow for the extrapolation or estimation of rock properties in areas where information may be lacking.

2.6.1 Velocity-porosity relationship

Wyllie's time average equation (Mavko *et al*., 1998) is a simple relationship between porosity and P-wave velocity in a fluid saturated rock of uniform mineralogy under high effective stress. It states that the transit time ($\propto 1/V$) is equal to the sum of the transit time in the mineral frame and the pore fluid, which is

$$\frac{1}{V_P} = \frac{\Phi}{V_{P-fl}} + \frac{1-\Phi}{V_{P-0}} \qquad (2\text{-}15)$$

where Φ is the porosity and V_P, V_{P-fl} and V_{P-0} are the P-wave velocities of the saturated rock, pore fluid and the mineral respectively.

2.6.2 Velocity-porosity-clay relationship

Whilst empirical relationships between velocity and porosity are good for clean sandstones, Wyllie's time average or Raymer-Hunt-Gardner relationship (Mavko *et*

al., 1998), they fail in the presence of clay. The presence of clay introduces compliant pores compared to the stiffer pore spaces of the sandstone matrix. Mavko *et al*., (1998) report two sets of empirical relationships that account for the volumetric fraction of clay which allows for a varying correction factor at different effective pressures.

2.6.3 Shear wave velocity prediction

The shear wave velocity can improve the interpretation of seismic signatures associated with changing lithology, pore fluid and pore pressure (Avseth *et al*., 2005) yet is often only known at well locations due to the dominance of P-wave surveys. Smith and Gidlow (1987) present an amplitude-versus-offset (AVO) approximation and inversion for fluid discrimination that requires knowledge of the S-wave velocity. Castagna *et al*. (1985) derived an empirical relationship from log measurements between P- and S-wave velocities in water-saturated clastic silicates, or mudrocks, so that

$$V_S = 0.8612V_P - 1.1724 \qquad (2\text{-}16)$$

where the velocities are in $km.s^{-1}$. I use this relationship in Chapter 5 to convert P-wave stacking velocities into S-wave velocities.

2.7 Real data estimates of τ

Despite the progression of theoretical models describing velocity dispersion there are few published accounts linking real data to these models. The following section is a review of the published literature on matching rock physics models to laboratory data.

Chapman (2001a) reported a quantitative interpretation of P- and S-wave velocity in rocks saturated with oil and brine (Sothcott *et al*., 2000). The data was acquired for frequencies between 3kHz and 30kHz and effective stress of 10MPa and 40MPa

(Sothcott *et al*., 2000). Chapman (2001a) picked three constants (ϵ_0, c_{cr} and ω_c) to best fit a microstructural poroelastic model (Chapman, 2001b), where the first two parameters are dependent on the rock and ω_c is dependent on the saturating fluid. The rock and fluid-dependent constants were used to fit the theoretical model with the laboratory measured P-wave velocity. The predicted dispersion curves and resonant bar measurements were in good agreement except when the effective stress was 10MPa.

Chapman *et al*., (2003) describes inferring values of ω_c, using the model of Chapman *et al*., (2002), from various published rock physics data. They report matching the theory to three sets of data, although in two cases they arrive at a relationship of ω_c which is either dependent on permeability or viscosity. The final rock physics data set they use is synthetic sandstone samples with controlled crack geometry published by Rathore *et al*., (1995). Chapman *et al*., (2003) considered the water saturated case when velocity and attenuation were measured as a function of polar angle. They performs a least squares inversion for ω_c to match the measured values against the theoretical values results in $\omega_c = 3.7\text{x}10^6$Hz. Linking ω_c to the relaxation parameter, τ, results in $\tau = 1/\omega_c = 2.7\text{x}10^{-7}s$.

Maultzsch *et al*., (2003) took the latter result from the Chapman *et al*., (2003) to generate an estimate for the relaxation time for a gas saturated Green River Formation. They corrected the earlier τ value obtained by calibrating the rock and fluid properties to the Green River Formation. They found that τ had to be increased by 123, yielding a value of $\tau_{GR} = 6\text{x}10^{-6}s$.

Payne *et al*., (2007) estimated the relaxation parameter from a broadband crosswell seismic dataset in an area of homogeneous chalk. They used Chapman's (2003) theory to match their measurements and to minimise the misfits between them. They found that a value of $\tau = 5\text{x}10^{-8}s$ best matched the theoretical model and the data best.

Finally, and most recently, Tillotson *et al*., (2010) has estimated relaxation parameters for, water saturated, synthetic porous rocks with penny-shaped fractures. They minimise the misfit between Chapman's (2003) theoretical model and the measured velocities at ultrasonic frequencies and calculated $\tau = 8\text{x}10^{-9}s$. This is on the same scale as the earlier published results. All of the published estimates of the relaxation parameter from real or synthetic rocks have been on the scale $1\text{x}10^{-9} - 1\text{x}10^{-6}s$. What Tillotson *et al*., (2010) do note is that, except for a clear minimum, the misfit between the model data and measured data is smallest for higher frequencies, implying larger values of tau. As tau increases, the transition frequency between the low and high frequency domain decreases and dispersion occurs at lower frequencies. It is therefore reasonable to consider the case of a real rock, saturated with a lower bulk modulus than water (gas), with rock properties such that the combination results in velocity dispersion within the seismic bandwidth. Whilst this has yet to be measured it would be of interest to estimate the relaxation parameter from these synthetic rocks under both oil and gas saturation to directly compare the effect of the saturating fluid and the lower bulk modulus.

2.8 Discussions and conclusions

I have discussed Gassmann's theory and how it can be used to predict rock properties when substituting one fluid for another. The theory makes no assumption on pore geometry and assumes zero fluid viscosity. Biot theory includes the local flow that prevents pore pressure equalisation and the elastic tensor becomes frequency-dependent although it reduces to Gassmann theory for zero frequency. Squirt flow introduces another, grain-scale, flow where the saturating fluid is squeezed from compliant cracks into stiffer pores and accounts for the discrepancy of Biot theory and ultrasonic measured velocities. Chapman (2003) derived a poroelastic model with a linear elastic solid with ellipsoidal cracks and spherical pores. It can model strong velocity dispersion between the low-frequency fracture scale flow and the high-frequency grain scale flow. It has been suggested that fluid mobility, combining viscosity and permeability, can cause velocity dispersion to be in the seismic

bandwidth. This has important implications as velocity dispersion results in frequency-dependent reflection coefficients and AVO which should be measured. Measurements of the relaxation parameter on both real and synthetic rocks have suggested very small values, implying dispersion outwith the seismic bandwidth. However, there is evidence to suggest that the correct combination of rock properties and saturating fluid can result in velocity dispersion within the seismic bandwidth. Hydrocarbon-bearing formations are likely to display exaggerated, anomalous levels of dispersion compared to brine-saturated areas and could be used to detect and monitor such reservoirs.

Chapter 3: AVO theory

3.1 Introduction

Linear approximations to the exact Zoeppritz reflection coefficients can provide useful insights into subsurface properties and have been an important tool in the search for hydrocarbon gas. Amplitude versus offset, AVO, seismic data can be inverted to provide qualitative estimates of a selection of parameters and should only be considered quantitative with appropriate well control. Inverted parameters, such as the fluid factor and Poisson's reflectivity, can be used to identify anomalous areas which deviate from a background trend that could be the result of hydrocarbon saturation. With careful consideration of the pitfalls associated with linear approximations, an interpretation can be made across a large lateral area of the subsurface to help identify prospective reservoirs.

3.2 Exact Zoeppritz equations

The exact solutions to the reflection and transmission coefficients at a single interface were first published by Zoeppritz (1919). I have chosen to reproduce the simpler matrix representation of the equations (from Hilterman 2001),

$$\begin{pmatrix} sin\theta_1 & cos\phi_1 & -sin\theta_2 & cos\phi_2 \\ -cos\theta_1 & sin\phi_1 & -cos\theta_2 & -sin\phi_2 \\ sin2\theta_1 & \frac{\alpha_1}{\beta_1}cos2\phi_1 & \frac{\rho_2\beta_2^2\alpha_1}{\rho_1\beta_1^2\alpha_2}sin2\theta_2 & -\frac{\rho_2\beta_2\alpha_1}{\rho_1\beta_1^2}cos2\phi_2 \\ cos2\theta_1 & -\frac{\beta_1}{\alpha_1}cos2\phi_1 & -\frac{\rho_2\alpha_2}{\rho_1\alpha_1}cos2\phi_2 & -\frac{\rho_2\beta_2}{\rho_1\alpha_1}sin2\phi_2 \end{pmatrix} \begin{pmatrix} RP \\ RS \\ TP \\ TS \end{pmatrix} = \begin{pmatrix} -sin\theta_1 \\ -cos\theta_1 \\ sin2\theta_1 \\ -cos2\phi_1 \end{pmatrix} \qquad (3\text{-}1)$$

where RP and RS are the reflected P- and S-wave coefficients, TP and TS are the transmitted P- and S-wave coefficients and $\theta_{1,2}$ and $\phi_{1,2}$ are the P- and S-wave angles of incidence and transmission respectively. To write the exact P-wave reflection coefficient using an analytical formula requires "*more than 80 multiplications and additions*" (Hilterman 2001) and I feel it is unnecessary to express it here. Whilst I gave some linear approximations to the exact P-wave reflection coefficient the Zoeppritz equations are used in their place for ultra-far offset AVO (Avseth *et al*., 2005) to model and invert beyond the critical angle. Roberts (2001) used the Zoeppritz equations to show the benefit in estimating S-wave velocity from ultra-far offset (up to 70°) data. However, due to the accuracy of linear approximations to the Zoeppritz equations up to 30° (Avseth *et al*., 2005), these are more commonly used (e.g. Cambois, 2000).

3.3 Approximations to Zoeppritz equations

The use of amplitude-versus-offset (AVO) as a lithology and fluid analysis tool has been utilised for over twenty years. Ostrander (1984) extended the early work of Muskat and Meres (1940) by calculating reflection coefficients for gas sands at non-normal angles of incidence by varying Poisson's ratio. He concluded that, with careful analysis of seismic reflection data, it was possible to distinguish between amplitude anomalies related to gas saturation and those due to other causes. There are many approximations to the exact P-wave reflection coefficients which provide insights into the more cumbersome Zoeppritz equations. All the approximations tend to follow the assumption that the differences in elastic properties between the reflecting mediums are small, where $\Delta V_P/V_P$, $\Delta V_S/V_S$ and $\Delta\rho/\rho$ are much less than one (Aki and Richards, 1980).

3.3.1 Bortfield approximation

Bortfield (1960) used a physical approach to determine an approximation to the exact P-wave reflection and transmission by introducing a transition layer between two mediums. He then developed a series expansion whereby the approximate reflection

coefficient is a superposition of all internal multiples. The series is then truncated so that only the zero- and first-order multiples are summed and the thickness of the transition layer is allowed to approach zero. The resultant P-wave reflection coefficient is

$$R(\theta_1) \approx \frac{1}{2}\log_e\left(\frac{V_{P2}\rho_2 cos\theta_1}{V_{P1}\rho_1 cos\theta_2}\right) + sin^2\theta_1\left(\frac{1}{q_1^2} - \frac{V_{P2}^2}{V_{P1}^2 q_2^2}\right)\left(2 + \frac{\log_e \rho_2/\rho_1}{\log_e V_{P2}/V_{P1} - \log_e q_2/q_1}\right). \quad (3\text{-}2)$$

The terms θ, V_P, ρ and q are defined in the Conventions and notations table (page xvi). Hilterman (2001) modified the above equation by removing the natural logarithms and I find it easier to gain an insight into the physical meaning using this approach,

$$R(\theta_1) \approx \frac{\rho_2 V_{P2} cos\theta_1 - \rho_1 V_{P1} cos\theta_2}{\rho_2 V_{P2} cos\theta_1 + \rho_1 V_{P1} cos\theta_2} + \left(\frac{sin^2\theta_1}{V_{P1}}\right)(V_{S1} + V_{S2})\left[3(V_{S1} - V_{S2}) + 2\frac{(V_{S2}\rho_1 - V_{S1}\rho_2)}{\rho_1 + \rho_2}\right]. \quad (3\text{-}3)$$

The first term is the reflection coefficient for a fluid-fluid interface and the second term, which depends on the shear-wave velocity, is called the rigidity factor. Hilterman (2001) compared the Bortfield approximation to the exact solution for a shale-sand interface at three depths under gas and water saturation. He concluded that;

(i) the rigidity term is almost identical under gas and water saturation,

(ii) the difference in the AVO response is almost solely the effect of the fluid-fluid term, and

(iii) the accuracy of the approximation reduces with depth.

The dependence on the fluid-fluid term shows how varying fluid saturation, along a horizon for example, can be measured and distinguished on the recorded seismic gathers.

3.3.2 Aki and Richards approximation

Aki and Richards (1980) calculated an approximation for reflection and transmission coefficients between similar half-spaces (where $\Delta V_P/V_P$, $\Delta V_S/V_S$ and $\Delta\rho/\rho$ are much less than one) and the P-wave reflection coefficient that is given as,

$$R(\phi) \approx \frac{1}{2}\left(1 - 4\frac{V_S^2}{V_P^2}sin^2\phi\right)\frac{\Delta\rho}{\rho} + \frac{1}{2cos^2\phi}\frac{\Delta V_P}{V_P} - 4\frac{V_S^2}{V_P^2}sin^2\phi\frac{\Delta V_S}{V_S} \qquad (3\text{-}4)$$

Again the terms ϕ, V_P, V_S, ρ, ΔV_P, ΔV_S and $\Delta\rho$ are defined in the Conventions and notations table (page xvi). A common simplification is to replace the angle ϕ with the angle of incidence θ_i so that equation 3-4 becomes

$$R(\theta_i) \approx \frac{1}{2}\left(1 - 4\frac{V_S^2}{V_P^2}sin^2\theta_i\right)\frac{\Delta\rho}{\rho} + \frac{1}{2cos^2\theta_i}\frac{\Delta V_P}{V_P} - 4\frac{V_S^2}{V_P^2}sin^2\theta_i\frac{\Delta V_S}{V_S}. \qquad (3\text{-}5)$$

The later linear approximations are all based upon this initial work by Aki and Richards (1980) but they group terms differently and apply further simplifications.

3.3.3 Shuey approximation

Shuey (1985) started with Aki and Richards approximation, equation 3-4, and substituted the average Poisson's ratio and the contrast in Poisson's ratio, σ and $\Delta\sigma$, in favour of V_s and ΔV_s using,

$$V_S^2 = V_P^2\frac{1-2\sigma}{2(1-\sigma)} \qquad (3\text{-}6)$$

and its derivative (Hilterman, 2001)

$$\frac{\Delta V_S}{V_S} \approx \frac{\Delta V_P}{V_P} - \frac{1}{4}\left[\frac{\Delta\sigma}{(1-\sigma)}\right]\left[\frac{1}{(0.5-\sigma)}\right]. \qquad (3\text{-}7)$$

This results in

$$R(\phi) \approx NI_P + \left[A_0 NI_P + \frac{\Delta\sigma}{(1-\sigma)^2}\right] sin^2\phi + \frac{1}{2}\frac{\Delta V_P}{V_P}(tan^2\phi - sin^2\phi) \quad (3\text{-}8)$$

where

$$NI_P \approx \frac{1}{2}\left(\frac{\Delta V_P}{V_P} + \frac{\Delta\rho}{\rho}\right), \quad (3\text{-}9)$$

$$A_0 = B - 2(1+B)\frac{1-2\sigma}{1-\sigma} \quad (3\text{-}10)$$

and

$$B = \frac{\Delta V_P/V_P}{\Delta V_P/\Delta V_P + \Delta\rho/\rho}. \quad (3\text{-}11)$$

The approximation in equation 3-8 shows which rock properties are significant at different ranges of incident angles. The acoustic impedance is at zero offset, Poisson's ratio contributes at mid offsets $(10° - 30°)$ and P-wave velocity contributes at far offsets $(30° - 90°)$, dominating at sufficiently far offsets. Once again, the simple approximation of replacing the angle ϕ with the angle of incidence θ_i results in the following approximation

$$R(\theta_i) \approx NI_P + \left[A_0 NI_P + \frac{\Delta\sigma}{(1-\sigma)^2}\right] sin^2\theta_i + \frac{1}{2}\frac{\Delta V_P}{V_P}(tan^2\theta_i - sin^2\theta_i). \quad (3\text{-}12)$$

3.3.4 "Conventional" approximation

One of the most commonly seen linear AVO approximations is,

$$R(\theta_i) \approx A + Bsin^2\theta_i \quad (3\text{-}13)$$

where *A* and *B* are known as the intercept and gradient and it is referenced to both Wiggins *et al*., (1983) and Shuey (1985). Hilterman references Wiggins *et al*., (1983) as producing the approximation,

$$R(\theta_i) \approx \frac{1}{2}\left(\frac{\Delta V_P}{V_P} + \frac{\Delta\rho}{\rho}\right) + \left[\frac{1}{2}\frac{\Delta V_P}{V_P} - 2\left(\frac{V_S}{V_P}\right)^2\left(\frac{2\Delta V_S}{V_S} + \frac{\Delta\rho}{\rho}\right)\right] sin^2\theta_i + \frac{1}{2}\frac{\Delta V_P}{V_P} tan^2\theta_i sin^2\theta_i \quad (3\text{-}14)$$

whilst Avseth *et al*., (2005) reference Shuey (1985) when presenting the equation,

$$R(\theta_i) \approx \frac{1}{2}\left(\frac{\Delta V_P}{V_P} + \frac{\Delta\rho}{\rho}\right) + \left[\frac{1}{2}\frac{\Delta V_P}{V_P} - 2\left(\frac{V_S}{V_P}\right)^2\left(\frac{2\Delta V_S}{V_S} + \frac{\Delta\rho}{\rho}\right)\right] sin^2\theta_i + \frac{1}{2}\frac{\Delta V_P}{V_P}(tan^2\theta_i - sin^2\theta_i). \quad (3\text{-}15)$$

These two equations are identical except for a typographical error in the third term in Hilterman's (2001) published approximation. If I drop the third term from equation 3-15 for $\theta_i < 30^o$ then I once more obtain,

$$R(\theta_i) \approx A + Bsin^2\theta_i \quad (3\text{-}16)$$

where

$$A \approx NI_P \approx \frac{1}{2}\left(\frac{\Delta V_P}{V_P} + \frac{\Delta\rho}{\rho}\right) \quad (3\text{-}17)$$

and

$$B = \frac{1}{2}\frac{\Delta V_P}{V_P} - 2\left(\frac{V_S}{V_P}\right)^2\left(\frac{2\Delta V_S}{V_S} + \frac{\Delta\rho}{\rho}\right). \quad (3\text{-}18)$$

When $V_P/V_S = 2$, *B* reduces to,

$$B = \frac{1}{2}\frac{\Delta V_P}{V_P} - \frac{\Delta V_S}{V_S} - \frac{1}{2}\frac{\Delta \rho}{\rho} = NI_P - 2NI_S \qquad (3\text{-}19)$$

and Castagna and Smith (1994) followed the approach of Wiggins *et al*., (1983) to determine that,

$$NI_P - 2NI_S = (A + B)/2. \qquad (3\text{-}20)$$

For simplicity I will refer to equation 3-16 as the two-term Shuey approximation.

3.3.5 Smith and Gidlow approximation

Stolt and Weglein (1985) proposed a method whereby elastic parameters can be estimated from seismic reflection data by using a set of weighted stacks. Smith and Gidlow (1987) described how time and offset-variant weights can be applied to seismic data to extract P- and S-wave reflectivities (sometimes called fractional velocity, Zhang, 2008), which they define as $\Delta V_P/V_P$ and $\Delta V_S/V_S$. They started with the Aki and Richards' approximation, equation 3-3, and rearranged it to obtain

$$R(\phi) \approx \frac{1}{2}\left(\frac{\Delta V_P}{V_P} + \frac{\Delta \rho}{\rho}\right) - 2\frac{V_S^2}{V_P^2}\left(2\frac{\Delta V_S}{V_S} + \frac{\Delta \rho}{\rho}\right) sin^2\phi + \frac{1}{2}\frac{\Delta V_P}{V_P} tan^2\phi. \qquad (3\text{-}21)$$

Equation 3-21 can then be reorganised in the fashion of Shuey (1985) so that the terms become progressively more important with an increasing angle of incidence,

$$R(\phi) \approx \frac{1}{2}\left(\frac{\Delta V_P}{V_P} + \frac{\Delta \rho}{\rho}\right) + \left[\frac{1}{2}\frac{\Delta V_P}{V_P} - 4\frac{V_S^2}{V_P^2}\frac{\Delta V_S}{V_S} - 2\frac{V_S^2}{V_P^2}\frac{\Delta \rho}{\rho}\right] sin^2\phi + \frac{1}{2}\frac{\Delta V_P}{V_P}(tan^2\phi - sin^2\phi) \qquad (3\text{-}22)$$

which is similar to Shuey's approximation. Smith and Gidlow (1987) then removed the density variation from equation 3-21 by replacing it with the relationship between density and P-wave velocity for water-saturated rocks (Gardner *et al*., 1974)

$$\frac{\Delta\rho}{\rho} \approx \frac{1}{4}\frac{\Delta V_P}{V_P} \qquad (3\text{-}23)$$

resulting in

$$R(\phi) \approx \left(\frac{5}{8} - \frac{1}{2}\frac{V_S^2}{V_P^2}sin^2\phi + \frac{1}{2}tan^2\phi\right)\frac{\Delta V_P}{V_P} + \left(-4\frac{V_S^2}{V_P^2}sin^2\phi\right)\frac{\Delta V_S}{V_S} \qquad (3\text{-}24)$$

and if I once again make the assumption that $\theta_i \approx \phi$ then

$$R(\theta_i) \approx \left(\frac{5}{8} - \frac{1}{2}\frac{V_S^2}{V_P^2}sin^2\theta_i + \frac{1}{2}tan^2\theta_i\right)\frac{\Delta V_P}{V_P} + \left(-4\frac{V_S^2}{V_P^2}sin^2\theta_i\right)\frac{\Delta V_S}{V_S}. \qquad (3\text{-}25)$$

3.3.6 Fatti approximation

Fatti *et al*. (1994) started with the rearranged Aki and Richards' (1980) approximation, equation 3-21, and considered the case when Gardner's rule did not hold. In that case P- and S-wave impedances, $I = \rho V_P$ and $J = \rho V_S$, can be substituted in such a way that,

$$\frac{\Delta I}{I} = \frac{1}{2}\left(\frac{\Delta V_P}{V_P} + \frac{\Delta\rho}{\rho}\right) \qquad (3\text{-}26)$$

and

$$\frac{\Delta J}{J} = \frac{1}{2}\left(\frac{\Delta V_S}{V_S} + \frac{\Delta\rho}{\rho}\right) \qquad (3\text{-}27)$$

resulting in

$$R(\phi) \approx \frac{1}{2}\frac{\Delta I}{I}(1 + tan^2\phi) - 4\frac{V_S^2}{V_P^2}\frac{\Delta J}{J}sin^2\phi - \left[\frac{1}{2}\frac{\Delta\rho}{\rho}tan^2\phi - 2\frac{V_S^2}{V_P^2}\frac{\Delta\rho}{\rho}sin^2\phi\right]. \qquad (3\text{-}28)$$

For angles of incidence less than 30° the third term can be dropped resulting in the approximation

$$R(\phi) \approx \frac{1}{2}\frac{\Delta I}{I}(1 + tan^2\phi) - 4\frac{V_S^2}{V_P^2}\frac{\Delta J}{J}sin^2\phi \qquad (3\text{-}29)$$

and if I again make the assumption that $\theta_i \approx \phi$ then

$$R(\theta_i) \approx \frac{1}{2}\frac{\Delta I}{I}(1 + tan^2\theta_i) - 4\frac{V_S^2}{V_P^2}\frac{\Delta J}{J}sin^2\theta_i. \qquad (3\text{-}30)$$

Equation 3-30 can now be written in terms of zero-offset P- and S-wave reflectivities, NI_P and NI_S, so

$$R(\theta_i) \approx NI_P(1 + tan^2\theta_i) - 4NI_S\frac{V_S^2}{V_P^2}sin^2\theta_i. \qquad (3\text{-}31)$$

3.3.7 Verm and Hilterman approximation

Verm and Hilterman (1995) separated the normal incidence P-wave reflectivity term (NI_P) and the $\Delta\sigma$ term by incorporating equations 3-6, 3-10 and 3-11 into 3-12 to obtain

$$R(\phi) \approx NI_P\left[1 - \frac{4V_S^2}{V_P^2}sin^2\phi\right] + \frac{\Delta\sigma sin^2\phi}{(1-\sigma)^2}\frac{4V_S^2}{V_P^2}sin^2\phi + \frac{1}{2}\frac{\Delta V_P}{V_P}\left(tan^2\phi - \frac{4V_S^2}{V_P^2}sin^2\phi\right). \qquad (3\text{-}32)$$

Furthermore, they assumed a ratio of $V_P/V_S = 2$, $\theta_i = \phi$ and ignored the last term for $\theta_i < 30^o$, which results in the much simpler approximation

$$R(\theta_i) \approx NI_P cos^2\theta_i + PRsin^2\theta_i \qquad (3\text{-}33)$$

where *PR* is Poison's reflectivity $(\Delta\sigma/(1-\sigma)^2)$.

3.4 AVO inversion

As already stated, the weighted stacking method can be used to estimate P- and S-wave reflectivities using a least-squares inversion. Equation 3-25 is used for this process and is simplified below for clarity

$$R(\theta_i) \approx A_1(\theta_i)\frac{\Delta V_P}{V_P} + A_2(\theta_i)\frac{\Delta V_S}{V_S}. \qquad (3\text{-}34)$$

In AVO analysis it is assumed that the recorded amplitudes can be associated with the reflection coefficients through a basic transformation. This is a very simplified view and Liner (1999) gives a more in-depth discussion into the factors affecting the recorded amplitudes. The amplitudes, $D(t)$, are a result of a convolution of the reflectivity, $r(t)$, the wavelet, $w(t)$, and noise, $n(t)$, after Partyka *et al.*, (1999) in the form of

$$r(t) * w(t) + n(t) = D(t). \qquad (3\text{-}35)$$

Since I am interested in using the amplitude variation with offset information I must extend the data matrix, $D(t)$, to be offset dependent, $D(t,n)$, where amplitudes are described for all time samples, *t*, and all receivers, *n*. If I assume knowledge of the velocity model, either through modelling or stacking velocities, the coefficients $A_1(\theta_i)$ and $A_2(\theta_i)$ can be calculated through ray tracing where the raypaths obey Snell's law at each velocity contrast (e.g. Dahl and Ursin, 1991) to make the replacement,

$$A_1(\theta_i) = A_1(t,n) \qquad (3\text{-}36)$$

and

$$A_2(\theta_i) = A_2(t,n). \qquad (3\text{-}37)$$

For each time sample, the offset-dependent amplitudes,

$$D(t,n) = A_1(t,n)\frac{\Delta V_P}{V_P} + A_2(t,n)\frac{\Delta V_S}{V_S} \qquad (3\text{-}38)$$

can be rewritten as a multiplication of matrices,

$$\begin{bmatrix} D(t,1) \\ \vdots \\ D(t,n) \end{bmatrix} = \begin{bmatrix} A_1(t,1) & A_2(t,1) \\ \vdots & \vdots \\ A_1(t,n) & A_2(t,n) \end{bmatrix} \begin{bmatrix} \frac{\Delta V_P}{V_P} \\ \frac{\Delta V_S}{V_S} \end{bmatrix}. \qquad (3\text{-}39)$$

Substituting *R* for the reflection amplitudes and *A* for the offset-dependent constants results in

$$R = A. \begin{bmatrix} \frac{\Delta V_P}{V_P} \\ \frac{\Delta V_S}{V_S} \end{bmatrix} \qquad (3\text{-}40)$$

which can be solved using a basic least-squares inversion without weights (Sheriff and Geldart, 1995),

$$\begin{bmatrix} \frac{\Delta V_P}{V_P} \\ \frac{\Delta V_S}{V_S} \end{bmatrix} = (A^T A)^{-1} A^T R \qquad (3\text{-}41)$$

for every time sample, generating P- and S-wave reflectivity traces for each input central midpoint (CMP) gather. I can follow a similar approach to invert for the intercept, *A*, and the gradient, *B*, from equation 3-13.

3.5 Fluid factor

Smith and Gidlow (1987) extended the use of their weighted stacks to define the fluid factor trace, ΔF, as

$$\Delta F = \frac{\Delta V_P}{V_P} - 1.16\frac{V_S}{V_P}\frac{\Delta V_S}{V_S}. \qquad (3\text{-}42)$$

This expression uses the empirically-derived mudrock line discussed in section 2.6. For all water-saturated clastic silicates, or mudrocks, ΔF is close to zero. When gas (or oil to a lesser extent) is substituted for water the P-wave velocity reduces whilst scarcely affecting the S-wave velocity. This is simply a Gassmann (1951) fluid substitution effect where the bulk fluid modulus of the saturated rock (κ_{sat}) reduces which in turn reduces the magnitude of the P-wave velocity whilst the S-wave velocity is barely affected.

Smith and Gidlow (1987) concluded that the resultant fluid factor trace should be negative at the top of a gas-sand and positive at the bottom (assuming low impedance sand). They also concluded that for clastic sections a weighted stack should reduce all reflections to zero except for gas, making it a "*true direct hydrocarbon indicator*" (Smith and Gidlow, 1987).

Fatti *et al*., (1994) used the derivative of the mudrock line, equation 2-15, to substitute zero-offset P- and S-wave reflection coefficient, NI_P and NI_S, for the P- and S-wave reflectivities. They then defined the fluid factor trace as

$$\Delta F = NI_P - 1.16\frac{V_S}{V_P}NI_S. \qquad (3\text{-}43)$$

The velocity ratio can be replaced with a gain function, γ, so that equation 3-43 becomes

$$\Delta F = NI_P - \gamma NI_S \qquad (3\text{-}44)$$

where ideally γ is a locally-generated value. In the absence of local shear wave velocity Smith and Sutherland (1996) calculated a 'global' optimum fluid factor, γ,

of 0.63 from the twenty-five sets of gas sands, brine sands and shale reported in Castagna and Smith (1994). The Hampson-Russell AVO Theory (2004) defines the fluid factor by using Gardner's rule (equation 3-23) to replace the S-wave reflectivity with the intercept and gradient when $V_P/V_S = 2$, to obtain

$$\Delta F = 1.252A + 0.58B. \qquad (3\text{-}45)$$

I have chosen to follow the approach of Fatti *et al*., (1994) and used the optimum fluid factor of 0.63 and combined equations 3-17 and 3-19 into 3-44 so that

$$\Delta F = 0.685A + 0.315B \equiv NI_P - 0.63NI_S. \qquad (3\text{-}46)$$

This is approximately half the values described in equation 3-45, and reflects the different velocity approximations made in the two derivations.

Cambois (2000) argued that if an amplitude anomaly is the result of a statistical leak between the intercept and gradient then the resultant scaled fluid factor (or Poisson's reflectivity) is simply a far-angle stack and care must be taken to ensure the anomaly is a true geophysical signal. I have discussed crossplotting stacked amplitudes and gradients, which are statistically uncorrelated, to aid this type of interpretation in section 3.9.

3.6 Poisson's reflectivity

I have introduced the Poisson's reflectivity (PR) in equation 3-33 (Verm and Hilterman, 1995) as

$$PR = \frac{\Delta\sigma}{(1-\sigma)^2} \qquad (3\text{-}47)$$

as it controls the far-offset reflectivity. Smith and Gidlow (1987) defined it in terms of P- and S-wave velocity, as the "*pseudo-Poisson's ratio reflectivity*",

$$\frac{\Delta q}{q} = \frac{\Delta V_P}{V_P} - \frac{\Delta V_S}{V_S} \qquad (3\text{-}48)$$

where $q = \frac{V_P}{V_S}$.

These two expressions are equivalent and if I rewrite equation 3-48 using the definitions of *A* and *B* from equations 3-17 and 3-19, I obtain,

$$\frac{\Delta q}{q} = \frac{\Delta \mathrm{V_P}}{\mathrm{V_P}} + \frac{\Delta \rho}{\rho} - \frac{\Delta \mathrm{V_S}}{\mathrm{V_S}} - \frac{\Delta \rho}{\rho} = 2(NI_P - NI_S) = A + B = PR \qquad (3\text{-}49)$$

which is another linear combination of *A* and *B* where α and β are equal to one. Castagna and Smith (1994) consider the above linear combination of *A* and *B* to be an excellent hydrocarbon indicator, although they go on to argue that the weighted *A* and *B* of the fluid factor, is better at zeroing out the background trend.

3.7 AVO factors and problems

The ultimate goal of AVO analysis is to extract information regarding the subsurface, and any potential hydrocarbon reservoirs, from seismic data. Hilterman (2001) lists six reservoir properties that can be estimated;

(i) pore fluid,
(ii) porosity,
(iii) lithology,
(iv) thickness,
(v) water saturation and
(vi) permeability,

and believes that the first four have the highest probability of being successfully extracted. It is promising that Hilterman believes pore fluid has a high chance of being extracted as I am most interested in measuring dispersion associated with hydrocarbon saturation.

Whilst the theory behind AVO is well documented in literature, Avseth *et al*., (2005) argue that failures associated with AVO analysis are due to the improper application of the theory. Reconnaissance AVO can be used to create sub-stacks of the seismic data (intercept, gradient, Poisson's reflectivity and fluid factor) to be scanned for anomalies that can be qualitatively interpreted in terms of lithology and fluid content. It is within these sub-stacks that a background wet response must be identified and anomalies are classified as deviations from this trend. If well log data is lacking then rock physics depth trends (such as Gardner's rule and the mud-rock line) can be used but the resultant AVO analysis will be qualitative. Cambois (2000) argues that it is unlikely that standard P-wave AVO can ever be quantitative due to noise contaminating the inversion of shear reflectivity, and care must be taken to be sure an anomaly is a true AVO effect. Well control can provide unambiguous high resolution of geological variables that can aid in AVO parameter interpretation (Jain and deFigueiredo, 1982) as well as building synthetic models (e.g. Martinez, 1993). AVO modelling, using well log information, can be useful in determining the significance of inverted parameters (Sheriff and Geldart, 1995). Whilst well logs provide additional data to constrain AVO interpretation, they introduce extra cost and are only valid for isolated locations and do not provide the continual lateral coverage of surface seismic data. Despite the drawbacks of interpreting qualitative reconnaissance AVO without well control, the prevalence of P-wave seismic data makes it a useful tool in the continuing search for hydrocarbon deposits.

There are many factors that can alter the AVO signature in seismic data and Liner (1999) lists four mechanisms that affect the reflection amplitude in decreasing order;
(i) lithology, sandstone vs. shale,
(ii) gas effect, gas > 10% vs. gas < 10%,
(iii) porosity, high vs. low, and
(iv) clay content, high vs. low.
Whilst this is a useful rule-of-thumb, there are settings where the reflection amplitude gives a false AVO response. Both Liner (1999) and Avseth *et al*., (2005) noted that residual gas saturation can give the same AVO response as commercial or

full gas saturation and it is only through careful density estimation that these cases might be distinguished. Ross and Kinman (1995) describe how a shale-coal interface or a shale-calcareous shale can produce false bright spots. It is this type of uncertainty that led Houck (1999 and 2002) to develop a Bayesian statistical approach to help quantify geological interpretation and reduce ambiguity. His method attempts to reduce the uncertainties associated with both the AVO measurement and interpretation used to generate a probabilistic lithologic model of the subsurface.

Since AVO analyses exploit the relative amplitude relationships across time and offsets, care must be taken within the processing flow to preserve these and not introduce any artefacts. Automatic gain control (AGC) is a non-physical amplitude recovery algorithm that can be useful for imaging purposes (Yilmaz, 1999) but it is not consistent with AVO approximations for inversion. AGC is principled used as an imaging tool to artificially boost low amplitude reflections. The dataset with which I performed my reconnaissance AVO analysis, described in Chapter 5 has undergone processing steps that have preserved the relative amplitudes; source designator, noise attenuation, deconvolution and prestack time migration including normal moveout, dip moveout and spherical divergence corrections (Processing Report, 2004).

3.8 AVO class definition

Rutherford and Williams (1989) developed a classification system to distinguish AVO variations from the top of gas sands. Their three initial classes all have negative gradients whilst Castagna and Swan (1997) proposed an additional class, IV, with a positive gradient, for sands capped by shale with a larger V_P/V_S ratio. Ross and Kinman (1995) made a distinction between a typical Class II reflection with a negative intercept and a Class IIp reflection that has a positive intercept and undergoes a phase change (the top dashed line in figure 3.1). I have summarised the classifications in table 3.1 (from Avseth *et al*., 2005) where the quadrant refers to the

crossplot of intercept and gradient in figures 3.2 and 3.3. These are discussed further in the next section.

Class I sands are typically characterised by a dimming on CMP gathers. Class II sands have weak amplitudes on stacked data due to their small intercepts and Class IIp sands have phase reversals on CMP gathers. Class III sands are the classical bright spot anomalies that have accounted for a large percentage of AVO analyses (Rutherford and Williams, 1989). There has been a recent update of the AVO classification system by Young and LoPiccolo (2003) where they separated reflections into five conforming and five non-conforming sands. Whilst their approach is more thorough than those described previously, I prefer, and will use, the extended Rutherford and Williams' classification system as it offers a simple way of categorising AVO anomalies and in detecting false anomalies on crossplot and stacked data.

Class	**Relative Impedance**	**Quadrant**	***A***	***B***	***A*B* Product**
I	high-impedance	4^{th}	+	-	-
IIp	no or low contrast	4^{th}	+	-	-
II	no or low contrast	3^{rd}	-	-	+
III	low impedance	3^{rd}	-	-	+
IV	low impedance	2^{nd}	-	+	-

Table 3.1: Summary of the AVO classification (from Avseth *et al*., 2005).

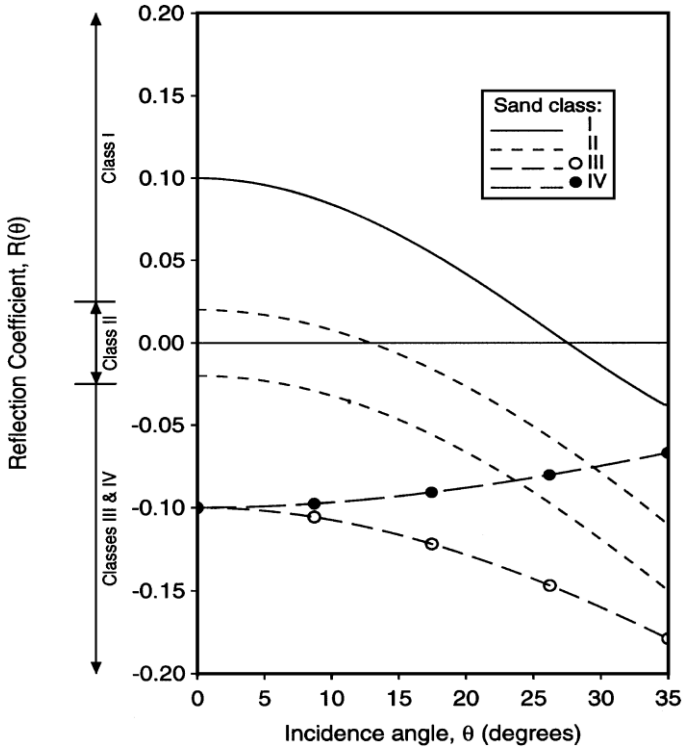

Figure 3.1: Reflection coefficient versus angle of incidence from top of gas-sands showing the distribution of the classification system; I, II, III and IV (from Castagna *et al.*, 1998).

3.9 Crossplotting

Following on from the summary of the intercept and gradient classes (table 3.1), sand classes can be graphically represented by crossplotting them onto the *x* and *y* axes. Figure 3.2 (from Castagna *et al*., 1998) shows how the extended Rutherford and Williams' AVO classification can be represented as a crossplot. It shows how anomalous AVO signatures vary from the theoretical background trend where the intercept is proportional to the negative value of the gradient. A more accurate background relationship between the intercept and gradient can be acquired through well calibration of shale and brine-filled sands (Sbar, 2000 and Smith and Sondergeld, 2001). An interpretation of deviations from a calibrated background trend will be more reliable than one made from an observed background trend with no well control.

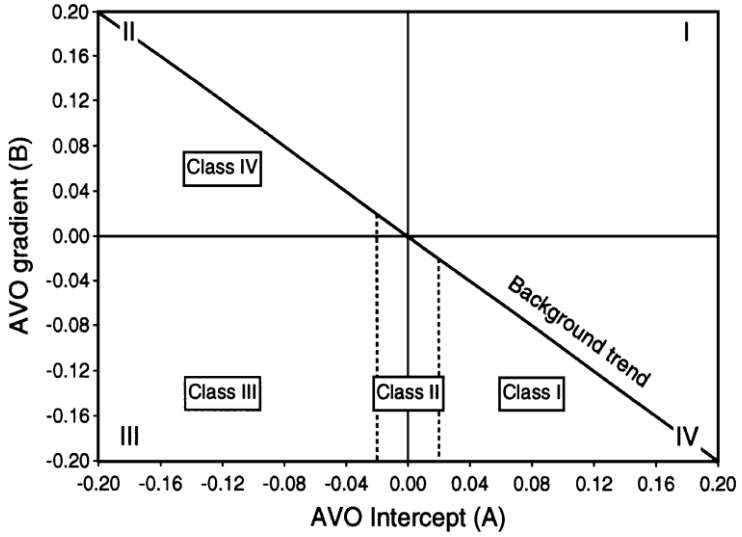

Figure 3.2: Crossplot of *A* versus *B* with AVO classification regions marked below the background trend line (from Castagna *et al.*, 1998).

Simm *et al*., (2000) described how noise on intercept and gradient crossplots can be minimised by using a horizon window rather than an arbitrary time window and by only selecting the maxima and minima amplitude points. When all sample points of the waveform are selected they argue that this introduces unwanted noise between clusters on the plots. They go on to describe how trends caused by random noise, variation in porosity, the introduction of gas and the shale content all mask rock property information contained within crossplots. Cambois (2000) described the leaking of noise from the intercept into the gradient which disguises the genuine signal. He demonstrated how the intercept and gradient become statistically correlated with a negative relationship, called "*crosstalk*". To determine whether anomalous areas are due to statistical artefacts or are true lithologic or pore-fluid indicators he argued that the stacked amplitudes and gradients are statistically uncorrelated and should be crossplotted to verify any anomalous trends. This influence of noise was also described by Cambois (1998) as causing the large difference in the order of magnitude of the gradient compared to the intercept witnessed in real data as well-log data shows that they should be similar.

Castagna and Swan (1997) argued that brine-saturated sandstone and shale *A*'s and *B*'s follow a well-defined background trend and that, within a limited depth range,

deviations from a background trend are indicative of hydrocarbons or unusual lithology. They made the recommendation "*that all AVO analysis be done in the context of looking for deviations from an expected background response*".

Figure 3.3 (from Ross, 2000) shows a crossplot of a large, Class III, amplitude anomaly due to gas saturation within a 200ms window. The background trend is highlighted in the central, grey ellipse and the deviations from this are marked in yellow and blue.

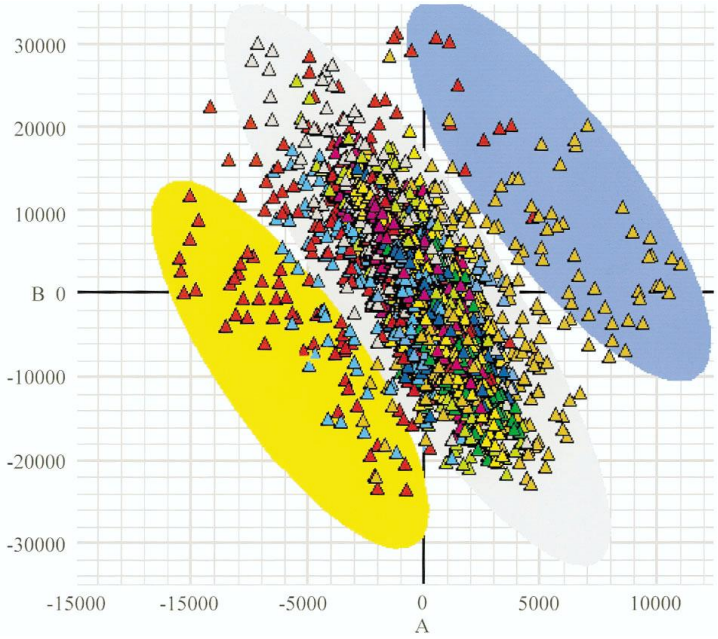

Figure 3.3: Crossplot of *A* versus *B* over a gas-sand bright spot in a 200ms window, the central grey ellipse is the background trend (from Ross, 2000). The blue and yellow ellipses capture the amplitudes from the top and bottom of a Class III reflection respectively.

3.10 4-D AVO

Improvements in seismic acquisition and processing have made the use of time-lapse, or 4-D, seismic data more common. A base survey is acquired over an area and then a monitor survey is acquired at a later date to match the original base survey, as closely as possible. The two are then processed with the aim of producing base, monitor and difference seismic volumes. Boyd-Gorst *et al.*, (2001) and

Gouveia *et al*., (2004) describe the application of 4-D seismic methods to two Palaeocene reservoir sands in the North Sea to characterise the drainage pattern and oil-water contact, OWC, movement. In both studies synthetic models were designed and they were able to detect the OWC movement as water replaced oil but the pressure change was below noise levels and not detectable. Tura *et al*., (2006) used time-lapse stacked seismic to determine the OWC in the Niger River Delta as the time-lapse AVO was not able to provide pressure-saturation discrimination.

Anderson and van Wijngaarden (2007) reported using AVO inversion outputs from two 3-D seismic data sets to measure the change in the acoustic impedance and the P- and S-wave velocity ratio over time. They concluded that this method was an excellent way to "*interpret and visualise 4D inversion data*". Smith *et al*., (2008) also reported successfully modelling 4-D AVO effects to differentiate changes in pressure and water or gas saturation. They were able to classify the effect that pressure increase and gas saturation had upon inverted intercept and gradient. Subsequently, they used this technique to distinguish between a pressure increase and an increase in gas saturation from a real 4-D dataset which appeared the same on a full stack difference plot. These recent results from Anderson and van Wijngaarden (2007) and Smith *et al*., (2008) show how 4-D seismic data analysis can be extended from the standard stacked seismic analysis for OWC movement to provide pressure and saturation discrimination to aid in reservoir monitoring and to aid in production.

3.11 Discussion and conclusions

I have shown how linear approximations to the exact Zoeppritz equations of the P-wave reflection coefficient can provide useful insight into invertible parameters at near offsets ($< 30°$). Using existing methodologies I can invert the two-term Shuey approximation for the intercept and gradient. These can be combined to generate the fluid factor and Poisson's reflectivity which are useful hydrocarbon indicators. I have also shown another linear approximation that can be inverted to find P- and S-wave reflectivities which depend on the velocity contrast between the two reflecting

mediums. This has potential for use in a frequency-dependent AVO scheme as I have previously shown how it is velocity dispersion that results in a frequency-dependent reflection coefficient. The next chapters discuss how spectral decomposition can be incorporated into the AVO analysis to take advantage of the theoretical prediction of strong velocity dispersion associated with hydrocarbons.

Many factors affect the AVO response making it difficult to extract reliable information due to false signals and noise. Whilst it is possible to make an interpretation of the saturating pore fluid, without well control to constrain the data, all inverted parameters should always be viewed as a qualitative description against a background trend and not as a quantitative analysis. Furthermore, I have shown how AVO class definitions and crossplotting of the intercept and gradient can help in the identification and interpretation of reflection events on seismic gathers. By carefully examining the AVO behaviour of a reflection on CMP gathers I can predict the expected background response on an *A* versus *B* crossplot and any deviations from it.

Chapter 4: Spectral decomposition

4.1 Introduction

Spectral decomposition offers a method for decomposing seismic traces into two dimensional time-frequency planes whose resolution is best approximated using a method with a variable window length. The matching pursuit method, MPM, is an adaptive process that searches for the best matched wavelet from a dictionary in order to decompose the signal rather than using an arbitrary wavelet, as found in the continuous wavelet transform, CWT. I will be describing a balancing methodology to remove the source overprint from decomposed data, to study the spectral amplitudes-versus-offset and to detect dispersion. I will show how the MPM offers superior resolution to the CWT and how tuning effects can be mistaken for dispersion.

4.2 Spectral decomposition methods

Spectral decomposition is a technique used to determine the temporal and frequency content of a time series. Whilst the Fourier integral (Mallat, 1998) can be used to compute instantaneous attributes using the real and imaginary terms of a signal (Taner *et al*., 1979 and Barnes, 1991) the signal content is averaged over the window length of the integral. The short time Fourier transform (STFT) uses a shorter window length so that the signal, $f(t)$, is transformed by a time-shifted window function, $\phi(t)$,

$$STFT(\omega,\tau) = \int_{-\infty}^{\infty} f(t)\bar{\phi}(t-\tau)e^{-i\omega t}dt \qquad (4\text{-}1)$$

where the Fourier integral is localised at the translation time, τ. Due to the fixed window length of the STFT it can be difficult to simultaneously achieve good temporal and frequency resolution. The above shortcomings of the Fourier integral are limited to non-stationary signals; a stationary signal has constant frequency

content in time (i.e. a sin or cosine signal). Seismic data are non-stationary and spectral decomposition techniques are able to resolve the time-dependence of the spectra "*whose locations vary in signal and time*" (Mallat and Zhang, 1993). Many spectral decomposition algorithms exist and the results are non-unique so an appropriate method should be chosen to suit the chosen setting. Castagna and Sun (2006) define spectral decomposition as "*any method that produces a continuous time-frequency analysis of a seismic trace*" and I require sufficiently high resolution to isolate frequency-dependent reflectivities and amplitudes as discussed in the previous chapter.

The classical Heisenberg Uncertainty Principle, HUP, states that the product of the temporal and frequency resolution is limited and thus spectral decomposition can never be exact. Mallat (1998) describes it as

$$\sigma_t^2 \sigma_\omega^2 \geq \frac{1}{4} \qquad (4\text{-}2)$$

where

$$\sigma_t^2 = \int_{-\infty}^{\infty} t^2 |g(t)|^2 dt \qquad (4\text{-}3)$$

and

$$\sigma_\omega^2 = \int_{-\infty}^{\infty} \omega^2 |G(\omega)|^2 d\omega \qquad (4\text{-}4)$$

are the temporal and frequency variances around average values of the time, *u*, and frequency, ξ, for a signal, $g(t)$, and its Fourier transform, $G(\omega)$. This implies that the best combined resolution achievable is constant and is not dependent on the spectral decomposition algorithm employed. Maultzsch (2005) describes Heisenberg boxes within which the decomposed energy is spread across the variances σ_t and σ_ω and that the area cannot be less than one half due to the HUP. Castagna and Sun

(2006) argue that non-windowing methods circumvent this limitation and are only limited by the bandwidth of the digital signal. However, the HUP is a fundamental limitation of sampling data and the overall resolution can never be better than that described in equation 4-2.

4.3 Comparison of methods

4.3.1 Synthetic test data

Following the methods described by both Castagna *et al*., (2003) and Zhang (2008) I generated a synthetic seismic trace to compare a windowing and non-windowing spectral decomposition method. I used a combination of nine Ricker wavelets with dominant frequencies, 10Hz, 20Hz, 30Hz and 40Hz at 0.1s, 0.3s, 0.5s and 0.8s. Table 4.1 summarises the exact arrangement of the wavelets and figure 4.1 shows the pre and post-stack traces. The superposition of the amplitudes results in higher amplitudes at 0.5s and 0.8s than at 0.1s and 0.3s and this is reflected in the time-frequency displays.

Time	Dominant Frequency
0.10 s	40 Hz
0.30 s	10 Hz
0.30 s	40 Hz
0.50 s	30 Hz
0.52 s	30 Hz
0.80 s	20 Hz
0.80 s	30 Hz
0.82 s	20 Hz
0.82 s	30 Hz

Table 4.1: Summary of times and dominant frequencies of the nine Ricker wavelets used to design the synthetic test trace.

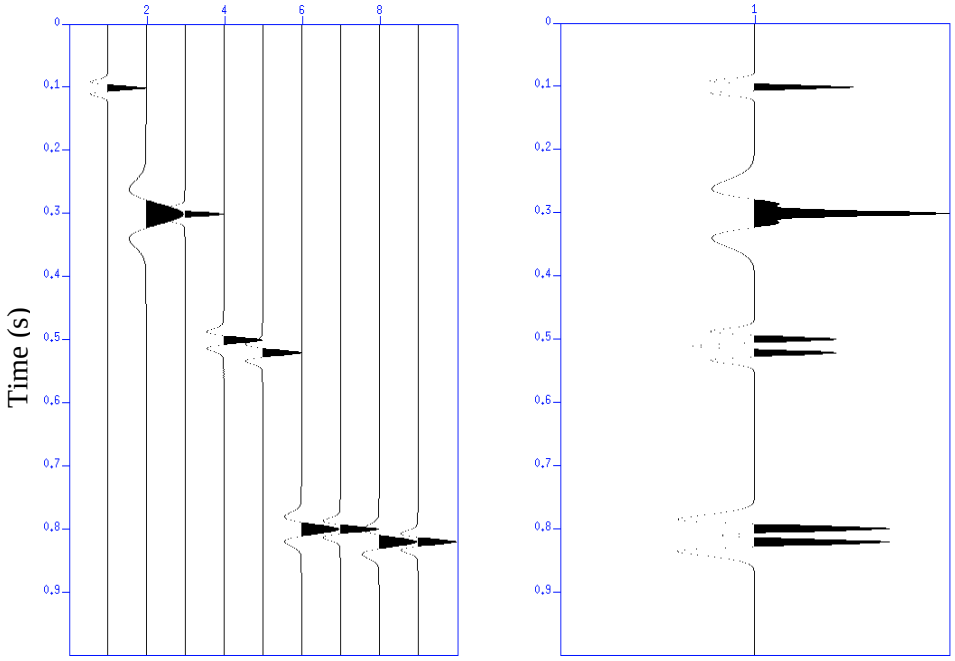

(a) (b)

Figure 4.1: Pre (a) and post (b) stack of the nine Ricker wavelets described in table 4.1 to generate a synthetic test trace.

4.3.2 Continuous wavelet transform

Seismic data decomposed using either the short-time Fourier transform, STFT, or the windowed Fourier transform, WFT, cannot achieve good simultaneous temporal and frequency resolution. A narrow time window offers good temporal resolution but poor frequency resolution whilst a wider window offers better frequency resolution to the detriment of the temporal resolution. The continuous wavelet transform, CWT, addresses this drawback by using a window that varies with both time and frequency. A kernel wavelet, ψ, is defined at time τ, called the translation, with window width σ, called the scale or dilation and frequency parameter ω, which must be greater than, or equal to, five to avoid problems at high temporal resolution (Chakraborty and Okaya, 1995). I have used the Morlet wavelet where $\psi(t)$ and $\bar{\psi}(\omega)$ are localised in time and frequency and is given by,

$$\psi(t) = e^{i\omega t}e^{-t^2/2}. \qquad (4\text{-}5)$$

The kernel wavelet satisfies two admissibility conditions (Chakraborty and Okaya, 1995 and Sinha *et al*., 2005) which are that (i) $\psi(t)$ should be absolutely integrable, $\int_{-\infty}^{\infty}|\psi(t)|dt < \infty$, and square integrable, $\int_{-\infty}^{\infty}|\psi(t)|^2 dt < \infty$, and (ii) $\psi(t)$ is band-limited with zero mean, $\int_{-\infty}^{\infty}\left|\frac{\bar{\psi}(\omega)}{\omega}\right| d\omega < \infty$. The CWT is then the convolution of the seismic trace, $g(t)$, with wavelets, $\psi(t)$, scaled by σ and translated along the time index by τ to calculate a time-scale map, $w(\sigma,\tau)$, or scalogram defined by Chakraborty and Okaya (1995) as,

$$W(\sigma,\tau) = \frac{1}{\sqrt{\sigma}}\int_{-\infty}^{\infty} g(t)\psi^*\left(\frac{t-\tau}{\sigma}\right) dt. \qquad (4\text{-}6)$$

I then converted the scalogram into the more intuitive time-frequency map by transforming the scale which is inversely proportional to the centre frequency, f_c, of the wavelet by using f_c/f (Sinha *et al*., 2005).

Due to the variable scale factor, Mallat (1998) described the CWT convolution as a "*wavelet transform with dilated band-pass filters*". I have recreated the approach of Zhang (2008) to test the bandwidth at 12.5Hz, 17.5Hz, 25Hz and 35Hz on my synthetic trace to determine the optimum parameter value. My results, figure 4.2, are similar to those reported by Zhang (2008). When the band is large (25Hz and 35Hz) there are strong stripes on the time axis due to noisy side lobes on the decomposed traces, as noted by Castagna and Sun (2006). When the band is smallest (12.5Hz) there appears to be a combination of horizontal and vertical noise stripes on both axes and this effect is minimised when a bandwidth of 17.5Hz is selected. Furthermore, it is at this parameterisation that the two different frequencies are separated at 0.8s whilst the other bandwidths spread the decomposed energy from 10Hz to 50Hz. The compromise between temporal and frequency resolution that I discussed earlier is apparent. As the bandwidth increases the temporal resolution increases and the frequency resolution decreases. The intermediate bandwidth value of 17.5Hz offers a compromise choice as it suppresses the horizontal and vertical noise stripes whilst generating the best combined time-frequency resolution. Whilst the CWT uses a time and frequency varying window compared with the STFT, the reliance on windowing and the arbitrary choice of the kernel wavelet that may not be best suited to the input data, degrades the achievable resolution (Torrence and Campo, 1998).

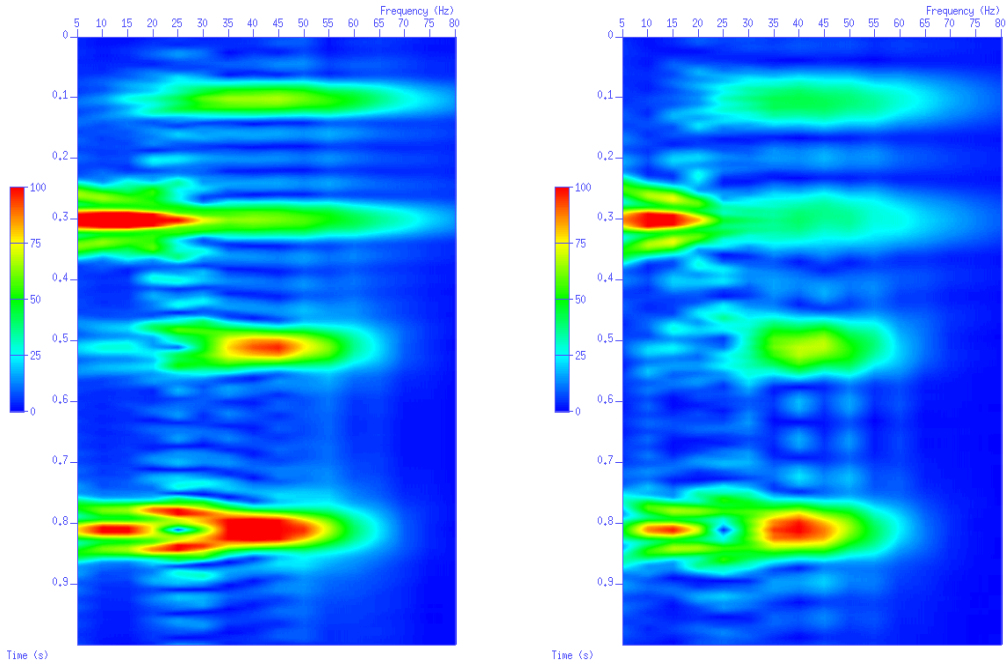

(a) bandwidth 12.5Hz (b) bandwidth 17.5Hz

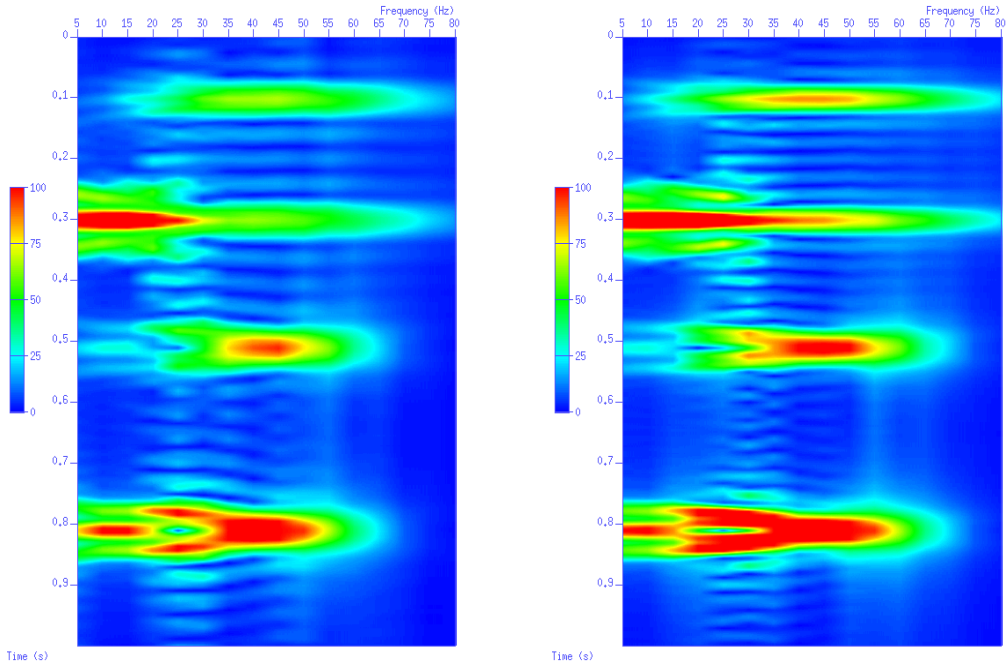

(c) bandwidth 25.0Hz (d) bandwidth 35.0Hz

Figure 4.2: CWT time-frequency planes for the test trace from figure 4.1b width frequency bandwidths of (a) 12.5Hz, (b) 17.5Hz, (c) 25.0Hz and (d) 35.0Hz.

4.3.3 Matching pursuit method

Rather than using an arbitrary kernel wavelet, the matching pursuit method, MPM, (Mallat and Zhang, 1993) selects wavelets from a redundant dictionary to give the best match to the signal structure. It iteratively selects a waveform, from a dictionary of time-frequency atoms, best adapted to approximate part of the seismic trace, $g(t)$. The waveforms in the dictionary are described by four variables, dilation (σ), translation (τ), modulation (ξ) and phase (ϕ). Mallat and Zhang's description of the MPM uses a dictionary of Gabor functions and the resultant time-frequency gather is the sum of the Wigner distributions or "*Gaussian blobs*" of the selected wavelets depending on σ_n, τ_n, ξ_n and ϕ_n. The Wigner distribution is given by (Wang, 2007)

$$Wg_\gamma = \frac{1}{2\pi}\int_{-\infty}^{\infty} m\left(t+\frac{\tau}{2}\right)\overline{m}\left(t-\frac{\tau}{2}\right)\exp[-i\omega\tau]d\tau \qquad (4\text{-}7)$$

where $\overline{m}$ is the complex conjugate of the wavelet, m.

I implemented the MPM algorithm using Morlet wavelets, $m(t)$, (Zhang *et al*., 2008)

$$m(t) = exp\left[-\left(\frac{\ln 2}{\pi^2}\right)\frac{\omega_m^2(t-\tau)^2}{\sigma^2}\right]exp[i(\omega_m(t-\tau)+\phi)] \qquad (4\text{-}8)$$

where the wavelet is centred at time τ, has mean angular frequency ω_m and σ controls the wavelet width and is similar to the expression shown in equation 4-5. Zhang *et al*., (2008) describe the MPM algorithm that I have used within this thesis and show how it is an iterative two-step process that adaptively extracts the best matching waveform to the data. The seismic trace can always be described as a combination of wavelets, $m_{\gamma_n}(t)$, with amplitude, a_n, and the residual energy, $R^n g(t)$, so that

$$g(t) = \sum_{n=0}^{N-1} a_n m_{\gamma_n}(t) + R^n g(t) \qquad (4\text{-}9)$$

where $R^0 g(t) = g(t)$. In stage one, three of the four wavelet parameters (τ_n, ξ_n and ϕ_n) I have estimated by performing complex trace analysis (Taner *et al*., 1979) and in stage two they are optimised whilst the remaining parameter (σ_n) is searched for within a comprehensive dictionary of wavelets and is based on the following equation,

$$m_{\gamma_n}(t) = \arg\max\left|\langle R^n g, m_{\gamma_n}\rangle\right|. \qquad (4\text{-}10)$$

Finally after obtaining the optimal parameterisation of $\gamma_n = (\sigma_n, \tau_n, \xi_n, \phi_n)$ I have calculated the amplitude of the wavelet using,

$$a_n = \left|\langle R^n g, m_{\gamma_n}\rangle\right| \qquad (4\text{-}11)$$

and the subsequent waveform is subtracted from the seismic trace leaving the residual energy, $R^{(n)} g(t)$. This iterative process continues until the residual falls below a user defined threshold and the remaining energy is considered to be data noise. The MPM is the cross-correlation of wavelets against the seismic trace which Castagna and Sun (2006) equate to an iterative CWT performing hundreds or thousands of wavelet transforms for each trace. This has a direct impact on the computational cost which for my synthetic test trace would take approximately ten minutes for a CWT decomposition and approximately three hours for an MPM decomposition.

In my synthetic test of the MPM I am determining the effect that residual noise has upon the resolution of the time-frequency gathers. I have chosen decomposed energy percentages values of 70%, 80%, 90% and 99.9%, corresponding to residual noise levels of 30%, 20%, 10% and 0.1%. The effect of increasing the decomposed energy is clear in figure 4.3. The MPM decomposition is able to resolve the higher amplitude events at 0.3s and 0.8s compared with the lower amplitude events at 0.1s and 0.5s. Even when decomposing 99.9% of the energy, no noise was introduced onto the resultant time-frequency gather. Like the CWT, the MPM has difficulty in

accurately defining the arrival of the interfering wavelets at 0.5s and 0.8s. It has, however, greatly improved the overall temporal and frequency resolution and there are no noise stripes on either of the axes. The MPM has generated exceptionally clean gathers with no side lobes and little noise. As a result of this synthetic test I have chosen to run the MPM decomposing 99.9% of the energy as the increased amplitude resolution is important when I am comparing the behaviour of spectral anomalies verses offset.

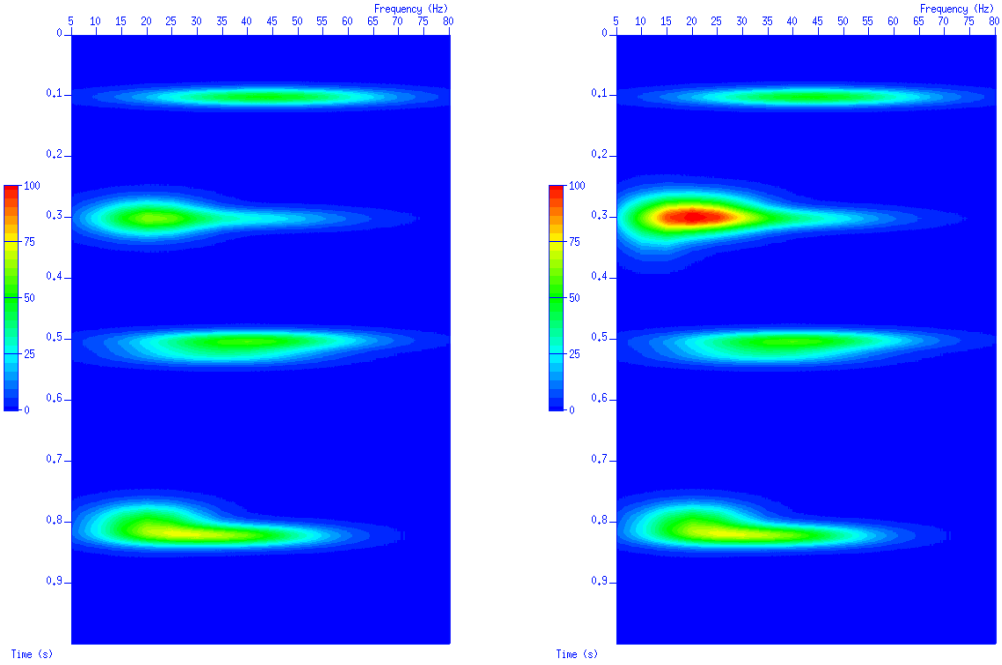

(a) decomposed energy 70%

(b) decomposed energy 80%

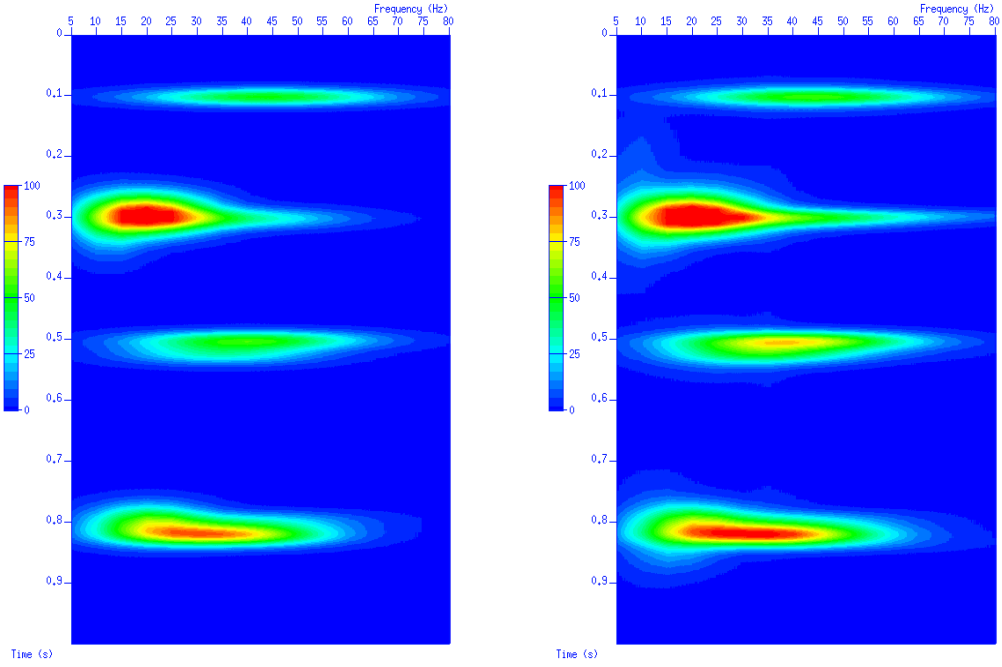

(c) decomposed energy 90%

(d) decomposed energy 99.9%

Figure 4.3: MPM time-frequency planes for the synthetic trace from figure 4.1b, when the decomposed energy percentage was (a) 70%, (b) 80%, (c) 90% and (d) 99.9%.

4.4 Spectral balancing

Spectral decomposition transforms seismic amplitudes, $D(t,n)$, at time t and receiver n into spectral amplitudes, $S(t,n,f)$, at frequency f such that,

$$D(t,n) \leftrightarrow S(t,n,f). \qquad (4\text{-}12)$$

Following Partyka *et al*., (1999) the seismic and spectral amplitudes have an overprint from the source wavelet and must be removed if the true spectral behaviour of the geology and saturating fluid is desired. Otherwise, the wavelet spectrum dominates. Various authors have described approaches to remove the effect of the source wavelet; spectral stabilisation (Burnett *et al*., 2003), spectral scaling (Marfurt and Kirlin, 2001) and spectral balancing (Odebeatu *et al*., 2006). I have designed a method for removing the effect of the source wavelet by designing a suitable weight function, $w(f)$, such that I balance the spectral amplitudes using

$$B(t,n,f) = S(t,n,f)w(f) \qquad (4\text{-}13)$$

and the amplitudes at different frequencies become comparable. There are two settings in which I consider spectral balancing within this thesis, two-layer and more than two-layer synthetics.

4.4.1 Two-layer balancing

In the simple two-layer synthetic case there is only one P-wave primary reflection. The top layer is always elastic whilst the bottom half-space is either an elastic or dispersive material. A dispersive material is defined by a separate elastic tensor at every frequency within the range $1\text{Hz} - 250\text{Hz}$. The elastic material is then defined by calculating V_P and V_S from the 1Hz dispersive tensor and the known density, ρ, using,

$$V_P = \sqrt{\frac{\lambda+2\mu}{\rho}} \qquad (4\text{-}14)$$

and

$$V_S = \sqrt{\frac{\mu}{\rho}}. \qquad (4\text{-}15)$$

I chose to select the dominant frequency of the source Ricker wavelet to be the reference frequency to which I balanced the spectrally decomposed amplitudes as it has the maximum amplitude. The reflected wavelets on each iso-frequency gather are windowed and I calculated the maximum amplitude at each frequency and receiver, $MAX\big(A(f,n)\big)$. The weight function is then designed using the elastic spectral amplitudes so that they are all mathematically equal to the amplitudes of the reference frequencies using,

$$w(f,n) = \frac{MAX\big(A_{ref}(f,n)\big)}{MAX\big(A(f,n)\big)}. \qquad (4\text{-}16)$$

The weight function designed from the elastic synthetic, $w_e(f,n)$, is subsequently used to balance the dispersive iso-frequency gathers so that,

$$B_e(t,n,f) = S_e(t,n,f)w_e(f,n) \qquad (4\text{-}17)$$

and

$$B_d(t,n,f) = S_d(t,n,f)w_e(f,n). \qquad (4\text{-}18)$$

Using this receiver by receiver approach retains the AVO character of the reflection and any frequency-dependence of the spectral amplitudes. It shows why obtaining accurate amplitude estimates from the spectral decomposition algorithms is important as any inaccuracies can be magnified during the balancing.

4.4.2 More than two-layer balancing

The two-layer spectral balancing method is designed as the base case. However, when more layers and primary reflections are added into the synthetic model the balancing is actually simplified. When working with synthetic data I ensured that the top two materials are elastic so that the first reflection is elastic. For real data I picked a shallow reflection event that I assumed to be from an elastic-elastic boundary. These shallow, elastic reflections are used to design a weight function that automatically balances all deeper spectral amplitudes and removes the source overprint whilst retaining any dispersive characteristics. The weight function, w, is dependent only on the two elastic materials and not on any deeper materials or reflections so that,

$$B(t,n,f) = S(t,n,f)w(f,n). \qquad (4\text{-}19)$$

The weight function exploits the fact that the seismic data can be expressed as a convolution of the reflectivity with the source wavelet (equation 3-35). In my balancing method I am effectively deconvolving the source wavelet from the spectral amplitudes to leave the reflectivities, represented as spectral amplitudes. Any elastic reflections will have approximately equal spectral amplitudes whilst dispersive spectral amplitudes will retain the frequency bias of the reflectivity.

4.5 Uses in seismic data analysis

Partyka *et al*., (1999) first proposed the use of spectral decomposition to image and map thin-bed sands and to identify geologic discontinuities in 3-D seismic data. They linked the behaviour of the amplitude spectra to the acoustic properties of thin-bedded sands. On the seismic data the reflections interfere, resulting in a composite event that has notches on the spectra. They linked the notches on the phase spectra to lateral discontinuities and mapped changes in the rock mass across horizon slices. Marfurt and Kirlin (2001) followed a similar approach by creating a multi-attribute, joining coherence and peak frequency to delineate structural units and channel

boundaries. They concluded that this technique was more robust than the spectral notch technique (Partyka *et al*., 1999) used to quantify the thickness of a thin sand channel in the presence of noise. Whilst they believe a well log constrained acoustic impedance inversion to provide a superior thin-bed attribute, the necessary well control is often lacking and the use of spectrally-decomposed attributes can be advantageous as it can be used across an entire seismic volume.

Castagna *et al*., (2003) suggest four ways in which spectral decomposition can be used in the detection of hydrocarbons. The first method is to help identify reservoirs with anomalously high attenuation related to hydrocarbon saturation in thick reservoirs. The second method is in the detection of low frequency shadows below bright spot gas reservoirs, which has been used as a substantiating hydrocarbon indicator for some time. Taner *et al*., (1979) detected them using the instantaneous frequency. Ebrom (2004) suggested ten mechanisms, six stack-related and four non-stack related, that could generate low frequency shadows seen on stacked data beneath gas reservoirs. It is worth noting that one of the non-stack mechanisms is "*very low Q in the reservoir*", which was the first suggestion that Castagna *et al*., (2003) made for the use of spectral decomposition as a hydrocarbon indicator. The third suggestion is in the detection of preferential reservoir illumination due to the tuning frequency. Burnett *et al*., (2003) shows results of spectral decomposition analysis from the Burgos basin in Mexico that support both the first and third method listed by Castagna *et al*., (2003). The fourth and final suggested use is with frequency-dependent AVO (discussed by Chapman *et al*., 2006 and Odebeatu *et al*., 2006), which I have studied in this thesis by introducing spectrally decomposed data into classical AVO analyses.

Zhao *et al*., (2006) apply spectral decomposition to a time-lapse dataset to generate another 4-D interpretation tool. Despite the potential of this application they reported difficulties in obtaining a reliable difference volume when performing spectral decomposition to either the base and monitor surveys or to the seismic difference volume. However, it remains an area that may provide additional insights into fluid

saturation change and the swept thickness of the reservoir if sufficiently high resolution can be obtained with an appropriate spectral decomposition algorithm.

4.6 Tuning cube

As mentioned in the previous section, Castagna *et al*., (2003) argue that spectral decomposition can be used to identify areas of preferential illumination due to tuning. Odebeatu *et al*., (2006) carried out an analysis on a wedge model using the Stockwell transform (Stockwell *et al*., 1996) and concluded that it can be difficult to distinguish between tuning and dispersion. I recreated their approach to determine the effect that the spectral decomposition method has on the tuning frequency. I created a wedge style model with eleven synthetic gathers composed of six receivers at 100m spacing with material parameters described in table 4.2. I used a 40Hz Ricker as my source wavelet, and varied the thickness of the third layer from 10m – 330m at 40m intervals to generate nine synthetics. I used ANISEIS (Taylor, 1990), which is a reflectivity code, to generate the synthetics and it outputs the *z*- and *r*-components separately which I added using the following relationship,

$$A_T = \sqrt{A_z^2 + A_r^2} \qquad (4\text{-}20)$$

to approximate the total amplitude. I applied a layered-model spherical divergence correction (Newman, 1973) and then applied a normal moveout, NMO, correction to flatten the gathers. Finally, I stacked the gathers and performed spectral decomposition on the post-stack traces (figure 4.4) using the CWT and MPM, and using the parameters I described in section 4.3, at frequencies 10, 20, 30, 40, 50, 60 70 and 80Hz. I used the elastic primary reflected wavelet from the top two layers to design my weight function and balanced the iso-frequency gathers, using 40Hz as my reference frequency.

I analysed both time-frequency displays for each synthetic, and time-synthetic displays for each frequency, to identify any tuning effects associated with the

interfering wavelets. However, for brevity I have chosen to display only a selection of the time-frequency displays here.

Layer	Thickness	V_P (ms^{-1})	V_S (ms^{-1})	Density ($g.cm^{-3}$)
1	500 m	2743	1394	2.06
2	500 m	2500	1250	2.02
3	10 – 330 m	2743	1394	2.06
4	Half-space	2571	1486	2.04

Table 4.2: Material parameters for the wedge synthetics to test the effect of tuning using the CWT and MPM decompositions.

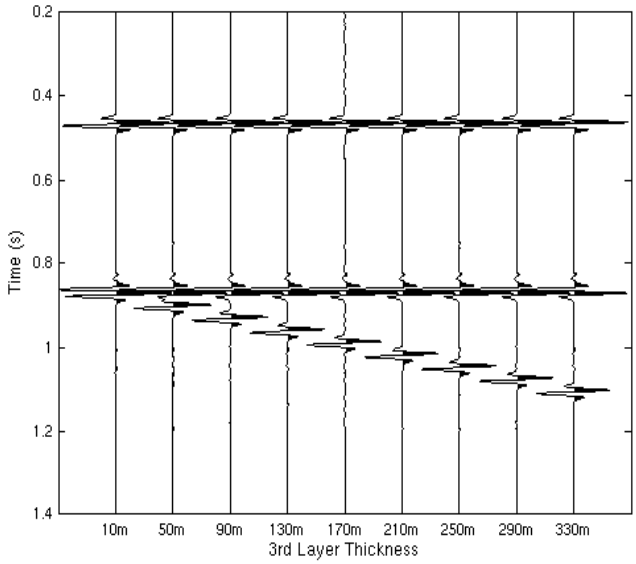

Figure 4.4: The nine stacked traces from the synthetic gathers with varying thickness of the third layer, from 10m to 330m at 40m intervals.

In figures 4.5, 4.6 and 4.7, I have plotted the results from the balanced spectrally decomposed traces, using the CWT and MPM, from the synthetic model when layer three is 10m, 130m and 330m thick. As observed in the earlier synthetic tests the MPM has achieved better frequency and temporal resolution than the CWT decomposition. The horizontal notching from the CWT is the result of side-lobes on the decomposed traces and this makes interpretation between two interfering or closely separated wavelets difficult. The MPM can resolve the two reflected wavelets

when layer three is just 50m thick but it is not until the third layer is approximately 130m thick that the CWT can resolve the two wavelets, figure 4.6(b). On the 10Hz and 20Hz decomposed traces the CWT leaves a distinctive notch at the peak amplitude which disappears as the frequency increases and wavelet width decreases. The 80Hz amplitude from both the CWT and MPM decompositions appears to have been balanced poorly and is most likely the result of systematic errors in the design of the weight function. When the initial spectral amplitude is small the balancing coefficient is large and any errors in the amplitude resolution become magnified. In this case there is little energy in the 80Hz decomposition using both the CWT and the MPM and, whilst the top reflection is mathematically balanced, the deeper reflections remain unbalanced. When the third layer is thinnest, 10m, both decompositions using the CWT and MPM are difficult to interpret and could be mistaken for frequency-dependent AVO. Figure 4.5(a) shows the result for the CWT and the spectral amplitude of the composite wavelet increasing with frequency, indicating dispersion. The MPM result shows a slight dimming at 40Hz and 50Hz compared with the other frequencies which also makes interpretation difficult. My results show that the MPM offers such a higher temporal resolution than the CWT that the uncertainty between tuning and dispersion without a detailed velocity model can be minimised.

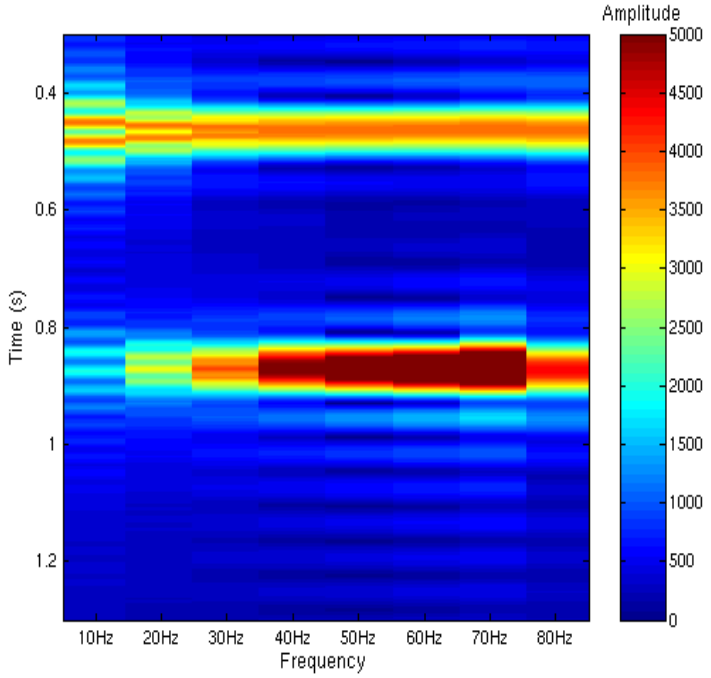

(a) CWT

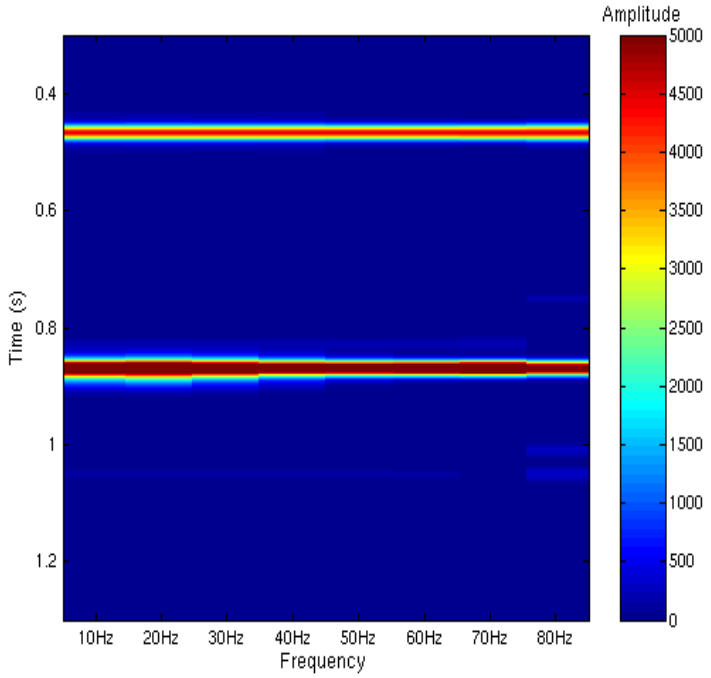

(b) MPM

Figure 4.5: The spectrally decomposed synthetic when layer three is 10m thick using the CWT and the MPM. Both methods show a "*tuned*" result due to the interfering wavelets.

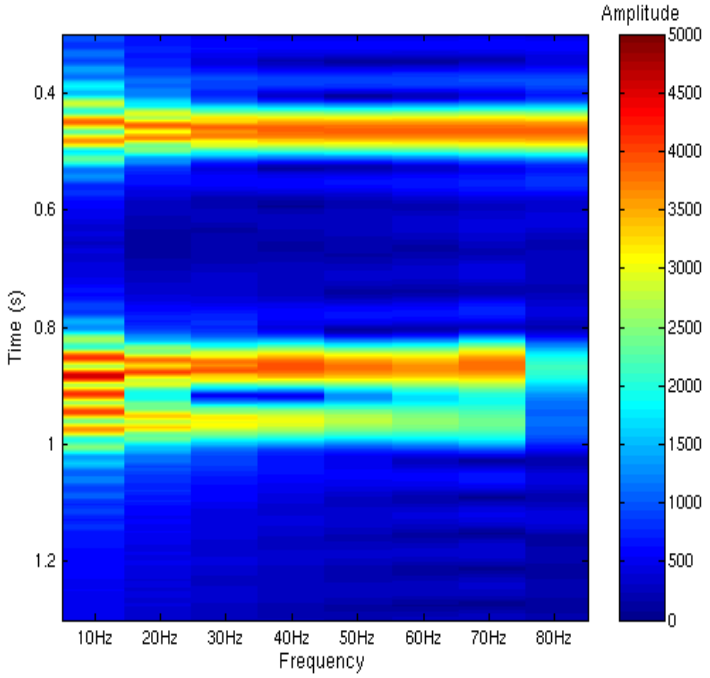

(a) CWT

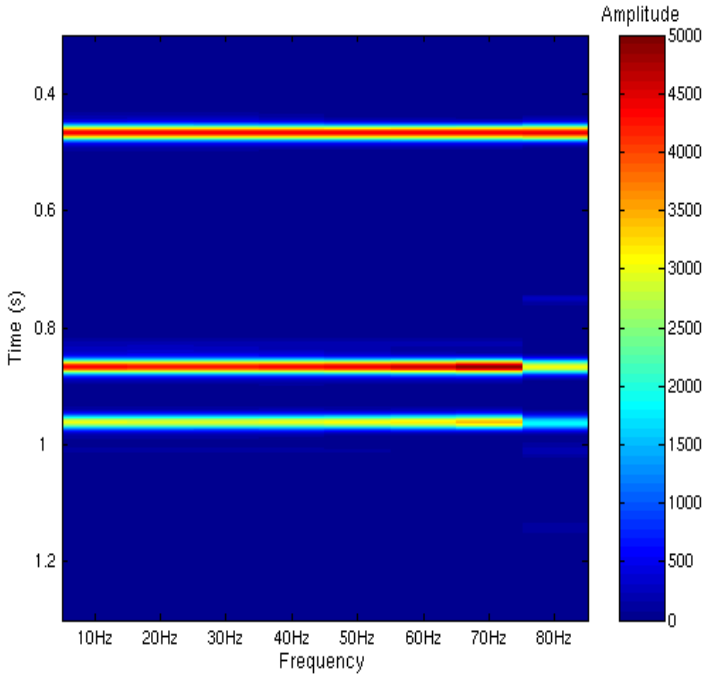

(b) MPM

Figure 4.6: The spectrally decomposed synthetic when layer three is 130m thick using the CWT and the MPM. This is the earliest that the CWT is able to properly resolve the second and third reflections, whilst the MPM achieved this at 50m thickness.

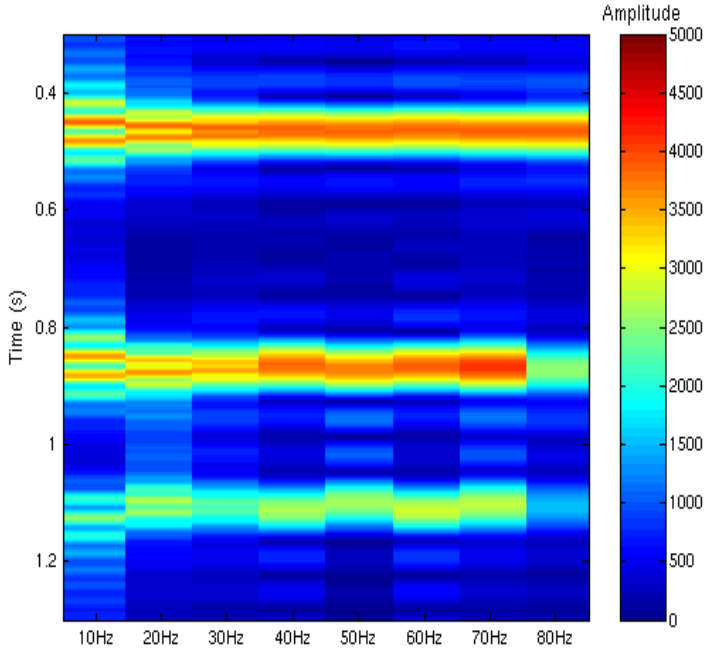

(a) CWT

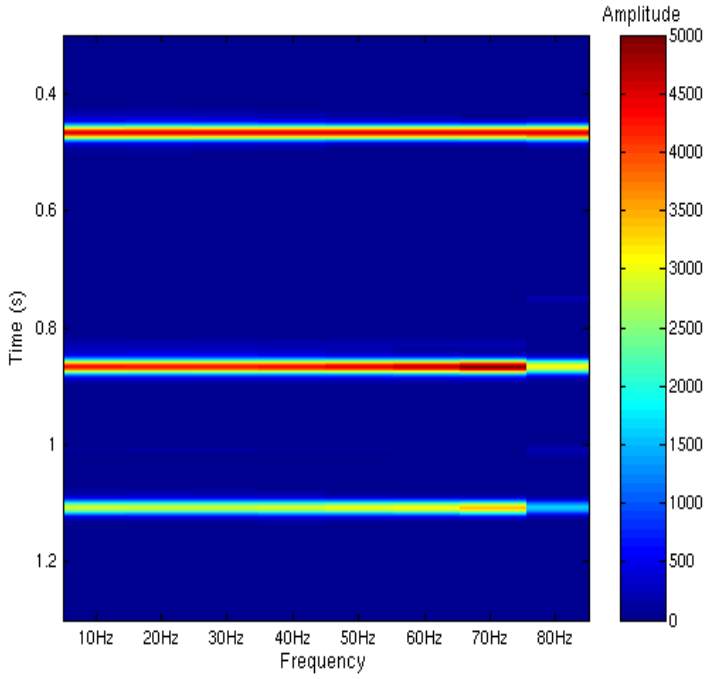

(b) MPM

Figure 4.7: The spectrally decomposed synthetic when layer three is 330m thick using the CWT and the MPM. Whilst both methods can resolve the two reflected wavelets the amplitude of the 80Hz iso-frequency trace has been poorly resolved using both techniques.

4.7 Discussions and conclusions

I have introduced spectral decomposition and shown how it allows the analysis of time-varying frequency content from seismic gathers. Achieving sufficiently high resolution is a key limitation in some of the older, windowing-based methods and the more recent MPM avoids this by using an adaptive dictionary of wavelets best suited to the data. It is more time-consuming due to the iterative nature of the algorithm but the width of the decomposed wavelet is on a similar scale to the original seismic wavelet whilst the CWT decomposed wavelet is almost double the width. I have measured and judged the temporal resolution of the two decompositions by looking at the alignment and spread of the decomposed energy and concluded that the MPM is superior to the CWT. I carried out synthetic tests on both the CWT and MPM to determine optimal parameter estimation and have concluded that using a band of 17.5Hz for the CWT and energy percentage of 99.9% for the MPM achieved the best resolution.

I have described spectral balancing methods for both a two-layer and more than two-layer models whereby the overprint of the source wavelet is removed from the decomposed spectral amplitudes. By designing a weight function I have interpreted the balanced spectral amplitudes in much the same way as classical AVO methods are used to identify frequency-dependent reflectivities associated with hydrocarbon saturation. I tested a synthetic wedge model to determine how the CWT and MPM dealt with decomposing interfering wavelets from thin bed reflections. The improved resolution of the MPM over the CWT minimises the interference of the decomposed wavelets as I was able to identify them separately at 50m for the MPM versus 130m for the CWT. I intend to incorporate balanced spectral decomposed amplitudes into a frequency-dependent AVO methodology to identify elastic and dispersive reflections. Good temporal, frequency and amplitude resolution is important to detect the subtle signatures associated with changes in the saturating fluid and its bulk modulus.

Chapter 5: Integrated AVO and spectral analysis

5.1 Introduction

In this Chapter I will describe how I performed an integrated AVO and spectral analysis of two marine seismic lines, provided to me with a high-density stacking velocity and three geologically picked horizons. After stacking the data I identified six anomalous areas along one of the horizons at approximately two seconds. Using a decimated and smoothed version of the stacking velocity I have been able to invert the data according to Shuey's linear two-term approximation to the exact P-wave reflection coefficient. I created substacks and crossplots using the inverted intercept and gradient and interpreted them following the extended Rutherford and Williams' classification scheme. I spectrally-decomposed the stacked lines using both the CWT and MPM algorithms at a selection of frequencies and balanced them using a shallow, elastic reflection between 0.8s and 1.0s. I have interpreted four of the six initial areas as being Class III reflections with low-frequency signatures as predicted from frequency-dependent AVO theory. I interpreted the other two areas as being Class III reflections but without a low-frequency signature. Integrating the spectral analysis with the AVO has enabled me to differentiate six Class III reflections with and without spectral responses that are consistent with frequency-dependent AVO theory.

5.2 Dataset

5.2.1 Inline and crossline

I was provided with NMO corrected central mid-point (CMP) gathers along two intersecting marine seismic lines from a North Sea dataset by the Marathon Oil Company; inline 620 (IL) and crossline 4921 (XL). The XL was generated by

extracting a succession of CMP gathers from inlines acquired using the same source geometry as the IL and it contained no extra anisotropic information.

The CMP gathers had been processed by a contractor and I was supplied with the report (Processing Report, 2004). A minimum-phase source designature was applied using a gun source signature. Noise was attenuated in the FX domain and in both the shot and receiver-based τ-p domain. Gun and channel scalars were applied to compensate for differences in amplitudes from the source and recording sensitivity. This step ensures that the input and recorded energy is comparable for all shots and receivers. Finally a pre-stack migration was applied to the gathers that incorporated a normal moveout, dip moveout and spherical divergence correction using a smooth velocity function. The resultant CMP gathers that I was provided with have retained their relative amplitudes and are suitable for AVO analyses.

The stacked IL and XL data are shown in figure 5.1 along with three picked structural horizons. The *Wdb 6Trov* transects six areas which have large stacked amplitudes at approximately 2s, three each on the IL and XL. These areas are highlighted in ellipses on figure 5.2 whilst table 5.1 summarises the CMP ranges over which they extend. The *Sele Trough* is just above and the *Balder Trough* is just below this area and shows more lateral continuity on their reflected horizons. Figure 5.2 shows the three horizons and anomalies in greater detail. It shows the structural geology that the horizons have been picked from. All sections in this Chapter are plotted on a normalised scale of ± 1, and all interpretations are done within the context of identifying deviations from a background trend (Castagna and Swan, 1997). The intersection point between IL 620 and XL 4921 is indicated with a black line on all subsequent sections.

Line	CMP Range	Area	Notes
IL 620	4600 – 4700	*1st*	
IL 620	4780 – 4870	*2nd*	
IL 620	4910 – 5020	*3rd*	Intersects the flank of *2nd* XL area
XL 4921	350 – 430	*1st*	
XL 4921	610 – 840	*2nd*	Intersects the flank of *3rd* IL area
XL 4921	950 – 1190	*3rd*	

Table 5.1: Summary and shorthand naming reference of the anomalous stacked amplitudes highlighted on figure 5.1.

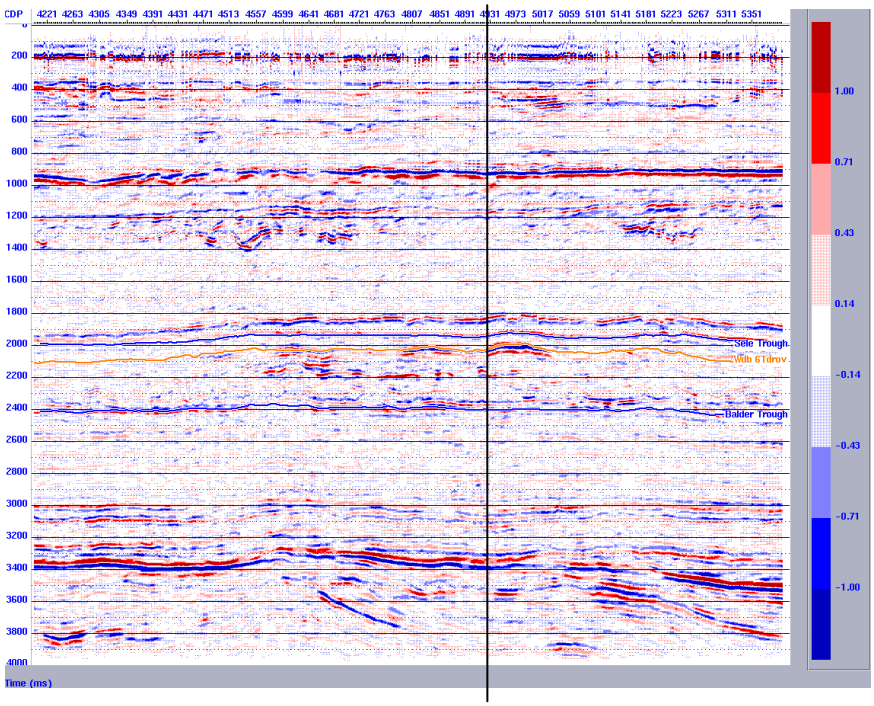

(a) IL

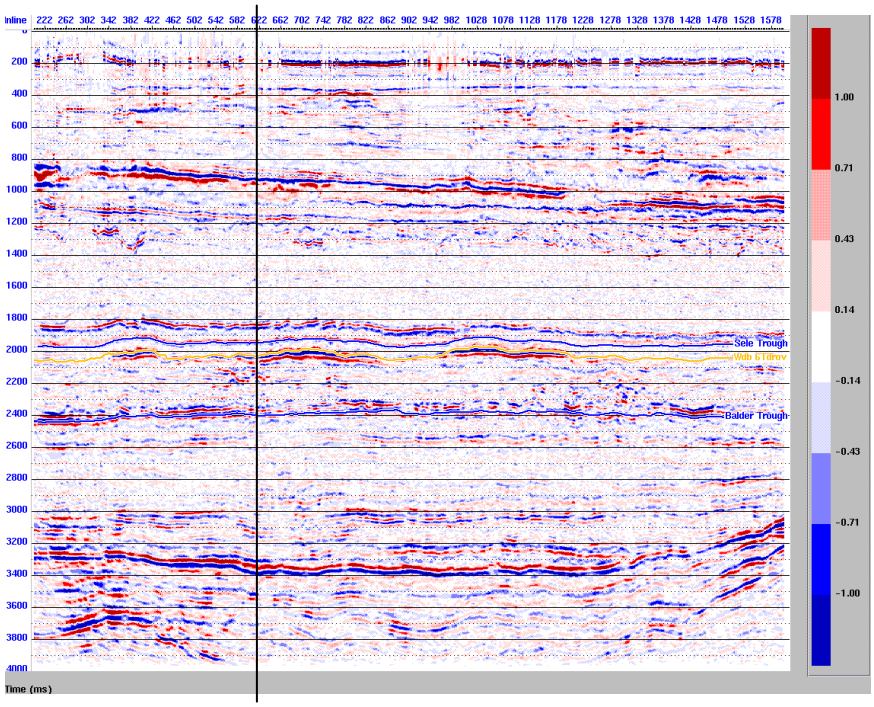

(b) XL

Figure 5.1: Stacked IL and XL with the three structural horizons shown. The intersection points are marked with a black line. The upper blue line at ~2000ms marks the *Sele Trough*, the yellow line at ~2100ms marks the *Wdb 6Trov* horizon and the lower blue line at ~2400ms marks the *Balder Trough* horizon.

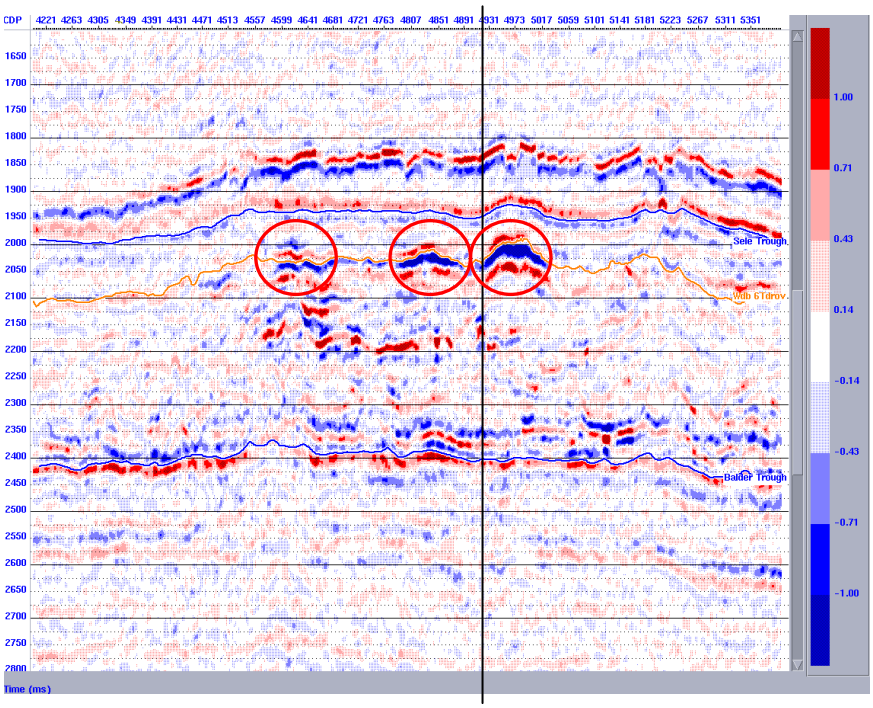

(a) IL

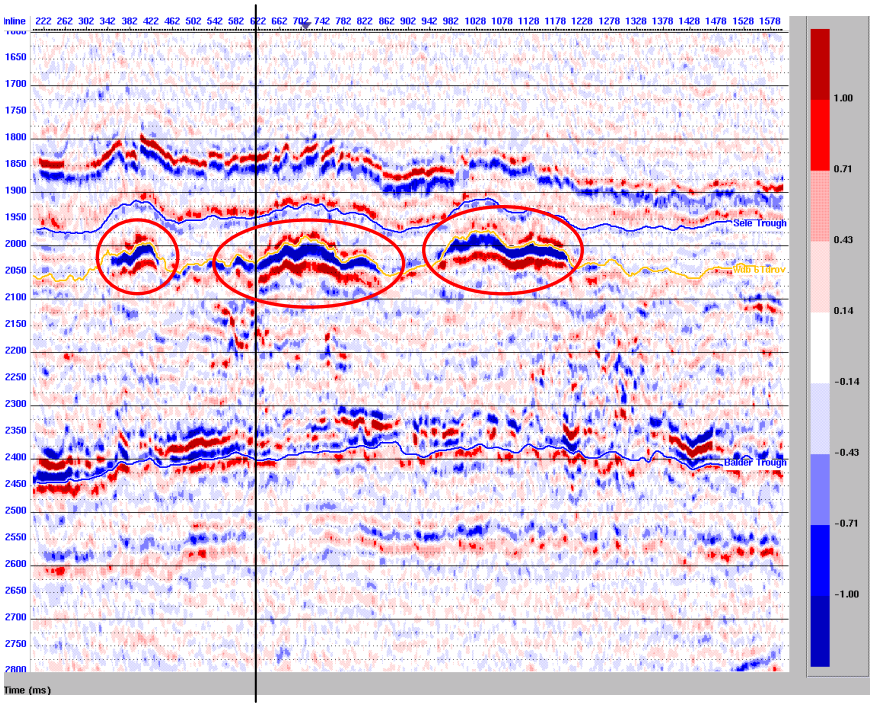

(b) XL

Figure 5.2: Zoomed in sections of the stacked sections in figure 5.1 showing the *Sele Trough*, *Wdb 6Trov* and *Balder Trough* horizons on the IL and XL and the six areas with anomalous amplitudes highlighted in red.

5.2.2 Velocity field

I was provided with a high-density stacking velocity field (figure 5.3). I used it to approximate the angle of incidences via ray tracing in the AVO inversion. To generate a smooth P-wave velocity field (Smith and Gidlow, 1987) that bears significance to the subsurface geology I decimated the field along five horizons (figure 5.4). I used the *Balder Trough* and four additional horizons (*vel h1*, *vel h2*, *vel h3* and *vel h4*) which I had picked myself following the trough of the wavelet. The *vel h3* and *Balder Trough* horizons encase the large amplitudes along the *Wdb 6Trov* horizon. I decimated the velocity field every 40 CMPs and recorded the data as a time-velocity table (tables 5.2 and 5.3) for use in the AVO inversion.

CMP	**4202**		**4240**		**4280**		**4320**	
Horizon	Time (ms)	Velocity (ms^{-1})	Time (ms)	Velocity (ms^{-1})	Time (ms)	Velocity (ms^{-1})	Time (ms)	Velocity (ms^{-1})
vel h1	345	1770	350	1765	355	1755	365	1760
vel h2	925	1925	950	1930	970	1940	965	1935
vel h3	1945	2190	1938	2180	1945	2185	1945	2175
Balder Trough	2415	2350	2414	2350	2425	2395	2415	2350
vel h4	3395	2870	3390	2965	3385	2925	3375	2870

Table 5.2: The start of the resampled velocity field used in the AVO inversion of the IL.

CMP	**202**		**240**		**280**		**320**	
Horizon	Time (ms)	Velocity (ms^{-1})	Time (ms)	Velocity (ms^{-1})	Time (ms)	Velocity (ms^{-1})	Time (ms)	Velocity (ms^{-1})
vel h1	345	1720	355	1730	335	1700	345	1610
vel h2	845	1830	855	1850	865	1810	865	1835
vel h3	1870	2100	1870	2105	1875	2085	1870	2105
Balder Trough	2445	2375	2445	2375	2445	2380	2430	2390
vel h4	3300	2850	3290	2950	3295	3015	3300	2990

Table 5.3: The start of the resampled velocity field used in the AVO inversion of the XL.

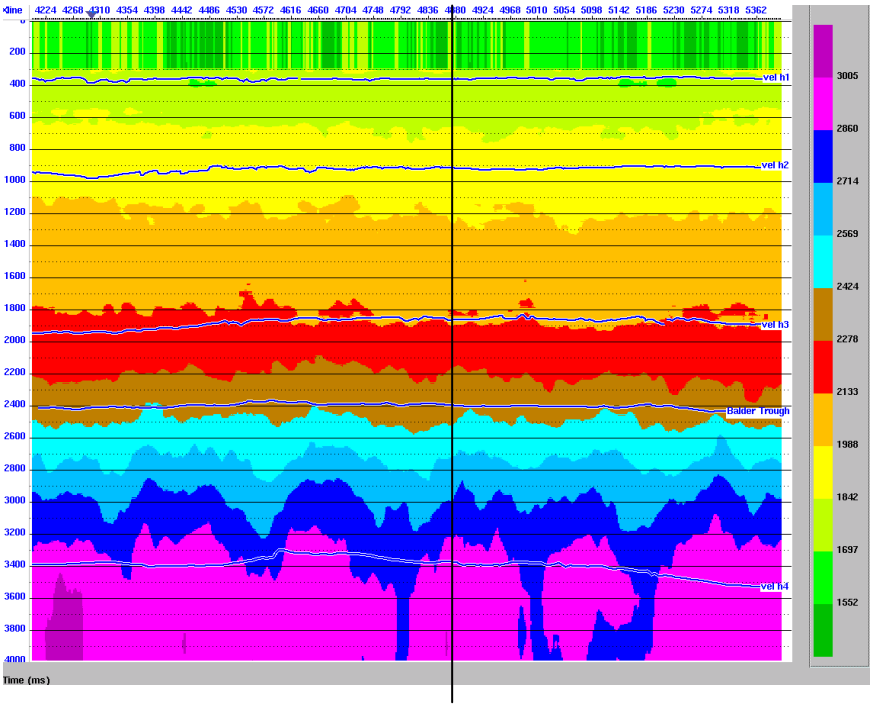

(a) IL

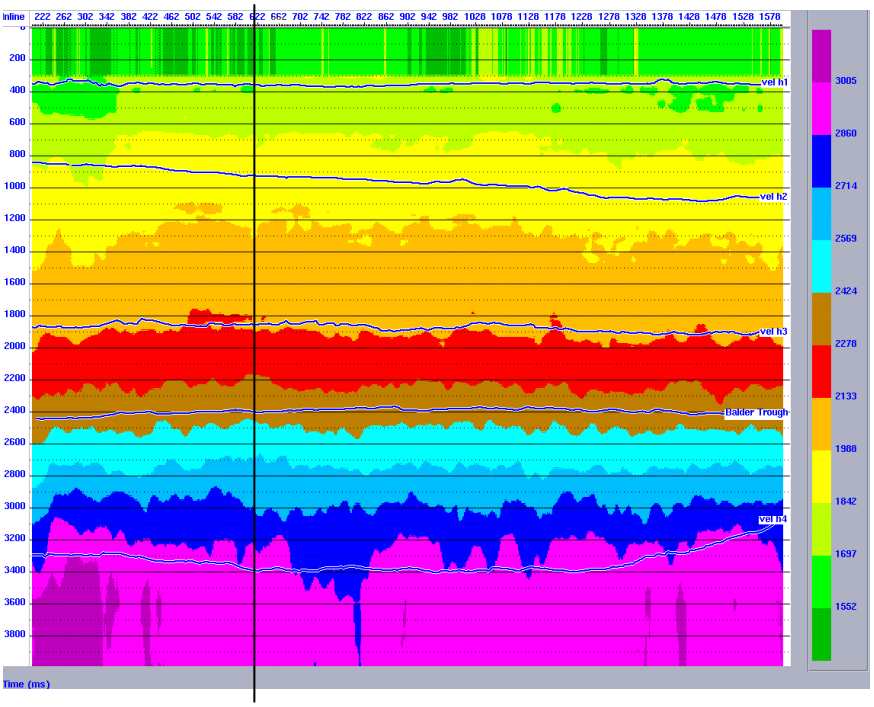

(b) XL

Figure 5.3: The high-density stacking velocity showing the *Balder Tough* and the four additional horizons (*vel h1*, *vel h2*, *vel h3* and *vel h4*) I had picked along geological structures to provide a smoother, sparser, velocity field.

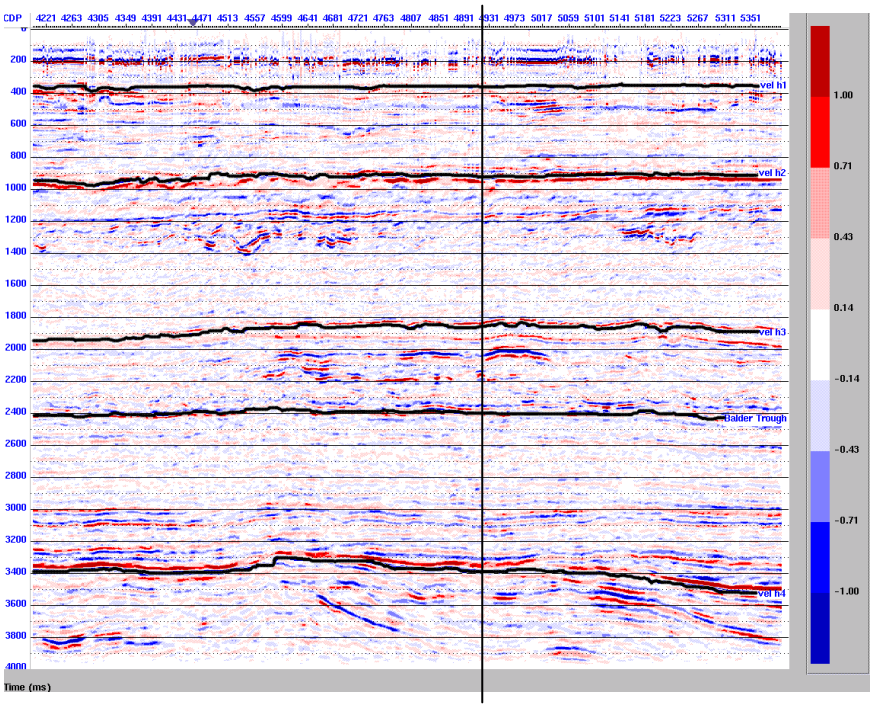

(a) IL

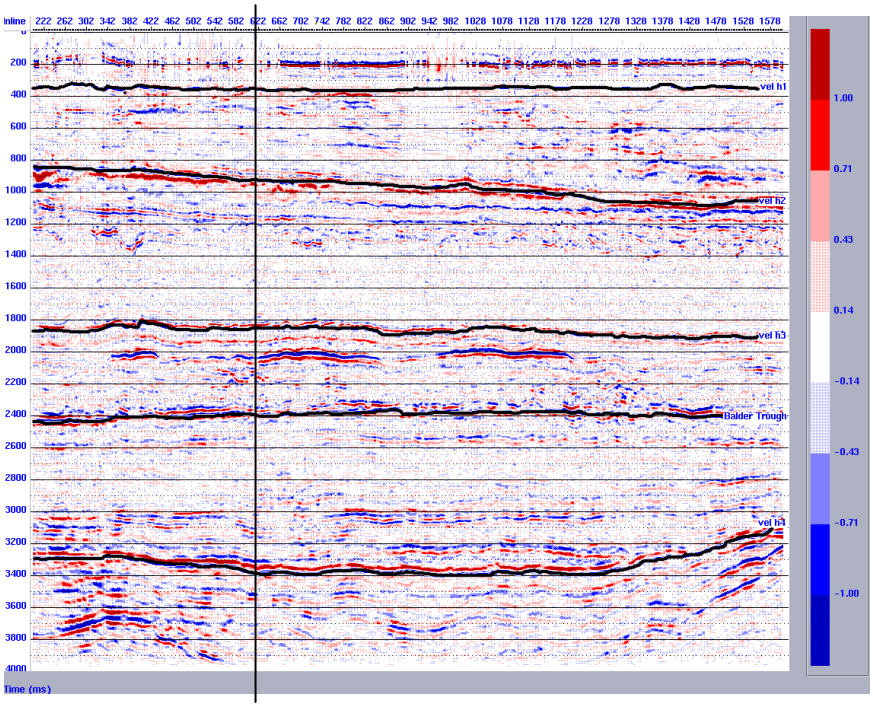

(b) XL

Figure 5.4: Stacked IL and XL sections showing the horizons used to resample the high-density velocity field.

5.3 AVO analysis

5.3.1 CMP gathers

I inspected gathers along the IL and XL *Wdb 6Trov* horizon to characterise the amplitude behaviour within the context of the extended Rutherford and Williams' classification. The general behaviour at all six of these areas is negative amplitude which increases with offset, as summarised in table 5.4. The three areas on the IL (figures 5.5a, b and c) all have small amplitudes at the near-offsets which increase with offset. The amplitude increase with offset appears to be smallest between CMPs 4600 – 4700 indicating a smaller gradient than the other two areas on the IL. This smaller gradient explains why it has smaller stacked amplitude than the other areas (figure 5.2a) which have a larger gradient. I have initially interpreted these areas as being Class III reflections. One of the ambiguities with any interpretation using a Rutherford and Williams' classification is where the separation between Class II and Class III reflections lie. Both have negative intercepts (discounting Class IIp) and negative gradients, where the amplitudes increase with offset. For my investigation I chose not to make a distinction between a Class II and a Class III reflection. Instead, I interpreted a negative intercept with increasing amplitude with offset as a Class III reflection. The first two areas on the XL (figures 5.5d and e) have small amplitudes at the near-offsets which increase with offset and I interpreted them both as Class III reflections. The final area on the XL, between CMPs 950 – 1190, has different factors contributing to the large stacked amplitude seen in figure 5.2b and I have split it into CMPs 950 – 1080 and 1080 – 1190. The first area (figure 5.5f) has large negative amplitude at the near-offsets and the amplitude decreases with offset, indicating a positive gradient. I interpreted this to be a Class IV reflection and the large stacked amplitude is due to the near-offsets. The second part of this area (figure 5.5g) has negative amplitude at near-offsets that increases with offset and I interpreted this as another Class III reflection. The large amplitude signature on the stacked section is, therefore, made up of the large, near-offset amplitudes (CMPs 950 – 1080) and the large, far-offset amplitudes (CMPs 1080 – 1190). My interpretation of these areas is summarised in table 5.4.

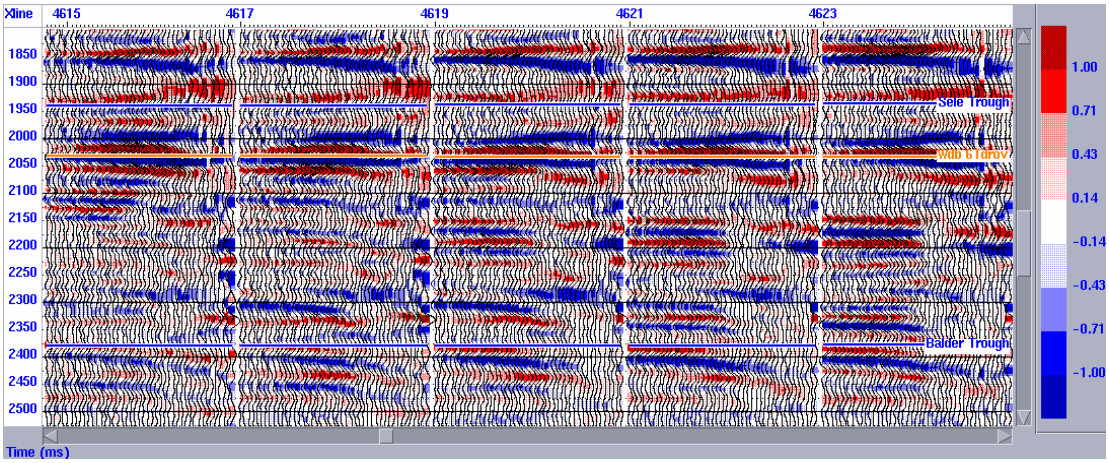

(a) *1st* area on IL

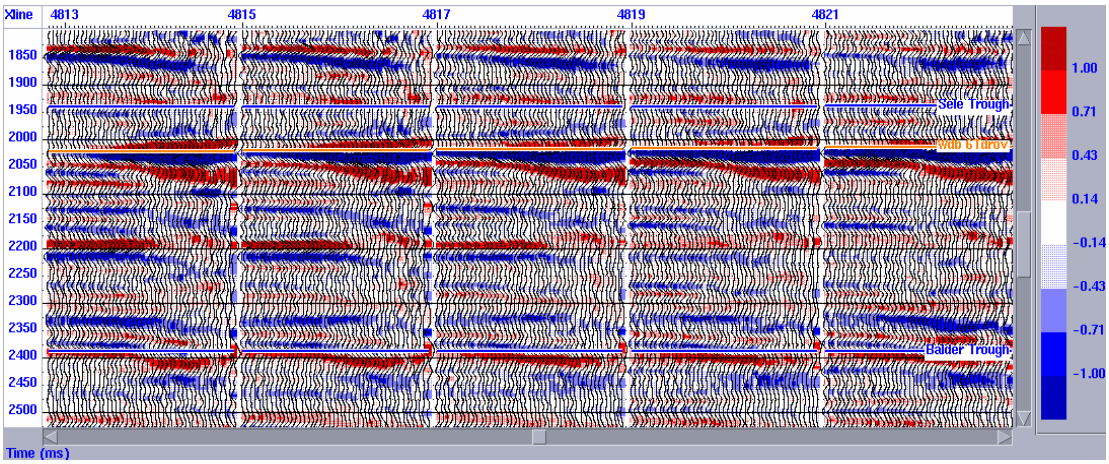

(b) *2nd* area on IL

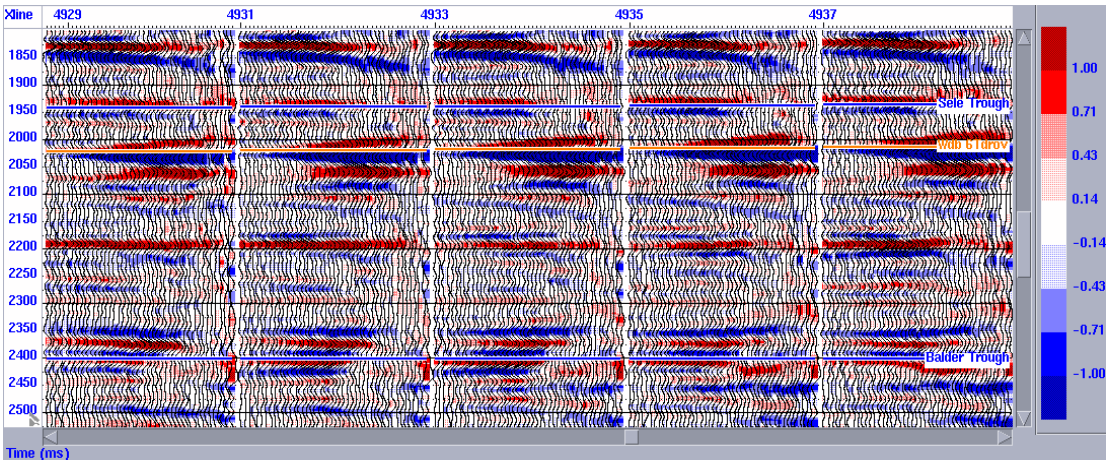

(c) *3rd* area on IL

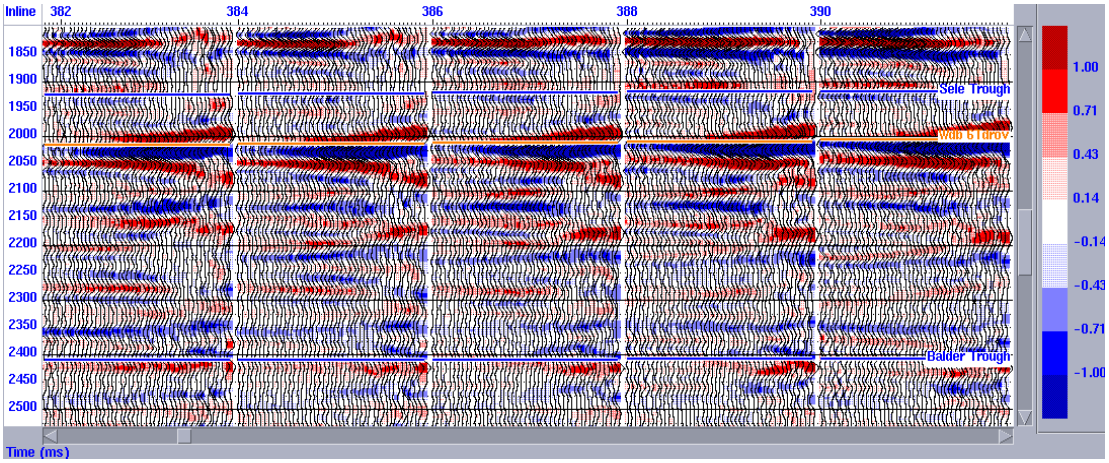

(d) *1st* area on XL

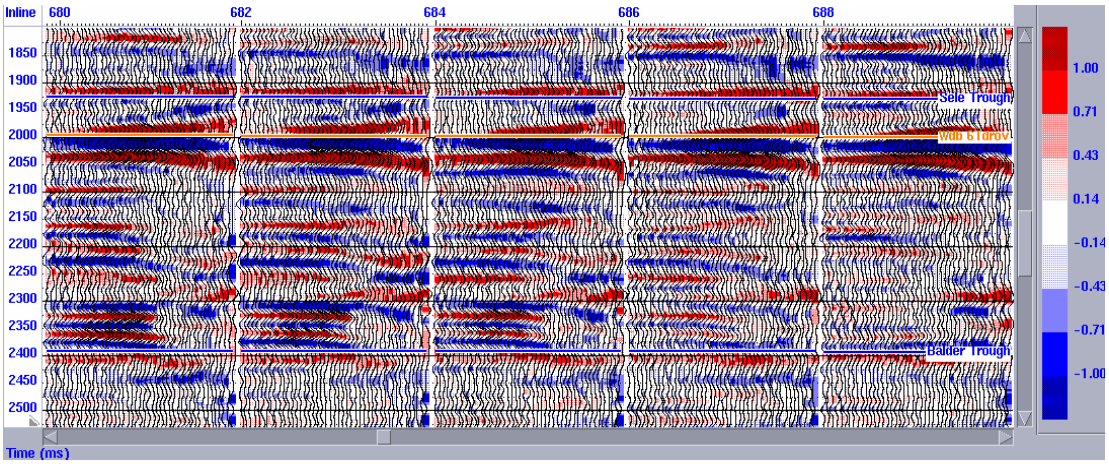

(e) *2nd* area on XL

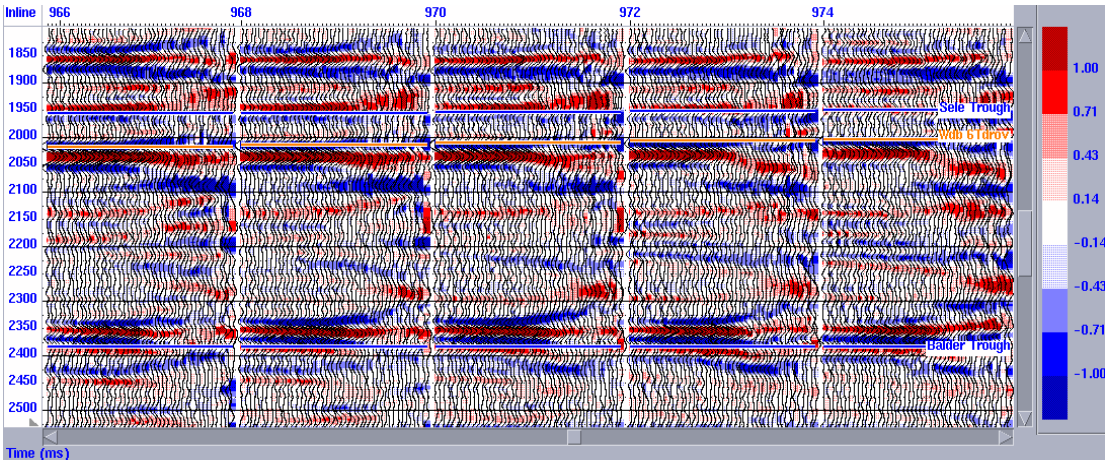

(f) First part of *3rd* area on XL

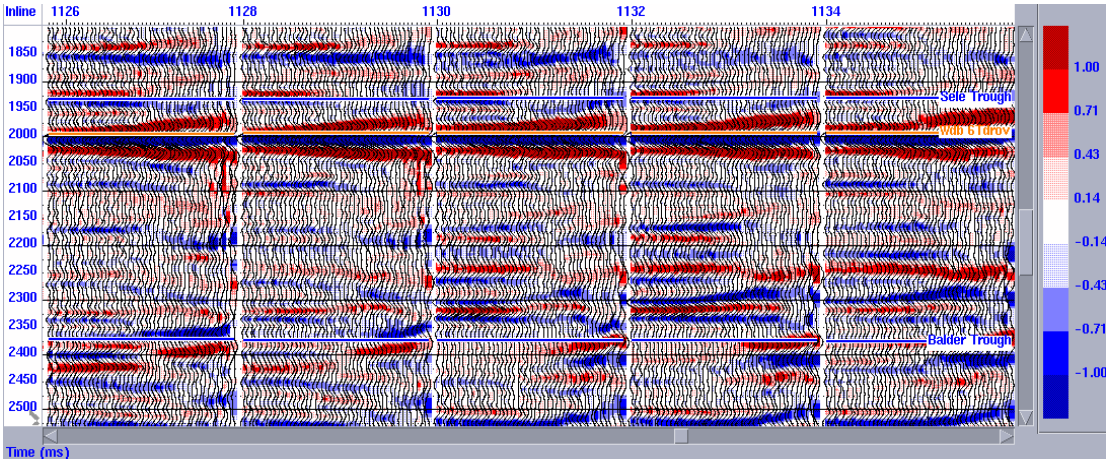

(g) Second part of *3rd* area on XL

Figure 5.5: A selection of CMP gathers from the six areas with large stacked amplitudes along the *Wdb 6Trov* horizon.

Area	CMP Range	Amplitude	Versus Offset	Interpretation	Figure
IL 1st	4600 – 4700	*-ve*	increasing	Class III	5.5a
IL 2nd	4780 – 4870	*-ve*	increasing	Class III	5.5b
IL 3rd	4910 – 5020	*-ve*	increasing	Class III	5.5c
XL 1st	350 – 430	*-ve*	increasing	Class III	5.5d
XL 2nd	610 – 840	*-ve*	increasing	Class III	5.5e
XL 3rd (i)	950 – 1080	*-ve*	decreasing	Class IV	5.5f
XL 3rd (ii)	1080 – 1190	*-ve*	increasing	Class III	5.5g

Table 5.4: Summary of my interpretation of the CMP gathers along the *Wdb 6Trov* horizon.

5.3.2 Intercept and gradient analysis

I have inverted both the IL and XL using the Shuey's two-term linear approximation, equation 3-16, to estimate the intercept, *A*, and gradient, *B*, using Hampson-Russell's GeoView software. The P-wave velocity field was smoothed over a 500ms window to calculate the angle of incidence up to 30° in accordance with the assumptions laid out in Chapter 3 and the S-wave velocity field was calculated using Castagna's mudrock line (equation 2-16). GeoView uses a multi-taper method (Walden, 1991) to

minimise the effects of outliers when calculating the gradient and I set the minimal acceptable correlation between subsequent traces to 0.7 to reduce the problems associated with low signal to noise ratio. My interpretations are qualitative not quantitative as I have no well-data and have not performed any forward modelling.

I have plotted sections of intercept (*A*), gradient (*B*) and intercept x gradient (*A*x*B*) along with Poisson's reflectivity (*PR*) and fluid factor (ΔF) using a combination of the intercept and gradient. On each display I have used the same red ellipses as in figure 5.2 to highlight the large stacked amplitudes. The intercept sections are shown in figure 5.6 and the areas between CMPs 4780 – 4870 on the IL and CMPs 1080 – 1190 on the XL have the largest relative amplitudes. The gradient sections are plotted in figure 5.7 and all six areas have large negative gradients indicating increasing amplitude with offset. The area between CMPs 950 – 1080 on the XL appears to have a small negative gradient, contrary to the CMP analysis, and this may be due to the limit of 30° on the angle of incidence excluding the far-offsets in the inversion.

The inverted intercept and gradient can be combined to aid in interpreting the data by creating sections of intercept x gradient (*A*x*B*). Positive amplitudes are the result of both negative intercept and gradient and indicate either a Class II or Class III reflection. It is negative for all other combinations and reflections. Castagna and Smith (1994) noted that *A*x*B* is typically only a useful hydrocarbon indicator for Class III sands and I have interpreted the six anomalous areas as Class III reflections. Figure 5.8 shows the *A*x*B* sections for both the IL and XL and the signature is positive for the six anomalous areas. The response is small between CMPs 4600 – 4700 on the IL and CMPs 350 – 430 on the XL and is approximately zero between CMPs 1080 – 1190 on the XL. My interpretation of Class III reflections is consistent with the inverted intercept, gradient and intercept x gradient sections.

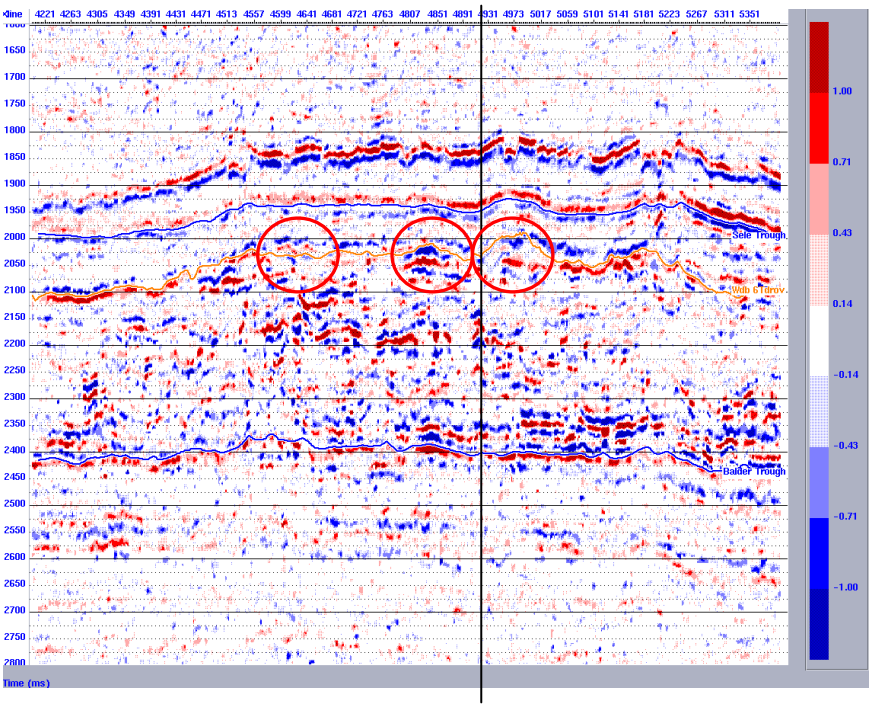

(a) IL

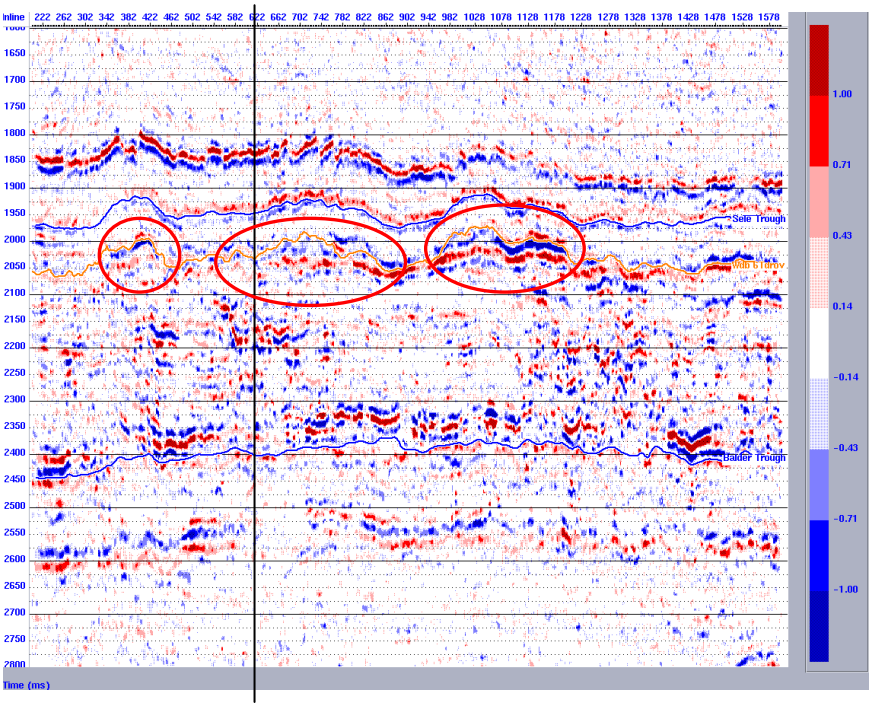

(b) XL

Figure 5.6: Inverted sections of the intercept, *A*, using the two-term AVO approximation given in equation 3-16.

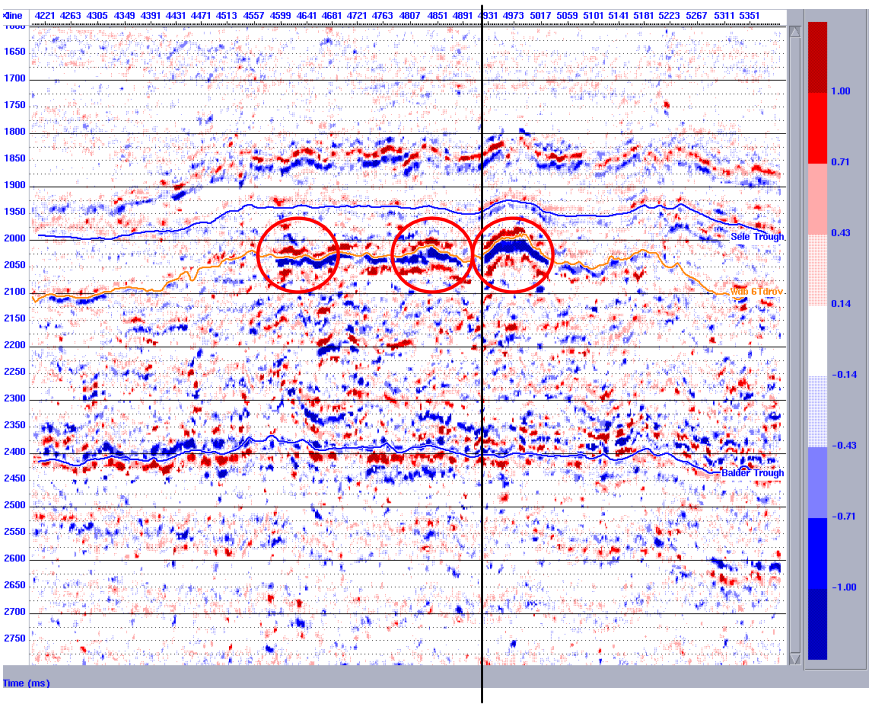

(a) IL

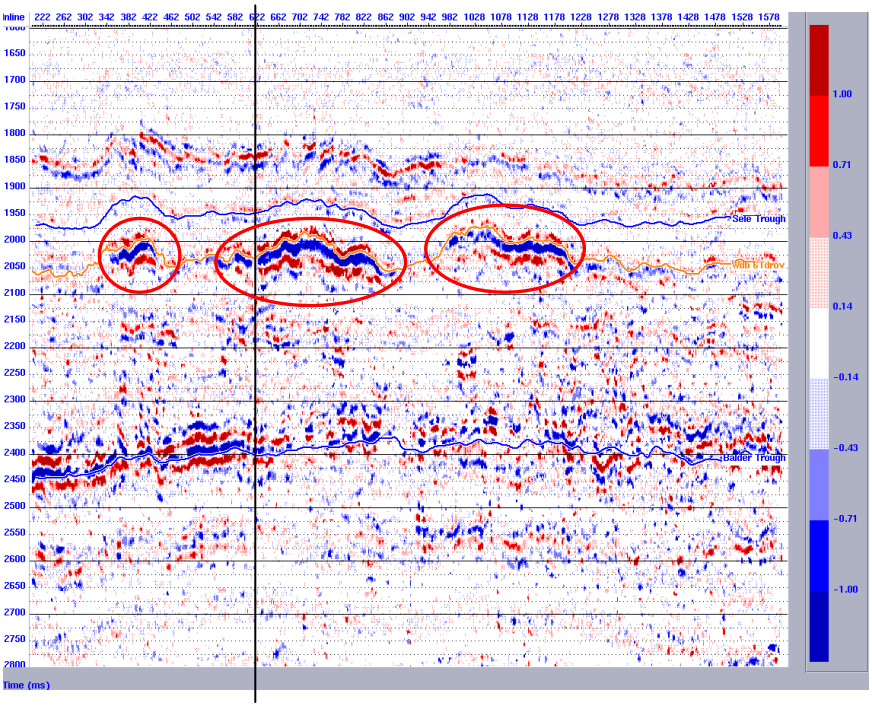

(b) XL

Figure 5.7: Inverted sections of the gradient, *B*, using the two-term AVO approximation given in equation 3-16.

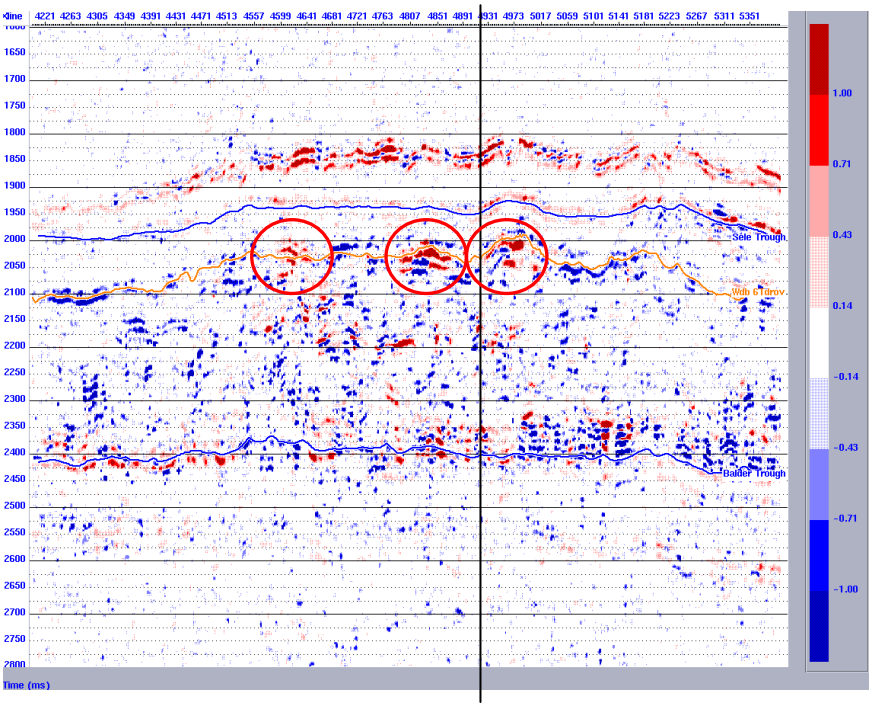

(a) IL

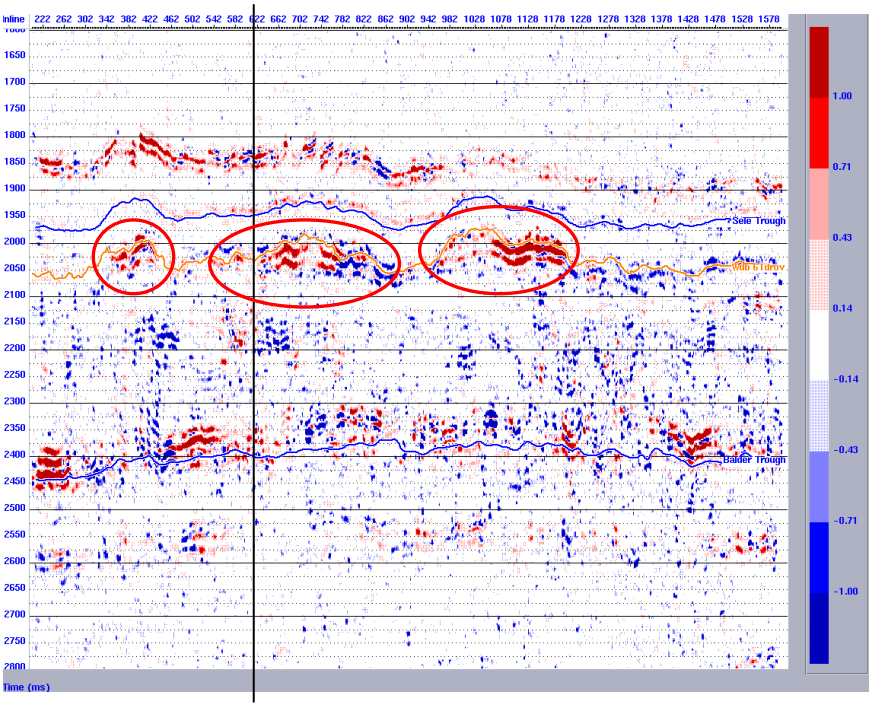

(b) XL

Figure 5.8: Inverted sections of intercept x gradient, *AxB*, using the two-term AVO approximation given in equation 3-16.

5.3.3 Poisson's reflectivity

I defined Poisson's reflectivity in equations 3-48 and 3-49 in terms of P- and S-wave velocity and the intercept and gradient respectively. The Poisson's reflectivity can be represented as a simple addition of the intercept and gradient, where the scaling coefficients α and β are both one. Using this scaled intercept–gradient method I generated Poisson's reflectivity sections for the IL and XL, figure 5.9. Both sections are relatively noisy but do show a strong response and correlation with the areas on the *A*x*B* sections. All six areas along the *Wdb 6Trov* horizon have a negative response due to the negative intercept and gradients, with the area between CMPs 4600 – 4700 on the IL showing the weakest response.

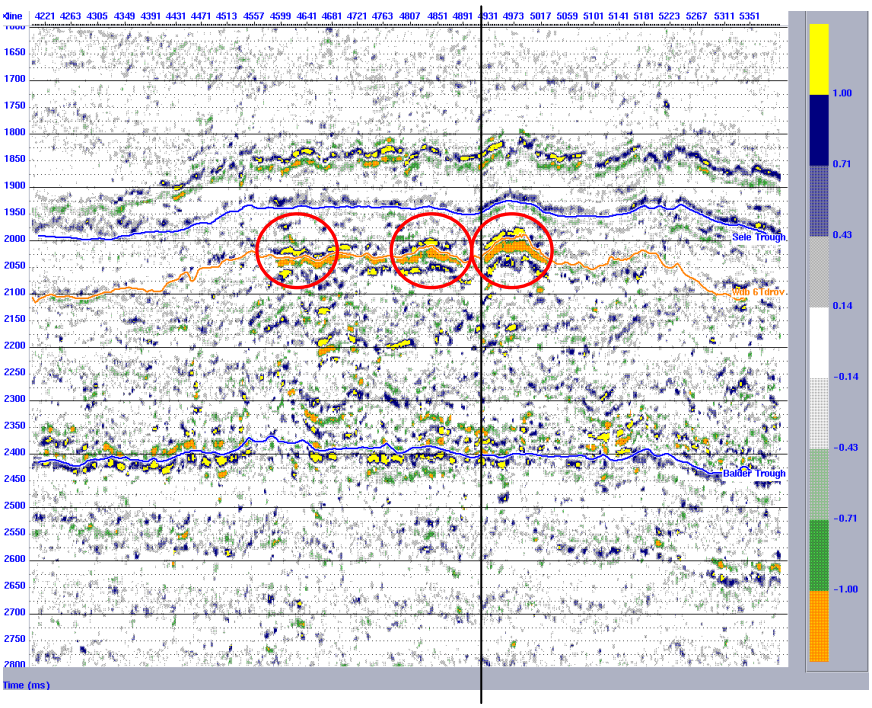

(a) IL

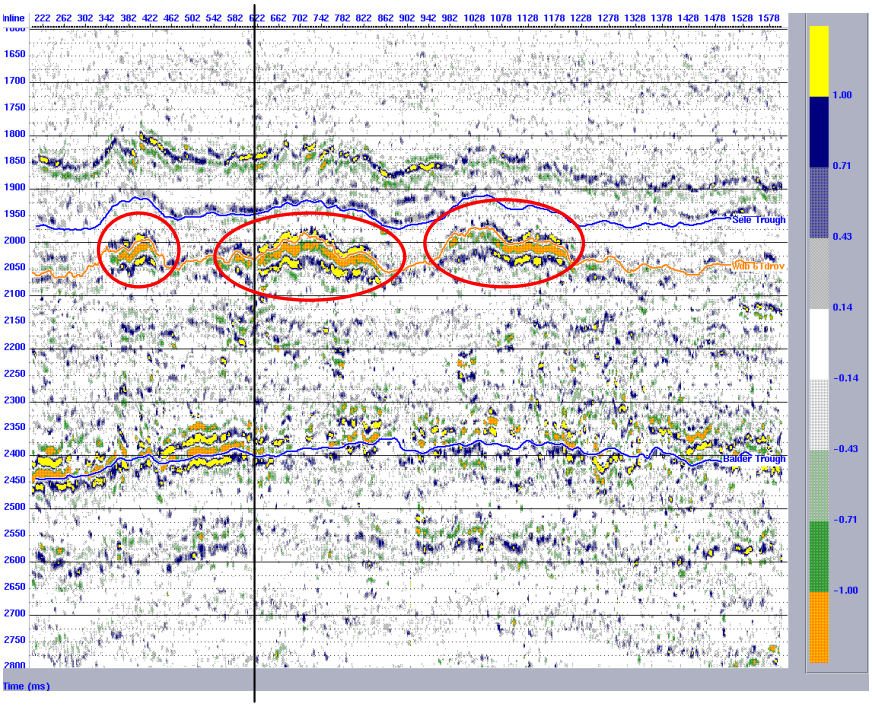

(b) XL

Figure 5.9: Inverted sections of Poisson's reflectivity, *A*+*B*, using the two-term AVO approximation given in equation 3-16.

5.3.4 Fluid factor

I defined Smith and Gidlow's (1987) fluid factor trace in equation 3-25 and went on to use Fatti *et al.*'s (1994) transformation of the P- and S-wave reflectivities to obtain,

$$\Delta F = NI_P - \gamma NI_S \qquad (5\text{-}1)$$

where NI_P and NI_S are the zero-offset reflectivities and γ is a gain function designed to minimise ΔF for water-saturated clastic silicates or non-pay regions. Smith and Sutherland (1996) calculated a global gain function of 0.63 that minimised the fluid factor from shale/brine-sand interfaces (non-pay regions) whilst being positive for gas-sand/brine-sand interfaces and negative for shale/gas-sand interfaces. Rather than calculate a local gain function, I use this empirically-derived global optimum gain function of 0.63 and define the fluid factor as a linear combination of the intercept and gradient,

$$\Delta F = NI_P - 0.63NI_S = \alpha A + \beta B. \qquad (5\text{-}2)$$

I satisfied equation 5-2 by choosing $\alpha = 0.685$ and $\beta = 0.315$ and the fluid factor becomes,

$$\Delta F = 0.685A + 0.315B. \qquad (5\text{-}3)$$

I used this calibrated intercept and gradient method to calculate the fluid factor sections shown in figure 5.10. By comparing the fluid factor sections with the Poisson's ratio sections I can see that the signal to noise ratio has been vastly improved using the fluid factor trace and has minimised the background trend, assumed to be water-saturated, to near zero amplitude as predicted by Castagna and Smith (1994). Furthermore, I noted the same weak amplitudes as I observed on the Poisson's reflectivity sections between CMPs 950 – 1080. I suspect that there is

different fluid saturation between there and CMPs 1080 – 1190 because of the change in the fluid factor response along the continuous reflection event.

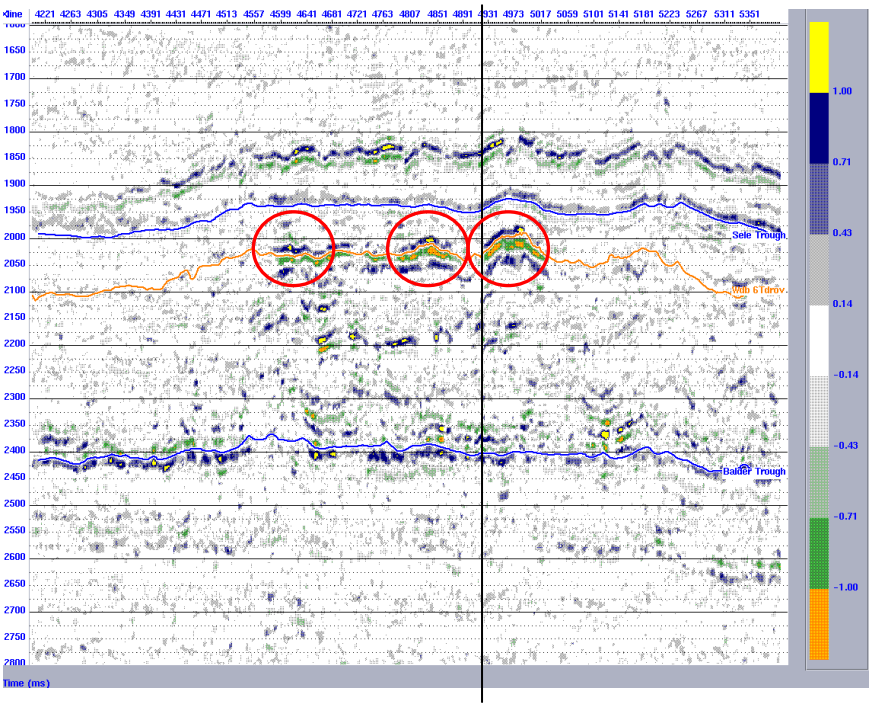

(a) IL

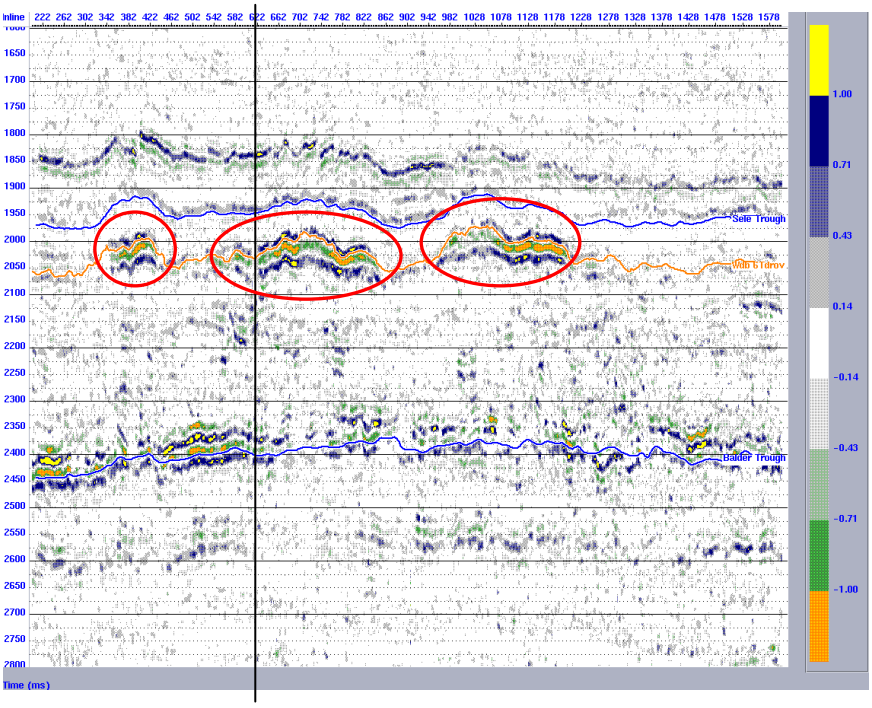

(b) XL

Figure 5.10: Fluid factor sections using the calibrated intercept and gradient method.

5.4 AVO analysis of crossplots and horizons

I have calculated crossplots of *A* versus *B* for the peak and trough data points, within a 100ms window centred on three horizons (*Sele Trough, Wdb 6Trov* and *Balder Trough*) for both the inline and crossline following arguments made by Simm *et al*., (2000). I have interpreted all the data within the context of deviations from the background trend (Castagna and Swan, 1997). On all the crossplots I have performed a linear regression showing the best fit to all of the data points and then zoned around this area with a grey ellipsoidal representing the wet, background trend. I then plotted a red and blue polygon to capture anomalous points outside of the wet-trend, similar to figure 3.3. The red polygon captures anomalous data points from Class II(p), II and III reflections. I have plotted cross-sections using the three colour-coded zones for both the IL and XL. The results from the *Sele* and *Balder Trough* show no anomalous areas with the data points all tightly packed within the background trend.

Figure 5.11 shows the crossplot from a 100ms window centred on the *Wdb 6Trov* horizon with the three zones selected highlighting the background trend (grey) and the anomalous AVO behaviour. I have plotted the colour coded regions as cross-sections in figure 5.12 and they highlight the same anomalous areas on the horizon detected using the earlier AVO analysis. On the IL, there are anomalous areas between CMPs 4600 – 4700, 4780 – 4870 and 4910 – 5020, whilst on the XL there are anomalous areas between CMPs 350 – 430, 610 – 840 and 1080 – 1190.

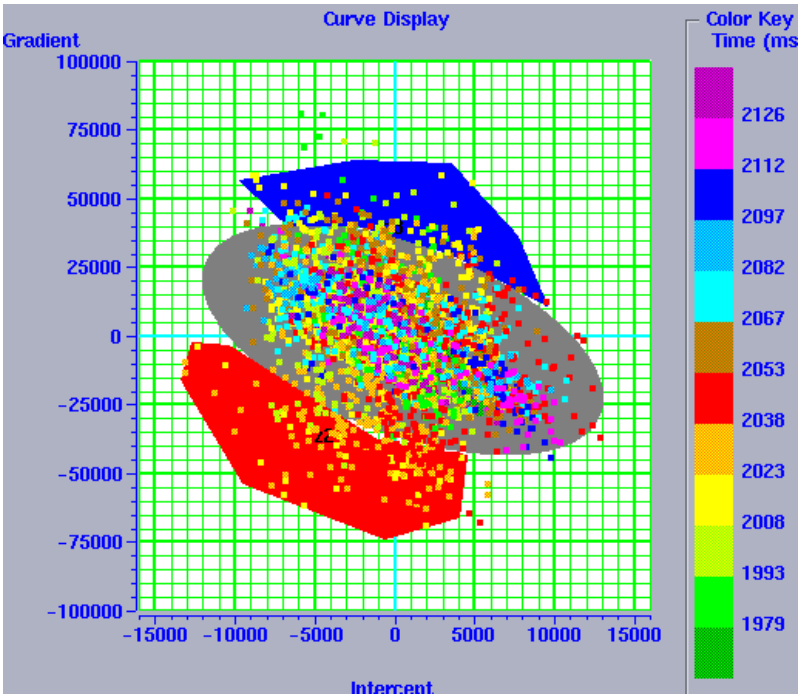

(a) IL

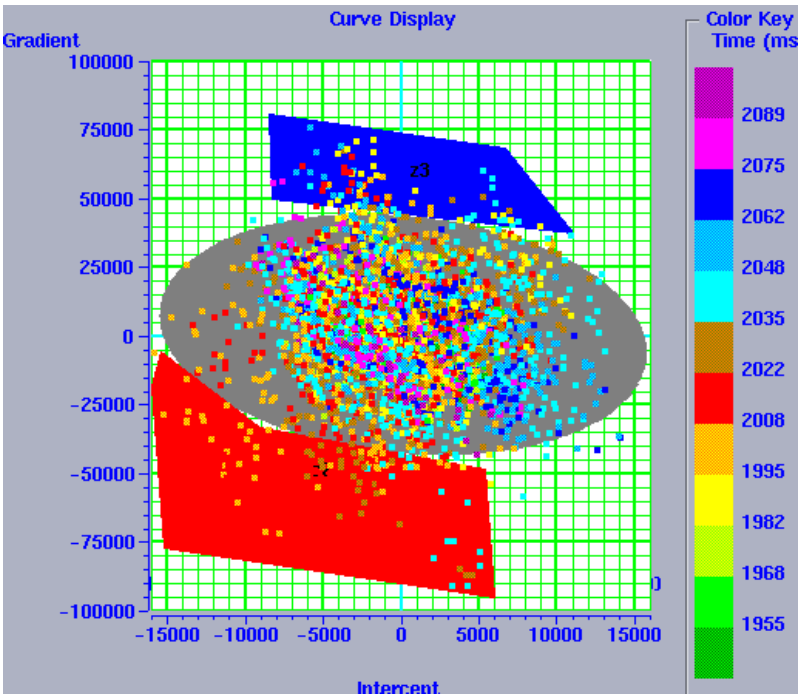

(b) XL

Figure 5.11: Crossplots of *A* versus *B* from a 100ms window centred on the *Wdb 6Trov* horizon.

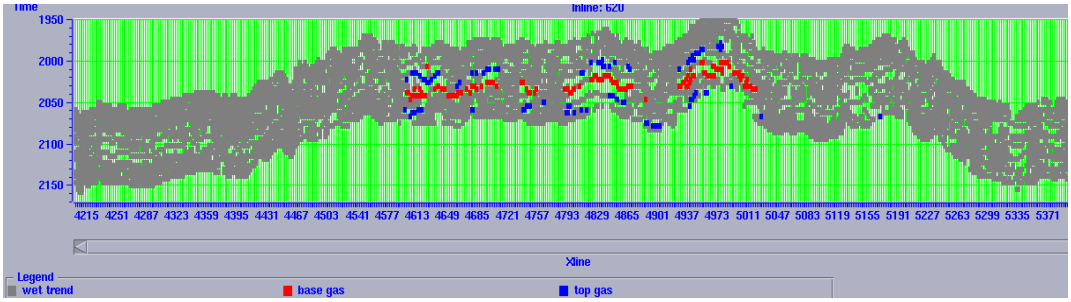

(a) IL

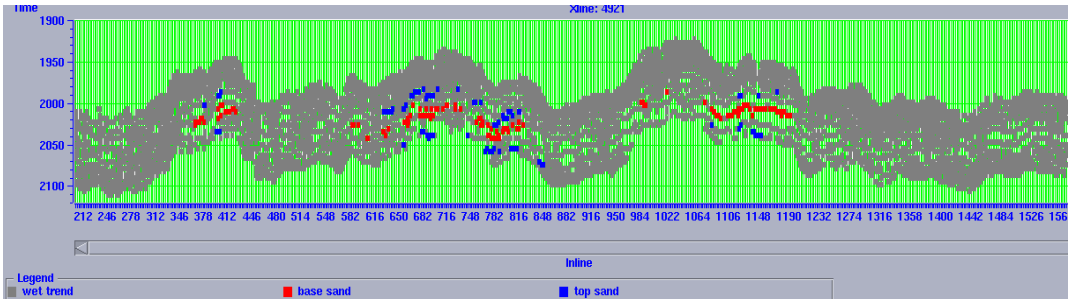

(b) XL

Figure 5.12: Cross-sections of the data crossplotted in figure 5.11 colour coded by the zones selected in the crossplots.

I also created crossplots of stacked amplitude versus gradient (figure 5.13) to check that these were true signals and not statistical artefacts caused by cross-talk between the intercept and gradient (Cambois, 2000). I used the same zones as those in the intercept versus gradient crossplots and then plotted cross-sections of them in figure 5.14. The data point shows a greater spread along the *x*-axis of the cross-sections since the stacked amplitudes have larger magnitude than the intercept values. Since there is no statistical correlation between the stacked amplitudes and the gradients, the data points I have selected in the crossplots of figure 5.11 and 5.13 represent true anomalous signals due to either lithology or fluid saturation. This also means that my sections describing Poisson's reflectivity and fluid factor are not simply far-offset stacks which can be a potential pitfall of AVO analyses as discussed by Cambois (2000).

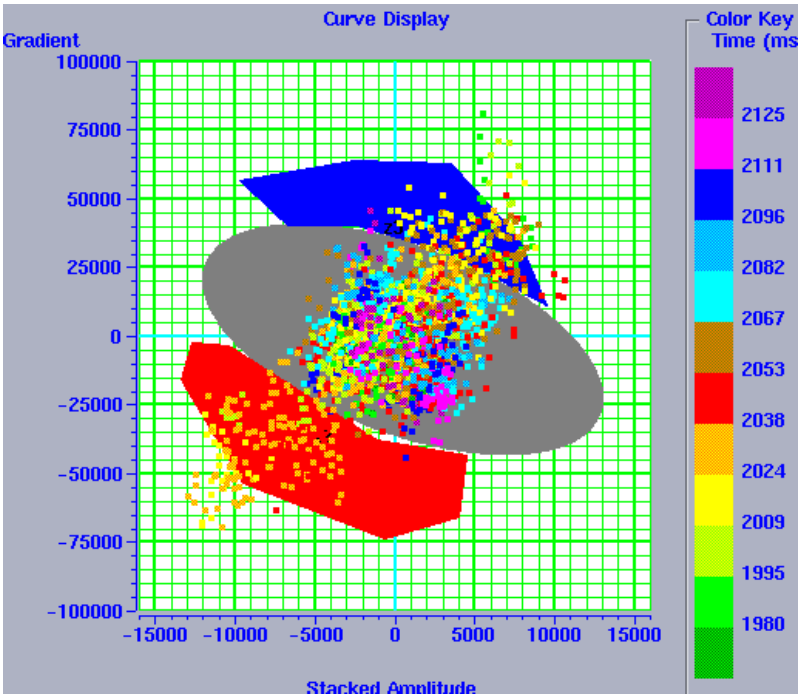

(a) IL

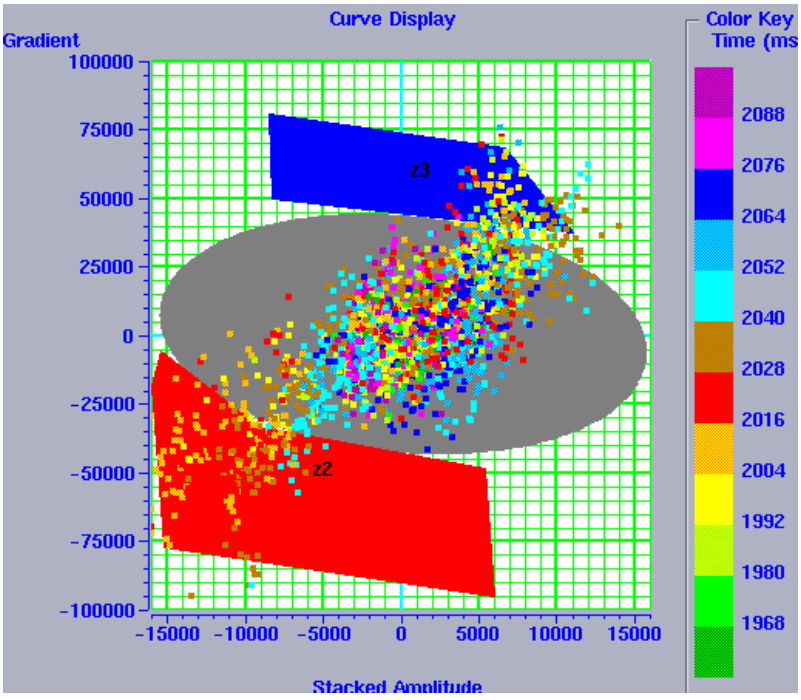

(b) XL

Figure 5.13: Crossplots of *stacked amplitude* versus *B* from a 100ms window centred on the *Wdb 6Trov* horizon using the zones from figure 5.11.

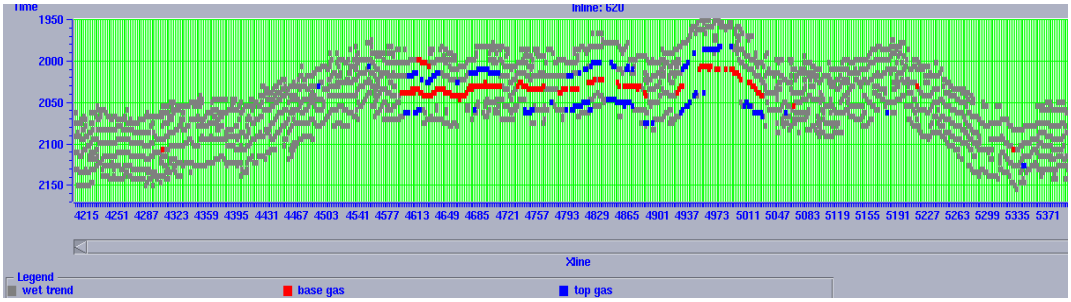

(a) IL

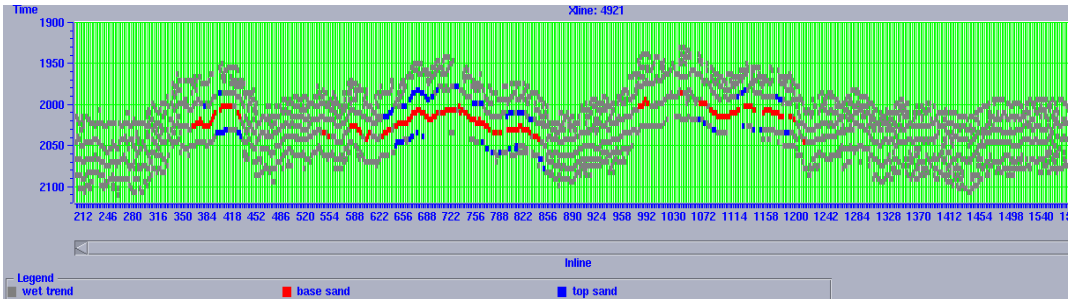

(b) XL

Figure 5.14: Cross-sections of the data crossplotted in figure 5.13 colour coded by the zones selected in the crossplots.

5.5 Spectral decomposition

I performed spectral decomposition on the stacked IL and XL using the continuous wavelet transform (CWT) and the matching pursuit method (MPM) using the parameters I described in Chapter 4. I decomposed both the IL and XL for a range of frequencies and decided that the frequency behaviour of the target anomalies was best characterised when decomposed at 10, 15, 20 and $25Hz$. I removed the overprint of the source signature (Partyka *et al.*, 1999) by balancing the spectrally-decomposed sections using a shallow reflection. The bias of the source signature at the different frequencies is evident by the varying amplitude scales on the unbalanced decomposed sections. I assumed that the reflection within the $0.8 - 1.0s$ window is brine saturated and part of the elastic background trend. I scaled the amplitudes, on a range of $0 - 100$, using the maximum amplitude value within the window. The resultant balanced sections are all now plotted displaying a consistent amplitude scale that allows me to directly compare the different spectral amplitudes.

5.5.1 CWT decomposition

I performed spectral decomposition on the IL and XL using the CWT with a band of $17.5Hz$ at frequencies 10, 15, 20 and $25Hz$. Following the balancing method described above, the spectrally-balanced sections of the IL and XL are plotted in figures 5.15 and 5.16 respectively.

On the IL, the area between CMPs 4600 – 4700 has near zero amplitude at 10Hz that increases with frequency. The area between CMPs 4780 – 4870 again has low amplitude at $10Hz$ but appears to be at a higher and constant amplitude at the other frequencies. The final area, between CMPs 4910 – 5020, has a strong low-frequency signature with large amplitude at $10Hz$ that reduces as the frequency increases. The results from the XL areas, between CMPs 350 – 430, 610 – 840 and 1080 – 1190, are slightly more difficult to interpret. Whilst the amplitudes on the 10Hz section are small, they appear to be similar and larger for the other iso-frequency sections. There is evidence on the $25Hz$ iso-frequency section that the area between CMPs 610 – 840 is not consistent across the entire CMP range and there is a dimming at approximately CMP 700.

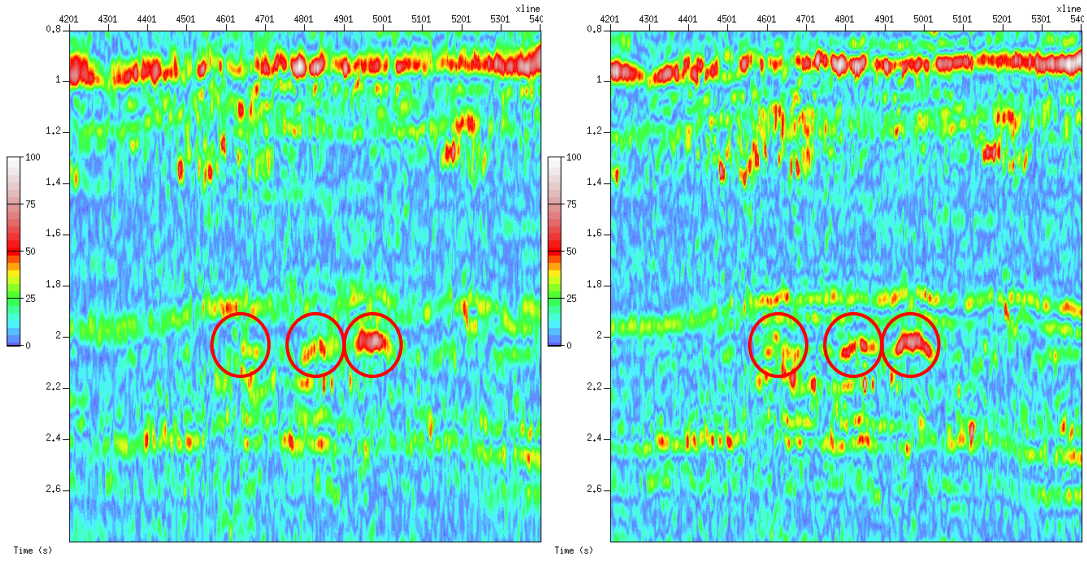

(a) $10Hz$ (b) $15Hz$

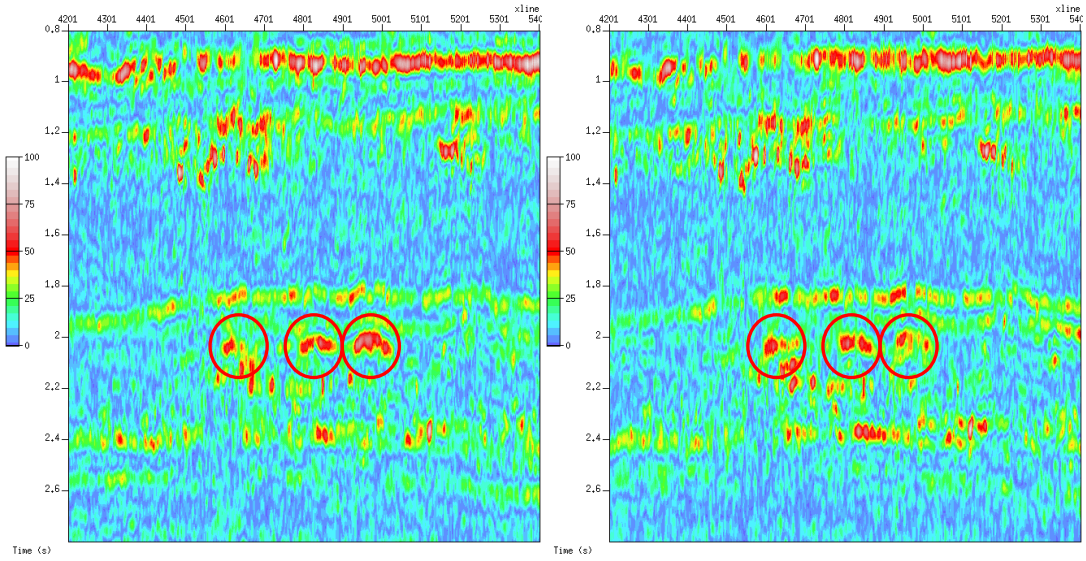

(c) $20Hz$ (d) $25Hz$

Figure 5.15: Balanced, spectrally-decomposed sections of the IL using the CWT algorithm.

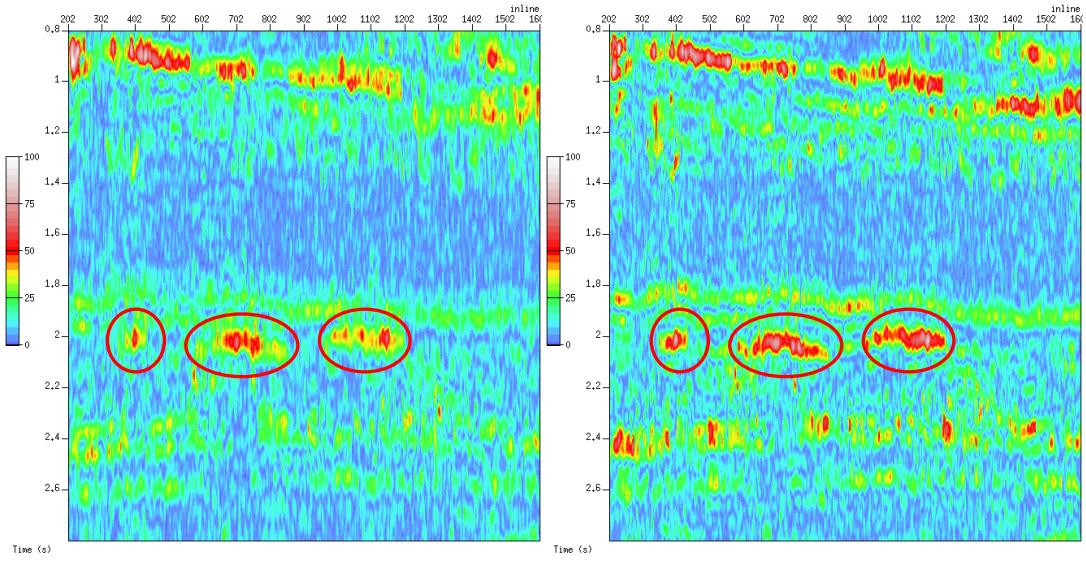

(a) $10Hz$ (b) $15Hz$

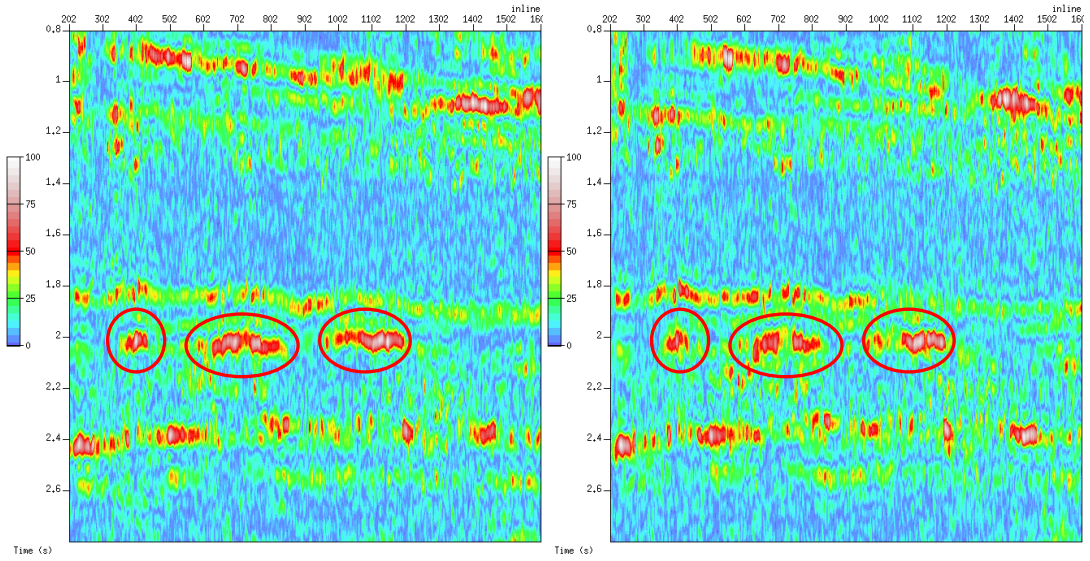

(c) $20Hz$ (d) $25Hz$

Figure 5.16: Balanced, spectrally-decomposed sections of the XL using the CWT algorithm.

5.5.2 MPM decomposition

I repeated the spectral decomposition of the IL and XL using the MPM as described in Chapter 4 using an energy percentage of 99.9% at frequencies 10, 15, 20 and $25Hz$. I again followed the balancing method described above to remove the effect of the source signature and the resultant balanced sections from the IL and XL are plotted in figures 5.17 and 5.18 respectively.

My first observation is in the reduction of the noise compared to the CWT decomposition, especially within the area of low seismic signal between 1.2s – 1.8s. On the IL, the area between CMPs 4600 – 4700 again has near zero amplitude that increases slightly with frequency. The area between CMPs 4780 – 4870 also displays an increase in amplitude with frequency whilst the area between CMPs 4910 – 5020 decreases in amplitude with frequency. My interpretation is in agreement with the CWT results and the improved resolution of the MPM has clarified the uncertainty of the amplitude behaviour between CMPs 4780 – 4870. On the XL, all three areas show near zero amplitude at $10Hz$ which may be due to the small initial energy on the unbalanced decomposed section and makes them unsuitable for inclusion in any

further interpretation. The other iso-frequency sections show large amplitude at $15Hz$ that decreases with frequency. The increased resolution of the MPM has again helped clarify my interpretation of the amplitude behaviour with frequency which was difficult to obtain following decomposition using the CWT.

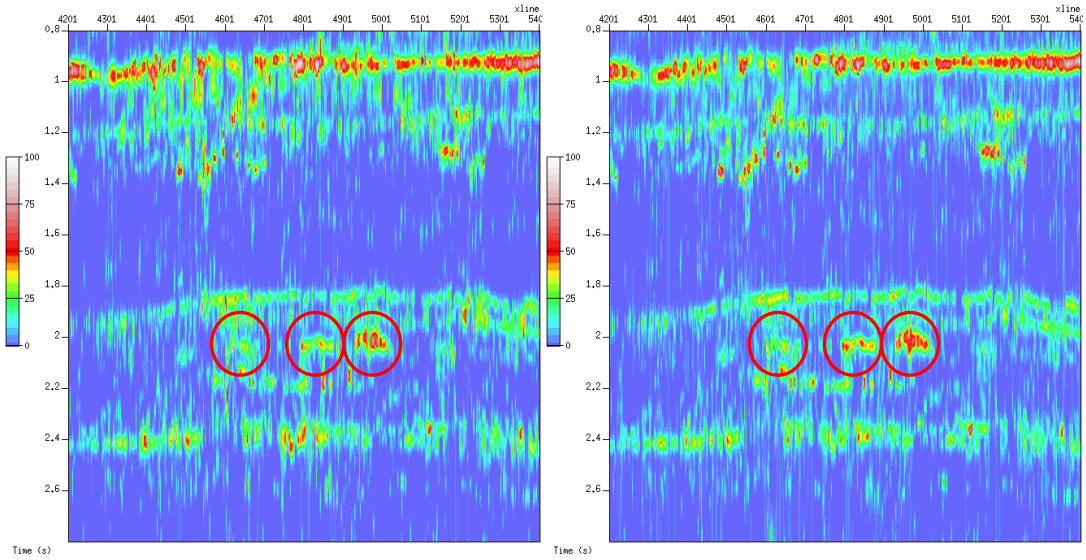

(a) $10Hz$ (b) $15Hz$

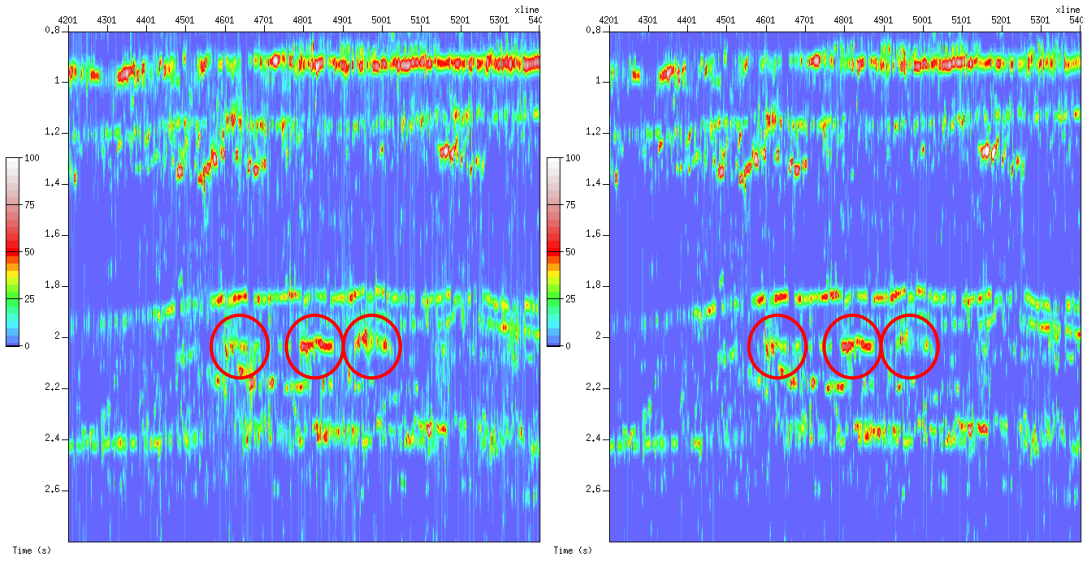

(c) $20Hz$ (d) $25Hz$

Figure 5.17: Balanced, spectrally-decomposed sections of the IL using the MPM algorithm.

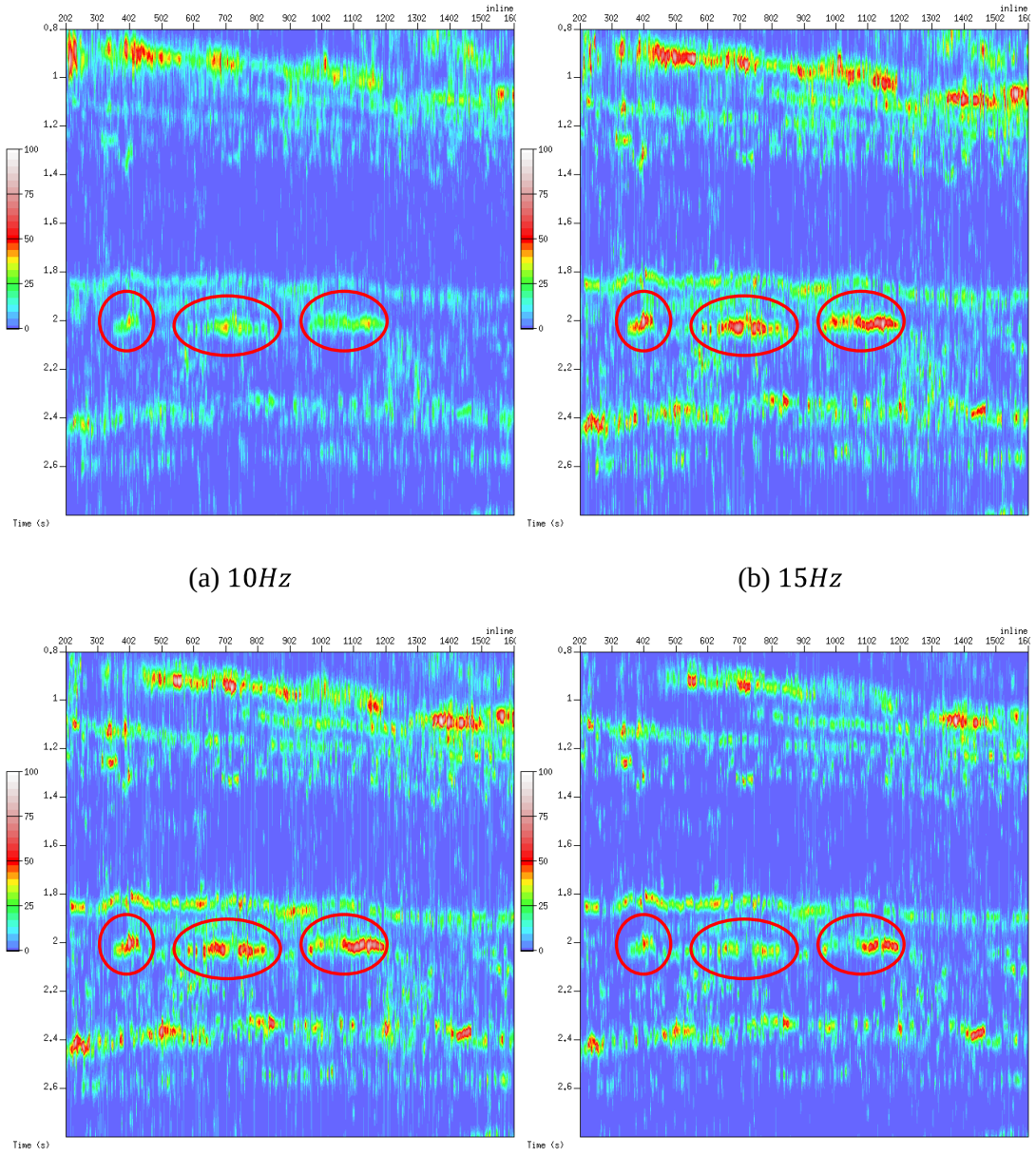

(a) $10Hz$ (b) $15Hz$

(c) $20Hz$ (d) $25Hz$

Figure 5.18: Balanced, spectrally-decomposed sections of the XL using the MPM algorithm.

5.5.3 Spectral difference plots

I have calculated difference plots of the $25Hz$ and the $15Hz$ balanced sections; I have not used the $10Hz$ section as there is almost zero amplitude on the MPM decomposed XL (figure 5.18a). In my calculation I have calculated the differential spectral amplitude, $Diff_{H-F}$, expressed as a percentage using

$$Diff_{H-F} = B_{25Hz} - B_{15Hz} \qquad (5\text{-}4)$$

where B_{25Hz} and B_{15Hz} correspond to the balanced spectral amplitudes from the $25Hz$ and $15Hz$ sections respectively. Figure 5.19 shows the difference plots from the IL using both the CWT and the MPM whilst figure 5.20 shows the difference plots from the XL using both the CWT and the MPM. The calculation of the difference sections according to equation 5-4 results in low frequencies coloured in blue and high frequencies coloured in red. The boost in either low or high frequencies can be due to either tuning or as a result of frequency-dependent AVO as discussed in the earlier Chapters.

The signal to noise ratio is greatly improved when I used the MPM rather than the CWT. The area between 1.2 – 1.8s corresponds to small amplitudes on the input sections. Using the CWT the residual noise is approximately ±15% whilst it is ±3% when the MPM is used. The MPM is not amplifying noise like the CWT does. The results from the area along the *Wdb 6Trov* horizon aren't consistent across the two methodologies. On the IL difference section the area between CMPs 4910 – 5020 has a strong negative signature following both CWT and MPM decompositions, indicating a boost in the lower frequencies. This low-frequency area is also evident on the transecting XL between CMPs 610 – 840. The other two areas on the IL have positive signatures following decompositions with both the CWT and MPM. On the XL, the MPM difference plot has a strong negative signature between CMPs 350 – 430 and 1080 – 1190 indicating a boost in the lower frequencies whilst the CWT difference plot has a zero and a weak negative signature. This disagreement in the difference sections between CMPs 350 – 430 on the XL using the CWT and MPM shows the noise that is introduced by the CWT which interferes with the true frequency-dependent signal. Following my testing of the decomposition algorithms in Chapter 4 and the improved signal to noise in this real data example, I am inclined to favour results produced using the MPM.

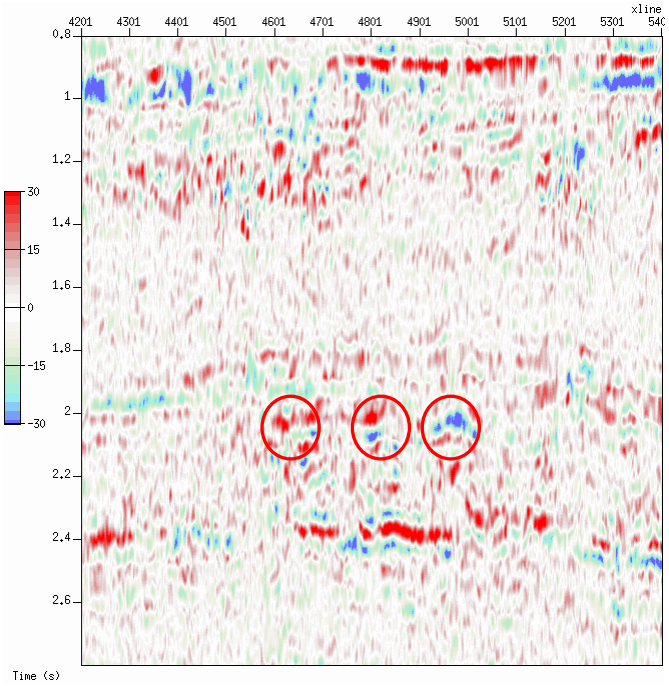

(a) CWT

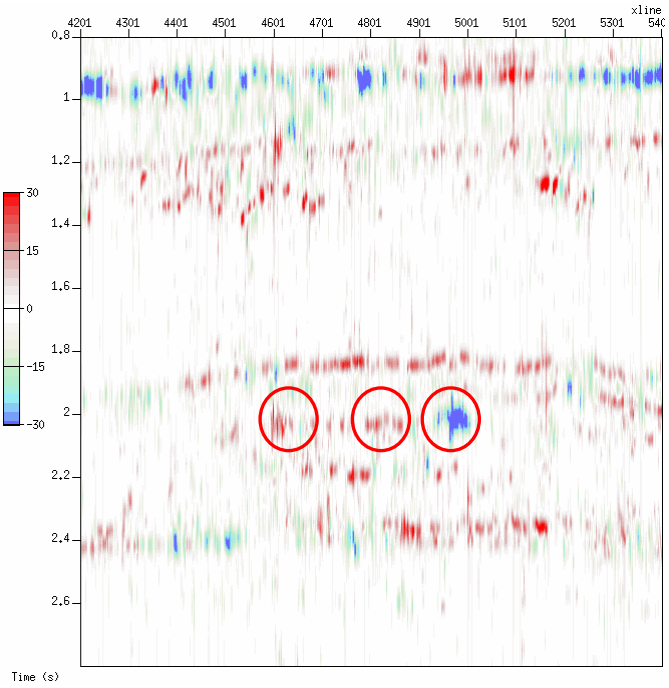

(b) MPM

Figure 5.19: Difference plots of $25Hz$ – $15Hz$ spectral amplitudes sections expressed in percentage for the inline using the CWT and the MPM. Background noise between 1.2 – 1.8s is approximately ±15% using the CWT and ±3% using the MPM.

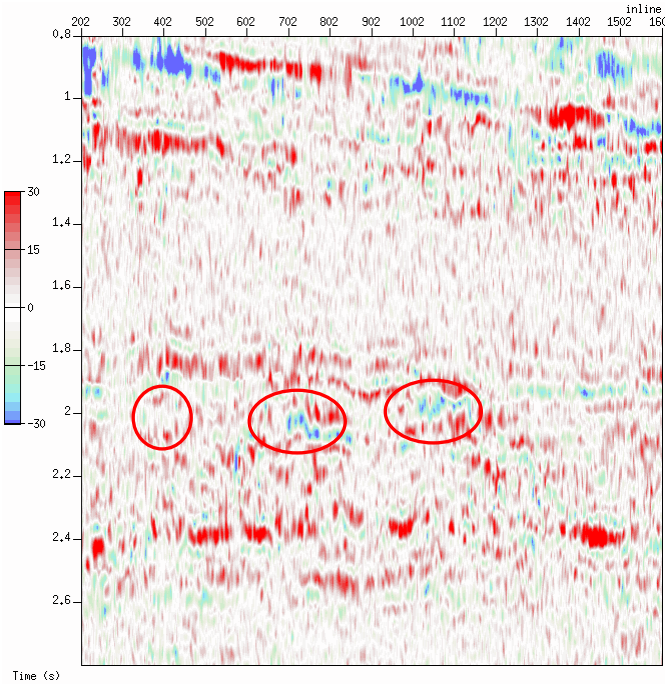

(a) CWT

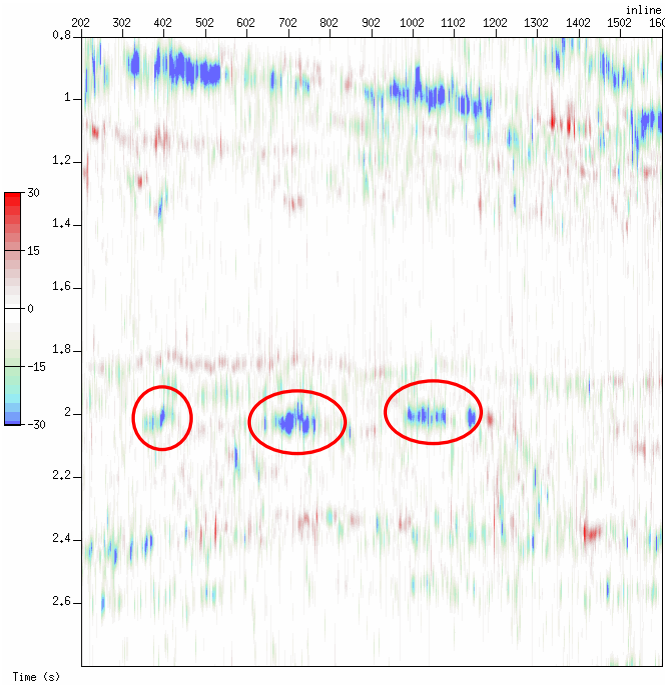

(b) MPM

Figure 5.20: Difference plots of $25Hz - 15Hz$ sections for the crossline using the CWT and the MPM.

5.6 Comparison of AVO and spectral decomposition sections

In my AVO analysis I identified six areas (three each on the IL and XL) that displayed large stacked amplitudes along the *Wdb 6Trov* horizon at ~2s. After inspecting the CMP gathers I interpreted five of these areas as Class III reflections. The final area displaying large stacked amplitude can be subdivided into a Class IV reflection between CMPs 950 – 1080 and a Class III reflection between CMPs 1080 – 1190 and my interpretation concentrated on the Class III reflection. The inverted intercept, gradient and intercept x gradient sections all separately confirmed my initial interpretation of Class III reflections. The weighted intercept and gradient section, representing the fluid factor trace, improved upon the Poisson's reflectivity section by minimising the background trend and further highlighting these areas as being anomalous. I must be cautious though as my AVO analysis is qualitative and I am unable to make any conclusions regarding the causes of these large stacked amplitudes; e.g. whether they are the result of fluid saturation changes or lithological effects. Crossplotting the gradient against the intercept and the stacked amplitude showed that these areas are independent of the background trend and not the result of statistical leakage in the inversion.

Chapman *et al*. (2006) argued that velocity dispersion as a result of fluid saturation can result in a frequency-dependent reflection coefficient. The amount of dispersion in both the velocity and reflection-coefficient is dependent on the saturating fluids where water or gas has the smallest bulk modulus and the most dispersion. This always results in the lower frequencies having a smaller reflection coefficient than the higher frequencies. In this example I have identified six Class III reflections and, if they are dispersive, then the absolute values of the reflection coefficients at lower frequencies would be larger, resulting in preferential illumination at low frequencies. Any subtle changes in the balanced iso-frequency sections of the IL and XL are difficult to interpret. Spectral difference plots highlight the amplitude difference between a high ($25Hz$) and low ($15Hz$) frequency and are akin to time-lapse seismic difference plots (e.g. Gouveia *et al*., 2004). The MPM spectral difference plots show

a strong low-frequency signature for the intersecting area on the IL between CMPs 4910 – 5020 and on the XL between CMPs 610 – 840. Without forward modelling or well control it is impossible for me to make a conclusive interpretation but this area has a strong low-frequency Class III AVO signature indicative of hydrocarbon saturation. The other two areas on the XL between CMPs 350 - 430 and 1080 – 1190 have a weaker low-frequency signature that could be caused by a number of factors such as improper balancing or tuning. However, the signature is consistent with a frequency-dependent Class III reflection and could be the result of hydrocarbon saturation that has a larger bulk fluid modulus. The two final areas on the IL, between CMPs 4600 – 4700 and 4780 – 4870, both have a small high-frequency signature that isn't consistent with a frequency-dependent Class III reflection; these areas could be due to either improper balancing or tuning. As I've already stated it is impossible to make a conclusive interpretation of any of these anomalies without further investigation, such as AVO modelling. The area with the largest stacked amplitude on the intersecting IL and XL can be interpreted as a frequency-dependent Class III AVO anomaly.

5.7 Discussion and Conclusions

I performed an integrated AVO and spectral analysis of intersecting IL and XL from a marine dataset. I identified six areas that had large amplitudes on the stacked sections. I initially interpreted CMP gathers according to standard, elastic, AVO theory and then inverted them according to Shuey's two-term linear approximation for intercept and gradient using a commercially available software package. I interpreted all six areas as being Class III reflections where their amplitudes increased with offset. I also used linear combinations of the intercept and gradient to create sections of Poisson's reflectivity and the fluid factor which minimise the background wet-trend and can enhance hydrocarbon detection. Crossplots and cross-sections of the inverted intercept and gradient showed that these areas were not statistical anomalies and are true deviations from the background trend.

I decomposed the IL and XL using both CWT and MPM algorithms with the latter obtaining better temporal and frequency resolution compared to the CWT. The higher amplitude background noise on the CWT sections affects the spectral difference plots making my interpretation difficult and it may be responsible for the discrepancy between the CWT and MPM spectral difference plots. Due to the improved signal to noise ratio and temporal and frequency resolution I was inclined to favour the MPM results on this real dataset.

Four of the six Class III AVO anomalies had a low-frequency spectral signature consistent with frequency-dependent AVO theory. The intersecting area on the IL between CMPs 4910 – 5020 and on the XL between CMPs 610 – 840 had the strongest low-frequency response and I have the most confidence in interpreting this area as being frequency-dependent due to hydrocarbon saturation. The other two Class III AVO anomalies had a small, near zero, high-frequency anomaly that isn't consistent with frequency-dependent AVO theory and I attribute this to either tuning or to problems in correctly balancing the raw iso-frequency sections. By performing a combined amplitude and spectral analysis of a real marine dataset I have been able to use frequency-dependent AVO theory to extend my interpretation of commonly observed Class III bright spots in the search for hydrocarbons.

This chapter has indicated the presence of velocity dispersion within the seismic bandwidth. Whilst the interpretation of spectral and AVO anomalies is non-unique it does lend credence to the concept of frequency-dependent AVO. In Chapter 2 I reviewed published estimates of the relaxation parameter that were all very small. The results of this chapter indicate that tau may in fact be larger than suggested in previously published work under certain circumstances. If this conclusion is correct then it should be possible to extend the current, standard, methodology to qualitatively estimate the velocity dispersion without having to link theoretical estimates with real data.

Chapter 6: New theory and methodology for frequency-dependent AVO

6.1 Introduction

In this Chapter I will show how I have extended Smith and Gidlow's (1987) two-term AVO approximation to be frequency-dependent by accounting for velocity dispersion in the reflecting mediums. Rather than using classical pre-stack seismic amplitudes, I have used pre-stack spectral amplitudes following spectral decomposition in a least-squares inversion to measure the P- and S-wave reflectivity dispersion. The magnitude depends on the amount of velocity dispersion in the reflecting mediums and the sign indicates the AVO classification. I have tested my approximation and inversion method on a simple two-layer synthetic model with varying amounts of velocity dispersion. I have calculated the approximate frequency-dependent reflection coefficient by comparing it to the exact Zoeppritz solutions and found it to be accurate. Following the inversion I calculated residual errors between the input amplitudes and the parameters and found them to be small ($< 5\%$). I inverted the synthetic models for frequency-dependent reflectivities and the reflectivity dispersion and have been able to detect and quantify the different levels of velocity dispersion in the input synthetics.

6.2 Frequency-dependent AVO approximation

Following my integrated amplitude and spectral analysis it is evident that a robust method must be developed to quantify the velocity dispersion that causes frequency-dependent AVO. Smith and Gidlow's (1987) two-term linear AVO approximation (equation 3-25) estimates the P- and S-wave reflectivities $\left(\frac{\Delta V_P}{V_P} \text{ and } \frac{\Delta V_S}{V_S}\right)$ using parameters that are either known or can be estimated. The two offset-dependent constants in their approximation depend on V_P, V_S and the angle of incidence (θ_i)

which can be calculated by way of ray tracing. For synthetic models V_S is known whilst in a real data example the smooth P-wave stacking velocity can be used with the mudrock line (equation 2-16) to estimate a smooth S-wave velocity profile. If I make the assumption that the constants A_1 and A_2 are frequency-independent and do not vary with velocity dispersion then I can extend the elastic AVO approximation to be frequency-dependent,

$$R(\theta_i, f_j) \approx A_1(\theta_i)\frac{\Delta V_P}{V_P}(f_j) + A_2(\theta_i)\frac{\Delta V_S}{V_S}(f_j). \qquad (6\text{-}1)$$

I then expanded $\frac{\Delta V_P}{V_P}(f_j)$ and $\frac{\Delta V_S}{V_S}(f_j)$ as a Taylor series around a representative frequency, f_0, so that

$$R(\theta_i, f_j) \approx A_1(\theta_i)\frac{\Delta V_P}{V_P}(f_0) + (f_j - f_0)A_1(\theta_i)I_a + A_2(\theta_i)\frac{\Delta V_S}{V_S}(f_0) + (f_j -$$
$$f0A2\theta iIb \qquad (6\text{-}2)$$

and I have introduced a new term called the reflectivity dispersion, I_a and I_b, such that,

$$I_a = \frac{d}{df}\left(\frac{\Delta V_P}{V_P}\right) \qquad (6\text{-}3)$$

and

$$I_b = \frac{d}{df}\left(\frac{\Delta V_S}{V_S}\right). \qquad (6\text{-}4)$$

6.2.1 Seismic versus spectral amplitudes

Seismic data contains both amplitude and phase information (Taner *et al*., 1979), whereby the amplitude contains information relating to the magnitude of the reflection coefficient and the phase contains information relating to the polarity of

the reflection. This means that, for an elastic inversion of equation 3-25, the P- and S-wave reflectivities contain both amplitude and phase information relating to the two mediums. The inverted reflectivities retain the wavelet shape of the input seismic and, if there is a phase reversal, it implies that there has been a velocity decrease from the top medium to the lower one ($V_2 < V_1$) and $\Delta V/V$ is negative. Whilst spectral decomposition algorithms can approximate both the amplitude and phase spectrums the decomposed spectral amplitudes have lost this phase information. When $\theta = 0$, $A_2 = 0$ and $A_1 > 0$, then $\frac{\Delta V_P}{V_P}\Big|_f > 0$ and the measured P-wave frequency-dependent reflectivity is technically $\left|\frac{\Delta V_P}{V_P}\Big|_f\right|$ and the frequency-dependent AVO inversion is actually calculating $\frac{d}{df}\left|\frac{\Delta V_P}{V_P}\Big|_f\right|$.

6.2.2 AVO reflectivity dispersion classification

I have argued above that spectral amplitudes do not contain phase information and that seismic amplitudes do since they are always positive and never negative. By referring to phase dispersion I am remarking on the way that the measured reflectivity dispersive value can be either positive or negative depending on the AVO classification of the reflection.

As I have shown in figure 2.1, for a dispersive material the velocity will always be greater at a higher frequency such that

$$V_2^L \leq V_2^H \qquad (6\text{-}5)$$

where V_2^L is the low-frequency velocity and V_2^H the high-frequency velocity and would be equal in the elastic case. If I now square both sides and subtract V_1^2 and add $V_2^H V_2^L$ to both sides then I obtain

$$(V_2^L)^2 - V_1^2 + V_2^H V_2^L \leq (V_2^H)^2 - V_1^2 + V_2^H V_2^L. \qquad (6\text{-}6)$$

Since $V_1V_2^H \geq V_1V_2^H$, I can subtract $V_1V_2^H$ from the left-hand side of equation 6-6 and $V_1V_2^H$ from the right-hand side without changing the inequality so that

$$(V_2^L)^2 - V_1^2 + V_2^H V_2^L - V_1V_2^H \leq (V_2^H)^2 - V_1^2 + V_2^H V_2^L - V_1V_2^H. \qquad (6\text{-}7)$$

I can then factorise the above relationship and divide each side by two so that

$$(V_2^L - V_1)\frac{(V_2^H + V_1)}{2} \leq (V_2^H - V_1)\frac{(V_2^L + V_1)}{2}. \qquad (6\text{-}8)$$

This can then be rearranged to the more familiar relationship

$$\frac{(V_2^L - V_1)}{\frac{(V_2^L + V_1)}{2}} \leq \frac{(V_2^H - V_1)}{\frac{(V_2^H + V_1)}{2}} \qquad (6\text{-}9)$$

or

$$\left.\frac{\Delta V}{V}\right|_L \leq \left.\frac{\Delta V}{V}\right|_H. \qquad (6\text{-}10)$$

This relationship always holds true and if I were able to invert for $\frac{d}{df}\left(\frac{\Delta V}{V}\right)$ it would provide no information regarding the AVO classification of the reflecting interface. But, as I mentioned in the previous section, I am inverting for $\left|\frac{\Delta V_P}{V_P}\right|$ and I can use the relationship between V_{P1} and V_{P2} to infer some extra information regarding the reflecting interface.

For a typical Class I reflection, $V_{P1} < V_{P2}$, so $\Delta V_P = V_{P2} - V_{P1} > 0$, resulting in

$$\left|\frac{\Delta V_P}{V_P}\right|_L < \left|\frac{\Delta V_P}{V_P}\right|_H \qquad (6\text{-}11)$$

and the measured value will be a positive quantity with

$$\frac{d}{df}\left(\frac{\Delta V_P}{V_P}\right) > 0. \qquad (6\text{-}12)$$

For a typical Class III reflection, $V_{P1} > V_{P2}$, so $\Delta V_P = V_{P2} - V_{P1} < 0$, resulting in

$$\left|\frac{\Delta V_P}{V_P}\right|_L > \left|\frac{\Delta V_P}{V_P}\right|_H \qquad (6\text{-}13)$$

and the measured dispersion will be a negative quantity,

$$\frac{d}{df}\left(\frac{\Delta V_P}{V_P}\right) < 0. \qquad (6\text{-}14)$$

For a typical Class II reflection the difference between V_{P1} and V_{P2} is small and the intercept may be positive or negative. So $\Delta V_P = V_{P2} - V_{P1} < 0 \; or \; > 0$ resulting in $\left|\frac{\Delta V_P}{V_P}\right|_L > 0$ or $0 < \left|\frac{\Delta V_P}{V_P}\right|_H$ and the measured dispersion could be either a positive or a negative quantity.

Finally, for a Class IV reflecting interface, (Castagna *et al.*, 1998), $V_{P1} > V_{P2}$, so $\Delta V_P = V_{P2} - V_{P1} < 0$ resulting in

$$\left|\frac{\Delta V_P}{V_P}\right|_L > \left|\frac{\Delta V_P}{V_P}\right|_H \qquad (6\text{-}15)$$

and the measured dispersion will be a negative quantity.

I have summarised how the different reflecting AVO classifications affect $\left|\frac{\Delta V_P}{V_P}\right|$ in figure 6.2.

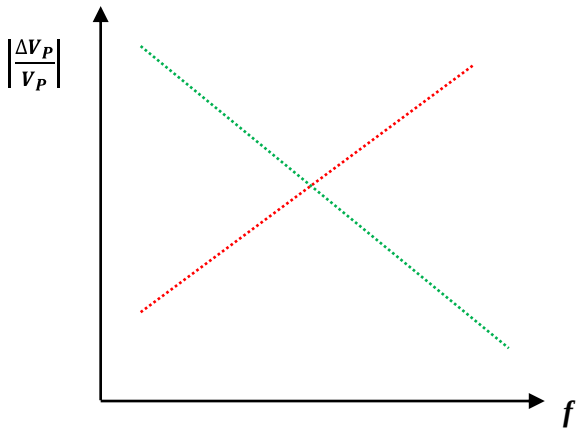

Figure 6.1: Sketch of the way $\left|\frac{\Delta V_P}{V_P}\right|$ varies with frequency. For Class I and IIp reflections (red line), $\frac{d}{df}\left(\left|\frac{\Delta V_P}{V_P}\right|\right)$ is positive, for Class II, III and IV reflections (green line), $\frac{d}{df}\left(\left|\frac{\Delta V_P}{V_P}\right|\right)$ is negative.

6.3 Frequency-dependent AVO inversion

In Chapter 3, I have transformed Smith and Gidlow's (1987) two-term AVO approximation from reflection coefficients into seismic amplitudes which I represented as matrices that could be inverted for reflectivities. To develop a frequency-dependent AVO inversion methodology I have to account for the change from seismic amplitudes into balanced spectral amplitudes. For each time sample, the offset-dependent amplitudes, $D(t,n)$, are spectrally-decomposed into spectral amplitudes, $S(t,n,f)$, for each frequency, *f*, so that

$$D(t,n) \rightarrow S(t,n,f). \qquad (6\text{-}16)$$

Following the balancing schemes I described in Chapter 4, to remove the effect of the source overprint on the spectral amplitudes using a weight function, $w(f,n)$, the balanced spectral amplitudes are

$$B(t,n,f) = w(f,n)S(t,n,f). \qquad (6\text{-}17)$$

The transformation from reflection coefficients to amplitudes has been extended to include spectral decomposition and spectral balancing to allow me to use the

resultant balanced spectral amplitudes in an inversion methodology. I defined A_1 and A_2 such that,

$$A_1(\theta_i) = \frac{5}{8} - \frac{1}{2}\frac{V_S^2}{V_P^2} sin^2\theta_i + \frac{1}{2} tan^2\theta_i \equiv A_1(t,n) \qquad (6\text{-}18)$$

and

$$A_2(\theta_i) = -4\frac{V_S^2}{V_P^2} sin^2\theta_i \equiv A_2(t,n) \qquad (6\text{-}19)$$

where the angle of incidences can be calculated for each receiver, *n*, using ray tracing. Then I could substitute in balanced spectral amplitudes at time *t* and receiver *n* into equation 6-2 to obtain

$$B(t,n,f) = A_1(t,n)\frac{\Delta V_P}{V_P}(t,f_0) + (f-f_0)A_1(t,n)I_a + A_2(t,n)\frac{\Delta V_S}{V_S}(t,f_0) + (f-f_0)A_2(t,n)I_b \qquad (6\text{-}20)$$

where $I_a = \frac{d}{df}\left(\left|\frac{\Delta V_P}{V_P}\right|\right)$, $I_b = \frac{d}{df}\left(\frac{\Delta V_S}{V_S}\right)$.

The actual frequency-dependent AVO inversion is a two-step process. First I inverted for $\frac{\Delta V_P}{V_P}(f_0)$ and $\frac{\Delta V_S}{V_S}(f_0)$ at the reference frequency. This is calculated by substituting $f = f_0$ in equation 6-30, which reduces to

$$B(t,n,f_0) = A_1(t,n)\left|\frac{\Delta V_P}{V_P}\right|(t,f_0) + A_2(t,n)\frac{\Delta V_S}{V_S}(t,f_0). \qquad (6\text{-}21)$$

Here the $f - f_0$ terms reduce to zero and the above equation bears a close resemblance to the original AVO inversion given in equation 3-38. In fact I can invert equation 6-30 for any frequency, f_j, using the following relationship

$$B(t,n,f_j) = A_1(t,n)\frac{\Delta V_P}{V_P}(f_j) + A_2(t,n)\frac{\Delta V_S}{V_S}(f_j). \qquad (6\text{-}22)$$

The second step is when I use all frequencies, f, and I can measure the reflectivity dispersion using equation 6-20. Rearranging and putting it into matrix form similar to equation 3-35 I obtain

$$\begin{bmatrix} B(t,1,f_1) - A_1(t,1)\frac{\Delta V_P}{V_P}(t,f_0) - A_2(t,1)\frac{\Delta V_S}{V_S}(t,f_0) \\ \vdots \\ B(t,n,f_m) - A_1(t,1)\frac{\Delta V_P}{V_P}(t,f_0) - A_2(t,1)\frac{\Delta V_S}{V_S}(t,f_0) \end{bmatrix} =$$
$$\begin{bmatrix} (f_1 - f_0)A_1(t,1) & (f_1 - f_0)A_2(t,1) \\ \vdots & \vdots \\ (f_m - f_0)A_1(t,n) & (f_m - f_0)A_2(t,n) \end{bmatrix} \begin{bmatrix} I_a \\ I_b \end{bmatrix}. \qquad (6\text{-}23)$$

This can be simplified to

$$RR = RM \begin{bmatrix} I_a \\ I_b \end{bmatrix} \qquad (6\text{-}24)$$

and solved using a least-squares inversion without weights (Sheriff and Geldart. 1995) for each time sample,

$$\begin{bmatrix} I_a \\ I_b \end{bmatrix} = (RM^T RM)^{-1} RM^T RR \qquad (6\text{-}25)$$

and I_a, I_b are the P- and S-wave reflectivity dispersion traces respectively.

6.4 Synthetic example – Class III reflection

6.4.1 Model

I tested my frequency-dependent AVO inversion on a simple two-layer synthetic for a Class III reflection. The model parameters are listed in table 6.1. The lower

sandstone half-space is initially defined under water-saturation then gas is substituted, resulting in the dispersive material used. The fluid substitution from water with bulk fluid modulus $2GPa$ to gas with bulk fluid modulus $200MPa$ reduces the P-wave velocity and density altering the reflection from a Class I to a Class III, shown in figure 6.3.

Material	**V_P (ms^{-1})**	**V_S (ms^{-1})**	**ρ_W ($g.cm^{-3}$)**	**ρ_G ($g.cm^{-3}$)**	**Φ (%)**	**ε (%)**
Shale	2743	1394	2.06	-	-	-
Sandstone	2835	1472	2.08	2.04	15	5

Table 6.1: Material parameters for numerical model as described in Chapman *et al*. (2005).

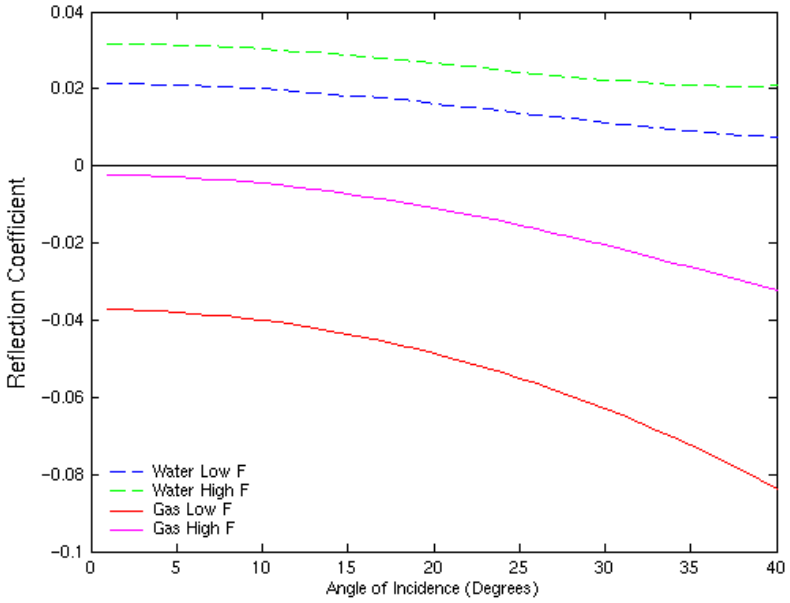

Figure 6.2: AVO low and high-frequency limit curves for the shale-sandstone boundary under water and gas saturation, where the relaxation parameter was set to $1e^{-6}s$ and $100s$ respectively.

The exact AVO curves for the low- and high-frequency limits are plotted in figure 6.3 which shows the dispersion between the low-frequency limit and the high-frequency limit for both the water and gas saturation. This is commonly thought of as the difference between seismic (low-frequency) and ultrasonic (high-frequency) velocities. The dispersion is much greater under gas saturation and, following

arguments made about fluid mobility (Batzle *el al*., 2001 and Hofmann *at al*., 2005) and fluid viscosity (Batzle *et al*., 2006), it is more likely that velocity dispersion detectable in the seismic bandwidth will be the result of hydrocarbon saturation. The water-saturated dispersion is more likely to be detected as a difference between frequency measurement scales.

I used the initial model parameters listed in table 6.1 to define the sandstone halfspace under water saturation. I then substituted gas for water at a lower bulk modulus using four different relaxation times ($\tau = 1e^{-6}s$, $\tau = 5e^{-3}s$, $\tau = 5e^{-2}s$ and $\tau = 100s$) where the $\tau = 1e^{-6}s$ synthetic is equivalent to an elastic sandstone layer under gas saturation. I used eleven receivers, (0m – 1000m) at 100m spacing, with a 40Hz Ricker wavelet as the source and the four resultant synthetic gathers are shown in figure 6.4.

Observation of the amplitudes shows that as I move from the elastic synthetic towards higher tau values, the amplitudes decrease. This agrees with the predicted AVO behaviour shown in figure 6.2; I have shifted the synthetics from the gas low-frequency curve to the gas high-frequency curve and am reducing the reflection coefficients and amplitudes. The elastic synthetic is in the low-frequency zone and the two dispersive synthetics are in the transition zone whilst the final synthetic is in the high-frequency zone. It is predicted that dispersion will be most noticeable in the two middle synthetics and I have calculated the exact, frequency-dependent, reflection coefficients under these two settings in figure 6.4. It is clear from this figure that the spread of the reflection coefficients is greater when $\tau = 5e^{-3}s$ compared with $\tau = 5e^{-2}s$.

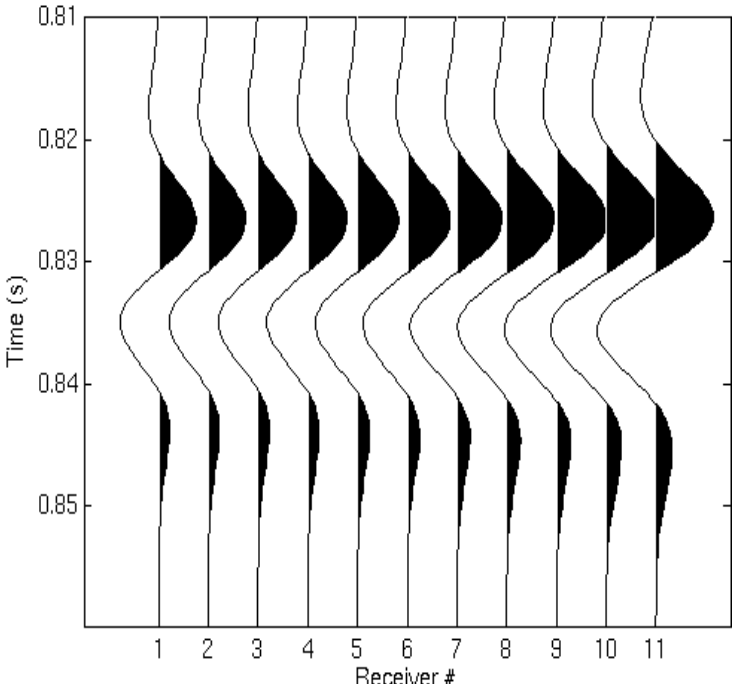

(a) Elastic, $\tau = 1e^{-6}s$

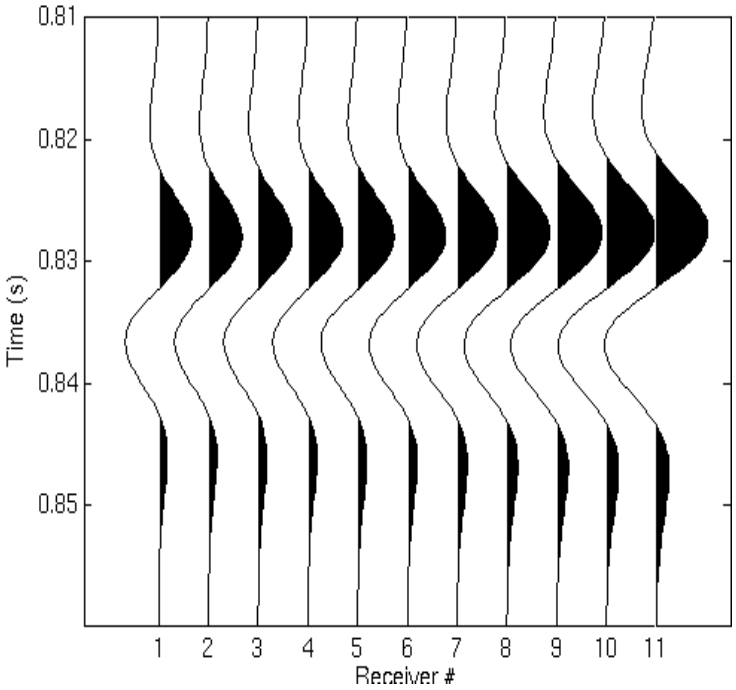

(b) $\tau = 5e^{-3}s$

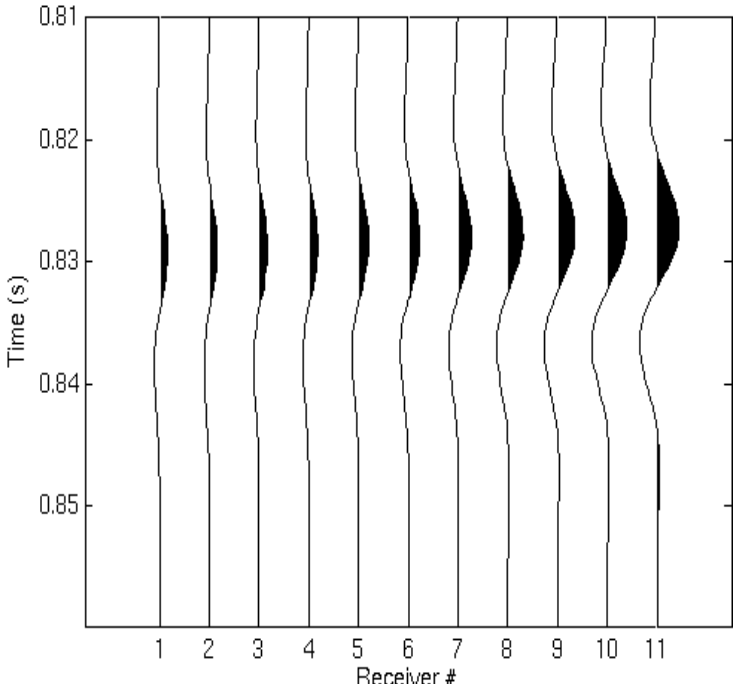

(c) $\tau = 5e^{-2}s$

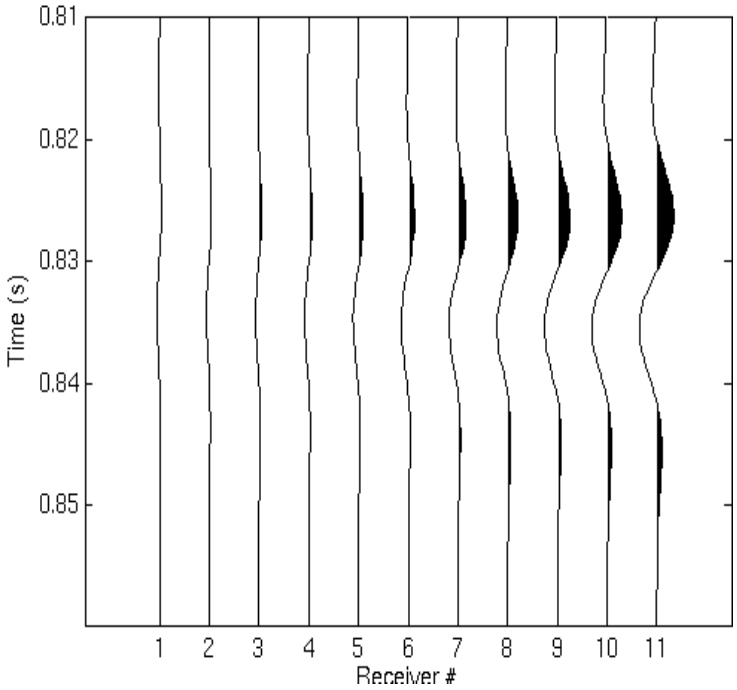

(d) $\tau = 100s$

Figure 6.3: Four synthetic reflection gathers for varying relaxation times and dispersion.

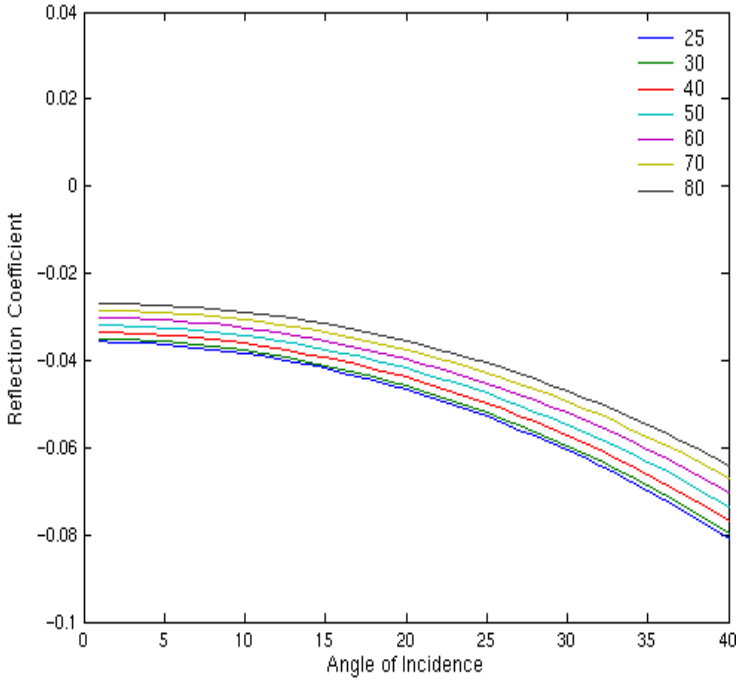

(a) $\tau = 5e^{-3}s$

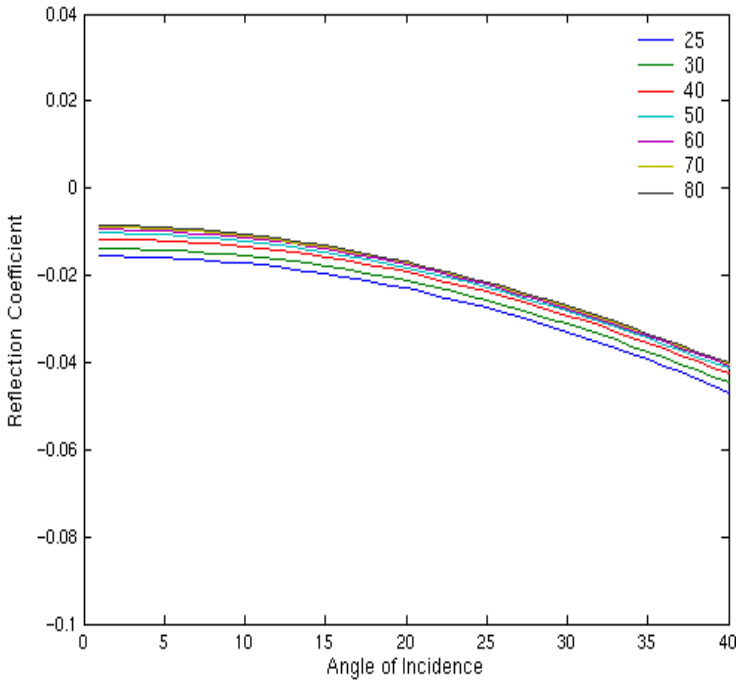

(b) $\tau = 5e^{-2}s$

Figure 6.4: The exact reflection coefficients for the two dispersive synthetics shown in figure 6.3; note the increased dispersion in (a) over (b). The different colours represent the different frequencies. The different frequencies have varying P-wave velocities in the lower layer as indicated in figure 2.1.

6.4.2 Approximation accuracy (i)

To test the accuracy of my frequency-dependent approximation I modelled the reflection coefficient for a selection of frequencies (10, 20, 30, 40, 50, 60, 70 and 80Hz) and for a range of angles of incidence (0°, 5°, 10°, 15°, 20°, 25°, 30°, 35° and 40°) using equation 6-32. I have plotted these for the case when $\tau = 5e^{-3}s$ along with the exact reflection coefficients. The average V_P and V_S values were calculated using V_{P2} and V_{S2} extracted from the relevant frequency-dependent elastic moduli and a summary is shown in table 6.2.

FREQ:	**10**	**20**	**30**	**40**	**50**	**60**	**70**	**80**
V_{p1}	*2743*	*2743*	*2743*	*2743*	*2743*	*2743*	*2743*	*2743*
ρ_2	2.04	2.04	2.04	2.04	2.04	2.04	2.04	2.04
λ+2μ	13.5122	13.5859	13.6969	13.8317	13.9774	14.1233	14.2627	14.3913
V_{p2}	**2574**	**2581**	**2591**	**2604**	**2618**	**2631**	**2644**	**2656**
V_{s1}	*1394*	*1394*	*1394*	*1394*	*1394*	*1394*	*1394*	*1394*
μ	4.5072	4.5079	4.5092	4.5109	4.5130	4.5155	4.5183	4.5213
V_{s2}	**1486**	**1487**	**1487**	**1487**	**1487**	**1488**	**1488**	**1489**

Table 6.2: Elastic moduli extracted from the elastic tensor to generate the frequency-dependent V_{P2} and V_{S2} to calculate the AVO approximations in figure 6.5.

Figure 6.6 shows both the reflection coefficients calculated using the exact Zoeppritz equation (solid lines) and my frequency-dependent approximation (points). The approximation has overestimated the amount of dispersion (approximately double at the near offsets) compared with the exact reflection coefficients. The greatest agreement between the exact and approximate values is at 40Hz (orange line and mauve circles), and the general agreement between the two increases with offset.

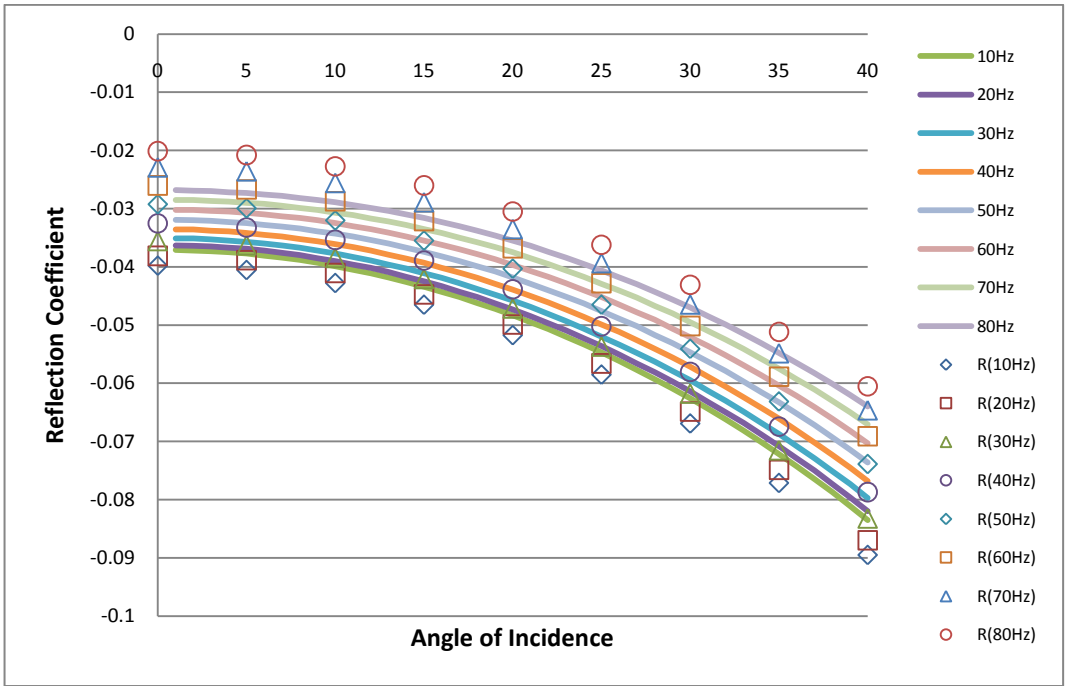

Figure 6.5: Exact frequency-dependent reflection coefficients (solid lines) with the frequency-dependent AVO approximations (points) for the dispersive $\tau = 5e^{-3}s$ synthetic.

6.4.3 Synthetic processing

I have used a reflectivity modelling code, ANISEIS (Taylor, 1990) to create all my synthetic seismograms in this thesis from point sources in plane-layered models. All my synthetics have azimuthal isotropy and it is the use of frequency-dependent materials, where an elastic tensor is defined for every frequency specified, that has allowed dispersion to be modelled. The reflectivity method uses the Kennet algorithm to iteratively calculate the response from plane waves by successively adding in the deeper layers (Mallick and Frazer, 1990). Plane waves are accumulated along summation paths, depending on the acquisition geometry, in complex horizontal slowness planes for the range of frequencies I have chosen (1 – 250Hz). The three-component data (*r*, *x*, *z*) is recorded (Taylor, 1990) but I only require the vertical (*z*) and radial (*r*) components. I apply a time-dependent amplitude correction assuming a constant velocity background to account for spherical divergence in the form of

$$Amp_{corr} = Amp_{uncorr} * t^2. \qquad (6\text{-}26)$$

I then applied an NMO correction to the data using the exact velocities as a starting point. Finally, the two components of the data were added together using Pythagoras theorem to calculate the total amplitude at each receiver

$$Amp_T = \sqrt{Amp_z^2 + Amp_r^2}. \qquad (6\text{-}27)$$

6.4.4 Spectral decomposition of synthetics

All four synthetics were spectrally-decomposed using both the CWT and MPM algorithms, with the parameters chosen in Chapter 4, at frequencies 10, 15, 20, 25, 30, 40, 50, 60, 70, 80, 85, 90 and 95Hz. I have decomposed a large number of frequencies in order to determine the largest suitable bandwidth for the inversion. The maximum spectral amplitudes from the elastic synthetic using the CWT decomposition and the MPM decomposition are shown in figures 6.7 and 6.8 respectively. Both the CWT and MPM decomposed amplitudes show smooth curves with increasing amplitude with offset as expected for a Class III reflection. Figure 6.8 shows the decomposed wavelets of the zero-offset trace, again from the elastic synthetic. The energy from the wavelet has been smeared over a much larger time period using the CWT whist the MPM has excellent temporal resolution. By comparing figures 6.7 and 6.8 both algorithms have, independently, achieved similar amplitude values but the MPM shows increased time-frequency resolution compared to the CWT as reported by others (Mallat and Zhang, 1993, Chakraborty and Okaya, 1995 and Castagna and Sun, 2006).

From figure 6.7, I have decided upon selecting frequencies 25 to 80Hz to be included in my inversion. I have rejected the lowest and highest frequencies as they have the smallest decomposed amplitude (< 400) which would result in a very large weight function to balance them and could introduce unnecessary errors into the inversion. I can also detect a flattening of the AVO curves at far offsets for frequencies greater

than 70Hz. It is these far offsets that have the largest NMO correction applied and some of the higher frequencies are lost due to the wavelet being stretched (Yilmaz, 1999).

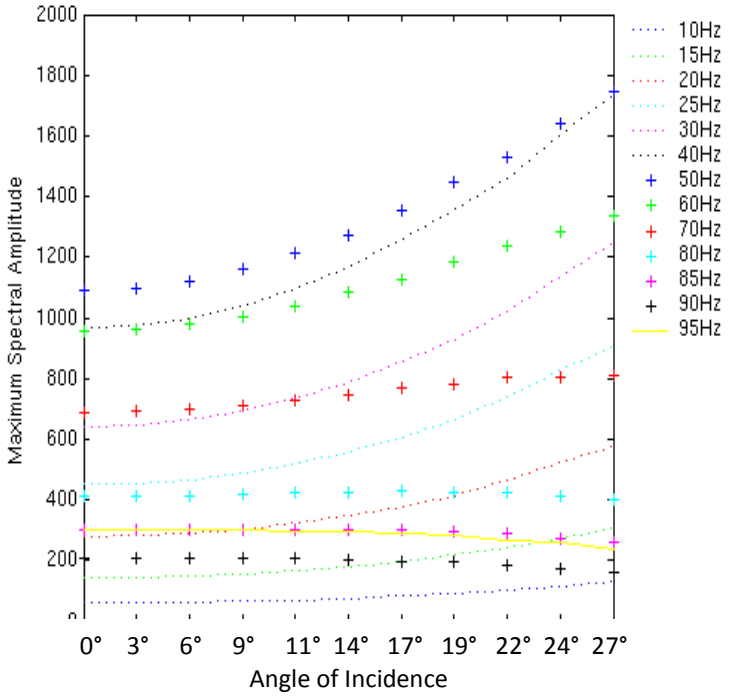

(a) CWT

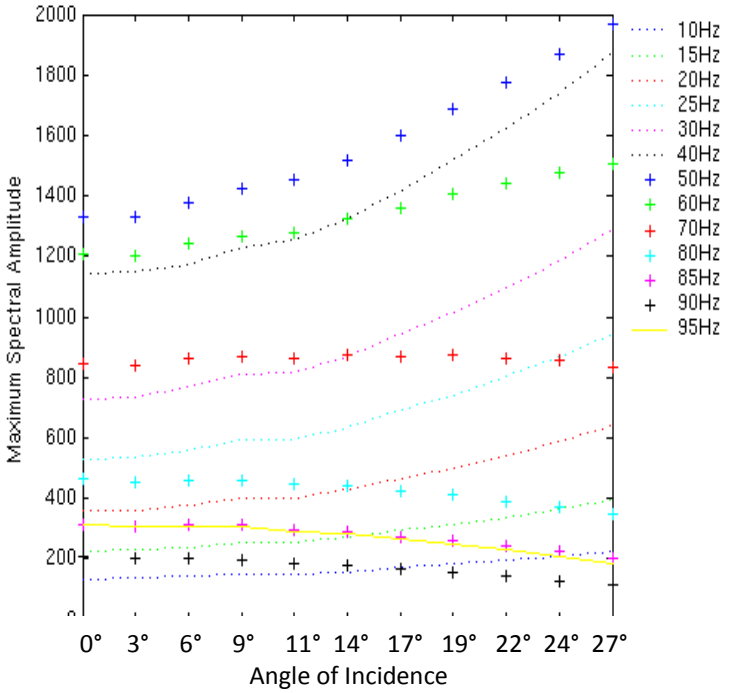

(b) MPM

Figure 6.6: Maximum decomposed spectral amplitudes using the CWT (a) and MPM (b) algorithms. The different colours represent the different frequencies.

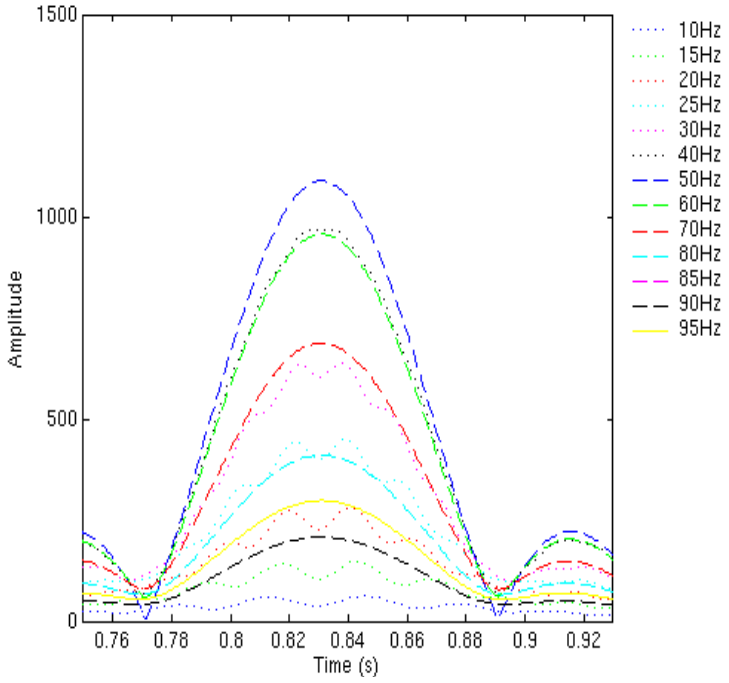

(a) CWT decomposed amplitudes

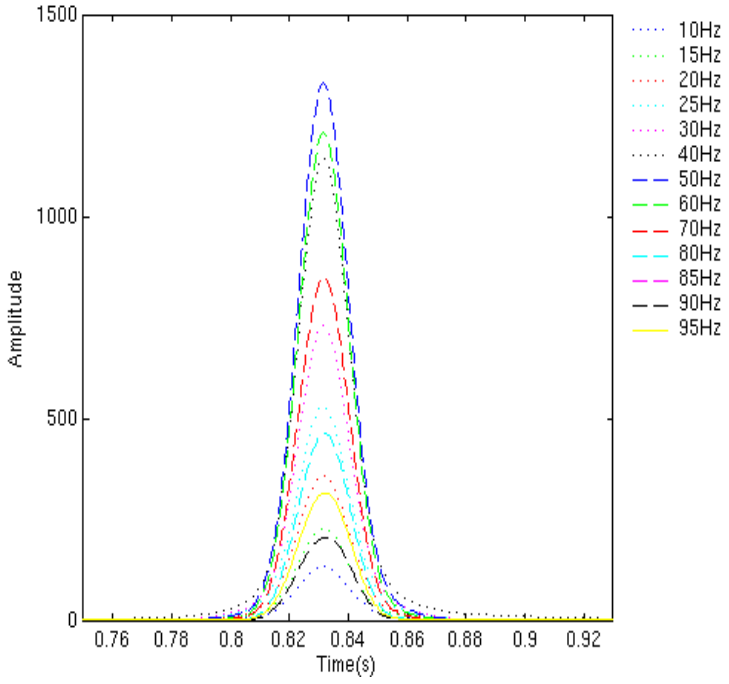

(b) MPM decomposed amplitudes

Figure 6.7: Decomposed zero-offset wavelet from the elastic synthetic using the CWT (a) and the MPM (b) algorithms.

Next, I designed a suitable weight function, as described in Chapter 3, using the elastic synthetic and subsequently applied it to the other synthetics. I cannot design a weight function directly from the dispersive synthetics as that would automatically remove any of the frequency-dependent variation within the data. I picked the maximum spectral amplitudes within the time window 0.81s – 0.86s and mathematically balanced them to equal the amplitude at the reference frequency, f_0. I have selected the reference frequency to be 40Hz, equal to the dominant frequency of the Ricker source wavelet. The weight function is defined for every frequency, *f*, and receiver, *n*, as the ratio of the maximum spectral amplitudes within the time window

$$w(f,n) = \frac{MAX\left(S_{f_0}(n)\right)}{MAX\left(S_f(n)\right)} \qquad (6\text{-}28)$$

which I then applied to the traces. Figure 6.8 shows the maximum amplitudes from the elastic synthetic and the dispersive, $\tau = 5e^{-3}s$, synthetic at 25, 30, 40, 50, 60, 70, and 80Hz balanced using two-different approaches; (i) offset-by-offset (solid lines) and (ii) zero-offset weight function only (dashed lines). If I only use the zero-offset weight function across the other offsets then the amplitudes are under-corrected and the AVO curve is lost. This effect appears to worsen as the frequency increases; the dashed lines in figures 6.8 flatten off at the higher frequencies and the increase in amplitude with offset is lost.

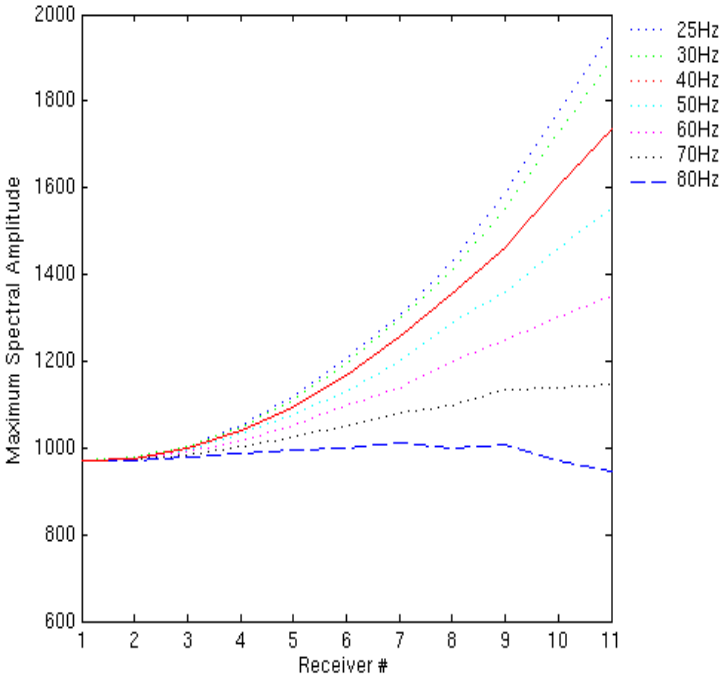

(a) Elastic maximum spectral amplitudes

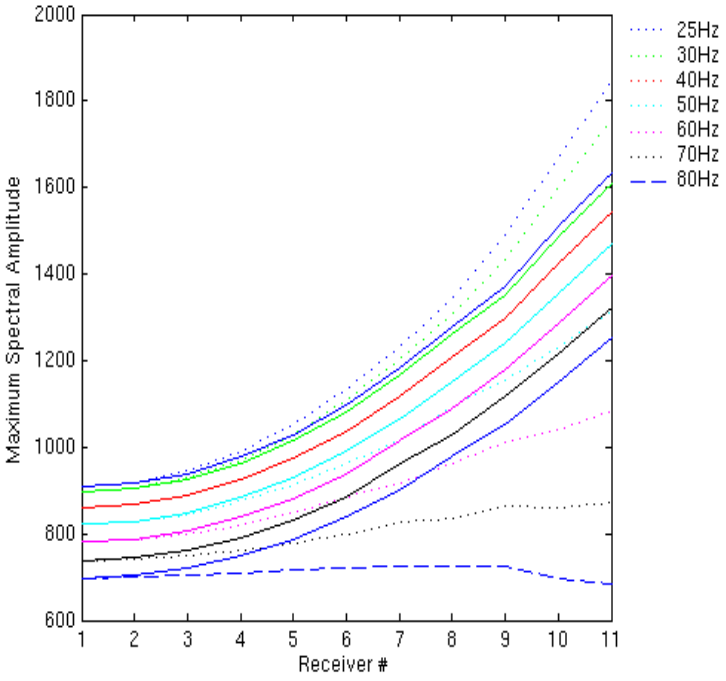

(b) Dispersive, $\tau = 5e^{-3}s$, maximum spectral amplitudes

Figure 6.8: The balanced maximum CWT spectral amplitudes (25 – 80Hz) for the elastic and $\tau = 5e^{-3}s$ synthetic using an offset-by-offset design (solid lines) or the zero-offset weight (dashed lines).

Figures 6.9 and 6.11 show the zero-offset unbalanced spectral amplitudes for the elastic and $\tau = 5e^{-3}s$ synthetics following a CWT and MPM decomposition. The largest unbalanced spectral amplitudes are at 40, 50 and 60Hz, close to the peak frequency of the source wavelet. Figures 6.10 and 6.12 show the resultant balanced spectral amplitudes using a weight function described by equation 6-28. The increased temporal resolution of the MPM over the CWT in figure 6.9 reduces the window of the wavelet from approximately 0.8-0.86s to 0.82-0.84s. The balanced time-frequency gathers clearly show the difference between the elastic and dispersive synthetics where the lowest frequencies have the largest amplitudes. This is the predicted result for a Class III reflection where the lowest frequencies have the largest reflection coefficients (figure 6.4).

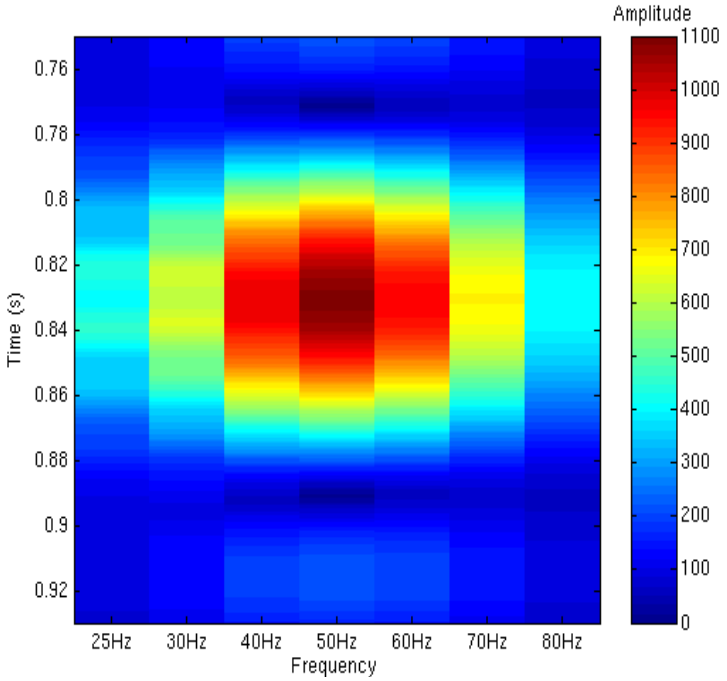

(a) Unbalanced CWT

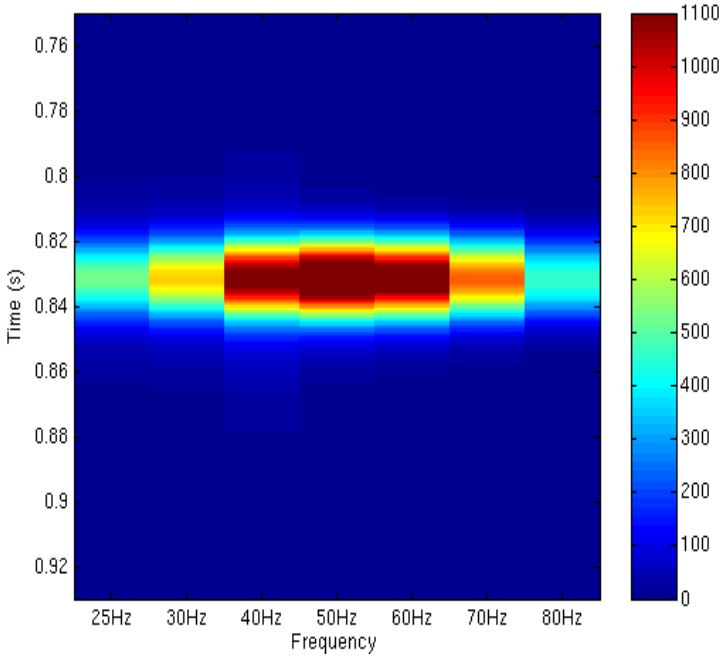

(b) Unbalanced MPM

Figure 6.9: The unbalanced decomposed frequency traces (25-80Hz) using the CWT and MPM decompositions for the zero-offset trace from the elastic synthetic.

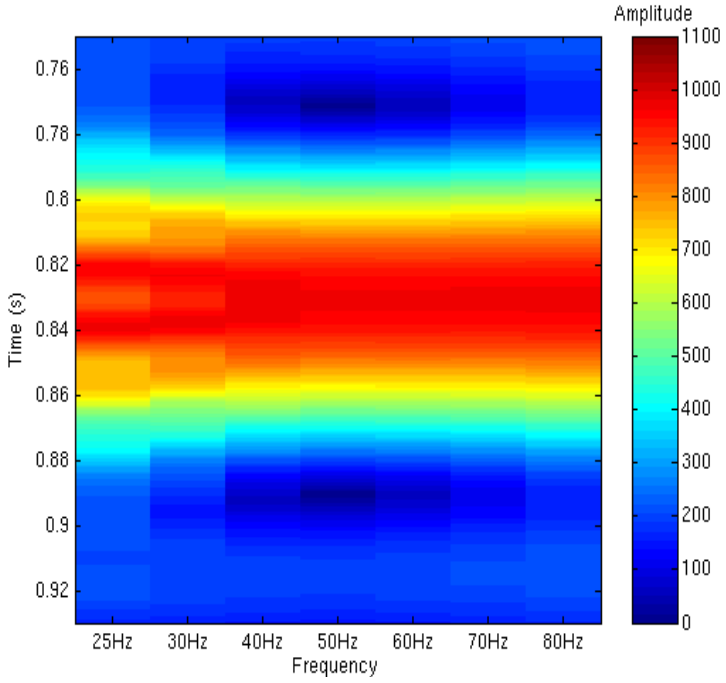

(a) Balanced CWT

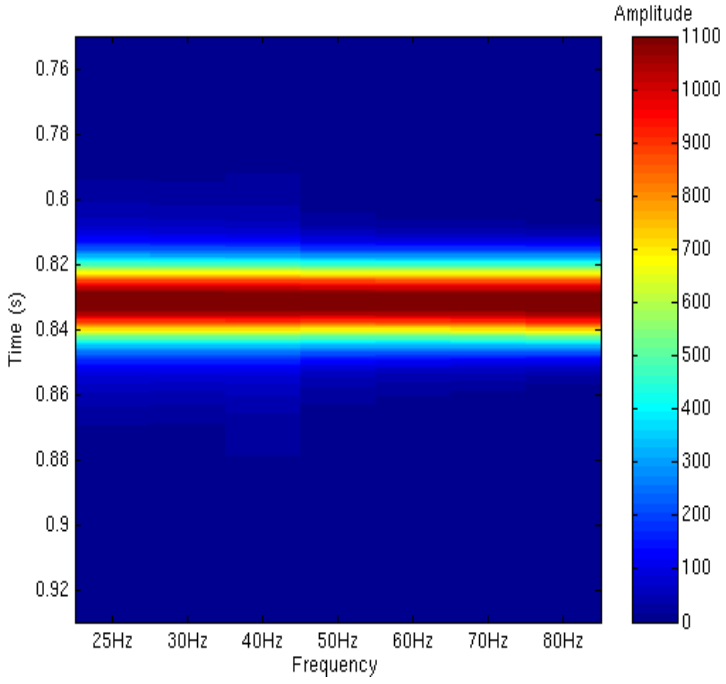

(b) Balanced MPM

Figure 6.10: The balanced decomposed frequency traces (25-80Hz) using the CWT and MPM decompositions for the zero-offset trace from the elastic synthetic.

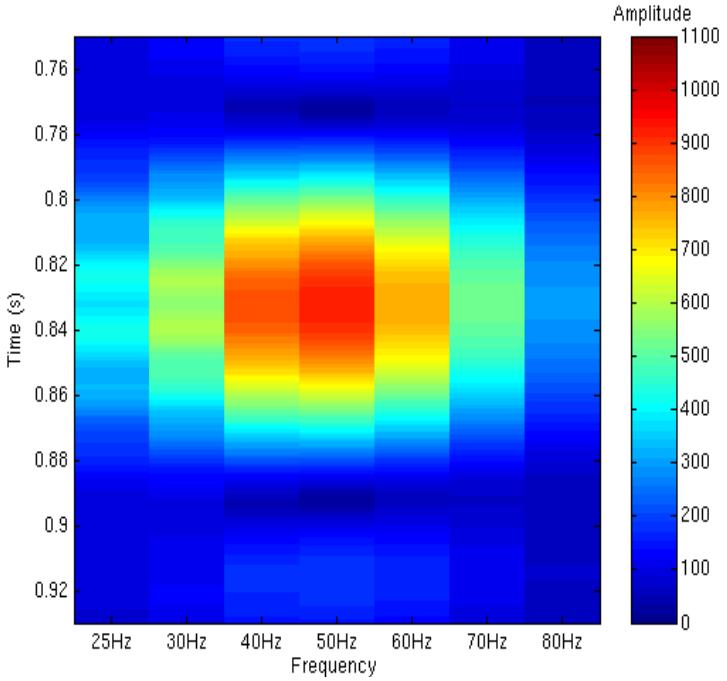

(a) Unbalanced CWT

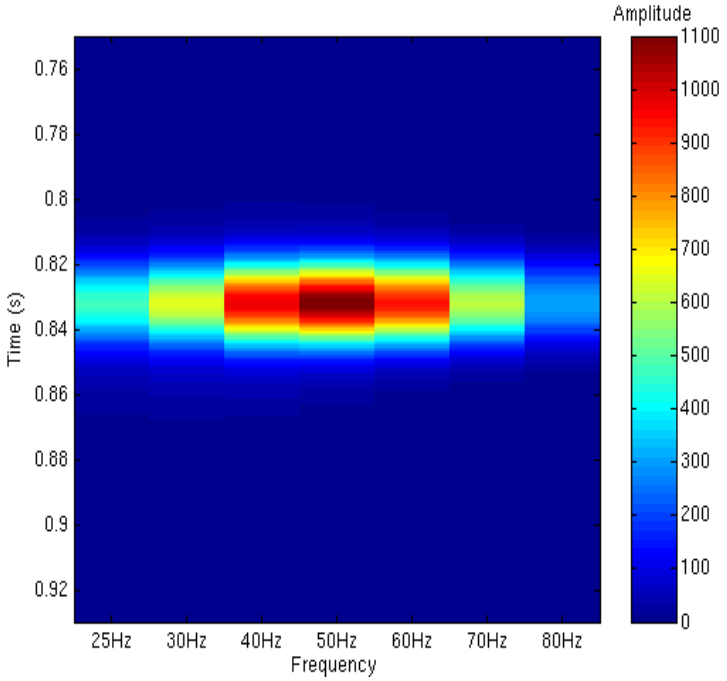

(b) Unbalanced MPM

Figure 6.11: The unbalanced decomposed frequency traces (25-80Hz) using the CWT and MPM decompositions for the zero-offset trace from the dispersive, $\tau = 5e^{-3}s$, synthetic.

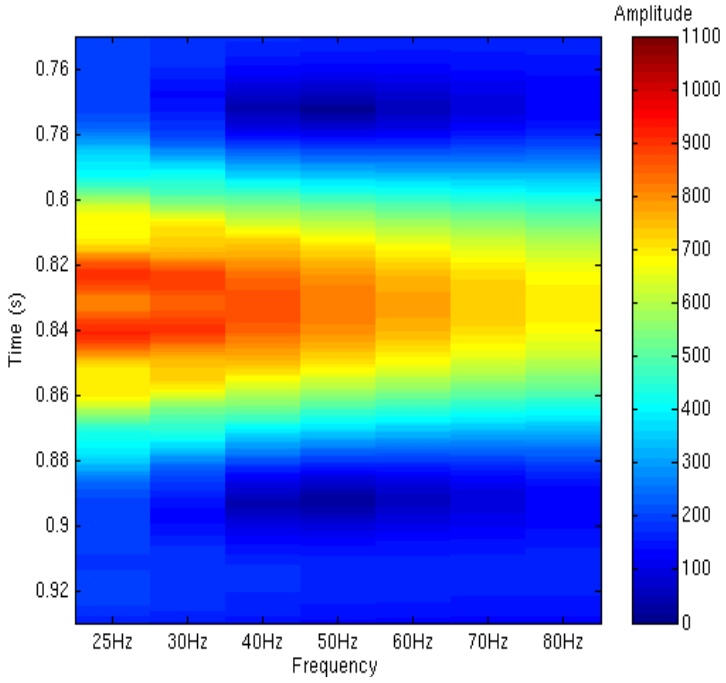

(a) Balanced CWT

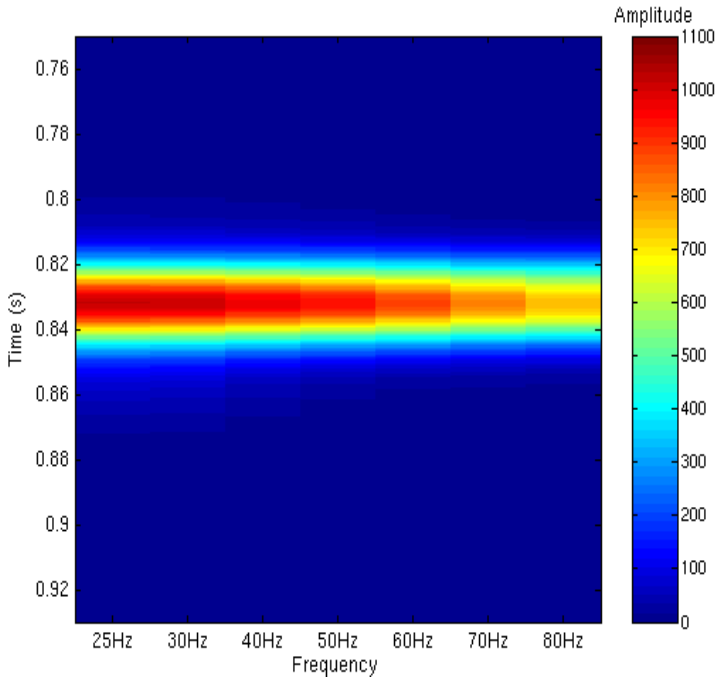

(b) Balanced MPM

Figure 6.12: The balanced decomposed frequency traces (25-80Hz) using the CWT and MPM decompositions for the zero-offset trace from the dispersive, $\tau = 5e^{-3}s$, synthetic.

6.4.5 Elastic inversion

I inverted all four synthetic models for the full bandwidth inversion to obtain the P- and S-wave reflectivities $\left(\frac{\Delta V_P}{V_P} \text{ and } \frac{\Delta V_S}{V_S}\right)$ as well as the frequency-dependent reflectivities $\left(\frac{d}{df}\left(\frac{\Delta V_P}{V_P}\right) \text{ and } \frac{d}{df}\left(\frac{\Delta V_S}{V_S}\right)\right)$ within the frequency range 25-80Hz. Figure 6.14 shows the P- and S-wave reflectivities using the Smith and Gidlow (1987) approximation for the four synthetics. The exact solutions to the numerical model are $\frac{\Delta V_P}{V_P} = -0.065$ and $\frac{\Delta V_S}{V_S} = 0.010$. Whilst I was able to resolve correct signs with the inversion, the S-wave reflectivity was of a similar magnitude to the P-waves. This may be due to having insufficient far offsets to sufficiently approximate the S-wave reflectivity accurately or due to inefficiencies in the algorithm.

The P-wave reflectivities have greatly varying magnitudes. The elastic synthetic has the largest magnitude due to the elastic sandstone having the lowest P-wave velocity of the synthetics. As I introduced larger tau values ($\tau = 5e^{-3}s$, $\tau = 5e^{-2}s$ and $\tau = 100s$) the seismic bandwidth shifted towards the high-frequency limit resulting in the sandstone P-wave velocity increasing. Since the reflection is a Class III, as the velocity increases, the P-wave reflectivity decreases, which is what I observed.

The S-wave reflectivity change was significantly less dramatic due to the much smaller level of shear wave velocity dispersion. As I increased tau from the elastic synthetic the increase in the S-wave sandstone velocity was small. The difference in magnitudes in figure 6.13b across the four synthetics does not follow the theoretical pattern and this is another indication of the difficulty in accurately inverting for S-wave reflectivity.

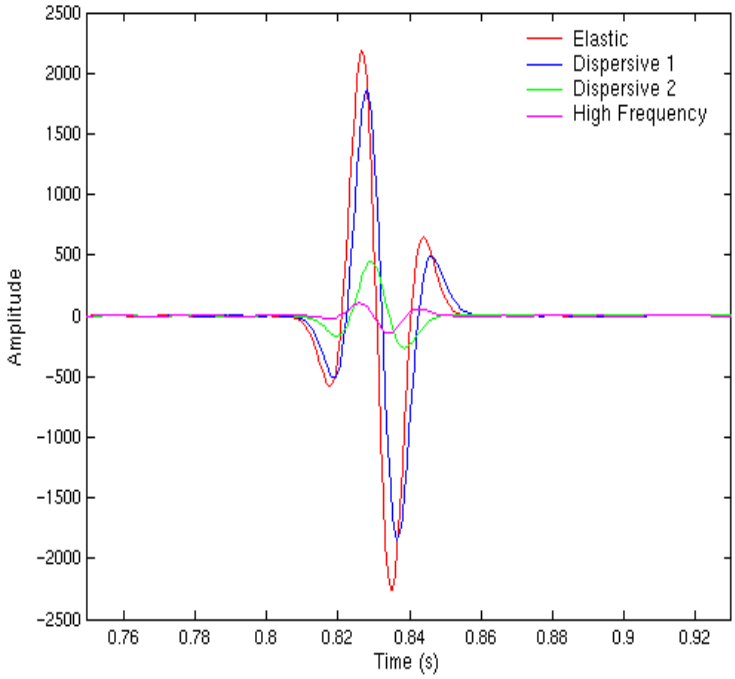

(a) P-wave reflectivity

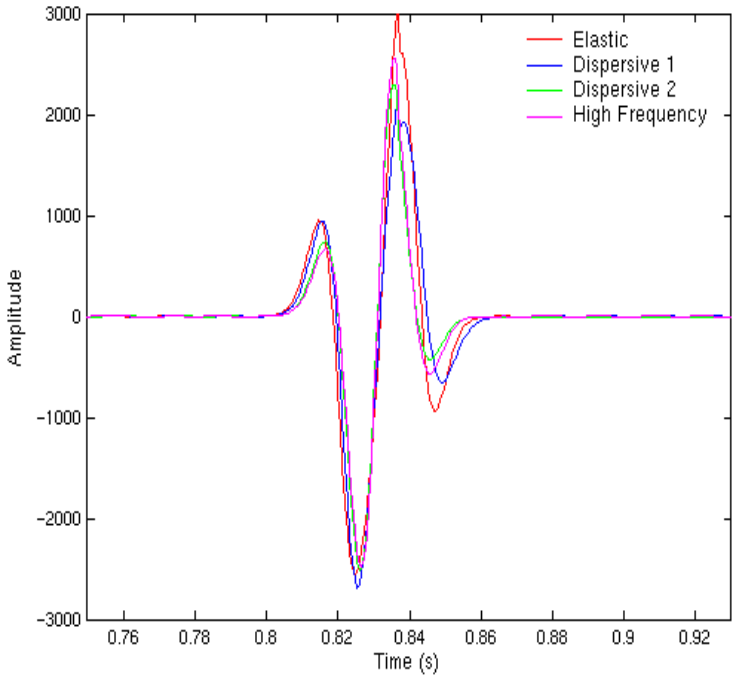

(b) S-wave reflectivity

Figure 6.13: The inverted P- and S-wave reflectivities for the four synthetics (elastic, $\tau = 5e^{-3}s$, $\tau = 5e^{-2}s$ and $\tau = 100s$).

6.4.6 Frequency-dependent reflectivities

I have calculated the frequency-dependent P- and S-wave reflectivities at 25, 30, 40, 50, 60, 70 and 80Hz according to equation 6-32 for all the synthetics following spectral decomposition using both the CWT and MPM. Figures 6.14, 6.15, 6.16 and 6.17 show the P- and S-wave reflectivities for the elastic and $\tau = 5e^{-3}s$ synthetics. Like the CWT decomposed traces in figures 6.10 and 6.12 there remains a slight wavelet shape on the 25 and 30Hz P-wave reflectivities. The P- and S-wave reflectivities resemble the shape of the input spectral amplitudes. Whereas, in the previous section, the full-waveform reflectivities correspond to a wavelet shape, the frequency-dependent reflectivities have bell-shaped curves.

The difference between the elastic and disperse P-wave spectral reflectivities is clear after spectral decomposition with both methods. The P-wave reflectivities in figures 6.14 and 6.15 correspond to the balanced character of the input spectral amplitudes. The elastic reflectivities all have similar magnitude whereas the dispersive reflectivities reduce in magnitude with frequency. The P-wave velocity in the dispersive layer increases with frequency, reducing the reflection coefficient and reflectivity between the two layers, which I am able to accurately invert for using the balanced spectral amplitudes rather than the full waveform.

The S-wave reflectivities show a sharp discontinuity at approximately 0.84s and this is because I used the exact velocities to invert for the reflectivities and should have applied a moving average to reduce the sharp velocity contrast between the two layers. As was the case with the full S-wave reflectivity inversion, I am still measuring large spectral S-wave reflectivities and this is another indication of the difficulty of accurately estimating the S-wave reflectivity.

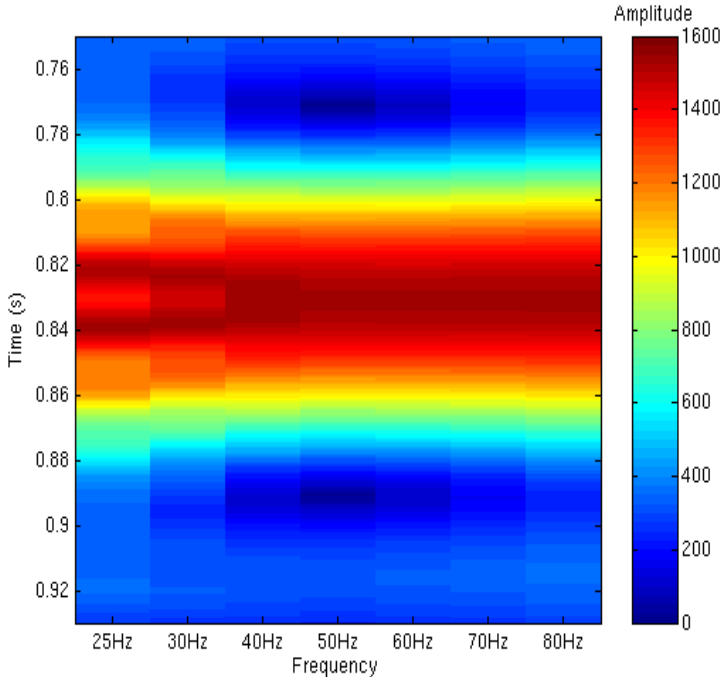

(a) CWT

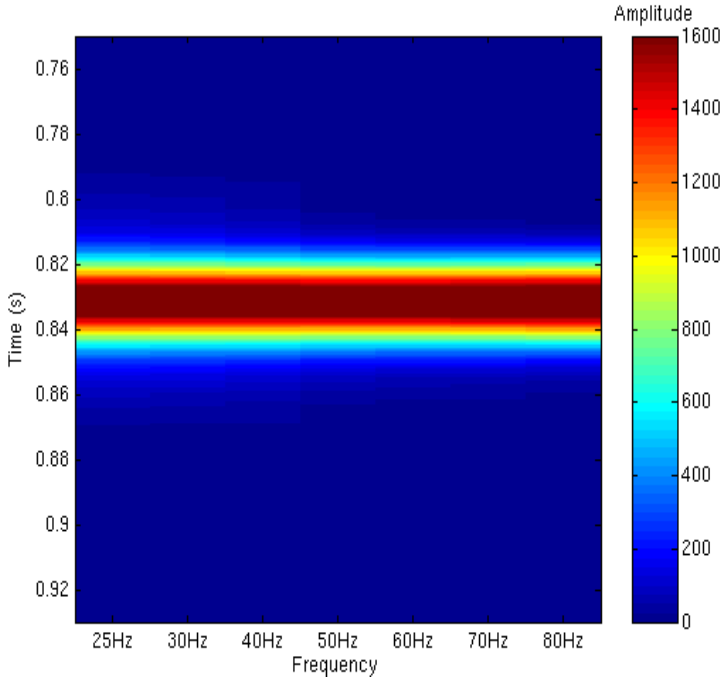

(b) MPM

Figure 6.14: Inverted P-wave reflectivity from the elastic synthetic using the CWT and MPM.

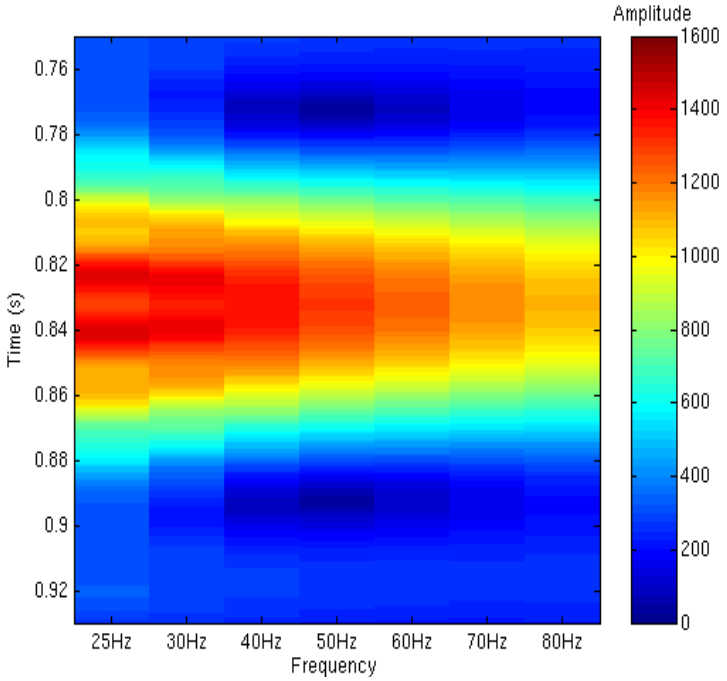

(a) CWT

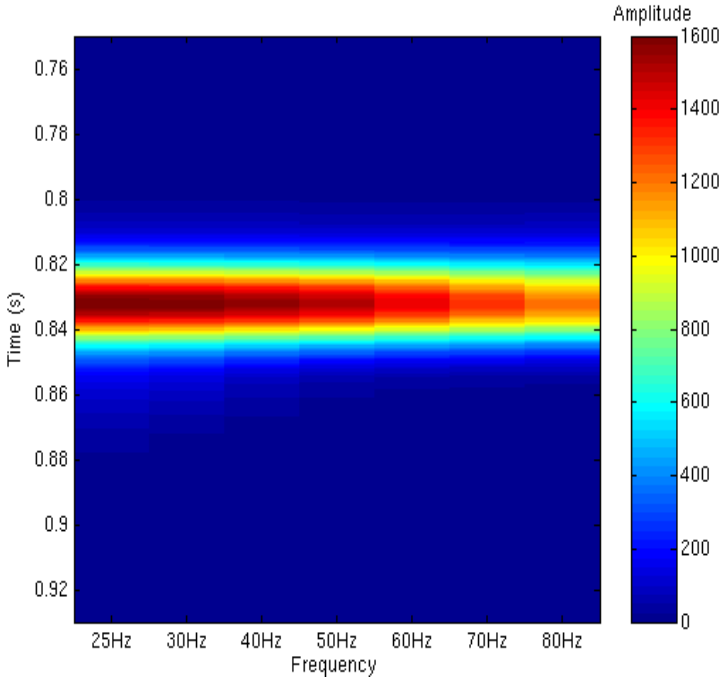

(b) MPM

Figure 6.15: Inverted P-wave reflectivity from the dispersive, $\tau = 5e^{-3}s$, synthetic using the CWT and MPM.

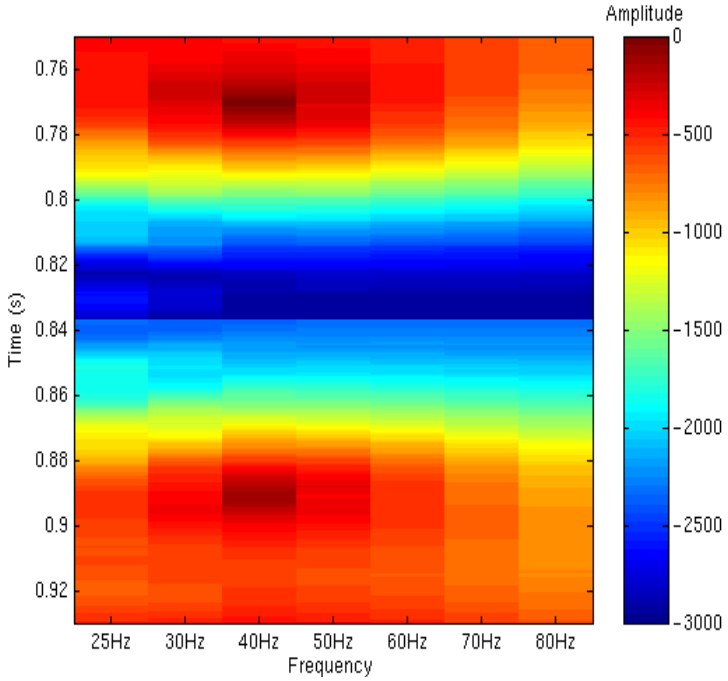

(a) CWT

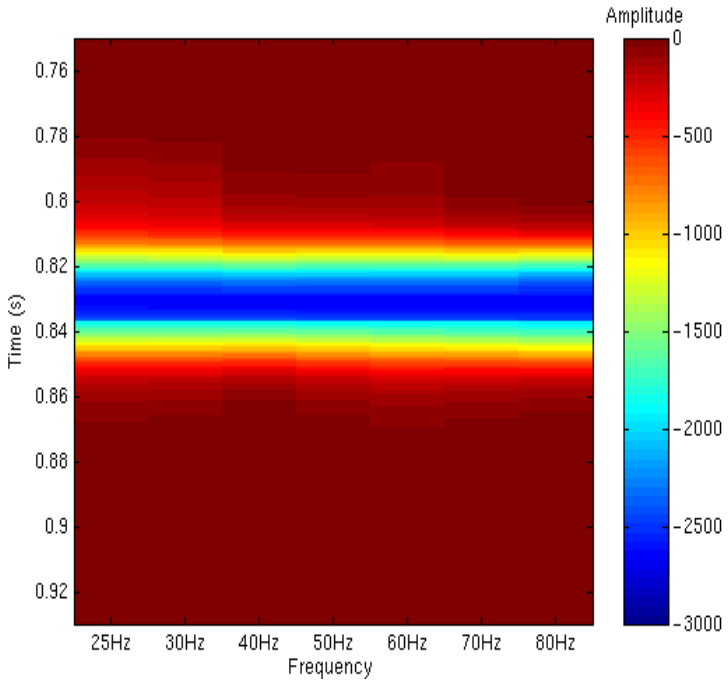

(b) MPM

Figure 6.16: Inverted S-wave reflectivity from the elastic synthetic using the CWT and MPM.

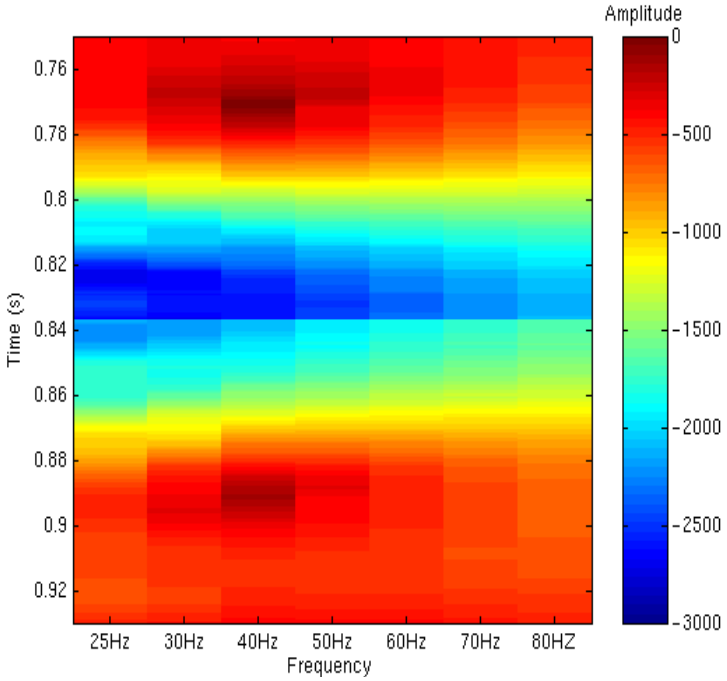

(a) CWT

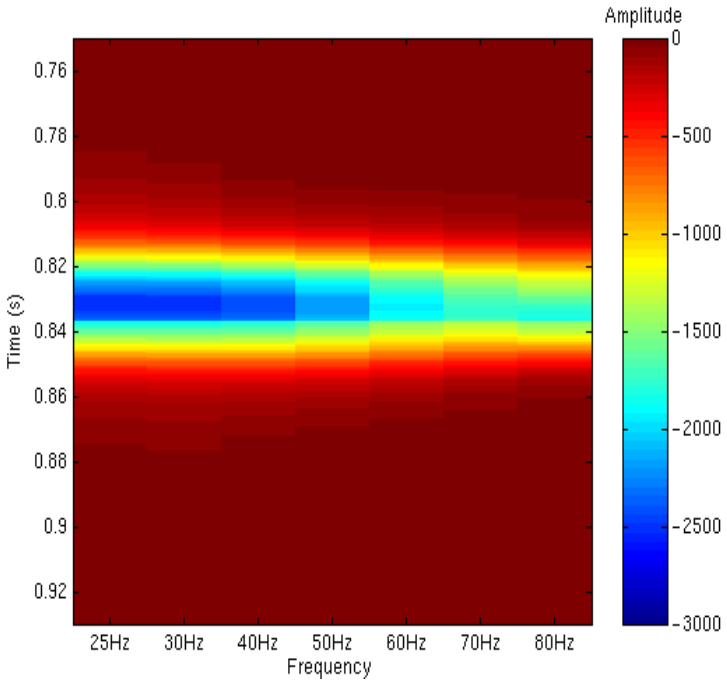

(b) MPM

Figure 6.17: Inverted S-wave reflectivity from the dispersive, $\tau = 5e^{-3}s$, synthetic using the CWT and MPM.

6.4.7 Dispersion results

To test the effect the choice of bandwidth and reference frequency has on the inverted reflectivity dispersion I ran three test cases on the CWT data. I inverted all four synthetics using (i) bandwidth $25-80Hz$ and $f_0 = 25Hz$, (ii) bandwidth $40-80Hz$ and $f_0 = 40Hz$ and (iii) bandwidth $25-80Hz$ and $f_0 = 40Hz$. A big problem with the CWT decomposition and the frequency-dependent reflectivities is the slight wavelet shape on the 25 and 30Hz traces. This is why, when I selected $f_0 = 25Hz$ in the first case, the reflectivity dispersion was overwhelmed by this ringing wavelet shape (figure 6.18). It is also worth noting that the inversion is measuring far larger values of S-wave reflectivity dispersion than theory predicts and this could be the result of inaccurately estimating the S-wave reflectivity. In the second example, I removed the 25 and 30Hz traces from my inversion and considered only $40-80Hz$ and increased the reference frequency to 40Hz. This has almost completely removed the previous noisy signal and I was able to detect dispersion on the side lobes outside of the true signal as ~0.77s and ~0.9s (figure 6.19). The introduction of false artefacts is one of the biggest drawbacks when using the CWT in this scheme. Figure 6.9 showed a snapshot of the side lobes. The MPM did not have any decomposed energy outside of the amplitude envelope of the original seismic wavelets. In my final example I returned to the original bandwidth of $25-80Hz$ but chose $f_0 = 40Hz$. Using these parameters I have minimised both the noisy artefacts from the low-frequency traces seen in the first case as well as the dispersion in the side lobes in the previous example. This has allowed me to pick the largest available bandwidth without introducing unwanted noise whilst quantitatively measuring the reflectivity dispersion. Following on from the parameter testing using the CWT data I repeated the inversion using a bandwidth of $25-80Hz$ and $f_0 = 40Hz$ on the MPM reflectivities (figure 6.21). The MPM decomposed traces, reflectivities and dispersion all benefited from the higher temporal resolution which has minimised the noise issues I encountered using the CWT.

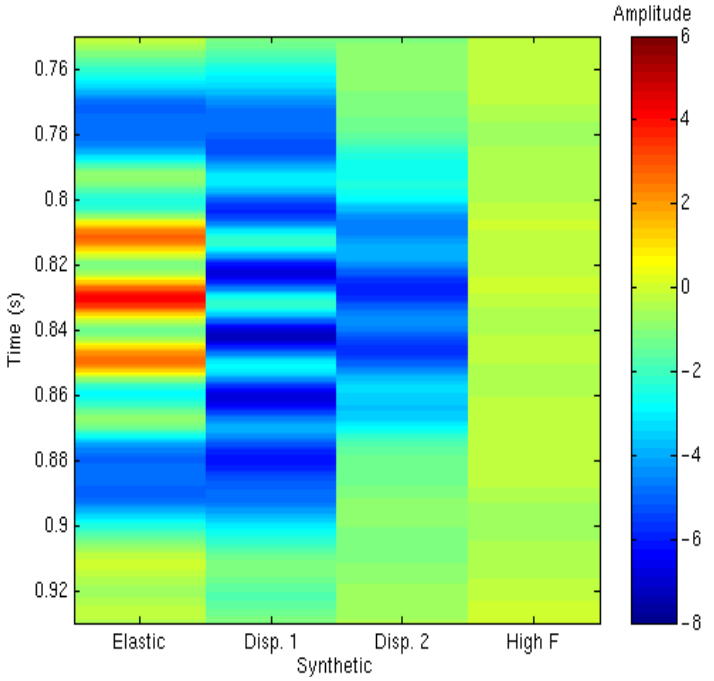

(a) $\frac{d}{df}\left(\left|\frac{\Delta V_P}{V_P}\right|\right)$

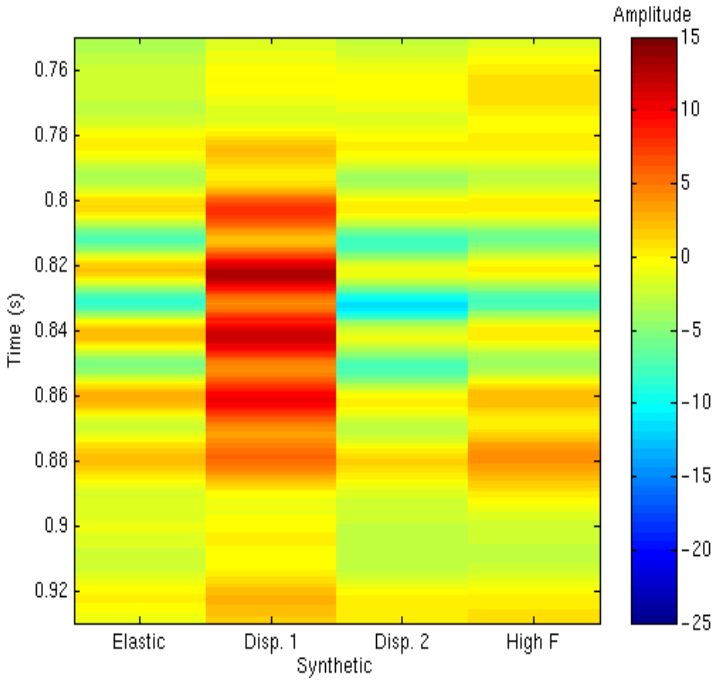

(b) $\frac{d}{df}\left(\frac{\Delta V_S}{V_S}\right)$

Figure 6.18: The inverted P- and S-wave reflectivity dispersion for the four synthetics using the CWT with a frequency range 25-80Hz and $f_0 = 25Hz$.

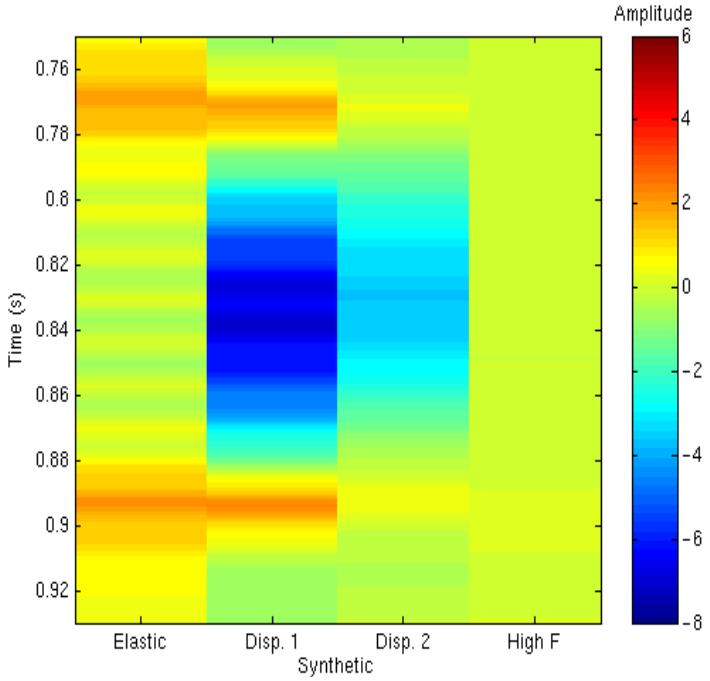

(a) $\frac{d}{df}\left(\left|\frac{\Delta V_P}{V_P}\right|\right)$

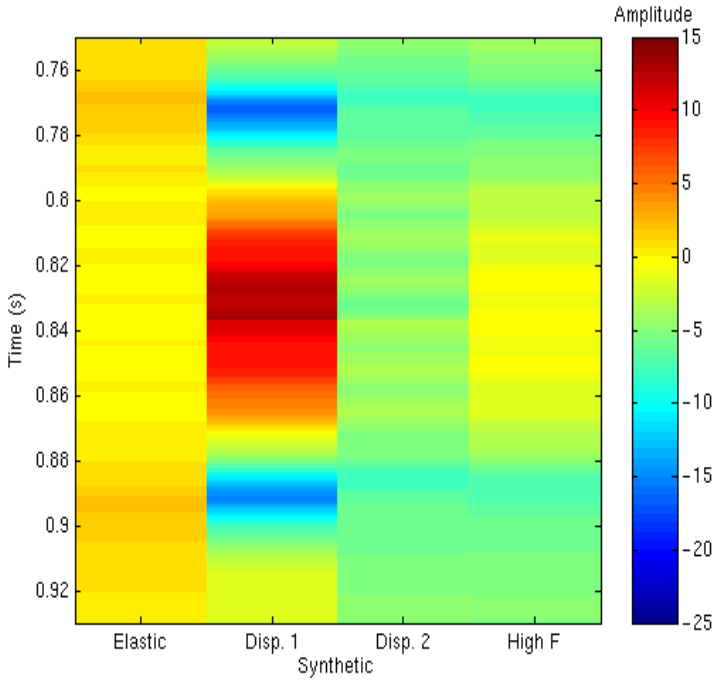

(b) $\frac{d}{df}\left(\frac{\Delta V_S}{V_S}\right)$

Figure 6.19: The inverted P- and S-wave reflectivity dispersion for the four synthetics using the CWT with a frequency range 40-80Hz and $f_0 = 40Hz$.

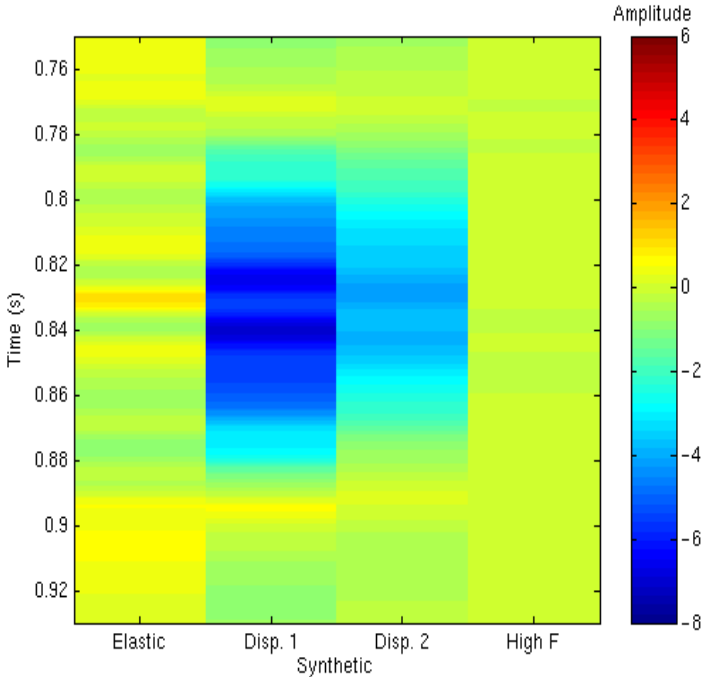

(a) $\frac{d}{df}\left(\left|\frac{\Delta V_P}{V_P}\right|\right)$

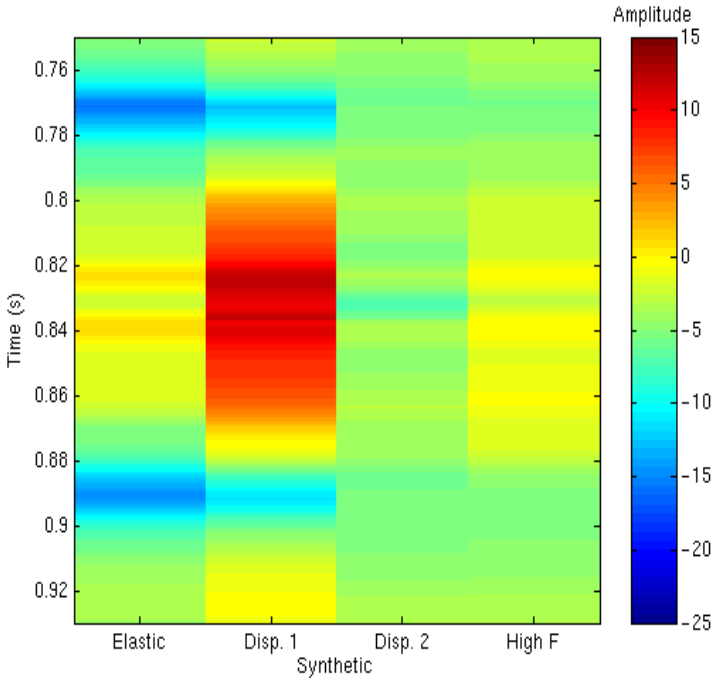

(b) $\frac{d}{df}\left(\frac{\Delta V_S}{V_S}\right)$

Figure 6.20: The inverted P- and S-wave reflectivity dispersion for the four synthetics using the CWT with a frequency range 25-80Hz and $f_0 = 40Hz$.

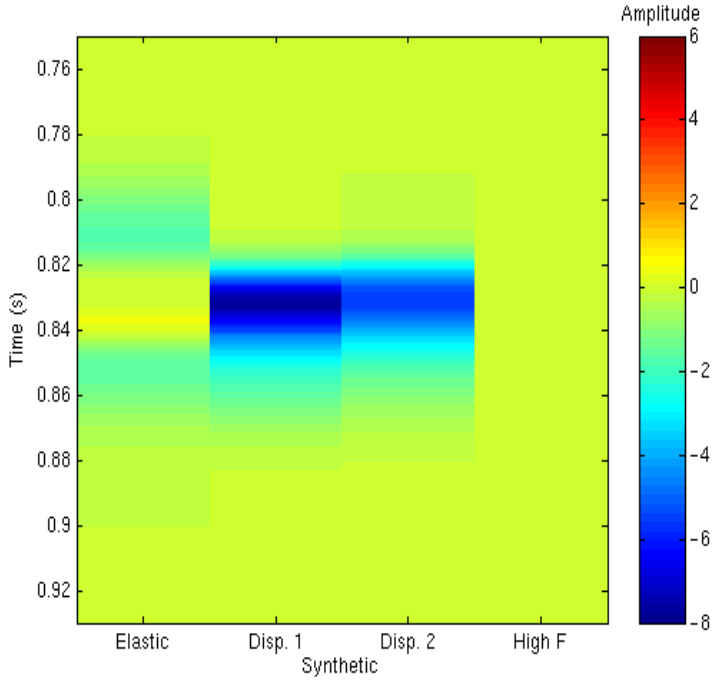

(a) $\frac{d}{df}\left(\left|\frac{\Delta V_P}{V_P}\right|\right)$

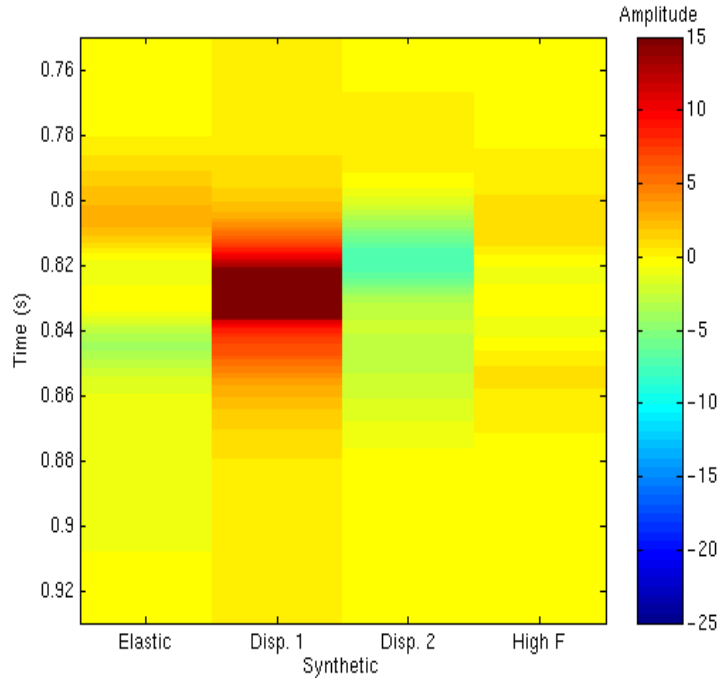

(b) $\frac{d}{df}\left(\frac{\Delta V_S}{V_S}\right)$

Figure 6.21: The inverted P- and S-wave dispersion for the four synthetics using the MPM with a frequency range 25-80Hz and $f_0 = 40Hz$.

The MPM P-wave reflectivity dispersion results in figure 6.21 closely correspond to my earlier theoretical predictions. On the low and high-frequency limit synthetics ($\tau = 1e^{-6}s$ and $\tau = 100s$) I have recorded almost zero dispersion. In the high-frequency case the reflection coefficients are smallest and this has resulted in a cleaner dispersive signal than for the elastic synthetic. On the other two synthetics, the amount of measured dispersion agrees with what I predicted from the exact, frequency-dependent, reflection coefficients in figure 6.4 where it is greater when $\tau = 5e^{-3}s$ than when $\tau = 5e^{-2}s$. Finally, the P-wave dispersive values are both negative as the lower frequencies have larger reflection coefficients and reflectivities as I showed in section 6.2.2. As I have already noted, the S-wave reflectivities and dispersion are far higher than expected as theory predicts that the S-wave velocity is insensitive to the saturating fluid (Chapman *et al*., 2000). This anomalous result could either be due to coupling in the inversion between the P- and S-wave, similar to intercept and gradient crosstalk described by Cambois (2000), or the result of poor S-wave reflectivity estimation.

6.4.8 Approximation accuracy (ii)

I further checked the accuracy of my inversion algorithm by calculating the residual between the input amplitudes and the inverted parameters. I reconstructed the amplitudes at each time sample, *t*, and receiver, *n*, by combining the constants A_1 and A_2, with the full bandwidth reflectivities, $\frac{\Delta V_P}{V_P}$ and $\frac{\Delta V_S}{V_S}$, and the residual is then

$$R(t,n) = D(t,n) - \left[A_1(t,n)\frac{\Delta V_P}{V_P}(t) + A_2(t,n)\frac{\Delta V_S}{V_S}(t)\right]. \qquad (6\text{-}29)$$

I have plotted the residuals from all receivers for the elastic and the $\tau = 5e^{-3}s$ synthetics, figure 6.22. In both, the residuals are small enough for me to conclude that the inversion has provided an accurate result. The residual has maxima of ± 60 on the far offset trace and approximately ± 20 at the other offsets. As the seismic amplitudes are on a scale of $\pm 1200 \leftrightarrow \pm 1800$ the residuals correspond to errors of between $2 - 5\%$.

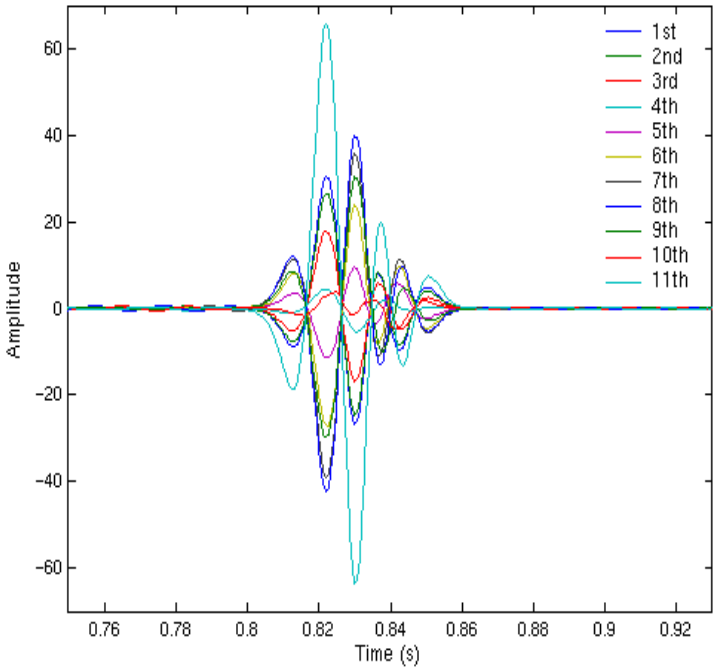

(a) Elastic residual

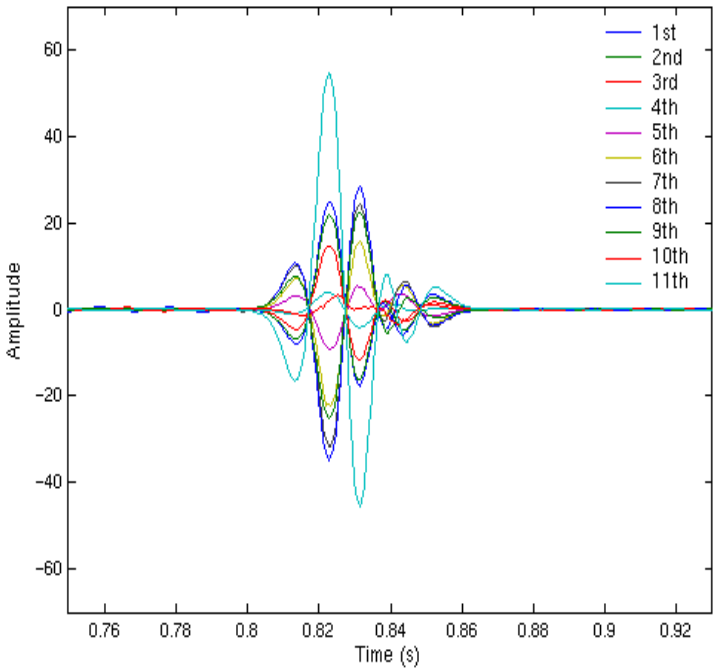

(b) Dispersive residual

Figure 6.22: The residuals, for all receivers, from the elastic and $\tau = 5e^{-3}s$ synthetics.

6.5 Discussion and conclusions

In this Chapter I have developed a new frequency-dependent AVO approximation based on Smith and Gidlow's (1987) two-term expression by including velocity dispersion in the reflectivity estimations. This was an attempt to marry the relatively new technique of spectral decomposition to existing AVO techniques in order to enhance the detection of hydrocarbon saturation. I showed how seismic amplitudes decomposed by either the CWT or MPM algorithms can be balanced by employing a weight function for use in a frequency-dependent inversion methodology. I used the balanced spectral amplitudes from a simple two-layer synthetic to calculate frequency-dependent reflectivities that capture the P-wave velocity dispersion in the lower medium. I converted these reflectivities into a matrix representation to perform a least-squares inversion to quantify the reflectivity dispersion. In my synthetic example I was able to vary the amount of velocity dispersion in the lower medium by using different relaxation times ($\tau = 5e^{-3}s$, $\tau = 5e^{-3}s$, $\tau = 5e^{-2}s$ and $\tau = 100s$) in my numerical modelling. These corresponded to the low-frequency (elastic) limit, two dispersive synthetics and the high-frequency limit. I was able to detect the input velocity dispersion on the frequency-dependent reflectivities and after testing found that a bandwidth of $25 - 80Hz$ and a reference frequency of $40Hz$ gave the best dispersive signature. This parameter selection minimised noise issues I had using the CWT, although the MPM doesn't suffer from these and has far superior temporal resolution. The frequency-dependent AVO inversion was able to detect and quantify varying levels of P-wave velocity dispersion present in four input synthetic datasets. The S-wave reflectivities did propose an anomalous result as they displayed large magnitudes of dispersion when theory predicted the shear wave to be insensitive to fluid saturation. This may be explained though by the inherent difficulty in accurately measuring S-wave reflectivity without far offsets.

Chapter 7: Testing of inversions

7.1 Introduction

Following the successful inversion of a two-layer synthetic described in the previous Chapter, I extended the model to three-layers, including a shallow elastic reflection to simplify the spectral balancing. I prepared the data for inversion by applying a layered medium spherical divergence correction, NMO corrected the gathers, applied a smoothing function to the velocity profiles and performed ray-tracing to accurately measure the angles of incidence. I performed a frequency-dependent AVO inversion to synthetics with an elastic and dispersive bottom reflection and was able to measure the different magnitudes of P-wave reflectivity dispersion. I extended the analysis by using offset-limited gathers to determine that the inverted dispersion magnitude was sensitive to NMO stretch which introduced lower frequencies into the amplitude spectra at far-offsets. I carried on to show that dispersion is controlled by the crack density, all other parameters being equal, by running a further four synthetic gathers through my inversion. I swapped the order of the NMO and spherical divergence correction and, limiting the inversion to only near-offsets, reduced the contamination of the raw spectra from the NMO stretch. I repeated the inversion methodology on a three-layer Class I synthetic to show that the sign of the P-wave reflectivity dispersion depended on the reflection classification and could help with interpretation. Finally, I ran an elastic wedge-type model through my inversion to highlight the dangers of tuning and interpreting dispersive signatures from thin layers and described how the spectral decomposition algorithm could affect any interpretation.

7.2 Class III three-layer synthetic

I have extended the simple two-layer synthetic of the previous Chapter by adding another layer to introduce a purely elastic reflection which I can use to balance the spectral amplitudes. I argued in Chapter 4 how balancing a shallow elastic reflection automatically removed the overprint of the source wavelet from the deeper amplitude spectra. I have arbitrarily created the additional shale layer, described in table 7.1, to create the shale (i) – shale (ii), elastic reflection, which I will use to balance the decomposed spectral amplitudes. I again defined the sandstone layer under water saturation with bulk fluid modulus $2GPa$ and substituted gas with bulk fluid modulus $200MPa$. That reduced the density and the P-wave velocity, defined in the resultant frequency-dependent elastic modulus, altering the reflection from a Class I to a Class III (figure 6.3). The thickness of the two shale layers was 1km and 300m respectively as this was sufficient to separate the two decomposed reflections using both the CWT and MPM.

Material	$\mathbf{V_P}$ **(ms^{-1})**	$\mathbf{V_S}$ **(ms^{-1})**	$\boldsymbol{\rho_W}$ $(\mathbf{g.cm^{-3}})$	$\boldsymbol{\rho_G}$ $(\mathbf{g.cm^{-3}})$	$\boldsymbol{\Phi}$ (%)	$\boldsymbol{\varepsilon}$ **(%)**
Shale (i)	2500	1250	2.02	-	-	-
Shale (ii)	2743	1394	2.06	-	-	-
Sandstone	2835	1472	2.08	2.04	15	5

Table 7.1: Material parameters for the three-layer synthetic model that introduces an additional elastic reflection.

I used the same acquisition parameters as before, eleven receivers (0m – 1000m) at 100m spacing with a 40Hz Ricker wavelet as the source. I created only two synthetic datasets this time with $\tau = 1e^{-6}s$ and $\tau = 5e^{-3}s$. The first simulated the low-frequency, elastic synthetic and the second was the synthetic with the maximum dispersion I measured in the two-layer synthetic described in Chapter 6.

I used a similar processing as I had previously although I now applied a spherical divergence correction for a layered medium (Newman, 1973),

$$D_{X,\theta} = \frac{\left[X^2 + 2X\sum_{i=1}^{n} d_i \tan^3\theta_i\right]^{1/2}}{\tan\theta_1} \qquad (7\text{-}1)$$

where X is the offset and d_i is the layer thickness, followed by an NMO correction to flatten the gathers. The final step was to add the vertical and radial components (z and r) together using Pythagoras theorem to calculate the total amplitude at each receiver

$$Amp_T = \sqrt{Amp_z^2 + Amp_r^2}. \qquad (7\text{-}2)$$

The processed synthetic gathers are shown in figure 7.1. It is difficult to detect any differences between the elastic and dispersive bottom reflections.

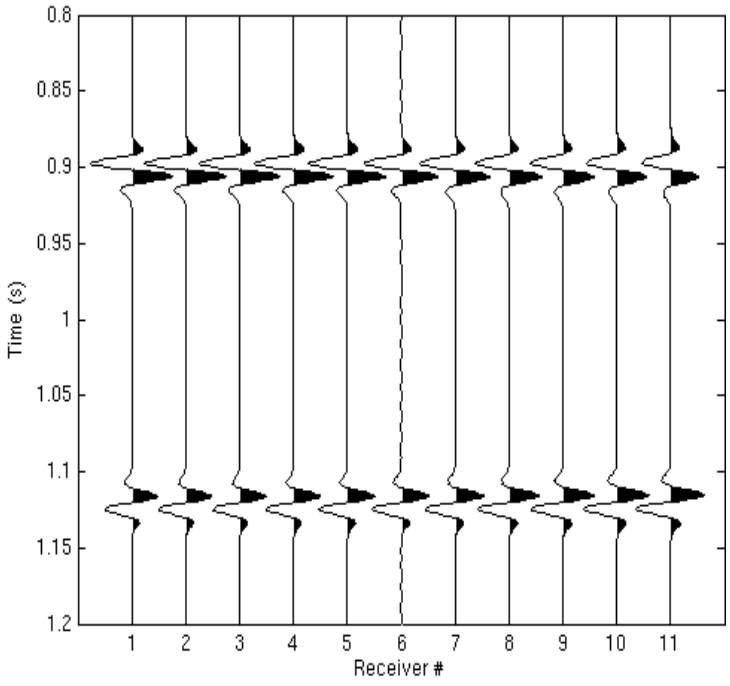

(a) Elastic, $\tau = 1e^{-6}s$

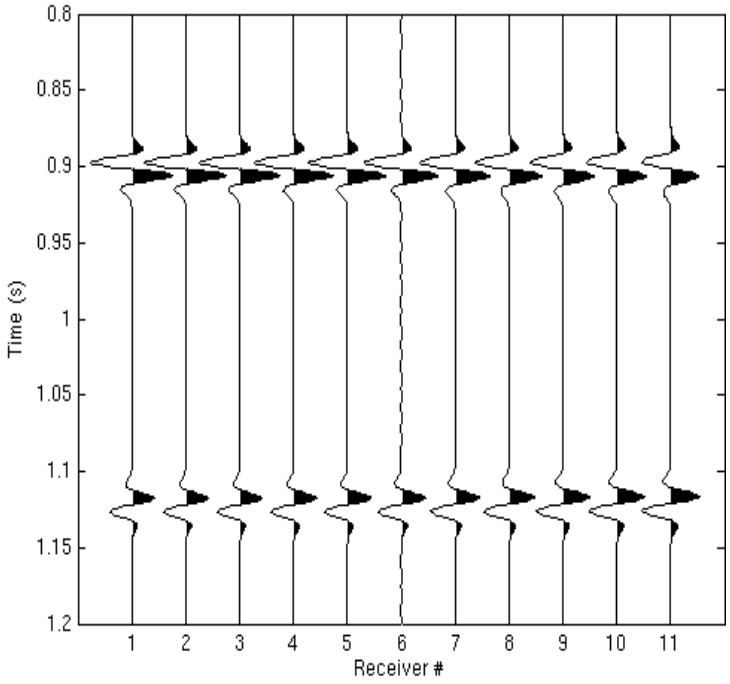

(b) Dispersive, $\tau = 5e^{-3}s$

Figure 7.1: The processed elastic and dispersive three-layer synthetic gathers.

Following my results from the two-layer synthetic I spectrally decomposed both gathers at 25, 30, 40, 50, 60, 70 and 80Hz using the CWT and MPM. Figures 7.2 and 7.3 show the unbalanced spectral traces from the zero-offset trace decomposed with both algorithms from the elastic and dispersive synthetics respectively. As with the two-layer synthetic the central frequencies (40, 50 and 60Hz) have the largest unbalanced amplitudes. Whilst I was able to detect the subtle differences in the amplitudes of the second reflection between the elastic and dispersive synthetic, without removing the bias from the source wavelet, I was limited in my interpretation.

Following the testing of the balancing I performed in the previous Chapter I used an offset-by-offset weight function, with 40Hz as my reference frequency, to balance the spectral amplitudes and remove the effect of the source wavelet. Figures 7.4 and 7.5 show the balanced spectral amplitudes for the zero-offset trace using the CWT and MPM from the elastic and dispersive synthetics respectively. Now that the

effects of the source wavelet have been removed the dispersive nature of the second reflection is much clearer. Where the top reflections are mathematically identical, irrespective of the synthetic, the bottom layer has retained the character of the input data. The weight function has balanced the magnitudes of the bottom reflection on the elastic synthetic whereas, in the dispersive case, the magnitude decreases with increasing frequency. This corresponds to the lower frequencies having larger reflection coefficients than the higher frequencies. The balanced spectral amplitudes highlight how the CWT has incorrectly aligned the second reflection. The central frequencies are all positioned at times slightly less than where the original wavelet was positioned (~1.13s). These frequencies correspond to the largest noisy artefacts and it is interference between the side lobes of the two decomposed wavelets that results in the deeper reflection being incorrectly positioned.

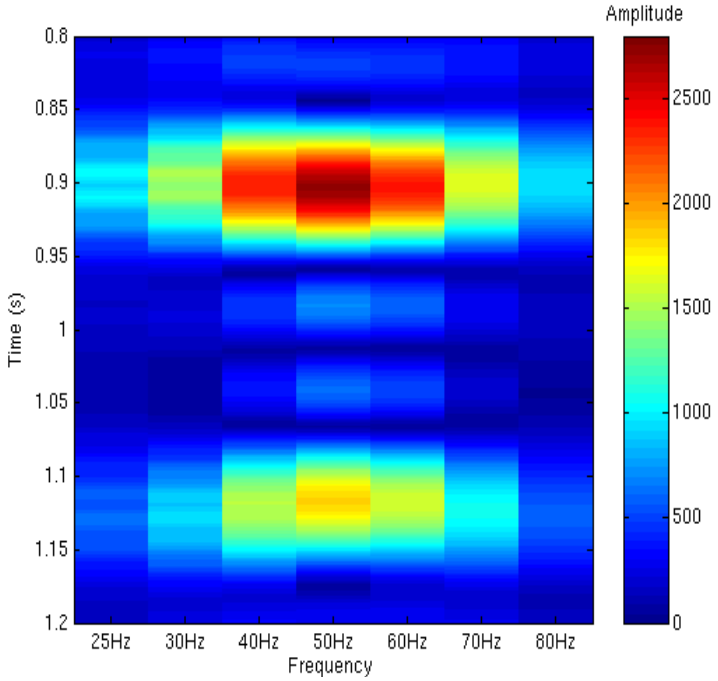

(a) CWT

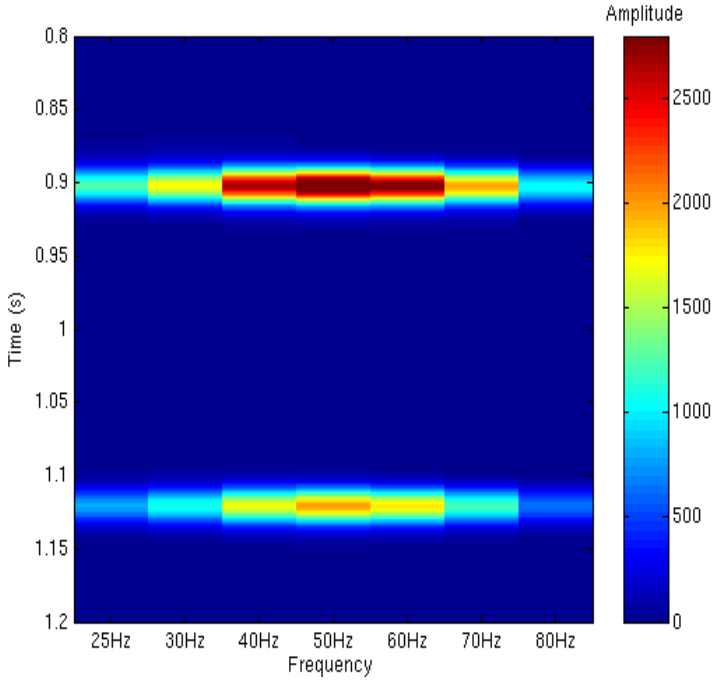

(b) MPM

Figure 7.2: The unbalanced decomposed frequency traces (25-80Hz) using the CWT and MPM decompositions for the zero-offset trace from the elastic synthetic.

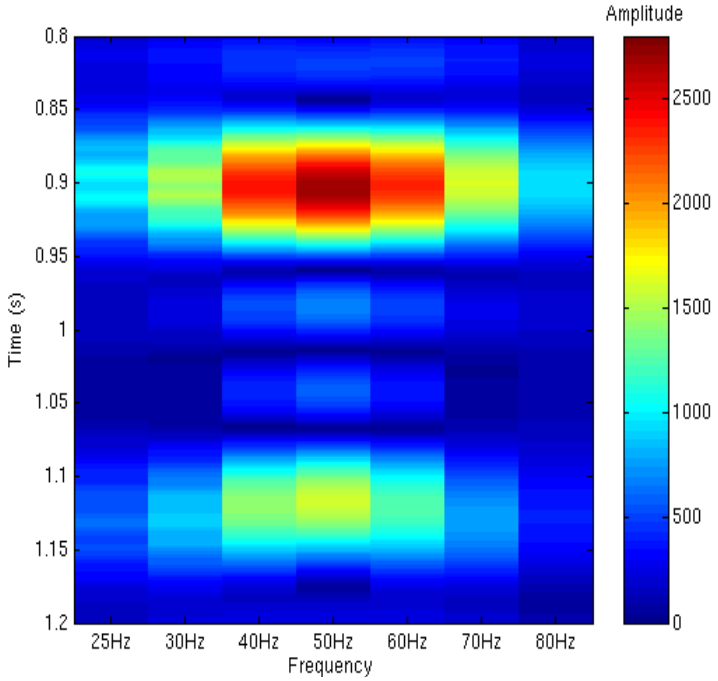

(a) CWT

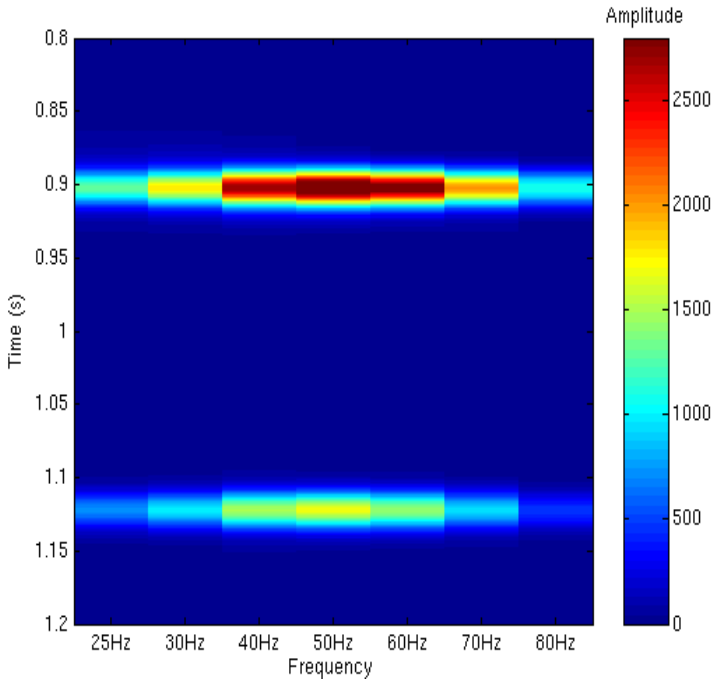

(b) MPM

Figure 7.3: The unbalanced decomposed frequency traces (25-80Hz) using the CWT and MPM decompositions for the zero-offset trace from the dispersive synthetic.

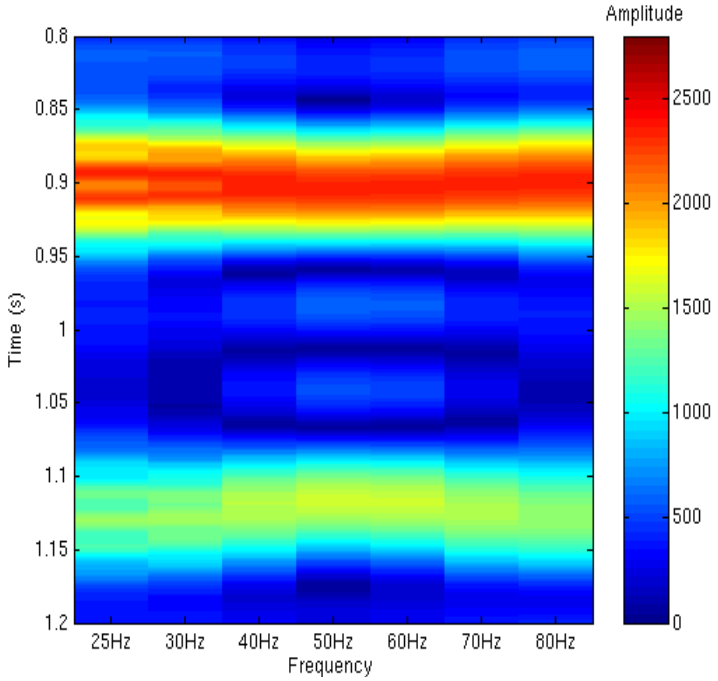

(a) CWT

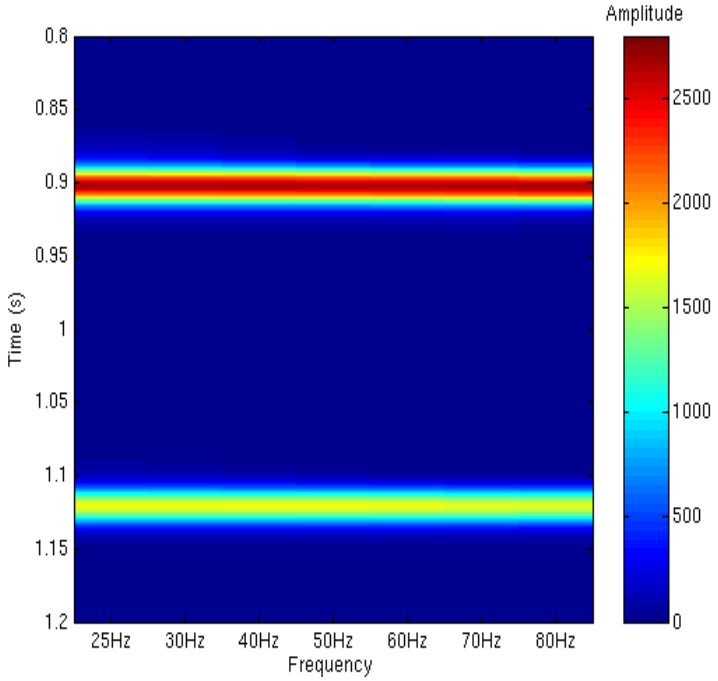

(b) MPM

Figure 7.4: The balanced decomposed frequency traces (25-80Hz) using the CWT and MPM decompositions for the zero-offset trace from the elastic synthetic.

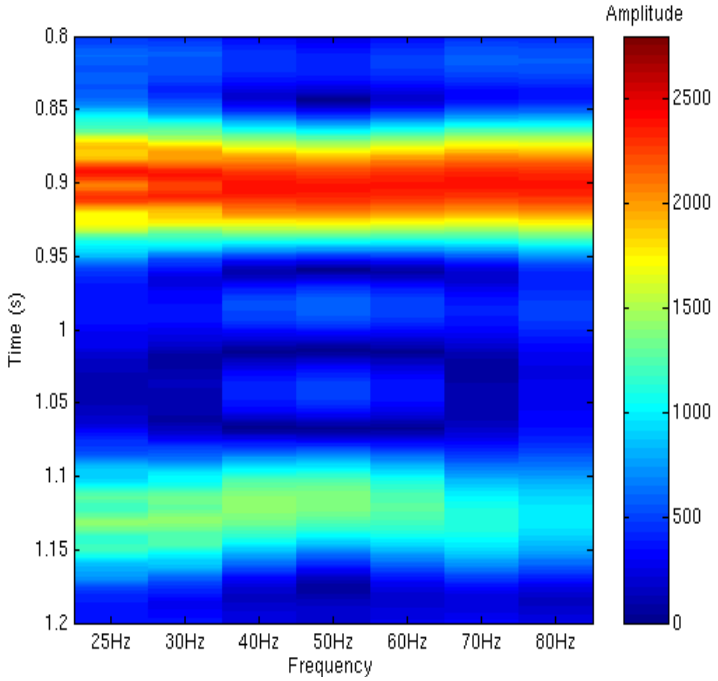

(a) CWT

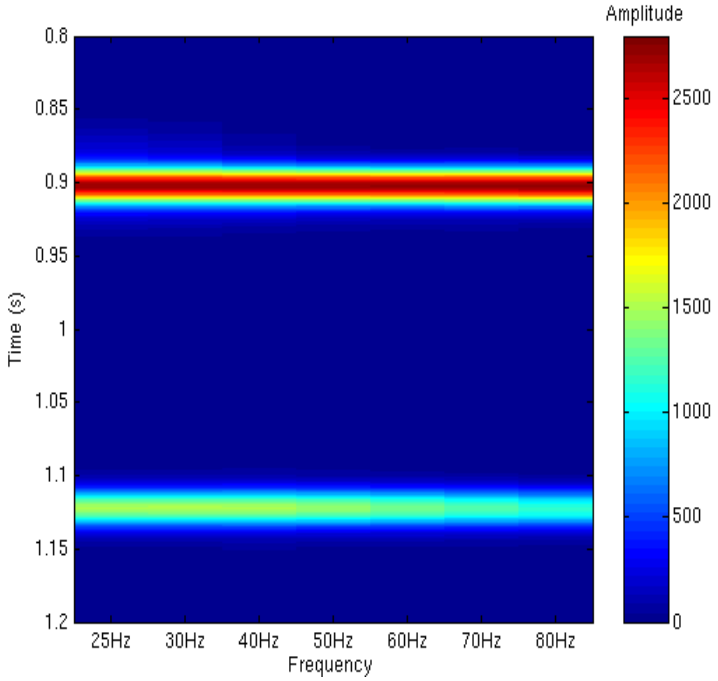

(b) MPM

Figure 7.5: The balanced decomposed frequency traces (25-80Hz) using the CWT and MPM decompositions for the zero-offset trace from the dispersive synthetic.

To prevent the sharp discontinuity on the S-wave reflectivities detected for the two-layer synthetic, I have applied a five point moving average to smooth the velocity profiles. I also needed to use ray tracing to correctly estimate the angles of incidence at the second interface. Whilst a direct ray would only approximate a fractionally smaller angle of incidence than the true ray-traced value, it improved the accuracy of the inverted reflectivities. This was an iterative procedure that searches to calculate the optimum ray parameter, p_i, that minimised the error between the calculated half-offset, y_i, and actual half-offset, $y_d = o/2$ (Dahl and Ursin, 1991), where o is the source-receiver offset. I started with an initial estimate for the slowness, p_0, using the direct ray angle of incidence, θ_0, where

$$\theta_0 = \tan^{-1}\left({}^{y_d}/_{d}\right) \qquad (7\text{-}3)$$

and d is the total depth (1300m). The slowness is then

$$p_0 = \frac{\sin\theta_0}{V_2} \qquad (7\text{-}4)$$

and the initial estimation of the half-offset is

$$y_0 = \sum_{i=1}^{2} \frac{V_i D_i p_0}{\sqrt{1 - V_i^2 p_0^2}} \qquad (7\text{-}5)$$

where V_i and D_i are the layer velocities and thickness respectively. I first calculated the difference in the actual and estimated half-offsets

$$\Delta y = y_d - y_0 \qquad (7\text{-}6)$$

and then calculated the new slowness

$$p_1 = p_0 + \Delta y \frac{\partial p}{\partial y} \qquad (7\text{-}7)$$

where

$$\frac{\partial p}{\partial y} = \left[\sum_{i=1}^{2} \frac{V_i D_i}{\sqrt{1 - V_i^2 p_0^2}^{3/2}} \right]^{-1}. \qquad (7\text{-}8)$$

The procedure was repeated until Δy was less than 1% of the desired offset and I finally estimated the new angle of incidence, θ_i,

$$\theta_i = \sin^{-1}(V_2 p_i). \qquad (7\text{-}9)$$

I inverted the balanced spectral amplitudes (figures 7.4 and 7.5) to estimate the frequency-dependent reflectivities for both synthetics using the smoothed velocity function and ray-traced angles of incidence according to equations 6-33 and 6-35. Figures 7.6 and 7.7 show the P-wave reflectivities for the elastic and dispersive synthetics respectively and the difference between them reflects the nature of the balanced traces. The top and bottom elastic reflectivities are constant across the frequency range. The dispersive synthetic reflectivities decrease in magnitude as the frequency increases, corresponding to the increasing P-wave velocity and reduction in the reflection coefficient. The CWT reflectivities show the time shift I discussed in the previous section at the central frequencies and I expected this misalignment to influence the measured dispersion. The MPM has achieved excellent temporal resolution once again where the width of the decomposed amplitudes and reflectivities closely corresponded to the amplitude envelope of the original seismic wavelets.

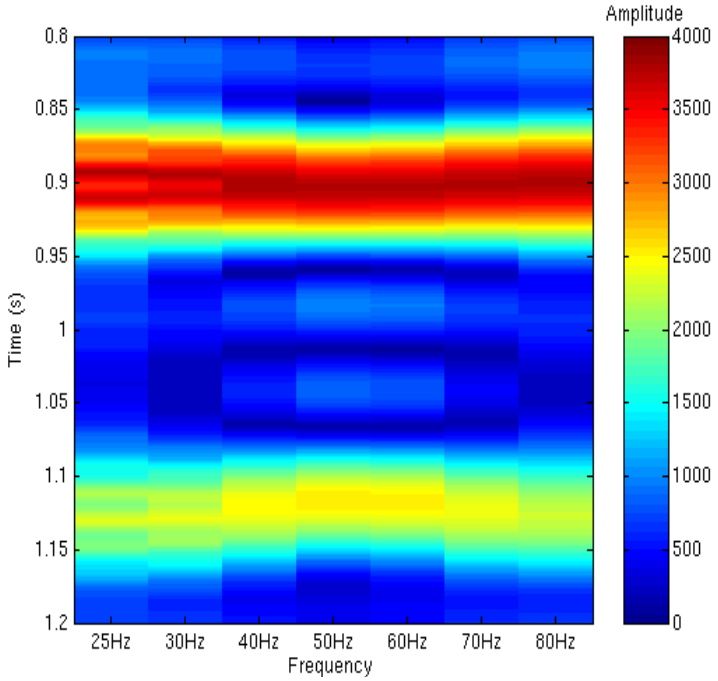

(a) CWT

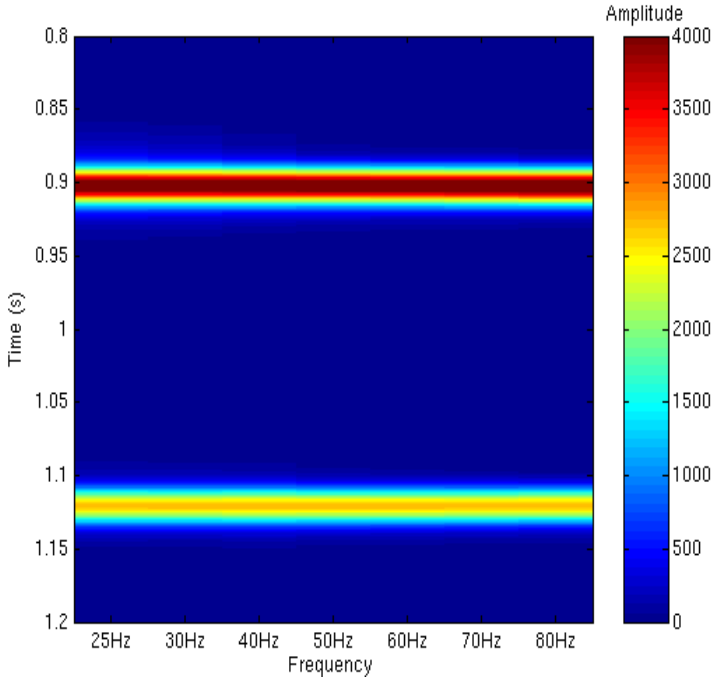

(b) MPM

Figure 7.6: Inverted $|\Delta V_P/V_P|_{f_i}$ from the elastic synthetic using the CWT and MPM.

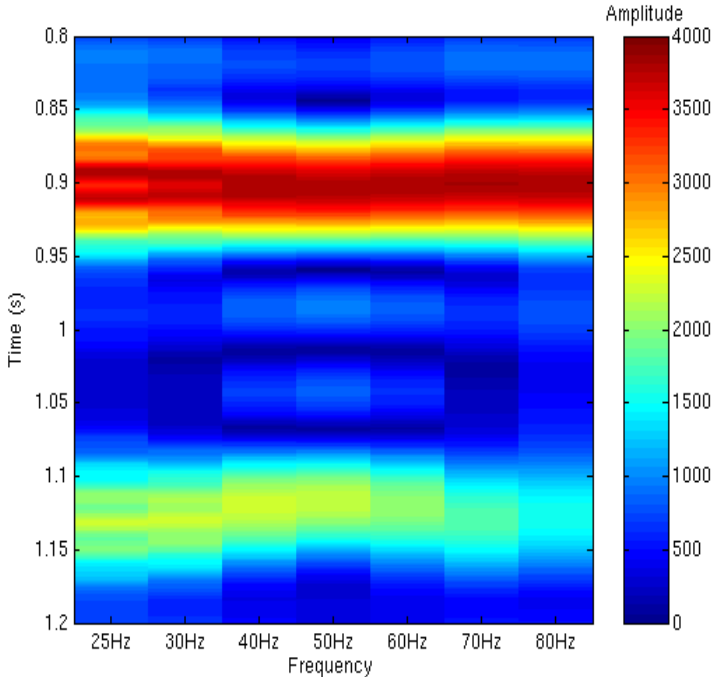

(a) CWT

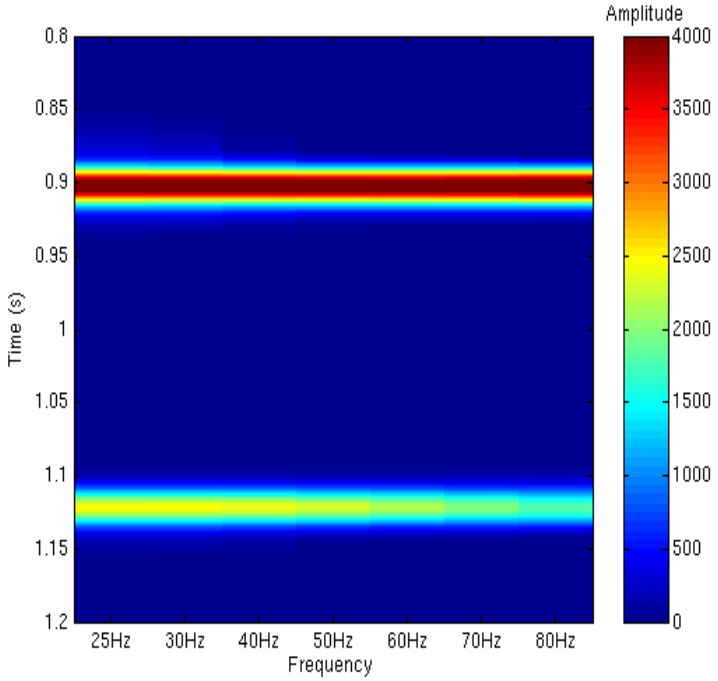

(b) MPM

Figure 7.7: Inverted $|\Delta V_P/V_P|_{f_i}$ from the dispersive synthetic using the CWT and MPM.

7.2.1 Dispersion results

I used the P- and S-wave reflectivities to estimate the reflectivity dispersion following spectral decomposition using both the CWT and the MPM. Figure 7.8 shows the P-wave dispersion for the elastic and dispersive synthetics. In the elastic synthetic, the bottom reflection has measured near zero dispersion as the reflectivities are all of similar magnitude. In the dispersive synthetic, the bottom reflection has been correctly quantified as negative due to the reduction of reflectivity with frequency. The misalignment of the CWT spectral traces and reflectivities has increased the time window over which the dispersion is spread. Both CWT inversions in figure 7.8 have more noise compared with the MPM inversions. The CWT decomposition carries the wide wavelets on the spectral traces and the noisy side-lobes into the final measured dispersion. The MPM has decomposed the seismic traces without introducing any noise and maintained the narrow window of the amplitude envelope of the original seismic traces. The MPM has introduced a wavelet shaped signature where the first, elastic reflection is positioned and this is the result of minor positioning errors on the decomposed traces that are not detectable on figures 7.4 and 7.5. The fact that this has produced a different result on the elastic and dispersive synthetics, where the original reflection is identical on both, shows that a change deeper on the trace has slightly affected either the spectral decomposition or the inversion.

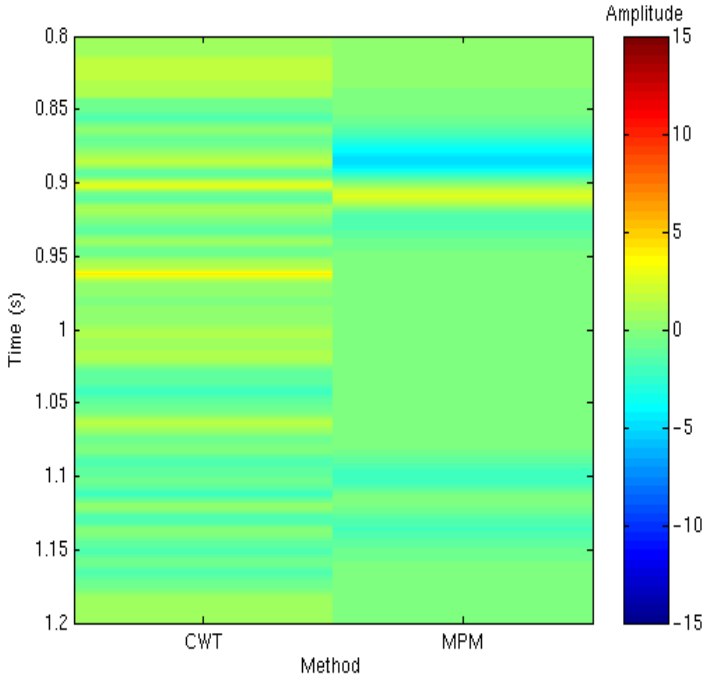

(a) Elastic

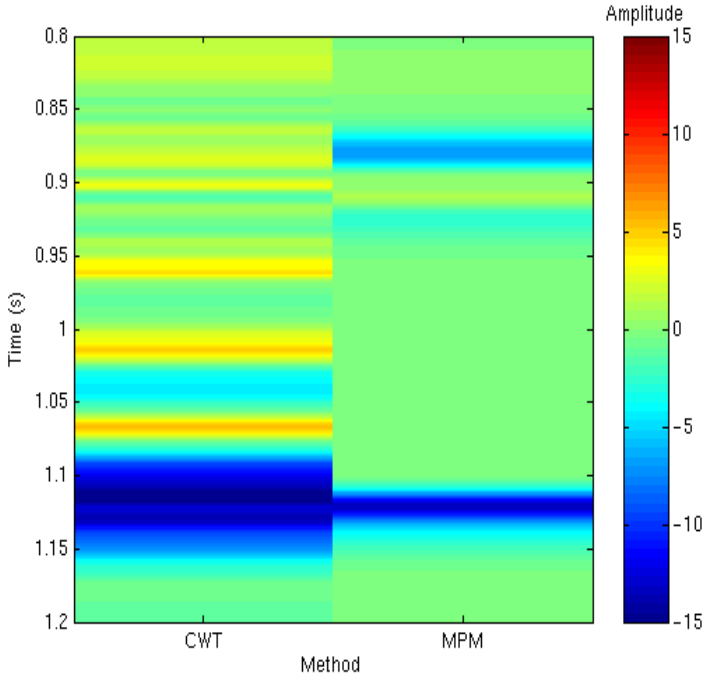

(b) Dispersive

Figure 7.8: The inverted P-wave dispersion for the elastic and dispersive synthetics using both the CWT and MPM with a frequency range 25-80Hz and $f_0 = 40Hz$.

7.3 Offset-dependent inversion

I demonstrated in the previous Chapter the difficulty in accurately determining the S-wave reflectivity without far-offsets. I am interested in the effect the offset range has on the inverted P-wave reflectivity dispersion. I tested the effect that the input offset range has on the P-wave dispersion by separating the elastic and dispersive synthetics into near, mid, and far-offset gathers. Each offset gather had five traces spread over a range of 400m and the angles of incidence at the bottom reflection are summarised in table 7.2.

Stack	Offset Range (m)	Angles of Incidence	Traces
Near	0 – 400	0° - 9.4°	5
Mid	500 – 900	11.7° - 20.5°	5
Far	1000 – 1400	22.6° - 30.6°	5

Table 7.2: Definition of the near, mid and far-offset gathers.

I processed the gathers in the same way as before - spherical divergence correction, NMO correction, addition of the two components and spectrally-decomposed the gathers using the CWT and MPM. I then calculated P- and S-wave frequency-dependent reflectivities at 25, 30, 40, 50, 60, 70 and 80Hz from CWT and MPM balanced spectral amplitudes and performed an offset-dependent inversion for the dispersion. Figure 7.9 shows the P-wave dispersion using a bandwidth of $25 - 80Hz$ with $f_0 = 40Hz$ for the elastic and dispersive offset stacks following spectral decomposition with the CWT and MPM. The near-offset inversions (leftmost traces) are the only ones that produce a result consistent with the theory. The elastic response is near zero whilst the dispersive response is negative and similar to the result I achieved when using the larger offset range, 0 – 1000m. In effect I have split my previous inversion of 0 – 1000m into what I have now classified as the near (0 - 400m) and mid-offsets (500 – 900m) and have combined them to provide the results detailed in figure 7.8.

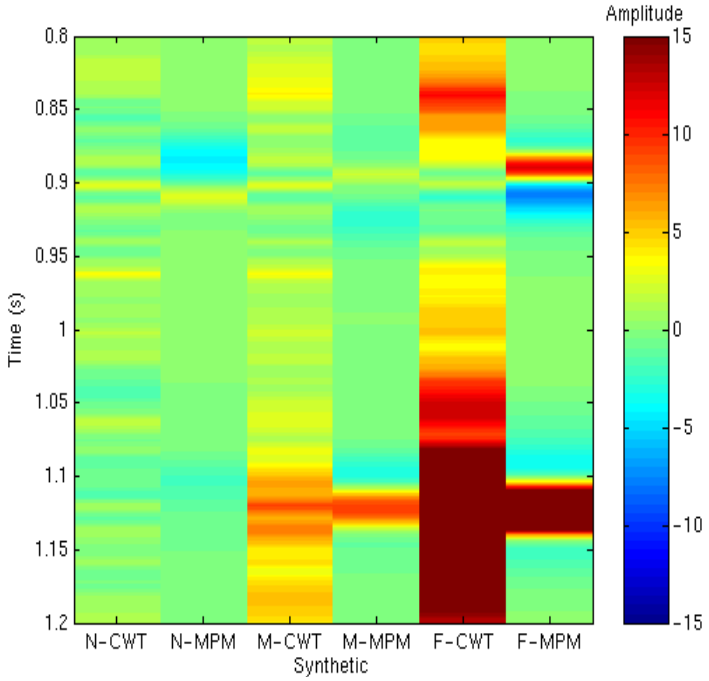

(a) Elastic

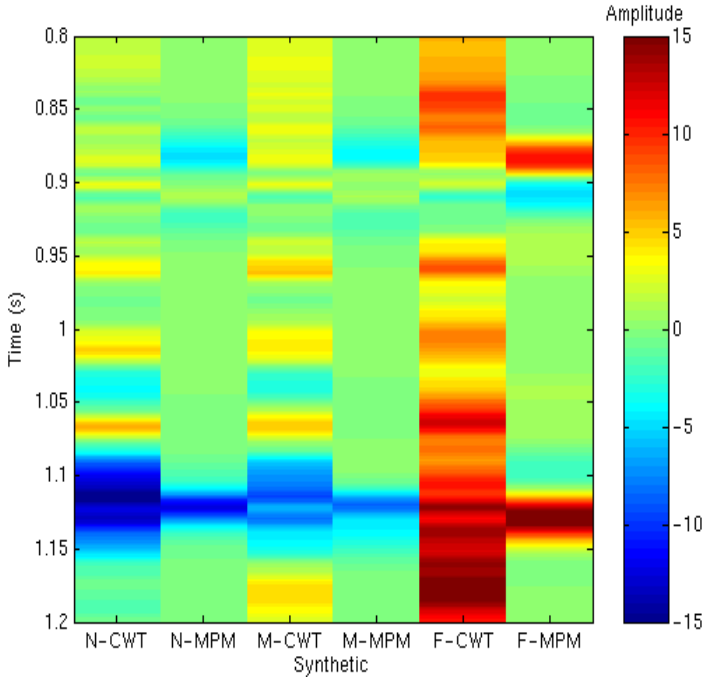

(b) Dispersive

Figure 7.9: The inverted P-wave dispersion for the elastic and dispersive offset limited synthetics using both the CWT and MPM with a frequency range 25-80Hz and $f_0 = 40Hz$.

On both synthetics, as I move to further offsets, the dispersion reduces and shifts towards positive magnitudes and must be a result of the processing I have applied to the synthetic gathers. The plane-layered spherical divergence correction is dependent upon both depth (time) and offset as it replaces the amplitudes lost during the wave propagation but is not known to produce any offset-dependent artefacts. However, the NMO correction is well-known to introduce stretch effects into the amplitude spectra (Dunkin and Levin, 1973 and Barnes 1992) and non-stretch NMO corrections are available (Perroud and Tygel, 2004) to counteract this problem. NMO stretch is due to the top of the wavelet being corrected more than the bottom of the wavelet and increases with the angle of incidence. It is greatest for my far-offset shallow elastic reflections.

To determine the effect that the spherical divergence and NMO stretch has on my amplitude spectra I have calculated spectral ratios (Tonn, 1991) of the top and bottom wavelets at each offset for the elastic synthetic. All spectral ratios have been plotted between ~24 – 88Hz, which covers the bandwidth of my inversion. Figure 7.10 shows the spectral ratio of the raw wavelets, which are flat, prior to either spherical divergence or NMO correction. Figure 7.11 shows the spectral ratio with the NMO correction applied whilst figure 7.12 shows the spectral ratio with both the spherical divergence and NMO correction applied. As the offset increases the gradients of the spectral ratios, which have had corrections applied, gradually become positive and their gradients increase. The difference between figures 7.11 and 7.12 is the absolute magnitude of the spectral ratios that represent the increased amplitude of the wavelets after the spherical divergence correction. It is clear that the offset dependence increase is due to the NMO correction and not the spherical divergence. The NMO stretch is worst for the top reflection which has a range of angles of incidence from 0° - 35°. Dunkin and Levin (1973) and Barnes (1992) derived an expression that can be used to restore an amplitude spectrum to its pre-NMO form. Dasgupta and Clark (1998) used the spectral ratio method to estimate Q from surface seismic reflection data and applied the correction factor to their amplitude spectra and concluded that it was accurate up to 20% stretch. However, no

such expression exists to correct a time-frequency gather. I have relied on the accuracy of the decomposed spectra from both reflections to balance the spectral amplitudes, to remove the overprint of the source spectrum and accurately estimate the P-wave reflectivity dispersion. The NMO stretch affects the top and bottom reflections differently and worsens with increased offset. The CWT and MPM algorithms are not decomposing the true amplitude spectra of the wavelets, but rather the "*nonlinear distortion of the amplitude spectrum*" (Barnes, 1992) after the NMO correction.

To reduce the impact of the NMO stretch on my dispersion inversion I have (i) applied spectral decomposition prior to applying the NMO correction and (ii) reduced the offset range that I invert. By spectrally decomposing the original wavelets, after the spherical divergence correction, I am able to estimate the actual time-frequency response of the seismic. The NMO correction subsequently stretches the decomposed amplitudes when applied. The spectral ratio in figure 7.12 is still essentially flat for the near-offset traces (0 – 400m). By only using the near-offset traces I have reduced the impact of the NMO stretch as the maximum angle of incidence to the top reflection is now only 11.3° rather than 35° at 1400m.

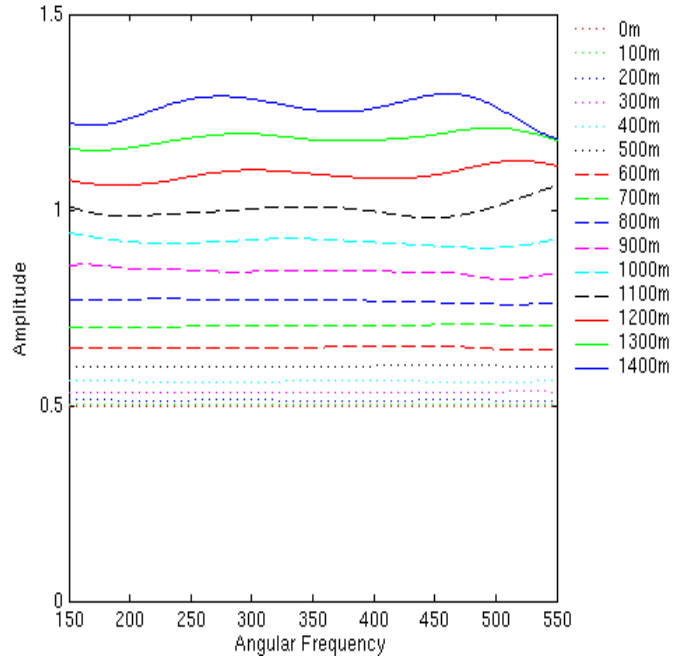

Figure 7.10: Spectral ratio of the elastic synthetic without spherical divergence or NMO correction applied at varying offsets.

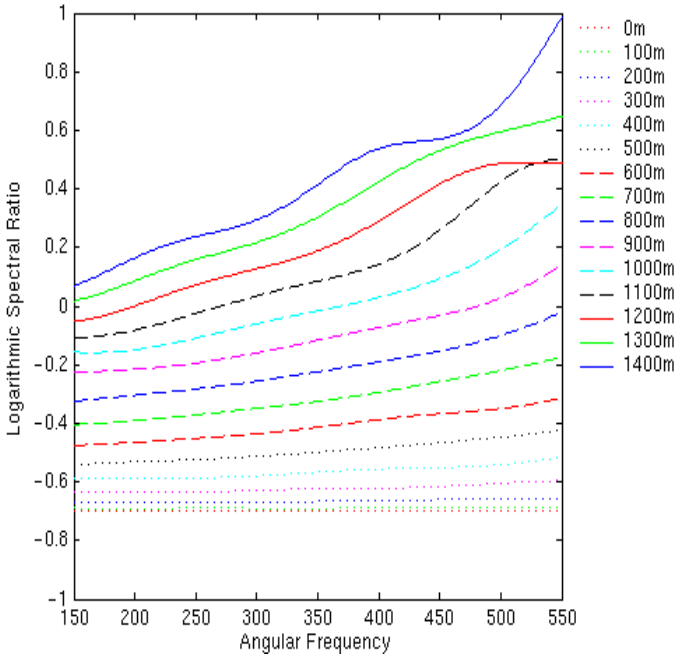

Figure 7.11: Spectral ratio of the elastic synthetic reflections after NMO correction but without the spherical divergence correction at varying offsets.

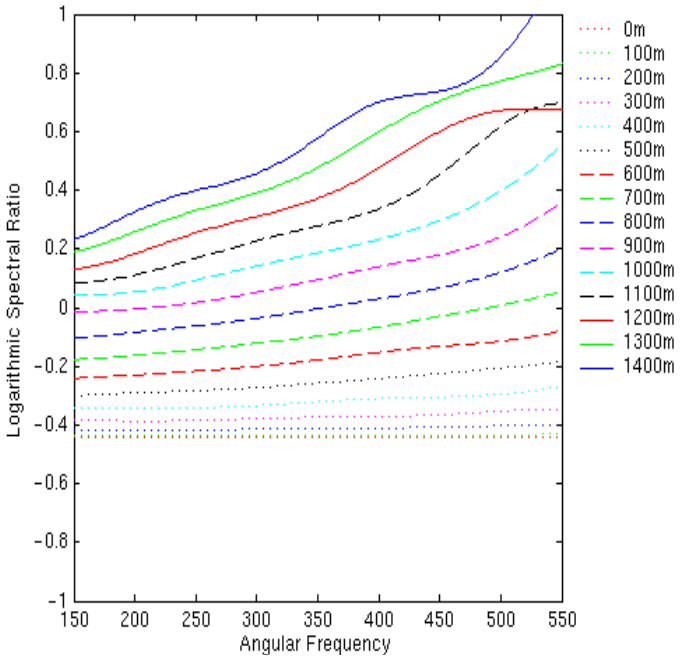

Figure 7.12: Spectral ratio of the elastic synthetic reflections after spherical divergence and NMO correction at varying offsets.

7.4 Fracture sensitivity

It is accepted in frequency-dependent AVO theory that, if all other parameters are equal, the crack density, ε, controls the amount of dispersion whilst the relaxation parameter, τ, controls the frequency range of the dispersion (Chapman *et al.*, 2006). In my previous two synthetic examples I used a constant crack density (5%) and varied the relaxation parameter, τ. I made the claim that I could distinguish between the different magnitudes of dispersion but, in reality, by varying the relaxation time I have been able to sample different parts of the dispersive transition between the low and high-frequency limits, (figure 6.1). In this example I compared the elastic synthetic, with $\varepsilon = 5\%$ in the sandstone half-space, with four synthetics with dispersive sandstone half-space, with $\tau = 5e^{-3}s$ and $\varepsilon = 5\%, 10\%, 15\%$ and 20%. This was a purely theoretical investigation and, mathematically, I increased the dispersion to determine the sensitivity of the frequency-dependent AVO inversion. Figure 7.13 shows the exact reflection coefficients for the shale (ii) – sandstone interface with varying crack density. The changing crack density increases the P-

wave velocity dispersion, which in turn increases the dispersion of the reflection coefficient of the interface.

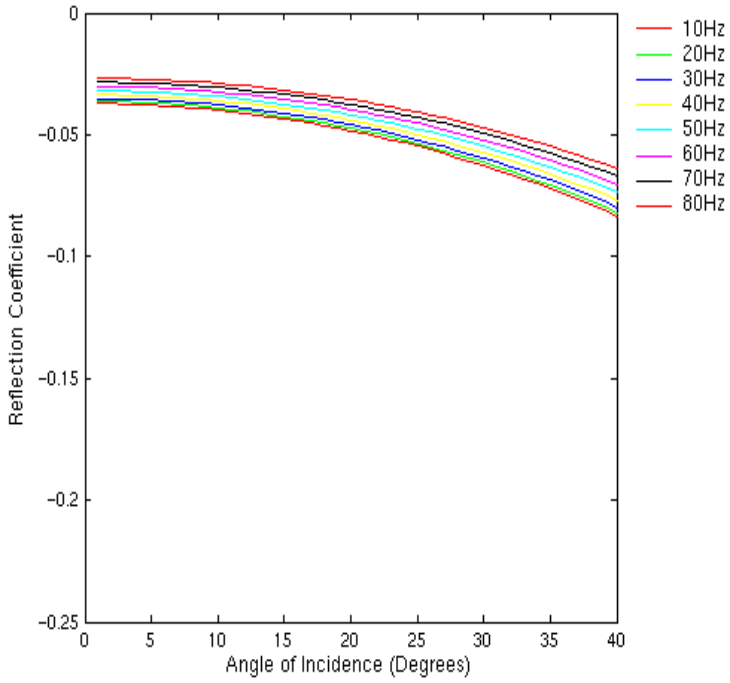

(a) $\varepsilon = 5\%$

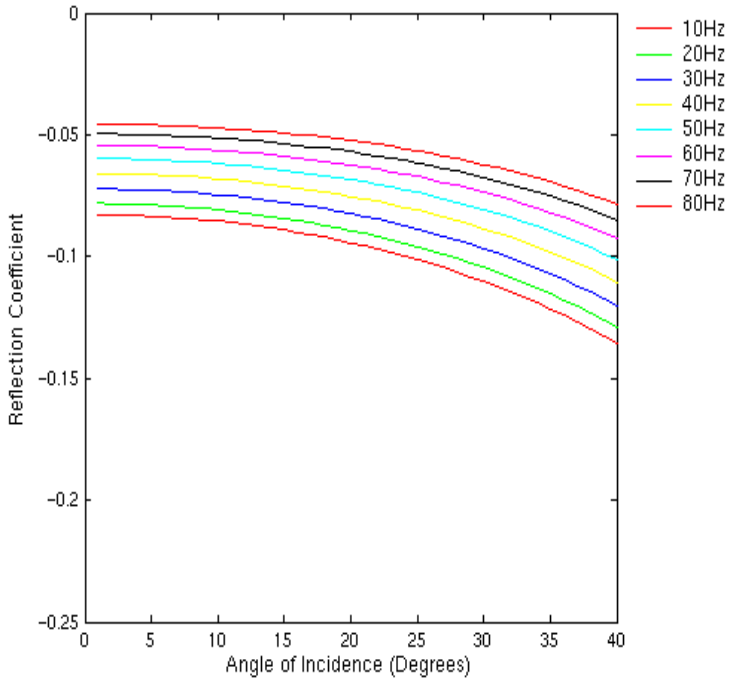

(b) $\varepsilon = 10\%$

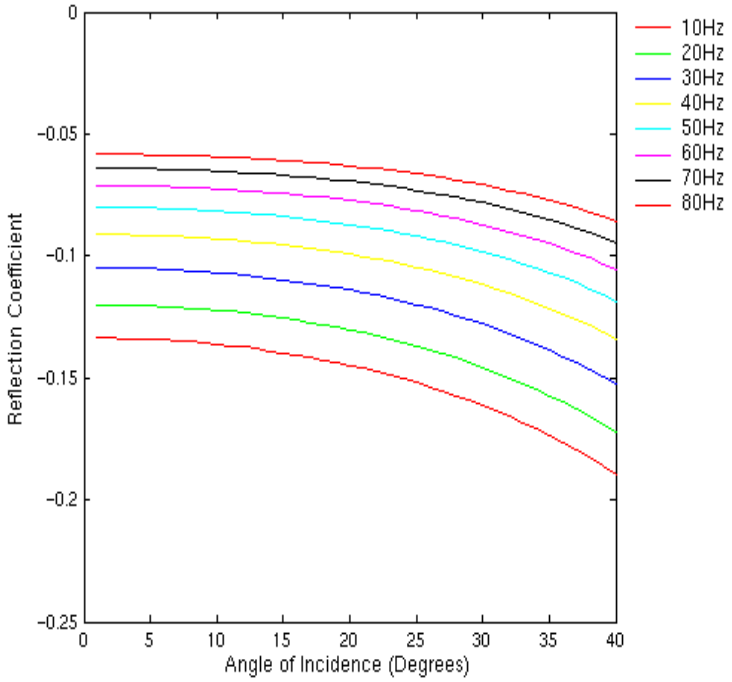

(c) $\varepsilon = 15\%$

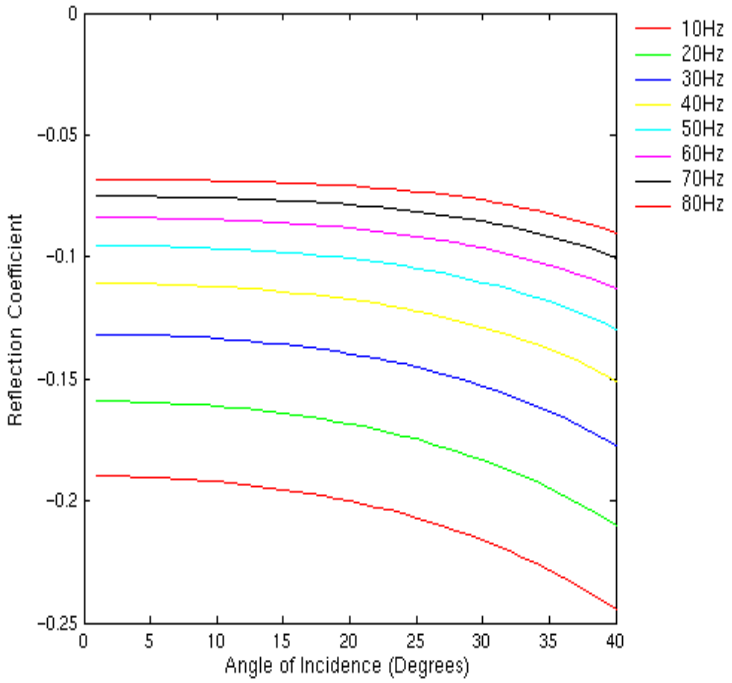

(d) $\varepsilon = 20\%$

Figure 7.13: Exact reflection coefficient curves for the shale (ii) – sandstone interface with varying crack density in the sandstone half-space. The different colours represent the different frequencies. The different frequencies have varying P-wave velocities in the lower layer as indicated in figure 2.1.

7.4.1 Spectral ratio

The increased crack density should be detectable by the change in the spectral ratio of the top and bottom reflected wavelets. Figure 7.14 shows the amplitude spectra of the bottom reflected wavelet from the zero-offset trace for the five synthetics - elastic 5%; dispersive 5%; dispersive 10%; dispersive 15% and dispersive 20%. When I moved from the elastic 5% to the dispersive 5% spectra I saw a decrease in amplitude as the P-wave velocity has increased reducing the reflection coefficient. As the crack density increases in the dispersive synthetics, the P-wave velocity in the sandstone half-space decreases resulting in larger amplitude spectra and reflection coefficients (figure 7.13).

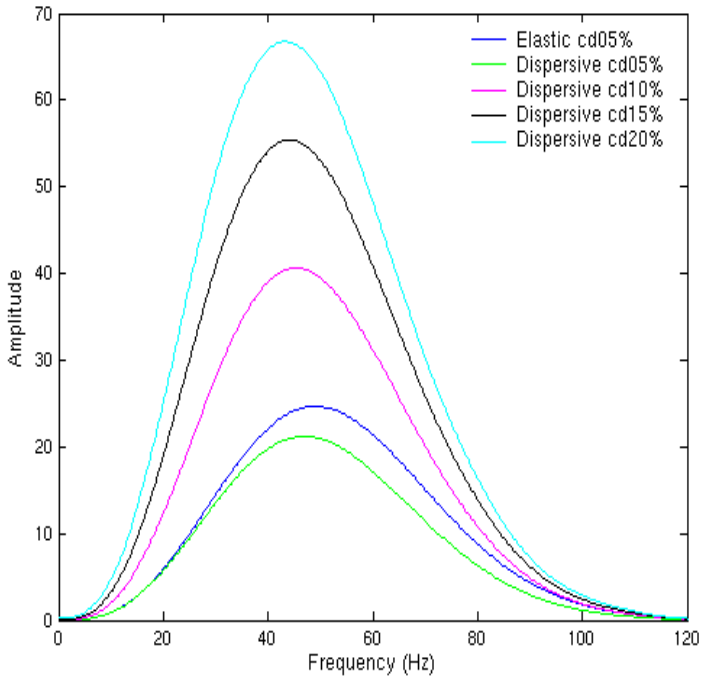

Figure 7.14: Amplitude spectra of the bottom reflection from the zero-offset trace for the five synthetics.

I have calculated the spectral ratio between ~24 – 88Hz as before on the zero-offset trace since no NMO correction is applied (figure 7.15). I have generated a linear best fit to the data within the angular frequency range $150 - 550Hz$, which incorporates my inversion bandwidth of $25 - 80Hz$. I have then estimated the apparent Q of the shale (ii) material using the relationship

$$Q = 2\pi/\left(1 - e^{4\pi p/\Delta t}\right) \qquad (7\text{-}10)$$

from Dasgupta and Clark (1998) where Δt is the time between the two reflections and p is the gradient. For the elastic synthetic the spectral ratio is flat and the apparent Q is infinite. When I substituted the dispersive layer with varying crack density then the apparent Q ranges from 122 to 52. Table 7.3 summarises the results. Classically this result would be interpreted as anelastic attenuation as the wave propagates through the shale (ii) layer; however, this layer is elastic and consistent across the synthetics. The only varying factor is the crack density in the sandstone half-space. The change in apparent Q is the result of the instantaneous reflection at the boundary of the dispersive half-space and is not due to wave propagation through an attenuating medium.

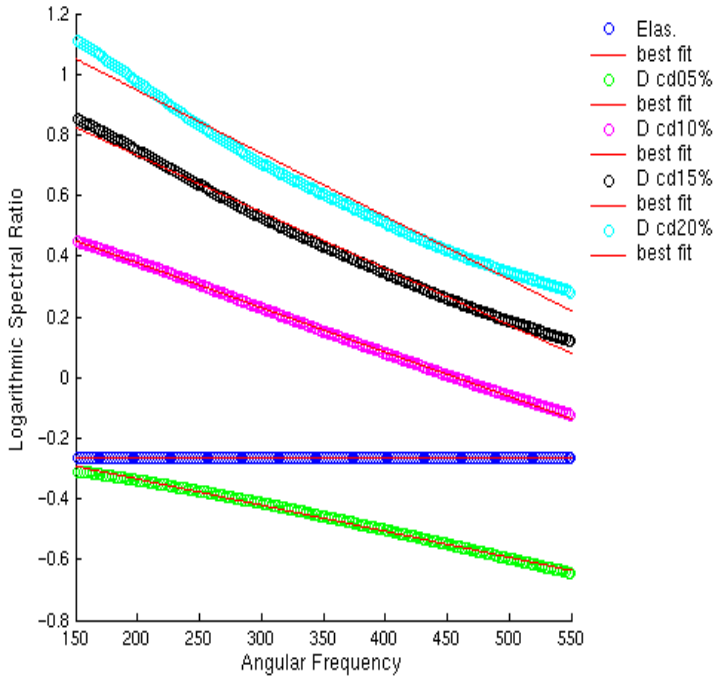

Figure 7.15: Spectral ratio for the zero-offset trace for the elastic and dispersive synthetics with a linear best fit.

Synthetic	Gradient	Apparent *Q*
Elastic	0	∞
Dispersive 5%	-0.0009	125
Dispersive 10%	-0.0015	76
Dispersive 15%	-0.0019	61
Dispersive 20%	-0.0021	55

Table 7.3: The spectral ratio method results for apparent *Q* from lines of best fit in figure 7.15.

7.4.2 Approximation accuracy

As in the previous Chapter, I have tested the accuracy of my frequency-dependent approximation for the varying crack densities. I have calculated the reflection coefficient for a selection of frequencies (10, 20, 30, 40, 50, 60, 70 and 80Hz) and for a range of angles of incidence (0°, 5°, 10°, 15°, 20°, 25°, 30°, 35° and 40°) using equation 6-32. I have calculated the frequency-dependent approximate values using the extracted P- and S-wave velocities from the relevant frequency-dependent elastic moduli. I have plotted these for the four dispersive synthetics in figure 7.16 along with the exact frequency-dependent reflection coefficients previously shown in figure 7.13. Once again my frequency-dependent AVO approximation is over-estimating the magnitude of the dispersion and this over-prediction is actually less as the actual dispersion increases. The approximation is relatively good at predicting the exact frequency-dependent reflection coefficient except for the 20% crack density reflection. This is an extreme case and it highlights the inability of the approximation to accurately model the reflection coefficients at large levels of dispersion.

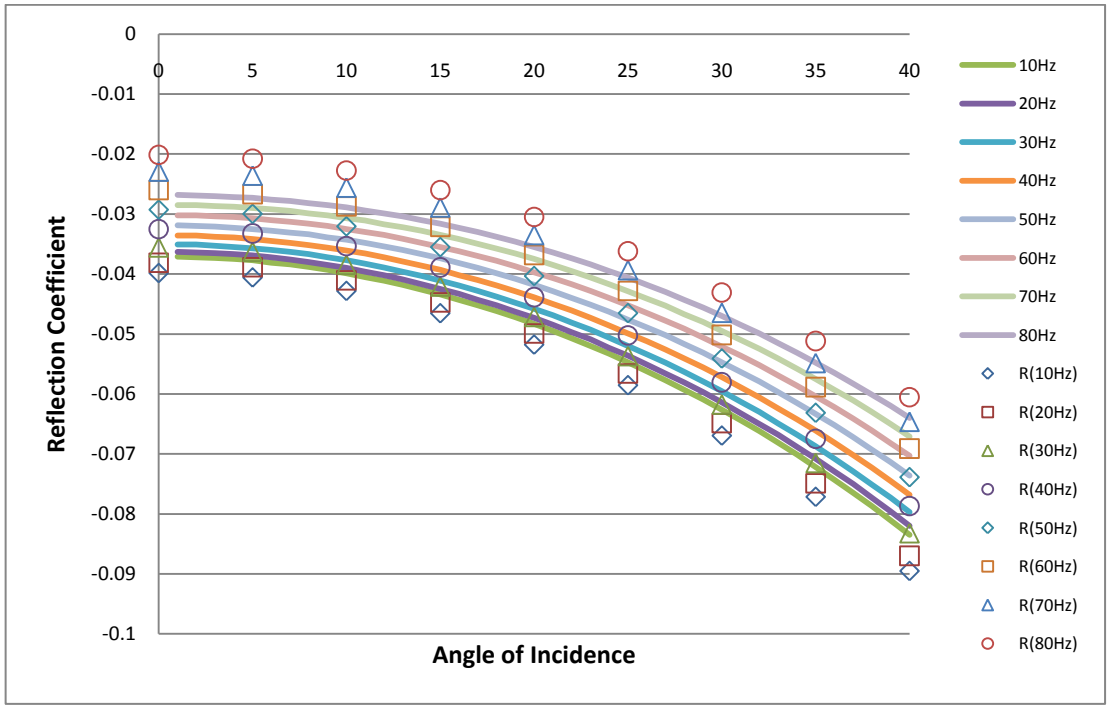

(a) $\varepsilon = 5\%$

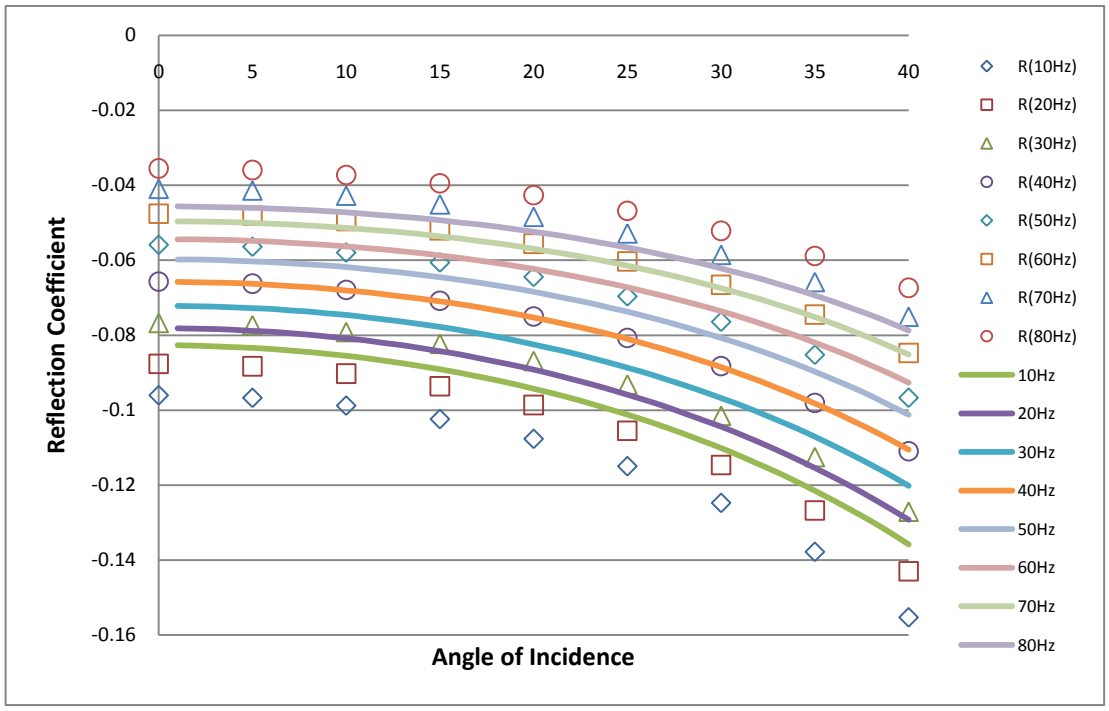

(b) $\varepsilon = 10\%$

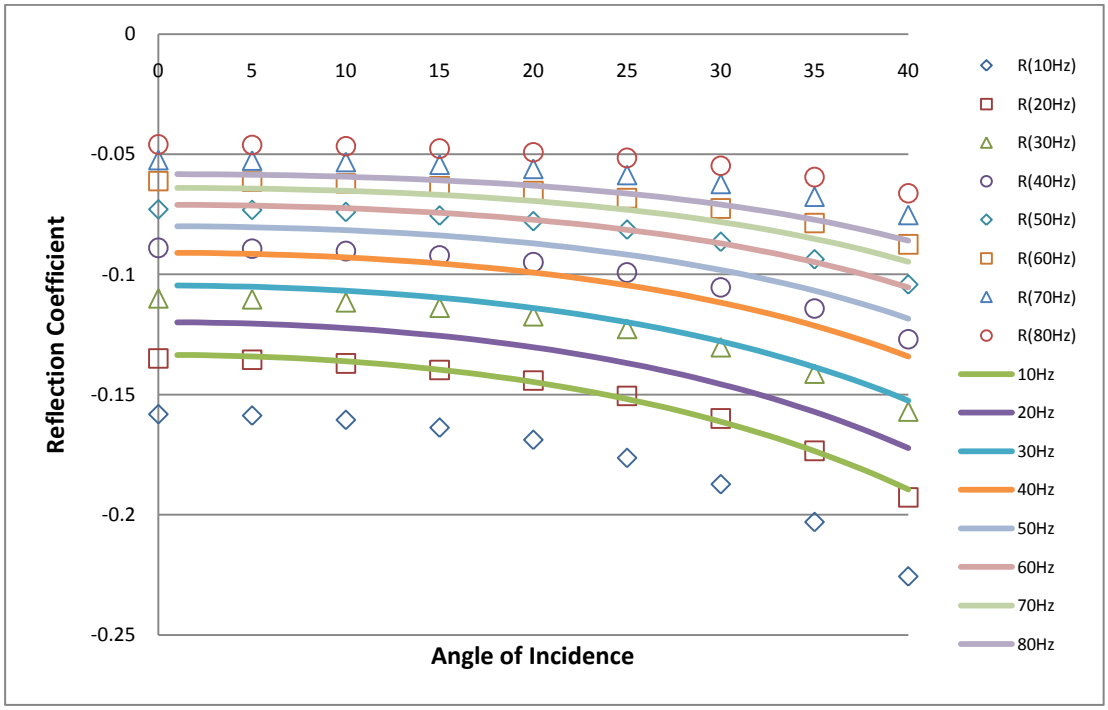

(c) $\varepsilon = 15\%$

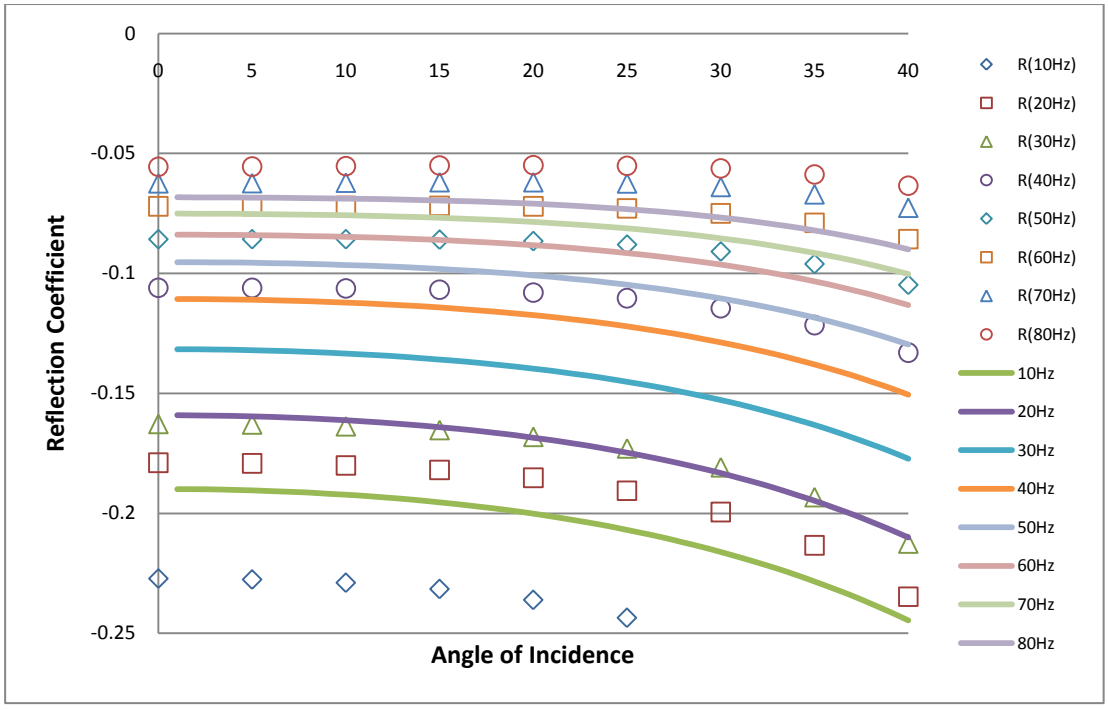

(d) $\varepsilon = 20\%$

Figure 7.16: Exact frequency-dependent reflection coefficients (solid lines) with the frequency-dependent AVO approximations (points) for the dispersive synthetics with crack density 5%, 10%, 15% and 20%.

7.4.3 Dispersion results

I have incorporated two approaches to minimise the effect of NMO stretch by running an alternative processing flow and using only the near-offset traces in my inversion. Table 7.4 shows how I have switched the order of the NMO correction and the spectral decomposition to reduce the effect of NMO stretch on the raw wavelets' spectra. Due to improved temporal resolution I have chosen to display only my results using the MPM decomposition. I have inverted the elastic and four dispersive synthetics have been limited to two different offset ranges; 0 – 1000m and 0 – 400m. Figures 7.17 to 7.21 show the inverted dispersion for the five synthetics using the two different offset ranges with the same bandwidth, 25-80Hz, and reference frequency, $f_0 = 40Hz$, as before.

Original	**Alternative**
spherical divergence	spherical divergence
NMO correction	spectral decomposition
spectral decomposition	NMO correction
summing *z* and *r* components	summing *z* and *r* components

Table 7.4: Comparison of the new, alternative, processing flow compared to my original order.

The differences between the full and near-offset inversion are minimal and show no degradation in the quality of the inverted P-wave reflectivity dispersion. The elastic synthetic shows near zero-magnitude dispersion in figure 7.17. The further four, dispersive, synthetic inversions are all plotted on the same scale to show the effect the crack density has had. At 5% crack density the P-wave reflectivity dispersion is approximately 20, at 10% crack density it is approximately 40, at 15% crack density it is approximately 70 and at 20% crack density it is approximately 110. The frequency-dependent AVO inversion has been able to quantitatively measure the different amounts of P-wave reflectivity dispersion.

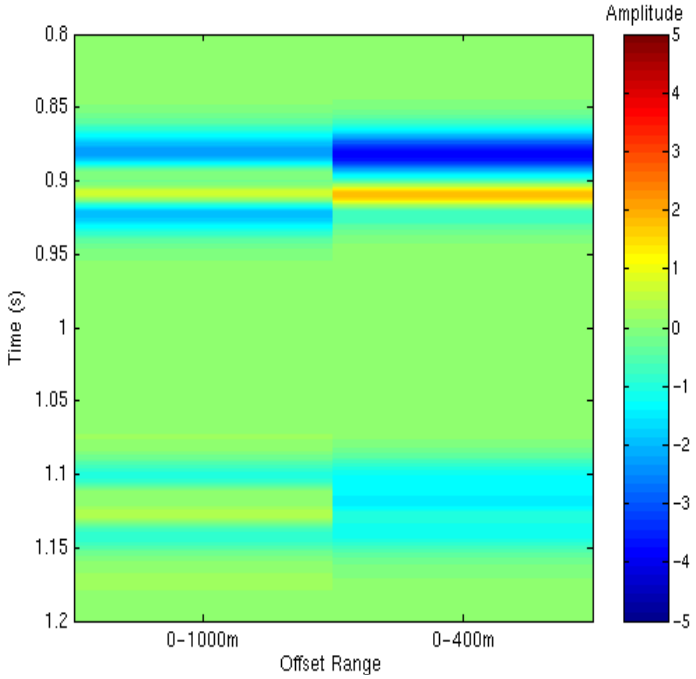

Figure 7.17: The inverted P-wave dispersion for the elastic synthetic with limited offset range of 0 – 1000m and 0 – 400m.

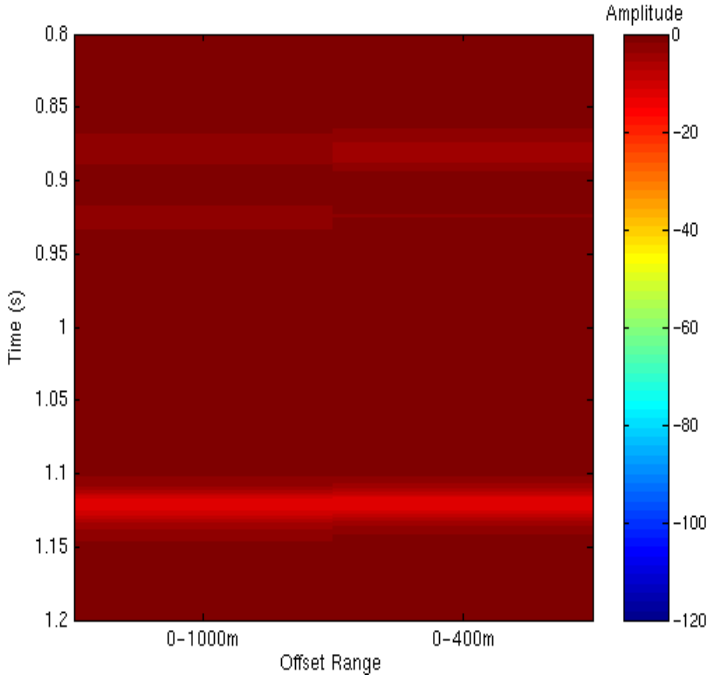

Figure 7.18: The inverted P-wave dispersion for the dispersive, $\varepsilon = 5\%$, synthetic with limited offset range of 0 – 1000m and 0 – 400m.

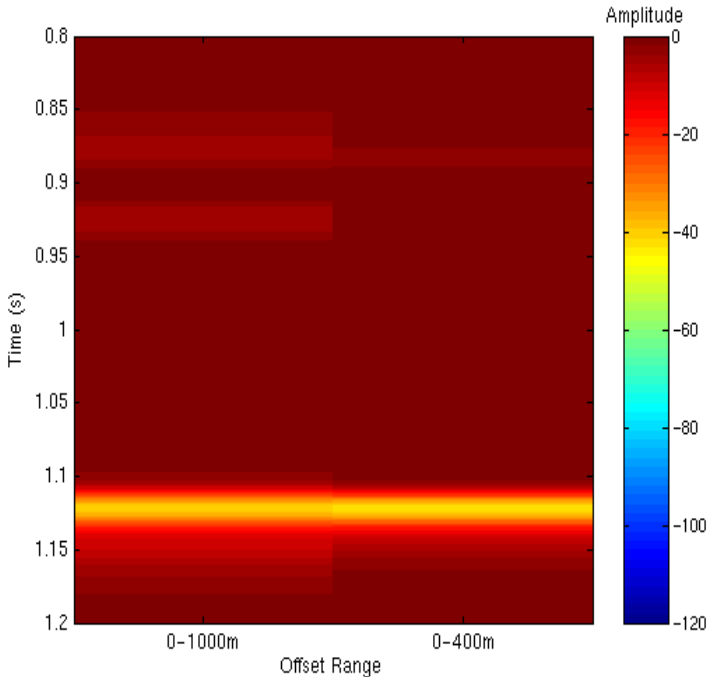

Figure 7.19: The inverted P-wave dispersion for the dispersive, $\varepsilon = 10\%$, synthetic with limited offset range of 0 – 1000m and 0 – 400m.

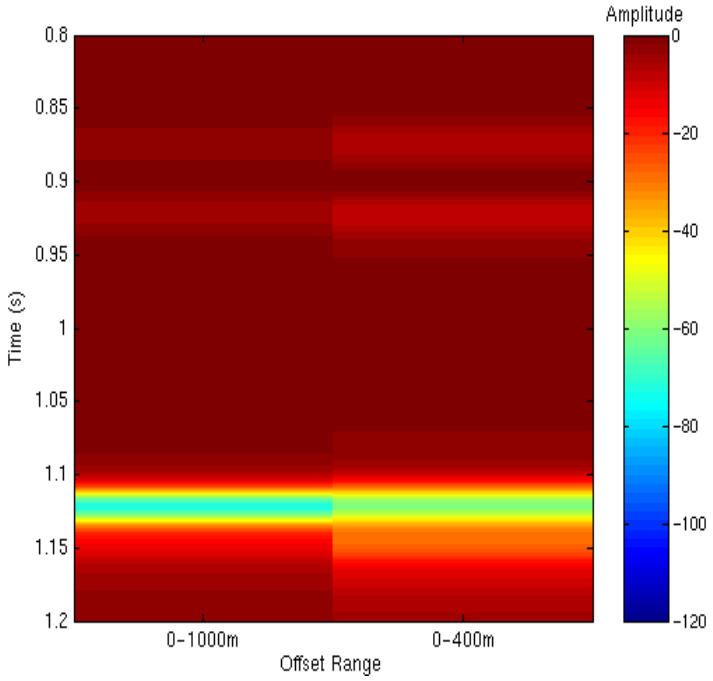

Figure 7.20: The inverted P-wave dispersion for the dispersive, $\varepsilon = 15\%$, synthetic with limited offset range of 0 – 1000m and 0 – 400m.

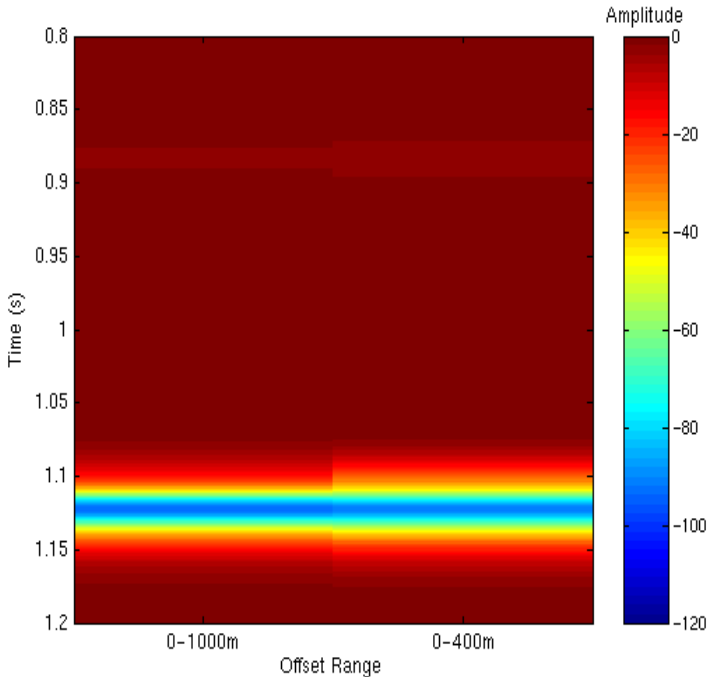

Figure 7.21: The inverted P-wave dispersion for the dispersive, $\varepsilon = 20\%$, synthetic with limited offset range of 0 – 1000m and 0 – 400m.

7.5 Class I three-layer synthetic

I have created three synthetic gathers for a three-layer model to look at the differences between the dispersive responses from a Class III and a Class I reflection. I have used a slightly edited set of model parameters reported by Zhang (2008) and added an additional shale layer to create the elastic reflection I used to balance the spectral amplitudes. Table 7.5 lists the parameters of the three materials and the fluid bulk modulus of gas was taken to be $200MPa$ in this example. I used a 40Hz Ricker wavelet as my source and used five receivers (0 – 400m) at 100m spacing, limiting myself to only the near-offsets.

Material	$\mathbf{V_P}$ **(ms^{-1})**	$\mathbf{V_S}$ **(ms^{-1})**	$\boldsymbol{\rho_W}$ $(\mathbf{g.cm^{-3}})$	$\boldsymbol{\rho_G}$ $(\mathbf{g.cm^{-3}})$	$\boldsymbol{\Phi}$ (%)	$\boldsymbol{\varepsilon}$ **(%)**
Shale (i)	3900	2100	2.2	-	-	-
Shale (ii)	4300	2500	2.4	-	-	-
Sandstone	5150	3180	2.7	2.53	15	5 (10)

Table 7.5: Material parameters for the Class I three-layer synthetic model.

The first synthetic had a relaxation time of $\tau = 1e^{-6}s$ to approximate the low-frequency, elastic case where there is no dispersion in the sandstone material. The other two synthetics had a relaxation time of $\tau = 5e^{-3}s$ with crack densities of 5% and 10%. Figure 7.22 shows the low and high-frequency limits of the reflection coefficient for the shale-sandstone boundary under water and gas saturation. The lower fluid bulk modulus of gas compared to water reduces the P-wave velocity, making $\Delta V_P/V_P$ smaller and decreasing the reflection coefficient. Figure 7.23 shows the exact frequency-dependent reflection coefficients for the two dispersive cases when the crack densities are 5% and 10%. As was the case in figure 7.13 the dispersion increases when the crack density is larger. Unlike the Class III reflection I showed earlier in this Chapter, the reflection coefficient now increases with frequency, rather than decreases. The difference between the low and high-frequency limits after fluid substitution with gas is smaller than the Class III limits despite using a smaller fluid bulk modulus. The amount of velocity dispersion may be the

same but the relative change in the velocity is smaller due to the larger original velocity in the layer, $5150ms^{-1}$ compared with $2835ms^{-1}$ earlier.

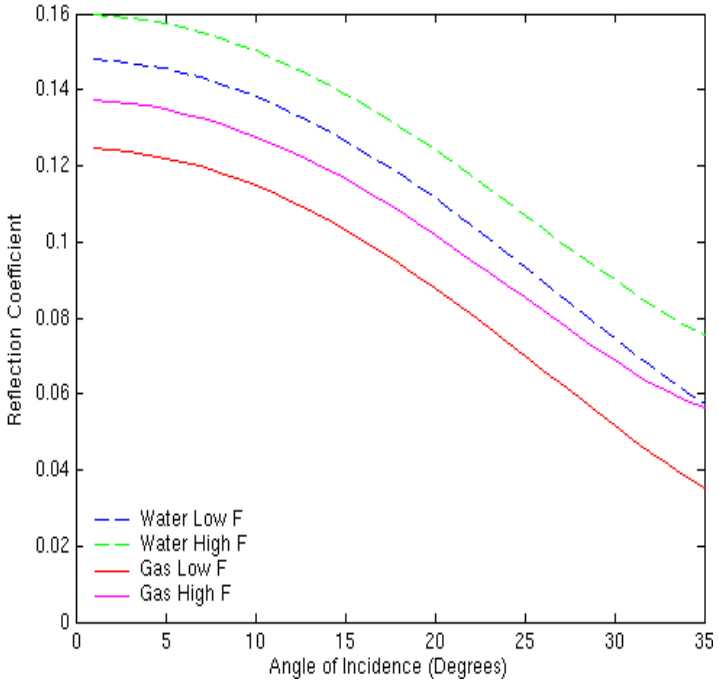

Figure 7.22: AVO low and high-frequency limit curves for the shale-sandstone boundary under water and gas saturation.

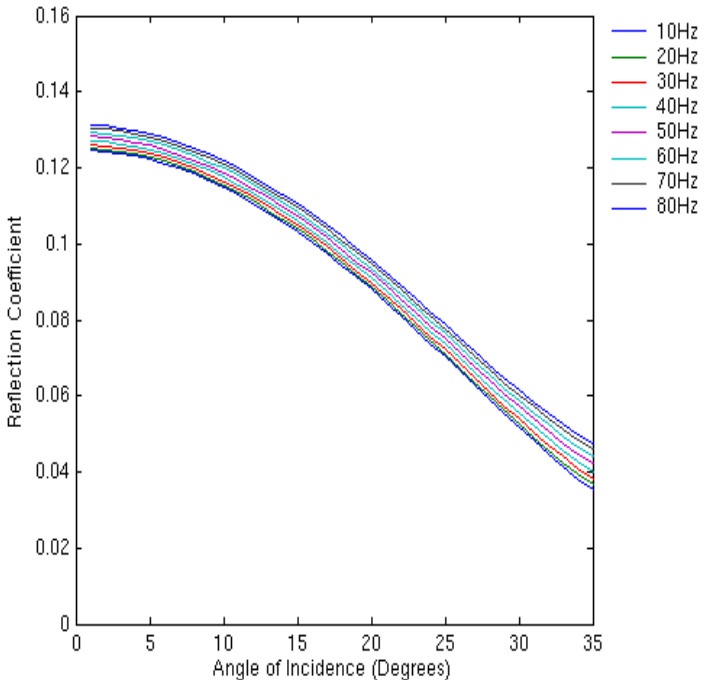

(a) ε 5%

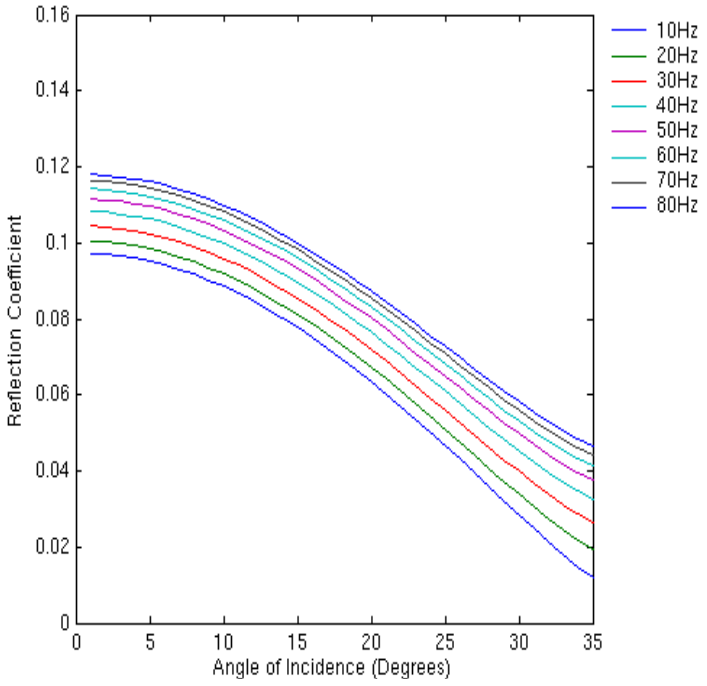

(b) ε 10%

Figure 7.23: The exact reflection coefficients for the two dispersive synthetics with different crack densities. The different colours represent the different frequencies. The different frequencies have varying P-wave velocities in the lower layer as indicated in figure 2.1.

7.5.1 Synthetic gathers

It is difficult to detect the subtle differences that crack density and dispersion have had on the NMO corrected gathers. Figure 7.24a shows the elastic synthetic under gas saturation and the bottom reflection at ~0.75s has a small decrease in amplitude as the offset increases. For the dispersive synthetic with 5% crack density, figure 7.24b, there should be an increase in the magnitude as the reflection coefficients are larger than for the elastic synthetic. Finally, in the dispersive synthetic with 10% crack density, figure 7.24c, there should be a reduction in the amplitudes compared to the previous two synthetics as the reflection coefficients are smaller. The differences between the NMO corrected amplitudes on the synthetics are much more subtle than on the Class III synthetics tested earlier and are harder to detect due to the small offset range used.

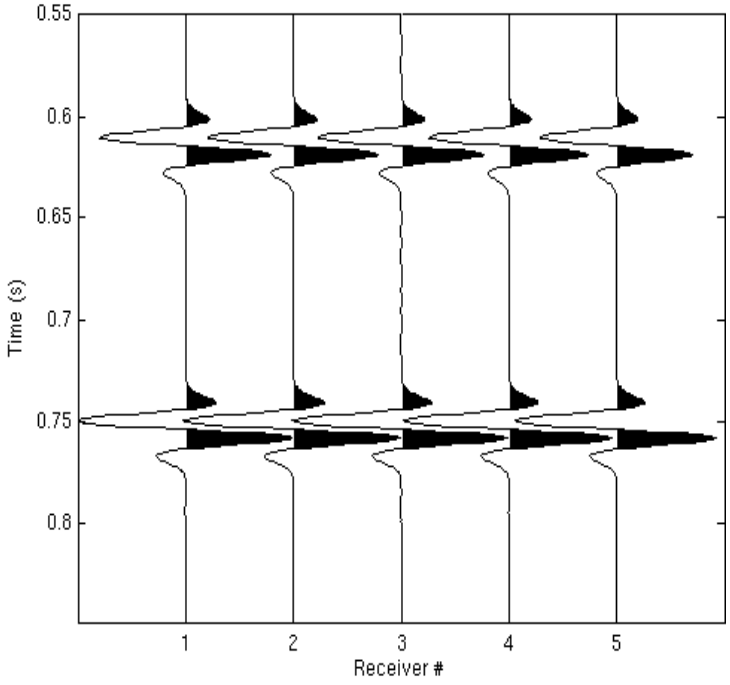

(a) Elastic

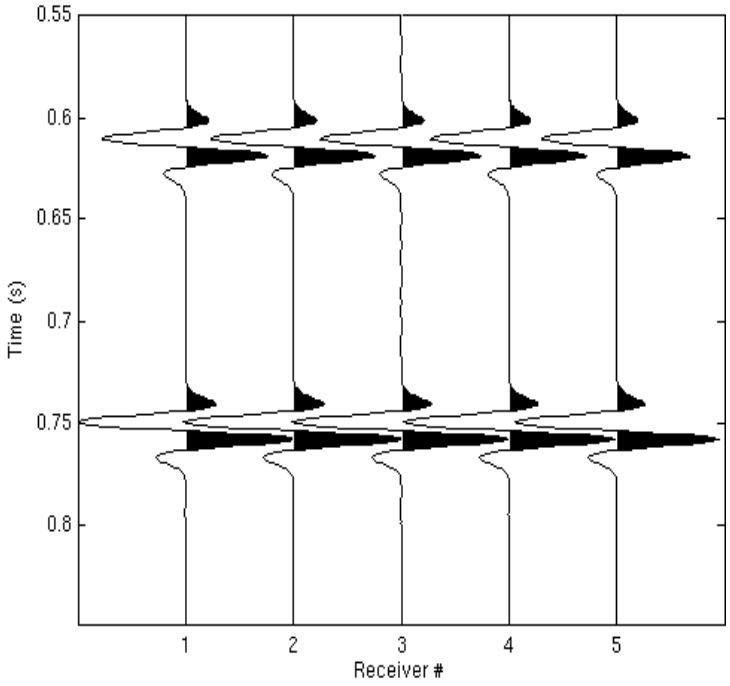

(b) Dispersive, $\varepsilon = 5\%$

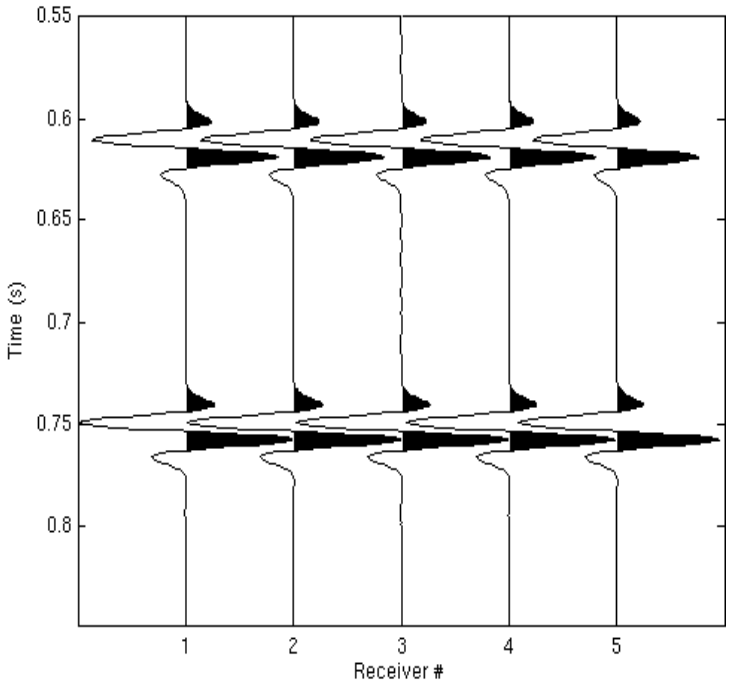

(c) Dispersive, $\varepsilon = 10\%$

Figure7.24: NMO corrected gathers for the elastic and dispersive synthetics.

7.5.2 Spectral ratio and amplitudes

I have calculated the spectral ratio of top and bottom reflections of the zero-offset trace from the three synthetics and plotted a linear best fit. For the elastic synthetic the gradient of the spectral ratio is flat but the dispersive reflections result in a positive gradient that implies a negative *Q*. Table 7.6 summarises the results. Once again, the only difference between the synthetics is in the bottom half-space and this change must be due to the instantaneous frequency-dependent reflection coefficient between the shale (ii) and the sandstone and not the result of energy lost during wave propagation. The slope and apparent *Q* are much less than for equivalent fluid substitution and crack density in the Class III synthetic and I predicted that this would result in a smaller measured dispersion from the inversion due to the smaller relative velocity dispersion in this synthetic compared to the original layer velocity.

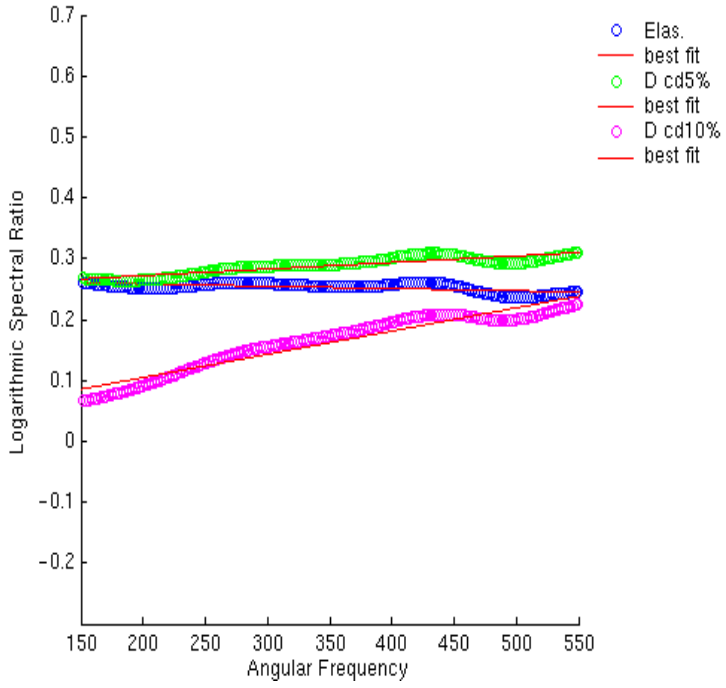

Figure7.25: Spectral ratio for the zero-offset trace for the elastic and dispersive synthetics with a linear best fit.

Synthetic	Gradient	Apparent *Q*
Elastic	~0	∞
Dispersive 5%	0.000108	-645
Dispersive 10%	0.000382	-180

Table 7.6: The spectral ratio method results for apparent *Q* from lines of best fit in figure 7.25.

I have plotted the balanced spectral amplitudes for the zero-offset trace from the three synthetics in figure 7.26. The top reflection at ~0.62s is balanced after the overprint of the source wavelet has been removed. The bottom reflection at ~0.75s is balanced on the elastic synthetic, whilst the first dispersive synthetic, with $\varepsilon = 5\%$, has larger amplitudes corresponding to the larger reflection coefficients. I can also detect a slight increase in magnitude with frequency. The second dispersive synthetic, with $\varepsilon = 10\%$, has smaller amplitudes and I can again detect an increase in magnitude with frequency. These changes in amplitude with frequency will be clearer on the dispersive reflectivity inversion as it quantifies these subtle changes.

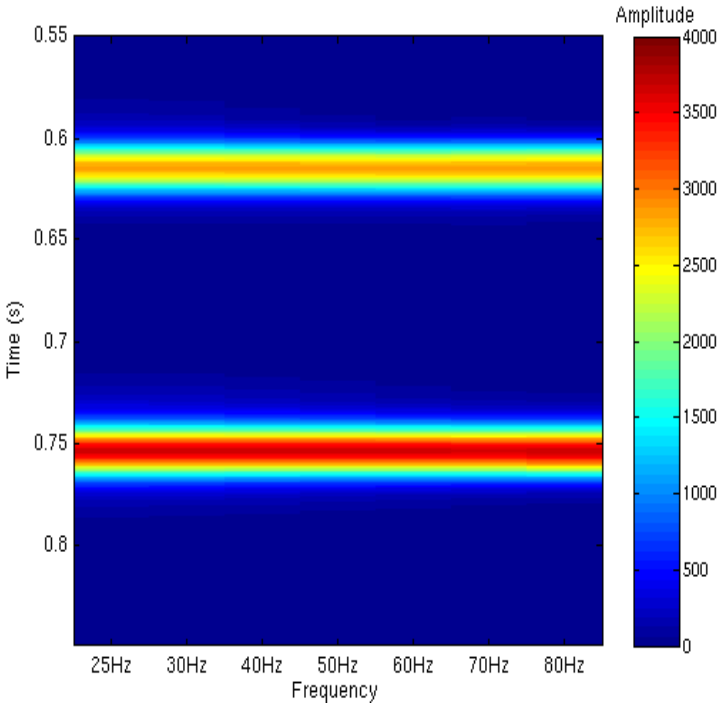

(a) Elastic

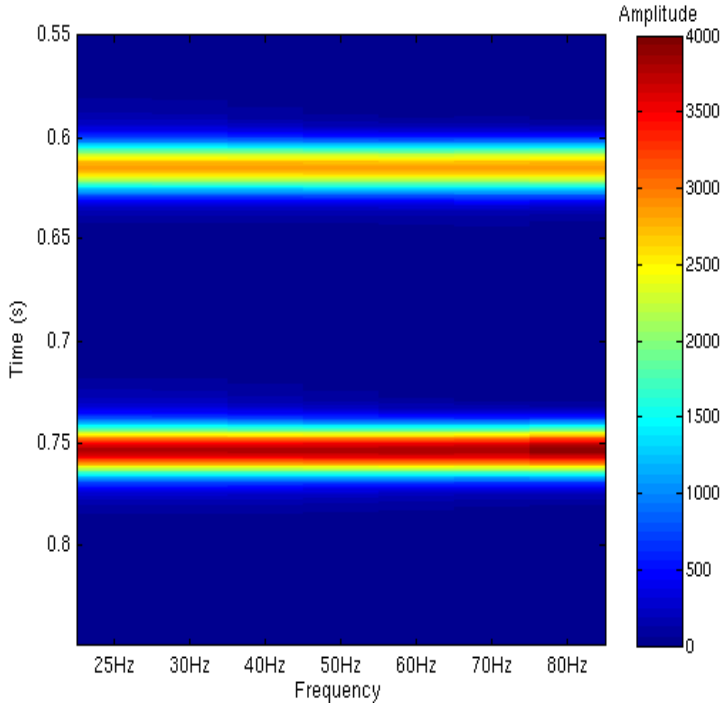

(b) Dispersive, $\varepsilon = 5\%$

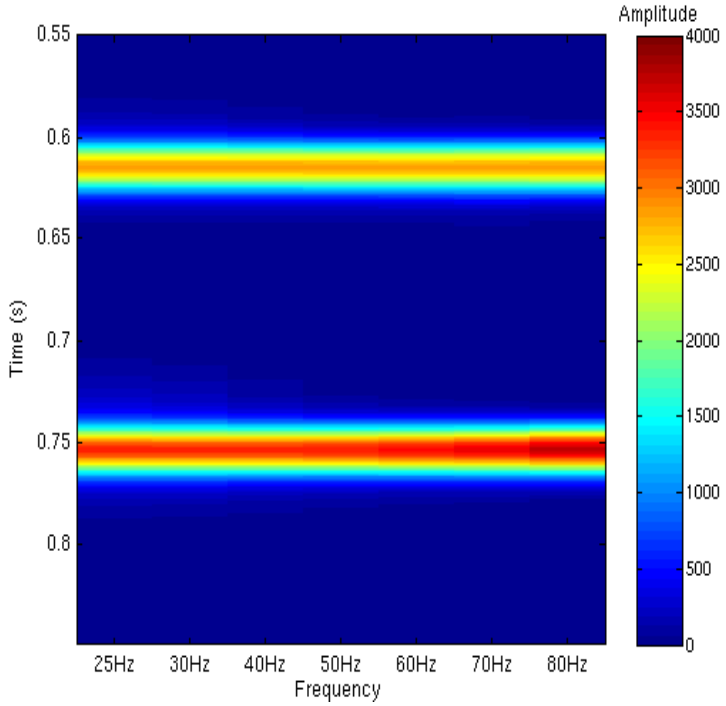

(c) Dispersive, $\varepsilon = 10\%$

Figure7.26: Balanced spectral amplitudes from the zero-offset trace for the three synthetics.

7.5.3 Dispersion results

I have plotted the P-wave dispersion results for the three synthetic gathers in figure 7.27 which shows positive reflectivity dispersion, indicating a Class I reflection, that increases with crack density. Where the changes with frequency of the balanced spectral amplitudes and reflectivities are difficult to interpret, the frequency-dependent AVO inversion clearly quantifies this effect. The result is as I predicted from the frequency-dependent AVO theory; for a frequency-dependent Class I reflection I measured positive dispersion and for a Class III frequency-dependent reflection I measured negative dispersion due to the relative change in the reflection coefficients with frequency. The magnitude is less than the Class III reflection described earlier in the Chapter and this is due to the larger P-wave velocities in the synthetics layers meaning the dispersion is relatively smaller.

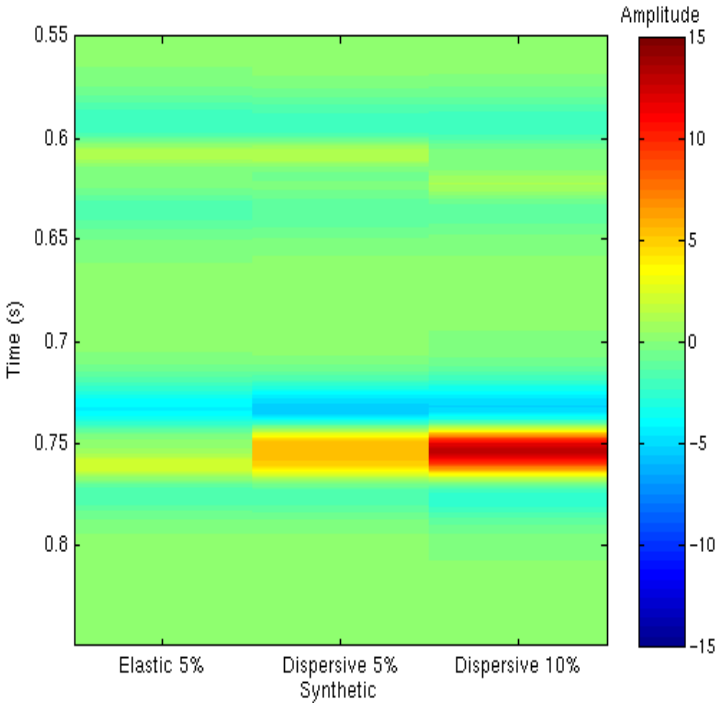

Figure7.27: The measured P-wave dispersion for the three synthetics.

7.6 Noise sensitivity

In Chapter 5, I demonstrated how an integrated AVO and spectral analysis could be used to identify frequency-dependent anomalies on a marine seismic dataset. So far in this thesis I have measured reflectivity dispersion using noise-free synthetic gathers. The positive results from Chapter 5 indicate that it may be possible to extend this technique to real datasets where the signal quality is affected by random noise. On inspection of the stacked sections in figures 5.1 and 5.2 the true signal reflection amplitudes areas at ~2s are ±1 and the background noise between ~1.4 – 1.8s is approximately ±0.15. The signal-to-noise ratio (SNR) is defined as the ratio of the power spectrum (Sheriff and Geldart, 1995) such that,

$$SNR = \frac{P_{signal}}{P_{noise}} = \left(\frac{A_{signal}}{A_{noise}}\right)^2. \qquad (7\text{-}11)$$

The SNR of the seismic dataset in Chapter 5 is approximately 44.

I used both the elastic and dispersive three-layer Class III synthetics from section 7.2. I added Gaussian distributed random noise to the raw synthetic gathers output from ANISEIS. I used SNR values (defined as the ratio of relative energy or amplitude squared) of 40 and 20 to model the impact of poor signal-to-noise on my reflectivity dispersion inversion. I then applied the spherical divergence correction for a layered medium (Newman, 1973). Following my earlier results I limited the offset range to 400m and used the alternative processing flow outlined in table 7.4: spectral decomposition then NMO correction. The subsequent synthetic gathers for a single realisation are shown in figures 7.28 (elastic) for $\tau = 1e^{-6}s$ and 7.29 (dispersive), for the case where $\tau = 5e^{-3}s$.

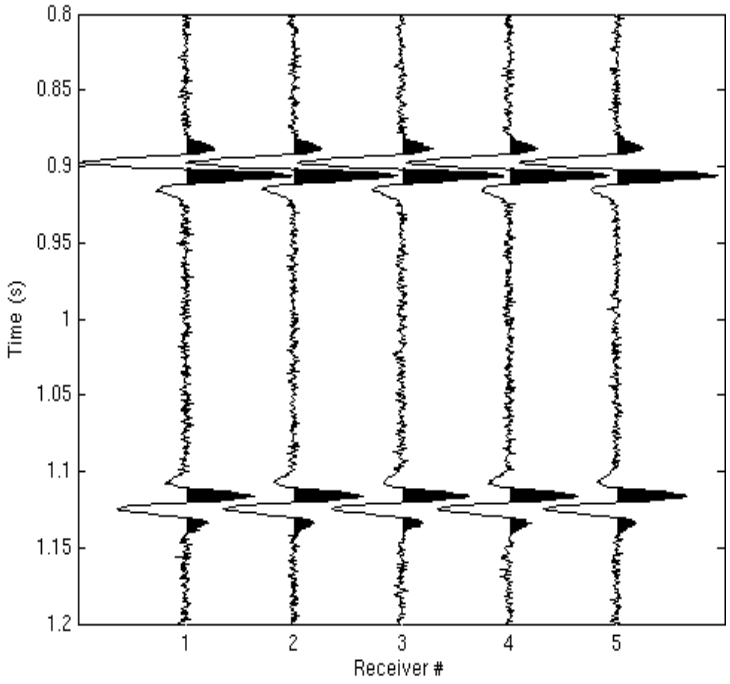

(a) $SNR = 40$

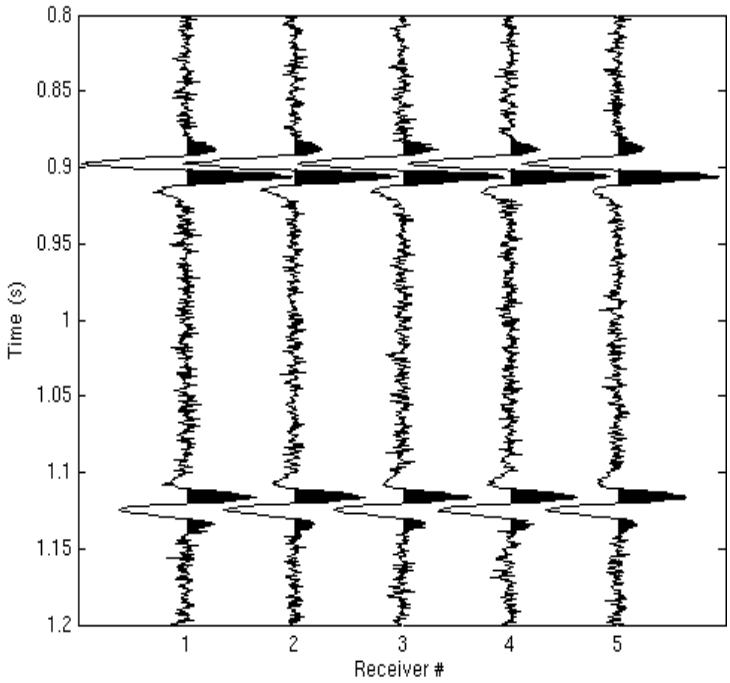

(b) $SNR = 20$

Figure 7.28: The processed elastic ($\tau = 1e^{-6}s$) three-layer synthetic gathers with SNR = 40 and 20.

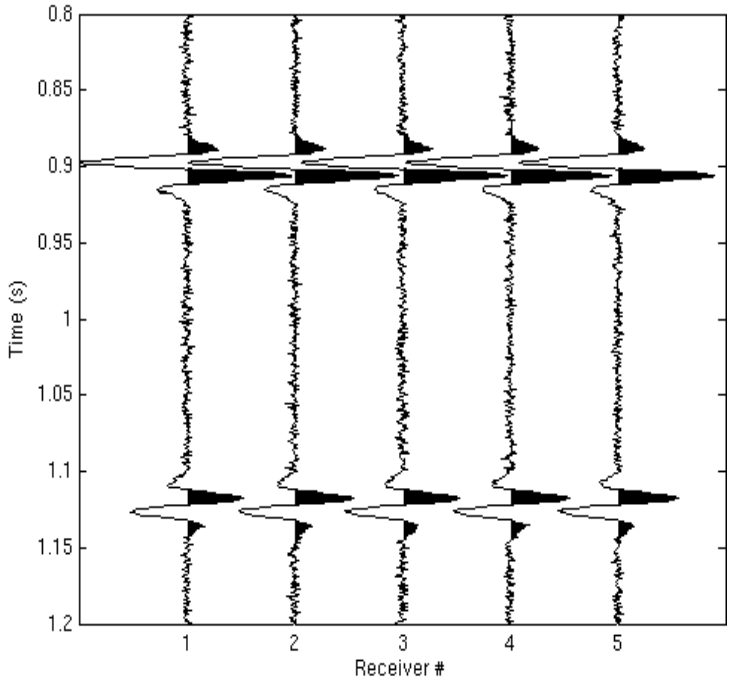

(a) $SNR = 40$

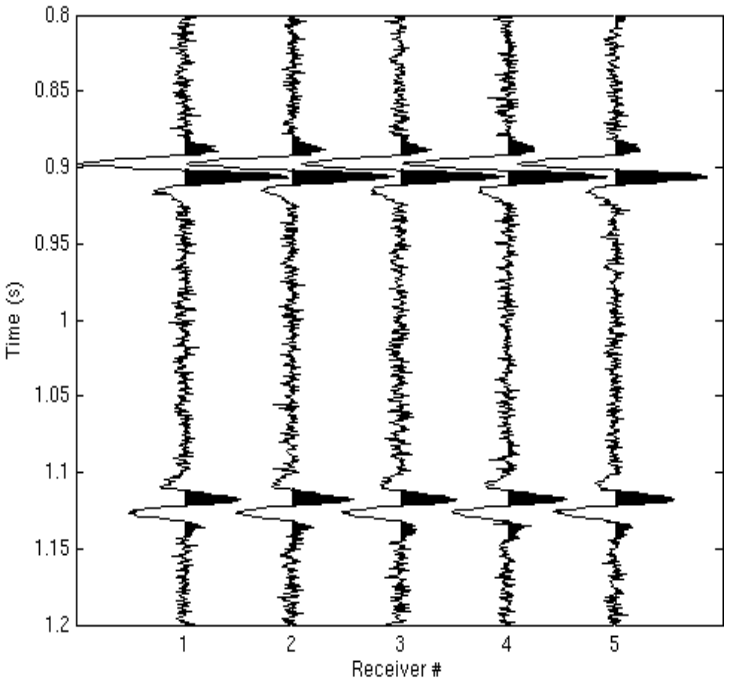

(b) $SNR = 20$

Figure 7.29: The processed dispersive ($\tau = 5e^{-3}s$) three-layer synthetic gathers with SNR = 40 and 20.

I then spectrally decomposed all four synthetics using the MPM at 25, 30, 40, 50, 60, 70 and 80Hz. Using the same methodology as before I inverted the resultant spectral gathers to calculate the P-wave reflectivities. The initial noise-free synthetic P-wave reflectivities are shown in figures 7.6(b) and 7.7(b). Figures 7.30 and 7.31 show, respectively, the inverted P-wave reflectivities for the elastic and dispersive noisy synthetics. It is clear from both sets of figures that as the SNR increases the spectral decomposition is losing some of its high frequency resolution. In the elastic synthetic, the second reflection at ~1.12s should have flat reflectivity amplitudes across the frequency range 25 – 80Hz. When the SNR is 40 the 80Hz reflectivity is slightly less than the other frequency and when the SNR is 20 both the 70 and 80Hz reflectivities have slightly higher reflectivity amplitudes. The random noise is distorting both the spectral decomposition at the higher frequencies but also the balancing process using the top reflection.

In the dispersive synthetic case the effect of the noise when the SNR is 40 is less clear. The P-wave reflectivities decrease as predicted with frequency. When the SNR is 20 the reflectivity at 70 and 80Hz has again been increased compared to the noise free reflectivities in figure 7.7.

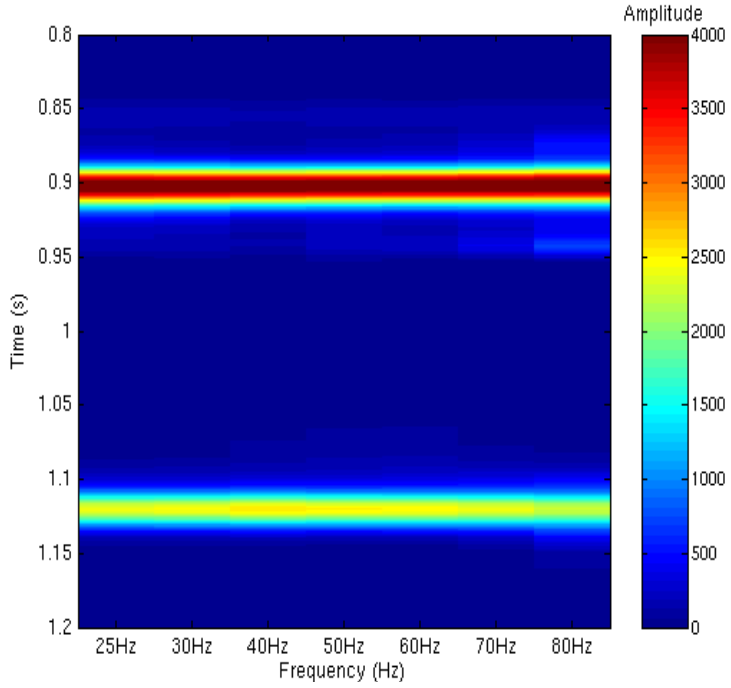

(a) $SNR = 40$

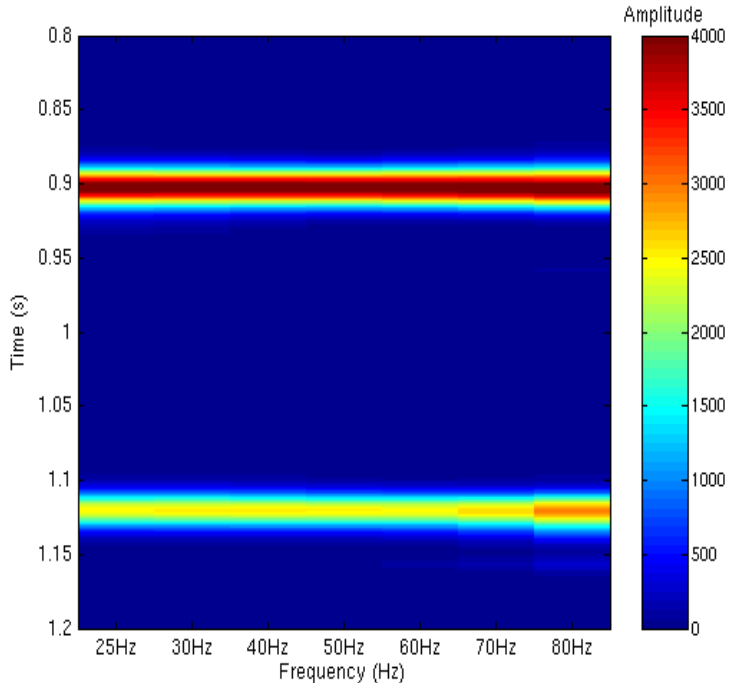

(b) $SNR = 20$

Figure 7.30: Inverted $|\Delta V_P/V_P|_{f_i}$ from the elastic synthetic gathers with SNR = 40 and 20.

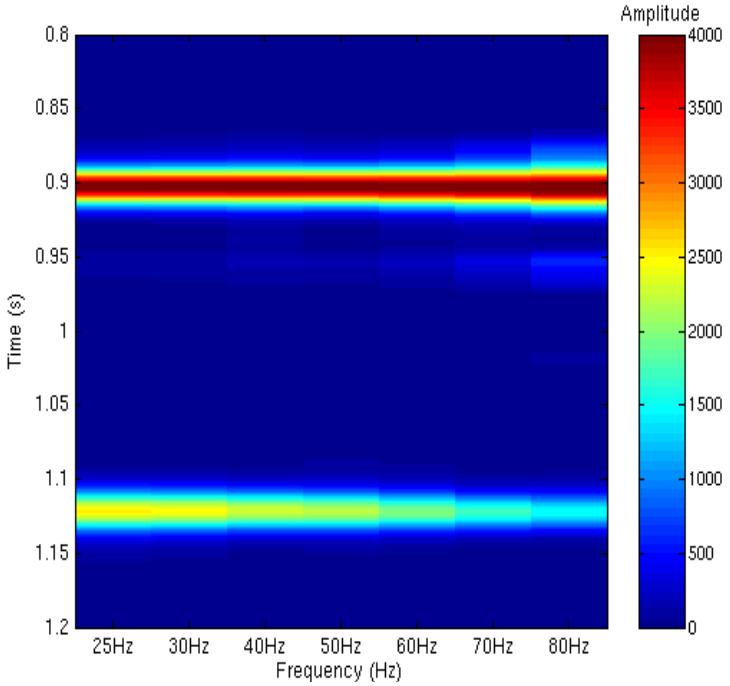

(a) $SNR = 40$

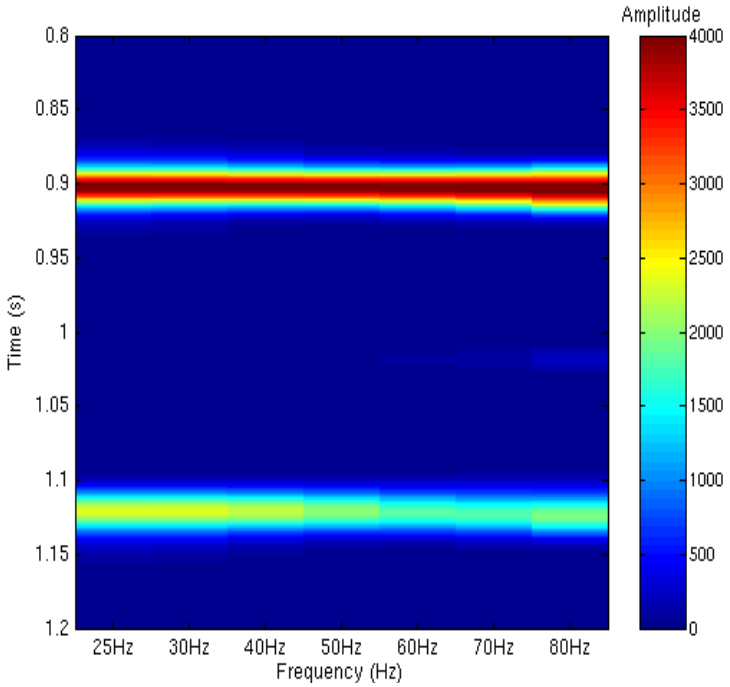

(b) $SNR = 20$

Figure 7.31: Inverted $|\Delta V_P/V_P|_{f_i}$ from the dispersive synthetic gathers with SNR = 40 and 20.

Finally I inverted the P-wave reflectivities to estimate the reflectivity dispersion in the four synthetic gathers. I compared the results from the noisy synthetics against the values I obtained from the noise-free synthetics. It should be noted that the earlier reflectivity dispersion values were calculated using 11 traces, up to 1000m offset, and using the original processing order. Figure 7.21(a) shows the P-wave reflectivity dispersion from the three elastic synthetics; noise-free, $SNR = 40$ and $SNR = 20$. The amplitude by the second reflection at ~1.12s is approximately zero in the noise-free synthetic. When the $SNR = 40$, the amplitude is a small negative value indicating a small increase in reflectivity with frequency. This result is consistent with my observation that the 80Hz reflectivity was slightly less than the other frequencies seen in figure 7.30(a). When the $SNR = 20$, the amplitude is a small positive value indicating a small decrease in reflectivity with frequency. Again, this result is consistent with my observation that the 70 and 80Hz reflectivities are slightly larger than the other frequencies seen in figure 7.30(b). Whilst the noise-free reflectivity dispersion signature clearly indicates an elastic reflection, when noise is introduced the response is unclear and could be misinterpreted as either a Class III or Class I frequency-dependent reflection. Figure 7.21(b) shows the P-wave reflectivity dispersion from the three dispersive synthetics; noise-free, $SNR = 40$ and $SNR = 20$. The amplitude by the second reflection at ~1.12s is negative in all three of the synthetics. Whilst it would be possible to interpret all three as Class III frequency-dependent reflection, the nature of the signatures when noise is introduced changes significantly with respect to the noise-free solution.

In all of the synthetics where random noise has been introduced, the shallower elastic reflection at 0.9s exhibits reflectivity dispersion which is not present on the synthetic gathers. This reflection is used to balance the deeper reflection so that subtle changes in the spectral content can be measured. When noise is introduced this affects both the spectral decomposition and the balancing process. Whilst I have demonstrated that a Class III frequency-dependent reflection can be quantified in the presence of noise up to a SNR of 20, care must be taken when interpreting reflectivity dispersion which may have been tainted, especially in low *Q* media.

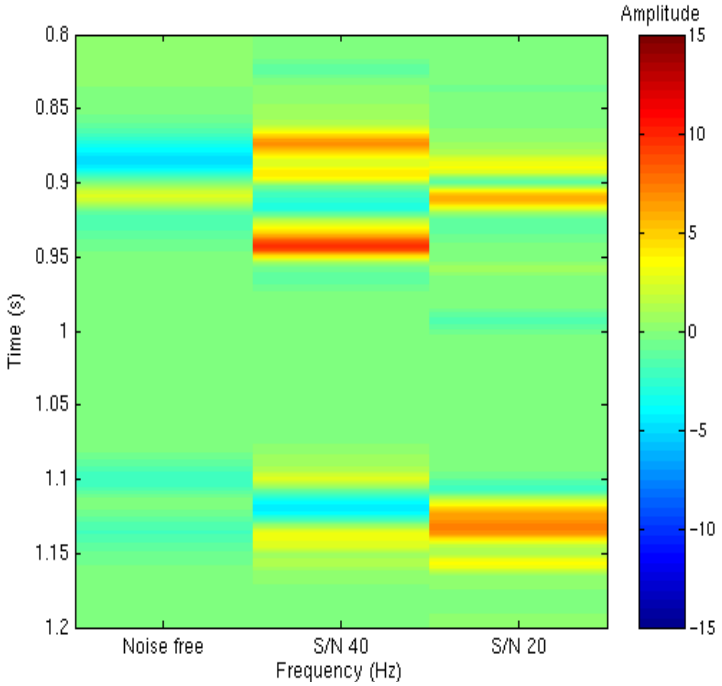

(a) Elastic

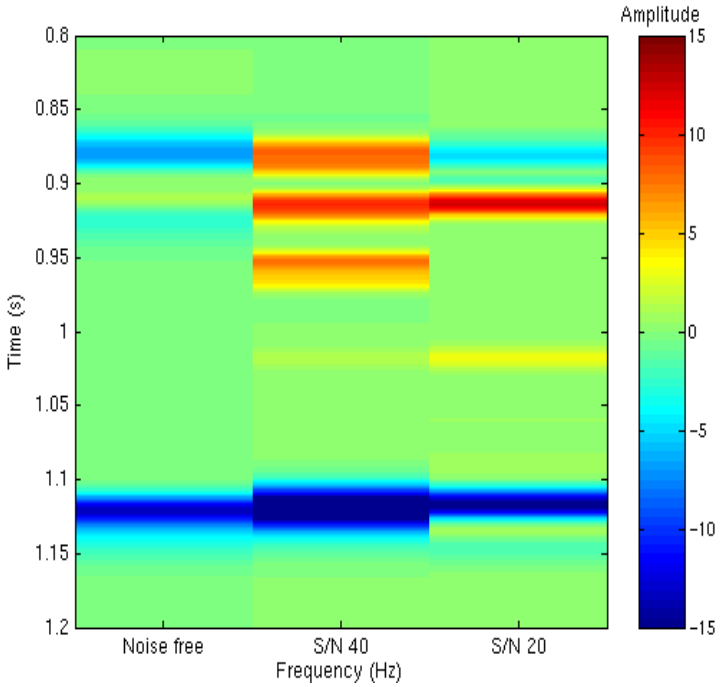

(b) Dispersive

Figure 7.32: Inverted P-wave reflectivity dispersion from the noise-free, $SNR = 40$ and $SNR = 20$ elastic and dispersive synthetic gathers.

7.7 Tuning inversion

In Chapter 4, I showed how tuning can introduce spectral anomalies that can be mistakenly interpreted as dispersion anomalies. The increased temporal resolution of the MPM over the CWT minimised the size of the decomposed wavelet. I looked at the spectrally-decomposed stacked amplitudes from the multi-layer synthetic (figure 4.4) and could correctly separate the two, tuned reflections, at 50m and 130m separation, using the MPM and CWT respectively.

In this inversion I have used near-offsets (0 – 500m) gathers and followed the alternative processing flow outlined in table 7.4. I applied spherical divergence, performed spectral decomposition, applied NMO correction and then added the vertical and radial components of the data. As a result of using only the near-offset traces I effectively limited myself to estimating only the P-wave reflectivity dispersion as I didn't have sufficiently large offsets to estimate the S-wave reflectivities. Therefore, I only showed the results of the P-wave dispersion from the nine elastic synthetics using the CWT and MPM decompositions (figures 7.33). I have reduced the bandwidth of the spectrally decomposed amplitudes to 25 – 70Hz due to the anomalous spectral amplitudes at 80Hz seen in figures 4.5 – 4.7 and used $f_0 = 40Hz$ as the reference frequency.

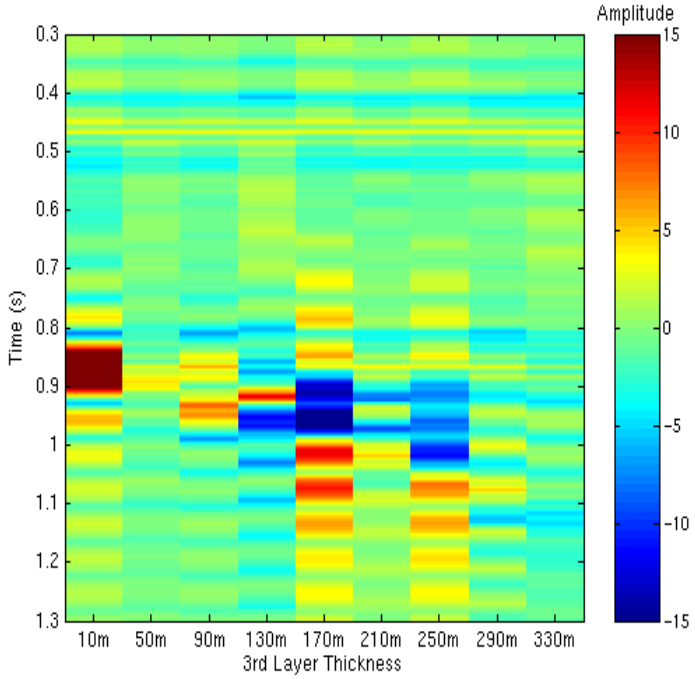

(a) CWT

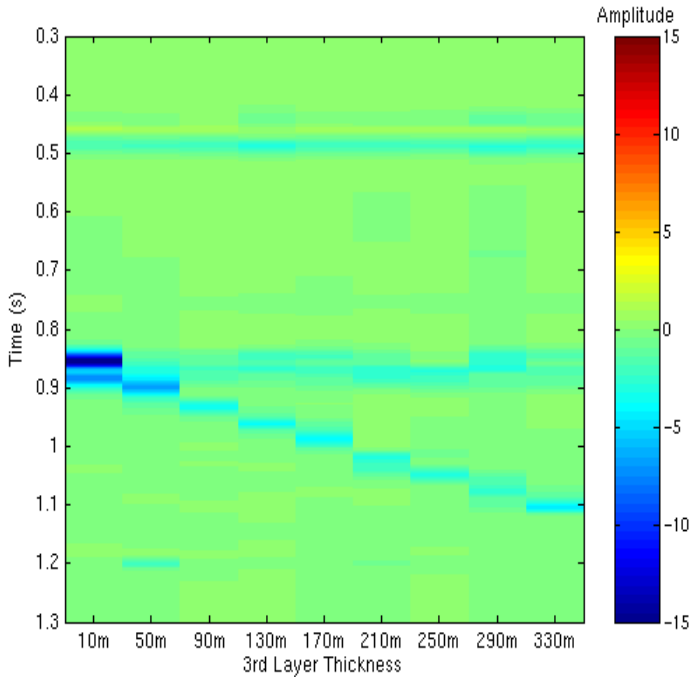

(b) MPM

Figure 7.33: The inverted P-wave dispersion for the elastic "*tuning*" synthetics following decomposition using the CWT and MPM.

The top reflection (~0.46s) was used to balance the spectral amplitudes and the reflectivity dispersion reflects this with near zero amplitude across all of the synthetics. When the third layer is only 10m thick the reflections from the top and bottom of the layer interfere and the resulting amplitude spectra from the top and bottom reflections are shown in figure 7.34. I have plotted the spectral ratio and fitted a linear best fit (figure 7.35), which has a positive gradient. This signature corresponds to positive dispersion following the frequency-dependent AVO inversion. Using the CWT I measured positive reflectivity dispersion for this synthetic gather, in agreement with figure 4.5, showing that the amplitudes increased with frequency. This could be mistakenly interpreted as a Class I dispersive reflection from a single layer. The MPM balanced spectral amplitudes displayed a slight dimming at 40 and 50Hz and the inversion measured negative reflectivity dispersion, the opposite of what I would classify as the correct response according to the spectral ratio. This could be mistakenly interpreted as a Class III dispersive reflection from a single layer. However, as the thickness of the third layer increases, the MPM is able to decompose the two reflected seismic wavelets without interference. The MPM inversion has measured a small negative anomaly at 50m thickness but after that correctly measures near zero reflectivity dispersion. The results from the CWT show how the poorer temporal resolution introduces relatively strong dispersive signals, as the decomposed wavelets interfere, rather than the original seismic wavelets. This spectral interference distorts the balancing I have applied and results in my measuring reflectivity dispersion up to 250m thickness. Whilst tuning can produce a similar response as a dispersive reflection, using a flexible spectral decomposition algorithm, such as the MPM with good temporal resolution, allows the uncertainty to be minimised when analysing thin-bed reflections.

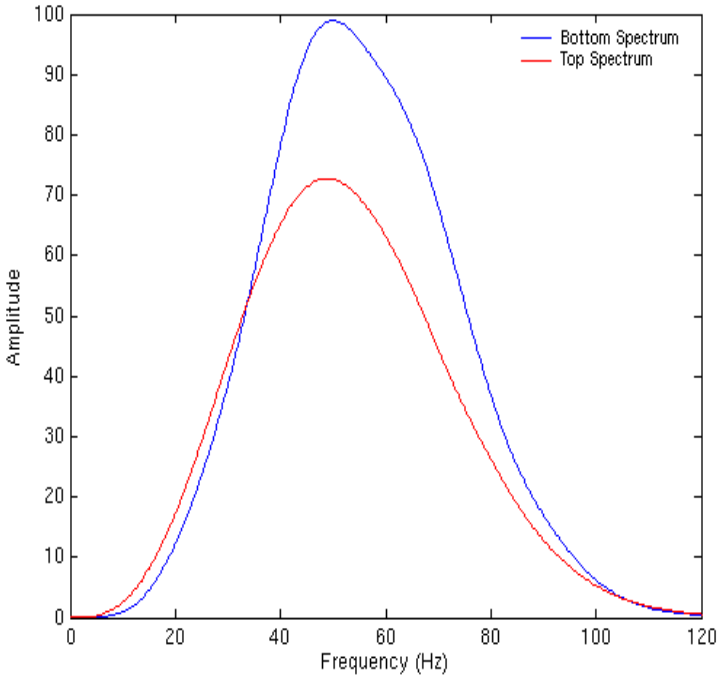

Figure 7.34: Amplitude spectra of the top and bottom reflections from the zero-offset trace on the 10m thick synthetic.

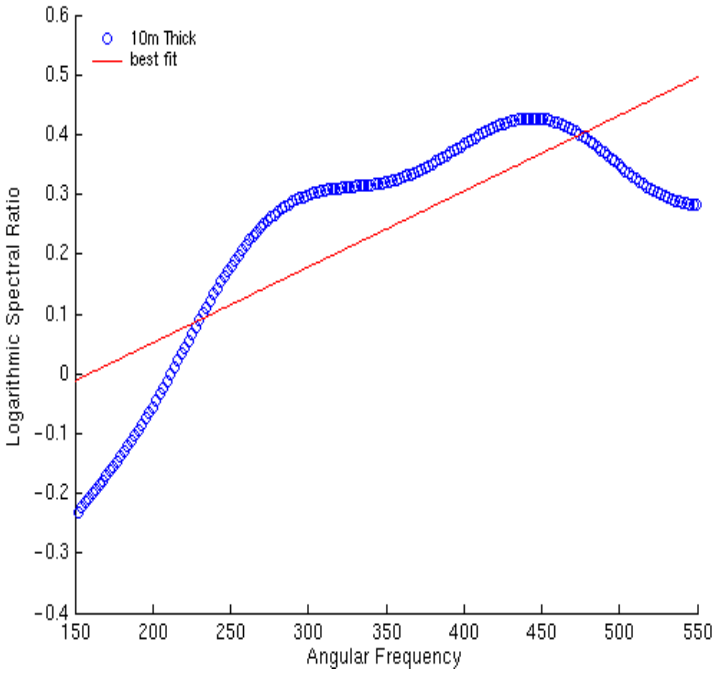

Figure 7.35: Spectral ratio of the two amplitude spectra in figure 7.34 with a linear best fit.

7.8 Discussion and conclusions

In this Chapter I have extended the frequency-dependent AVO inversion to include an extra elastic layer so that I can use the resultant elastic reflection to balance the spectral amplitudes. By adding another layer I was able to use a layered medium spherical divergence correction and I also used ray tracing to calculate the angle of incidence. I inverted a three-layer synthetic with an elastic and dispersive Class III reflection and was able to accurately quantify the P-wave reflectivity dispersion. I found that the measured dispersion varied according to the offset range of the input gathers, the accuracy of the result decreasing with further offsets. I looked at the spectral ratios of the elastic amplitude spectra from the zero-offset trace and found that NMO stretch was adversely affecting my balancing by introducing low frequencies at far-offsets. In an effort to reduce this I limited the input gathers to near-offsets only and changed the processing order by performing spectral decomposition on the raw gathers and applying the NMO correction to the spectral amplitudes. By only using the near-offsets I was effectively discarding the S-wave reflectivities as they are difficult to accurately measure without further offsets. I was able to accurately measure the P-wave reflectivity dispersion using only these near-offsets. I further verified the theoretical predictions that crack density controls the amount of dispersion, all other parameters being equal, by inverting four synthetic gathers with varying crack densities. The relaxation time, which I had earlier varied, changes the frequency band of the dispersive velocity. I repeated my frequency-dependent AVO inversion for another three-layer synthetic with a Class I reflection and measured positive P-wave reflectivity dispersion. This was in agreement with my earlier theoretical prediction that the sign of the dispersion depends on the AVO classification of the inverted reflection and can be used to confirm a frequency-dependent AVO interpretation. Finally, I returned to the hypothesis that tuning can produce signatures on spectral gathers which can be mistaken for dispersion. I inverted a four layer wedge-type model, where I varied the thickness of the third material, to determine when the inversion can correctly identify the two separate wavelets. I discovered that the high temporal resolution of the MPM is able to do a

far superior job correctly separating the interfering wavelets at just over 50m compared with over 250m using the CWT. Using a flexible spectral decomposition algorithm allows for more detail to be correctly interpreted using my frequency-dependent AVO inversion.

Chapter 8: Discussion and conclusions

8.1 Discussion

My intention in this thesis has been to develop a new technique to allow rock physics knowledge to be linked to the analysis of seismic amplitudes and the measurement of velocity dispersion. There is a growing body of theory that predicts frequency-dependence velocity related to fluid saturation results in frequency-dependent AVO and I have developed a new mathematical technique to quantitatively measure this from pre-stack gathers. I have not addressed the fluid-related mechanisms that may cause velocity dispersion as this remains an open problem in rock physics theories. I have created the ability to measure a property of fluid-saturated rocks that may be of use to improve fluid detection from seismic data. However, the absence or detection of reflectivity dispersion should be carefully interpreted into a local geological and geophysical model to ensure an accurate interpretation of any dispersive signature.

I have taken different theoretical strands from rock physics, AVO and spectral decomposition to determine how an integrated analysis of seismic data can aid in the identification and interpretation of amplitude anomalies that could, in principle, be due to hydrocarbon saturation. Recent rock physics experiments have led to the hypothesis that velocity dispersion can be present within the seismic bandwidth (Batzle *et al.*, 2001 and 2006). Frequency-dependent AVO theory has shown that velocity dispersion is sensitive to fluid saturation and will affect the P-wave more than the S-wave which is relatively insensitive to the pore fluid. The recent uptake of spectral decomposition methods in geophysics provided the relevant tools to link these theories and methods together to develop a frequency-dependent AVO approximation and inversion methodology.

Theory predicts fluid saturated formations can be frequency-dependent and I attempted to detect this on CMP gathers along two seismic lines from a marine

dataset. I investigated whether a standard reconnaissance AVO analysis and interpretation can be improved by integrating results from spectrally-decomposing the stacked sections. I observed six large amplitude events on the two lines and focused my analysis on these areas. Analysis of the CMP gathers showed these areas all to be Class III reflections. I made no distinction between Class II and III reflections as they both have negative intercept and gradients. I inverted the gathers using Shuey's two-term AVO approximation for intercept and gradient and combined them to further create Poisson's reflectivity and fluid factor sections. In the absence of well control my interpretation was based on qualitative deviations from a background trend that is assumed to brine saturated. I created crossplots of both intercept versus gradient and stacked amplitude and gradient to ensure that my sub-stacks were not artificial anomalies due to statistical correlation between the intercept and gradient. Three of the initial six areas had strong signatures differing from the background trend which indicated the anomaly was due to a change in fluid saturation. Frequency-dependent AVO theory predicts that Class I dispersive reflections are rich in high frequencies whilst Class III reflections are rich in low frequencies. It is important to make the distinction between an elastic and frequency-dependent reflection and I would only expect a spectral anomaly in the latter. I spectrally decomposed the stacked sections using both the continuous wavelet transform (CWT) and the matching pursuit method (MPM). I balanced the resultant iso-frequency sections using a shallow reflection that I assumed was elastic. The CWT had a relatively poorer signal-to-noise ratio than the MPM which also had an improved temporal resolution. This is a measure of the variance around an average time of the wavelet and results in a narrower spread of the decomposed energy. I attempted to describe the spectral behaviour of the six anomalous areas using the balanced iso-frequency sections. However, the change in amplitude with frequency was quite subtle and difficult to determine through direct observation. I created spectral difference sections using an arbitrary high and low-frequency panel to capture the frequency-dependence of the reflections. The three areas with the strong Class III AVO signature displayed strong low-frequency signatures whilst the other areas had weaker signatures. I tentatively interpreted three of the signatures as

frequency-dependent due to hydrocarbon saturation and the other three as simple elastic Class III reflections. In the absence of any well control or forward modelling I believe the reconnaissance AVO analysis has benefitted from integrating the results from the spectral decomposition. Where I have evidence that the Class III reflection is frequency-dependent then I have more confidence in the interpretation that the amplitude anomaly is the result of hydrocarbon saturation. Where the results are inconsistent with the frequency-dependent AVO theory, I suspect that the amplitude anomalies are a combination of changes in the local geology and fluid saturation.

I have tested and used both the CWT and MPM algorithms throughout this thesis. The improved temporal resolution of the MPM I described was essential as I propose detecting subtle frequency-dependent amplitude variations that can be masked by noisy artefacts created by the CWT. The MPM is, in essence, an improved and iterative wavelet transform that searches for the most suitable parameters to match time-frequency atoms from a dictionary to the seismic signal. The increased computational time is worth the improved resolution it achieved and I favour using the MPM over the CWT for future frequency-dependent AVO investigations.

I developed a frequency-dependent AVO approximation by considering velocity dispersion in the reflecting mediums. I had to assume that the velocity ratio within a medium was frequency-independent, otherwise my approximation would have been unconstrained. Whilst theory predicts that the S-wave velocity will have significantly less velocity dispersion I make no such assumption and the approximation provides a means by which P- and S-wave reflectivity dispersion can be calculated. The above statement comes with the caveat that S-wave reflectivity is difficult to quantify accurately without far offsets and most AVO approximations are valid for angles of incidence less than thirty degrees. When I compared the exact reflection coefficients against those estimated from my approximation I found that I was always overestimating the dispersion. This may be due to the simplification of the P- and S-wave velocity ratio or it may be an inherent feature of the original approximation which I extended.

I developed an inversion methodology using my frequency-dependent AVO approximation to quantitatively estimate reflectivity dispersion. It essentially adds another dimension to the well recognised elastic AVO inversion by considering frequency. The inversion is a two-step process. Firstly, the balanced spectrally-decomposed amplitudes are each inverted to obtain estimates of the frequency-dependent P- and S-wave reflectivities. Secondly, these reflectivities are used to calculate the P- and S-wave reflectivity dispersion around a reference frequency. I tested the inversion to check whether it was consistent over a broad offset range and determined that NMO stretch effects on the amplitude spectra at far offsets influenced the balancing and disrupted the inversion. To avoid this, I limited the input gathers to near offsets only and performed the NMO correction before spectral decomposition so that the stretch affects the spectral and not the raw traces. This effectively means that I am unable to obtain an accurate estimate of the S-wave reflectivities which contribute to the reflection coefficient at far offsets and am only reliably estimating the P-wave reflectivity dispersion. Since theory predicts shear waves to be relatively insensitive to fluid saturation and to have smaller velocity dispersion than the P-wave this is a sensible compromise.

I have created a range of elastic and dispersive synthetic gathers using a variety of parameters. By adjusting the relaxation parameter I am changing the frequency range of the dispersive transition zone from the low to the high frequency domain. When I adjust the crack density I am altering the ratio of ellipsoidal cracks and spherical pores in the model and changing the magnitude of the dispersion. The model makes no assumptions of the mechanisms causing the velocity dispersion but is a simple mathematical model to create a means of measuring the interactions between frequency-dependent materials. I inverted both Class I and Class III reflections and quantified the positive and negative reflectivity dispersion respectively. Class I dispersive reflections are rich in high frequencies whilst Class III dispersive reflections are rich in low frequencies. The inversion measures a linear change in the frequency-dependent reflectivities but the frequency-dependent reflection coefficient is non-linear in the high dispersion synthetics. Nevertheless, the inversion is able to

estimate the different magnitudes of the dispersion associated with varying crack densities. For similar fluid substitutions of gas in the Class III and Class I synthetics I measure different scales of dispersion. This is because the P-wave velocity dispersion is relative to the original, low frequency, elastic value. For example a change of $300ms^{-1}$ at $2300ms^{-1}$ equates to a 13% change, whilst it is only 6% at $5000ms^{-1}$. It is important to consider the elastic P-wave velocity when considering the magnitude of the dispersion.

I had to pay careful attention to tuning which can cause spectral anomalies similar to dispersion on seismic data. Reflections from the top and bottom of thin beds can interfere and the spectrum of the composite wavelet is distorted and can be mistaken for dispersion. I created a synthetic wedge-type model to evaluate the effect this interference has on my frequency-dependent inversion. I detected two types of tuning interference on my synthetic test data. There was the expected interference from the top and bottom reflections at 10m thickness but there was also interference of the CWT decomposed wavelets up to 250m thickness. The poor temporal resolution of the CWT and the large variance around the average time, along with noisy side lobes, means that even when the reflections from the top and bottom of the material are no longer interfering, the CWT decomposed wavelets are. The MPM has good temporal resolution and this is vital in separating the reflections from the top and bottom of a thin bed. The variance of the MPM decomposed wavelet is comparable to the original seismic wavelet. However, for both algorithms at 10m thickness the composite amplitude spectrum of the interfering wavelets is no longer strictly elastic and reflectivity dispersion was measured.

Finally, I must address the fact that I have only considered dispersive materials saturated with gas and not water; there is a two-fold argument for this. Theoretically, the dispersion associated with gas has been shown to be much larger than water due to its smaller bulk fluid modulus. Therefore, it has been my approach to consider the case with the largest magnitude of P-wave dispersion and I have successfully been able to invert for it. Secondly, I have only considered the relaxation parameter to

create my dispersive materials and have not considered arguments regarding fluid mobility and I have not adjusted the permeability or fluid viscosity. In water or brine-saturated formations the reflections are assumed to achieve pore pressure equalisation and be Gassmann consistent, which I have modelled with a small relaxation parameter.

8.2 Major conclusions from this thesis

8.2.1 Developing an integrated AVO and spectral analysis

Standard AVO analyses do not take into account any possible frequency-dependence of reflections due to velocity dispersion. I developed an integrated reconnaissance AVO and, using the spectral analysis of a marine seismic dataset, I combined the qualitative results from a classical elastic reconnaissance AVO analysis along with spectral difference plots and integrated the two separate interpretations. I found them to be consistent with frequency-dependent AVO theory and together they provided me with added confidence of my interpretation of six amplitude anomalies detected on the stacked sections. I believe that it can be of added value when performing initial amplitude analyses of seismic data to include spectral decomposition and to consider the use of fully frequency-dependent AVO when searching and monitoring hydrocarbon reservoirs as these may be associated with strong velocity dispersion.

8.2.2 New frequency-dependent AVO approximation

I have derived a frequency-dependent AVO approximation by considering P- and S-wave velocity dispersion. The AVO attributes of the approximation are new P- and S-wave terms which I have labelled reflectivity dispersion as they are measures of the frequency-dependence of the reflectivities. It is worth noting that, since spectral amplitudes are always positive and do not contain phase information like seismic data, the P-wave reflectivity dispersion will always be positive. This fact can be exploited to theoretically link the sign of the P-wave reflectivity dispersion to the AVO classification of the reflection. The approximation makes no assumptions as to

whether a layer is dispersive or elastic, only using the P- and S-wave velocities to describe the reflection coefficient. The accuracy of the approximation improves upon the current method whereby a single, frequency-independent, reflection coefficient is used to describe both elastic and dispersive boundaries.

8.2.3 Frequency-dependent AVO inversion methodology

I have incorporated my frequency-dependent AVO approximation into an inversion methodology using balanced spectral amplitudes rather than seismic amplitudes. The overprint of the source wavelet is removed by balancing the decomposed amplitudes using a weight function at a reference frequency and I determined that the peak frequency of the source wavelet was an appropriate choice. A bandwidth of frequencies is selected for the inversion that represents the central frequencies of the seismic data, minimising the size of the weight function that balances the spectral amplitudes. The weight function is designed on an offset-by-offset basis to retain the frequency-dependent AVO signature of the data which is otherwise lost. I created synthetic gathers with different levels of velocity dispersion by varying the relaxation parameter and crack density and have been able to quantitatively measure the P-wave reflectivity dispersion. I have shown how the sign of the inverted P-wave reflectivity dispersion correctly corresponds to the AVO classification of the frequency-dependent reflection.

8.2.4 Factors to consider when inverting for P-wave reflectivity dispersion

I found that the NMO stretch of the amplitude spectra at far offsets prejudices the weight function by amplifying the low frequencies in the elastic reflection used to balance the spectral amplitudes. The true dispersive signature on offset-limited synthetics can be overwhelmed by this and the spectral-ratio shows how the NMO stretch increases with offset. Where NMO stretch can often be muted or ignored for stacking or AVO analyses I rely on accurately measuring the true spectra from reflected wavelets. I found that using only the near offset traces and following an

adjusted processing flow minimised these errors and generated a more accurate measurement of the P-wave reflectivity dispersion.

8.2.5 Impact of the spectral decomposition method

Throughout this thesis I have used a windowing and non-windowing spectral decomposition algorithm; the continuous wavelet transform (CWT) and the matching pursuit method (MPM). Both were able to provide accurate estimates of the decomposed amplitudes but the windowing of the CWT resulted in poor temporal variance around the average time, introducing noisy artefacts. The MPM is a more flexible decomposition and has excellent temporal and frequency resolution. This improves the accuracy of the frequency-dependence AVO inversion and the inverted reflectivities and reflectivity dispersion closely correspond to events on the input seismic and do not introduce artificial signals.

8.3 Future work recommendations

8.3.1 Improving robustness for P-wave reflectivity dispersion

This work has shown the potential to invert standard seismic gathers for P-wave dispersion from only the near-offset traces. Work should be done to improve the robustness of the inversion to compensate for outliers in the spectrally-decomposed data. Where Hampson-Russell uses a multi-taper approach to minimise the effect of outliers in their AVO inversion, a similar approach should be investigated to reduce the effect of improperly balanced input data and to improve the overall reliability of the inversion. It is important to test the use of non-stretch NMO corrections to flatten CMP gathers and to investigate whether the use of further offsets, which I discarded, improves the inversion.

8.3.2 Real data applications

The application of my frequency-dependent AVO inversion has been restricted to synthetic data examples and would benefit from testing on real data. My approach

benefits from the use of widely available P-wave reflection CMP gathers and the main extra computational cost arises in performing the spectral decomposition. I believe this technique could be used in 4-D, time-lapse, surveys to help detect subtle changes in spectra due to swept fluid during reservoir production and to help in the process of reservoir characterisation.

8.3.3 Frequency-dependent anisotropy

In my investigations I have considered isotropic layers saturated with gas. I have not considered the relaxation mechanisms and interactions between fractures and cracks and the saturating fluid. P-wave attenuation anisotropy is a widely studied area and it is important to investigate and understand how azimuthal anisotropy, associated with fracture orientation and fluid saturation, affect the frequency-dependent AVO inversion and measured reflectivity dispersion.

References

Aki, K. and Richards, P.G., 1980. *Quantitative Seismology*. W.H. Freeman and Co.

Anderson, C.F. and van Wijngaarden, A-J., 2007. Interpretation of 4D inversion results using rock physics templates and virtual reality visualization, North Sea examples. Presented at **77th Ann. Internat. Mtg., Soc. Expl. Geophys.,** Expanded Abstracts, 2934-2938.

Avseth, P., Mukerji, T. and Mavko, G., 2005. *Quantitative Seismic Interpretation*. Cambridge University Press.

Barnes, A.E., 1992. Another look at NMO stretch. *Geophysics*, **57**, 749-751.

Batzle, M., Hofmann, R., Han, D-H. and Castagna, J.P., 2001. Fluids and frequency dependent seismic velocity of rocks. *The Leading Edge*, **20**, 168-171.

Batzle, M.L., Han, D-H. and Hofmann, R., 2006. Fluid mobility and frequency-dependent seismic velocity – Direct measurements. *Geophysics*, **71**, N1-N9.

Biot, M.A., 1956a. Theory of propagation of elastic waves in a fluid saturated porous solid. I. Low-frequency range. *Journal of the Acoustical Society of America*, **28**, 168-178.

— 1956b. Theory of propagation of elastic waves in a fluid saturated porous solid. II. Higher-frequency range. *Journal of the Acoustical Society of America*, **28**, 179-191.

Boyd-Gorst, J., Fail, P. and Pointing, L., 2001. 4-D time lapse reservoir monitoring of Nelson Field, Central North Sea: Successful use of an integrated rock physics model to predict and track reservoir production. *The Leading Edge*, **20**, 1336-1350.

Brown, R.L., 2009. Anomalous dispersion due to hydrocarbons: The secret of reservoir geophysics? *The Leading Edge*, **28**, 420-425.

Burnett, M.D., Castagna, J.P., Méndez-Hernández, E., Rodríguez, G.Z., García, L.F., Vázquez, J.T.M., Avilés, M.T. and Villaseñor, R.V., 2003. Application of spectral decomposition to gas basins in Mexico. *The Leading Edge*, **22**, 1130-1134.

Cambois, G., 2000. Can P-wave AVO be quantitative? *The Leading Edge*, **19**, 1246-1251.

Castagna, J.P., Batzle, M.L. and Eastwood, R.L., 1985. Relationships between compressional-wave and shear-wave velocities in clastic silicate rocks. *Geophysics*, **50**, 571-581.

Castagna, J.P. and Swan, H.W., 1997. Principles of AVO crossplotting. *The Leading Edge*, **16**.

Castagna, J.P., Swan, H.W. and Foster, D.J., 1998. Framework for AVO gradient and intercept interpretation. *Geophysics*, **63**, 948-956.

Castagna, J.P., Sun, S. and Siegfried, R.W., 2003. Instantaneous spectral analysis: Detection of low-frequency shadows associated with hydrocarbons. *The Leading Edge*, **22**, 120-127.

Castagna, J.P. and Sun, S., 2006. Comparison of spectral decomposition methods. *First Break*, **24**, 75-79.

Castle, R.J., 1994. A theory of normal moveout. *Geophysics*, **59**, 983-999.

Chakraborty, A. and Okaya, D., 1995. Frequency-time decomposition of seismic data using wavelet-based methods. *Geophysics*, **60**, 1906-1916.

Chapman, M., 2001a. The dynamic fluid substitution problem. Presented at **71st Ann. Internat. Mtg., Soc. Expl. Geophys.,** Expanded Abstracts, 1708-1711.

Champan, M., 2001b. Modelling the wide-band laboratory response of rock samples to fluid and pressure changes. *PhD Thesis*, **The University of Edinburgh**.

Chapman, M., Zatsepin, S.V. and Crampin, S., 2002. Derivation of a microstructural poroelastic model. *Geophysical Journal International*, **151**, 427-451.

Chapman, M., 2003. Frequency-dependent anisotropy due to meso-scale fractures in the presence of equant porosity. *Geophysical Prospecting*, **51**, 369-379.

Chaoman, M., Maultzsch, S. and Liu, E., 2003. Some estimates of the squirt-flow frequency. Presented at **73rd Ann. Internat. Mtg., Soc. Expl. Geophys.,** Expanded Abstracts, 1290-1293.

Chapman, M., Liu, E. and Li, X.Y., 2005. The influence of abnormally high reservoir attenuation on the AVO signature. *The Leading Edge*, **24**, 1120-1125.

— 2006. The influence of fluid-sensitive dispersion and attenuation on AVO analysis. *Geophysical Journal International*, **167**, 89-105.

Chui, C., 1992. *An introduction to wavelets*. American academic press.

Dahl, T. and Ursin, B., 1991. Parameter estimation in a one-dimensional anelastic medium. *Journal of Geophysical Research*, **96**, 20217-20233.

Dasgupta, R. and Clark, R..A., 1998. Estimation of *Q* from surface seismic reflection data. *Geophysics*, **63**, 2120-2128.

Dunkin, J.W. and Levin, F.K., 1973. Effect of normal moveout on a seismic pulse. *Geophysics*, **38**, 635-642.

Dvorkin, J., Mavko, G. and Nur, A., 1995. Squirt flow in fully saturated rocks. *Geophysics*, **60**, 97-107.

Ebrom, D., 2004. The low-frequency gas shadow on seismic sections. *The Leading Edge*, **23**, 772.

Endres, A.L. and Knight, R.J., 1997. Incorporating pore geometry and fluid pressure communication into modeling the elastic behaviour of porous rocks. *Geophysics*, **62**, 106-117.

Fatti, J.L., Smith, G.C., Vail, P.J., Strauss, P.J. and Levitt, R., 1994. Detection of gas in sandstone reservoirs using AVO analysis: A 3-D seismic case history using the Geostack technique. *Geophysics*, **59**, 1362-1376.

Foster, D.J. and Reilly, J.M., 1997. Another perspective on AVO crossplotting. *The Leading Edge,* **16**.

Gardner, G.H.F., Gardner, G.L. and Gregory, A.R., 1974. Formation velocity and density – The diagnostic basics for stratigraphic traps. *Geophysics*, **39**, 770-780.

Goloshubin, G., VanSchuyver, C., Korneev, V., Silin, D. and Vingalov, V., 2006. Reservoir imaging using low frequencies of seismic reflections. *The Leading Edge*, **25**, 527-531.

Goodway, B., Chen, T. and Downton, J., 1997. Improved AVO fluid detection and lithology discrimination using Lamé petrophysical parameters; "$\lambda\rho$", "$\mu\rho$" and "λ/μ fluid stack", from P and S inversions. Presented at **67th Ann. Internat. Mtg., Soc. Expl. Geophys.,** Expanded Abstracts, 183-186.

Gouveia, W.P., Johnston, D.H., Solberg, A. and Lauritzen, M., 2004. Jotun 4D: Characterization of fluid movement from time-lapse seismic and production logging tool data. *The Leading Edge*, **23**, 1187-1194.

Hampson-Russell Software Services Ltd., 2004. AVO Theory.

Hilterman, F.J., 2001. *Seismic Amplitude Interpretation*. No. 4 in Distinguished Instructor Series, Soc. of Expl. Geophys.

Hofmann, R., Batzle, M., Duranti, L. and Han, D-H., 2005. Frequency dependent velocities: Mechanisms and implications. *Proceedings, Rainbow in the Earth – 2nd International Workshop*.

Hudson, J.A., Liu, E. and Crampin, S., 1996. The mechanical properties of material with interconnected cracks and pores. *Geophysical Journal International*, **124**, 105-112.

Jain, K.C. and deFigueiredo, R.J.P., 1982. *Concepts and techniques in oil and gas exploration*. Society of Exploration Geophysicists.

Jones, T.D., 1986. Pore fluids and frequency-dependent wave propagation in rocks. *Geophysics*, **51**, 1939-1953.

Klimentos, T. and McCann, C., 1988. Why is the Biot slow compressional wave no observed in real rocks? *Geophysics*, **53**, 1605-1609.

Korneev, V.A., Goloshubin, G.M., Daley, T.M. and Silin, D.B., 2004. Seismic low-frequency effects in monitoring fluid-saturated reservoirs. *Geophysics*, **69**, 522-532.

Liner, C.L., 1999. *Elements of 3D seismology*. PennWell.

Liu, E. and Chapman, M., 2006. A practical guide to time-frequency representation and spectral decomposition methods. *EAP Report*, Volume **13**, C1 1-43.

Mallat, S., 1998.*A wavelet tour of signal processing*. Academic Press, 2nd edn.

Mallat, S. and Zhang, Z., 1993. Matching pursuits with time-frequency dictionaries. *IEEE Transactions on Signal Processing*, **41**, 2297-3415.

Mallick, S. and Frazer, L.N., 1990. Computation of synthetic seismograms for stratified azimuthally anisotropic media. *Journal of Geophysical Research*, **95**, 8513-8526.

Marfurt, K.J. and Kirlin, R.L., 2001. Narrow-band spectral analysis and thin-bed tuning. *Geophysics*, **66**, 1274-1283.

Marion, D., Mukerji, T. and Mavko, G., 1994. Scale effects on velocity dispersion: From ray to effective medium theories in stratified media. *Geophysics*, **59**, 1613-1619.

Martinez, R.D., 1993. Wave propagation effects on amplitude variation with offset measurements: A modelling study. *Geophysics*, **58**, 534-543.

Maultzsch, S., Chapman, M., Liu, E. and Li, X.Y., 2003. Modelling frequency-dependent seismic anisotropy in fluid-saturated rock with aligned fractures: implication of fracture size estimation from anisotropic measurements. *Geophysical Prospecting*, **51**, 381-392.

Maultzsch, S., 2005. *Analysis of Frequency-Dependent Anisotropy in VSP Data*. Ph.D. thesis, University of Edinburgh

Mavko, G. and Jizba, D., 1991. Estimating grain-scale fluid effects on velocity dispersion in rocks. *Geophysics*, **56**, 1940-1949.

Mavko, G., Mukerji, T. and Dvorkin, J., 1998. *The Rock Physics Handbook*. Cambridge University Press.

Newman, P., 1973. Divergence effects in a layered earth. *Geophysics*, **38**, 481-488.

Odebeatu, E., Zhang, J., Chapman, M., Liu, E. and Li, X.Y., 2006. Application of spectral decomposition to detection of dispersion anomalies associated with gas saturation. *The Leading Edge*, **25**, 206-210.

Ostrander, W.J., 1989. Plane-wave reflection coefficients for gas sands at nonnormal angles of incidence. *Geophysics*, **49**, 1637-1648.

Partyka, G., Gridley, J. and Lopez, J., 1999. Interpretational applications of spectral decomposition in reservoir characterization. *The Leading Edge*, **18**, 353-360.

Payne, S.S., Worthington, M.H., Odling, N.E. and West, L.J., 2007. Estimating permeability from field measurements of seismic attenuation in fractured chalk. *Geophysical Prospecting*, **55**, 643-653.

Perroud, H. and Tygel, M., 2004. Nonstretch NMO. *Geophysics*, **69**, 599-607.

Rathore, J.S., Fjaer, E., Holt, R.M. and Renlie, L., 1995. P- and S-wave anisotropy of a synthetic sandstone with controlled crack geometry. *Geophysical Prospecting*, **43**, 711-728.

Ross, C.P., 2000. Effective AVO crossplot modeling: A tutorial. *Geophysics*, **65**, 700-711.

Processing Report, 2004. Marathon Oil Company.

Rutherford, S.R. and Williams, R.H., 1989. Amplitude-versus-offset variations in gas sands. *Geophysics*, **54**, 680-688.

Sbar, M.L., 2000. Exploration risk reduction: An AVO analysis in the offshore Middle Miocene, Central Gulf of Mexico. *The Leading Edge*, **20**, 20-27.

Sheriff, R.E. and Geldart, L.P., 1995. *Exploration Seismology*. Cambridge University Press

Shuey, R.T., 1985. A simplification of the Zoeppritz equations. *Geophysics*, **50**, 609-614.

Sinha, S., Routh, P.S., Anno, P.D. and Castagna, J.P., 2005. Spectral decomposition of seismic data with continuous-wavelet transform. *Geophysics*, **70**, 19-25.

Smith, G.C. and Gidlow, P.M., 1987. Weighted stacking for rock property estimation and detection of gas. *Geophysical Prospecting*, **35**, 993-1014.

Smith, T.M. and Sondergeld, C.H., 2001. Examination of AVO responses in the eastern deepwater Gulf of Mexico. *Geophysics*, **66**, 1864-1876.

Smith, T.M., Sondergeld, C.H. and Rai, C.S., 2003. Gassman fluid substitutions: A tutorial. *Geophysics*, **68**, 430-440.

Smith, M., Gerhardt, A., Mee, B., Ridsdill-Smith, T., Wulff, A. and Bourdon, L., 2008. The benefits of early 4D seismic monitoring to understand production related effects at Enfield, North West Shelf, Australia. Presented at **78th Ann. Internat. Mtg., Soc. Expl. Geophys.,** Expanded Abstracts, 3159-3163.

Sothcott, J., McCann, C. and O'Hara, S.G., 2000. The influence of two different pore fluids on the acoustic properties of reservoir sandstones at sonic and ultrasonic frequencies. Presented at **70th Ann. Internat. Mtg., Soc. Expl. Geophys.,** Expanded Abstracts, 1883-1886.

Stockwell, R.G., Mansinha, L. and Lowe, R.P., 1996. Localization of the complex spectrum: The S transform. *IEEE Transactions on Signal Processing*, **44**, 998-1001.

Stolt, R.H. and Weglein A.B., 1985. Migration and inversion of seismic data, *Geophysics*, **50**, 2458-2472.

Taner, M.T., Koehler, F. and Sheriff, R.E., 1979. Complex trace analysis. *Geophysics*, **44**, 1041-1063.

Taylor, D.B., 1990. *The ANISEIS manual*, Macroc Ltd., Edinburgh, UK.

Tillotson, P., Chapman, M., Best, A.I., Sothcott, J., McCann, C., Shangxu, W. and Li, X-Y., 2010. Observations of fluid-dependent shear-wave splitting in synthetic porous rocks with penny-shaped fractures. *Geophysical Prospecting*. **IN PRESS**.

Tipler, P.A., 1999. Physics for scientists and engineers. W.H. Freeman and Company, 4th edn.

Tonn, R., 1991. The determination of the seismic quality factor Q from VSP data: A comparison of different computational methods 1.*Geophysical Prospecting*, **39**, 1-27.

Torrence, C. and Compo, G.P., 1998. A practical guide to wavelet analysis. *Bulletin of the American Meteorological Society*, **79**, 61-78.

Tura, A., Etuk, U. and Udo, S., 2006. Using time-lapse seismic for field development at Nembe Creek, Nigeria. *The Leading Edge*, **25**, 1142-1149.

Verm, R. and Hilterman, F., 1995. Lithology color-coded seismic sections: The calibration of AVO crossplotting to rock properties. *The Leading Edge*, **14**, 847-853.

Wang, Y., 2007. Seismic time-frequency spectral decomposition by matching pursuit. *Geophysics*, **72**, V13-V20.

Wang, Z., 2001. Fundamentals of seismic rock physics. *Geophysics*, **66**, 398-412.

Wiggins, R., Kenny, G.S. and McClure, C.D. 1984. *A method for determining and displaying the shear-wave reflectivities of a geologic formation*. European patent application 0113944 (Mobil Oil Company).

Winkler, K.W., 1986. Estimates of velocity dispersion between seismic and ultrasonic frequencies. *Geophysics*, **51**, 183-189.

Yilmaz, Ö., 1999. *Seismic data processing, investigations in geophysics No. 2*. Society of Exploration Geophysicists.

Young, R.A. and LoPiccolo, R.D., 2003. A comprehensive AVO classification. *The Leading Edge*, **22**, 1030-1037.

Zhang, J., 2008. *Joint PP and PS Wave Analysis for Lithology and Fluid Prediction*. Ph.D. thesis, University of Edinburgh

Zhang, T., Li, X.Y. and Chapman, M., 2008. Estimating frequency-dependent seismic attributes by matching pursuit: a case study. In *78th Internat. Mtg*., Expanded Abstracts, Soc. Expl. Geophys., 3023-3027.

Use of frequency dependent AVO inversion to estimate P-wave dispersion properties from reflection data

Authors

A. Wilson, M. Chapman and X-Y. Li, British Geological Survey

Summary

It has recently been suggested that fluid-sensitive dispersion can give rise to a frequency-dependent AVO response, and that the ability to detect such an effect could in principle help us to detect hydrocarbons. In this paper we develop an algorithm which allows us to estimate P-wave dispersion properties from reflection data. We begin by performing spectral decomposition on our pre-stack data, and perform balancing to remove the overprint of the wavelet. Under the assumption that the impedance contrast is a function of frequency, we develop a linearised AVO approximation for the frequency-dependent case. A Smith-Gidlow style inversion applied to the spectrally decomposed data allows us in principle to recover the variation of impedance contrast with frequency. We test the method on synthetic data, produced from both elastic and dispersive modelling, and find we can recover information on the dispersion properties. We feel our method may complement attempts to measure seismic attenuation from reflection data.

Introduction

In this paper we have developed an algorithm for detecting spectral anomalies that are often associated with hydrocarbons via inversion of iso-frequency data. The goal of the study is to be able to quantitatively infer P-wave dispersion properties from analysis of reflection data. Such an analysis will complement efforts to measure attenuation from reflection data.

The advances in the application of spectral decomposition in reservoir characterisation since Partyka et al. (1999) have led to many recorded examples of spectral anomalies in seismic data. Many of these are linked to hydrocarbon reservoirs; Castagna et al. (2003) showed examples of low-frequency shadows using instantaneous spectral analysis. Chapman et al. (2006) showed how equivalent medium theory can model large levels of attenuation and dispersion in hydrocarbon saturated rocks and showed how this gave rise to a frequency-dependent AVO response. Much work utilising spectral decomposition as a fluid indicator has been rather qualitative and there has yet to be a quantitative assessment of frequency-dependent AVO.

This paper shows how a frequency-dependent AVO analysis can be applied to reflection data. We have developed a new workflow to invert the data for a quantitative measure of dispersion. Our method is a generalisation of the Smith and Gidlow (1987) inversion scheme to multiple frequencies. We have tested our method on synthetic data calculated using both elastic and dispersive models. Our study suggests that information on dispersion properties can be recovered from the data, and this offers a promising method to detect areas of hydrocarbon saturation.

Theory

We extend the two-term Smith and Gidlow (1987) $\grave{P}\acute{P}$ approximation to include frequency-dependence. When we do this we make no assumption on either the P- or S-wave dispersion, despite theoretical prediction that the S-wave dispersion will be much less than for the P-wave dispersion (as in Chapman et al. (2006)). We take the original approximation, as shown in equation (1):

$$R(\theta_i) = A(\theta_i)\frac{\Delta\alpha}{\alpha} + B(\theta_i)\frac{\Delta\beta}{\beta} \tag{1}$$

and extend it to include frequency dependence, as shown in equation (2):

$$R(\theta_i, f_j) = A(\theta_i)\left(\frac{\Delta\alpha}{\alpha}\right)_{f_1} + (f_j - f_1)A(\theta_i)I_\alpha + B(\theta_i)\left(\frac{\Delta\beta}{\beta}\right)_{f_1} + (f_j - f_1)B(\theta_i)I_\beta \tag{2}$$

where $I_\alpha = \frac{d}{df}\left(\frac{\Delta\alpha}{\alpha}\right)$ and $I_\beta = \frac{d}{df}\left(\frac{\Delta\beta}{\beta}\right)$. In standard AVO, $A(\theta_i) = \frac{5}{8} - \frac{1}{2}\left(\frac{v_s^2}{v_p^2}\right)sin^2\theta_i + \frac{1}{2}tan^2\theta_i$ and $B(\theta_i) = -4\left(\frac{v_s^2}{v_p^2}\right)sin^2\theta_i$ are offset dependent variables that approximate the reflection amplitude on the seismic trace. In our case we are not using seismic amplitudes but iso-frequency amplitudes, in order to be compare amplitudes at different frequencies the traces must be balanced. We use multiple frequencies so a gather decomposed at frequency = f_j, $R(\theta_i, f_j)$ describes the iso-frequency amplitudes after balancing that are approximated in equation (2).

The amplitudes on the iso-frequency gathers are balanced on an offset-by-offset basis from a shallow, elastic-elastic interface. We scale the maximum values for the elastic reflection on the iso-frequency gathers to the amplitude of the 40Hz trace (we used a 40Hz ricker wavelet

as our source). Figure 1 shows the unbalanced (a) and the balanced (b) first traces from the iso-frequency gathers (10, 20, 25, 30, 40, 60 and 80Hz) produced from the elastic synthetic. The shallow elastic reflection at ~0.73s is mathematically balanced in 1b) and this process automatically balances the deeper, elastic, reflection at ~0.85s. It is only after balancing the iso-frequency traces that a comparison of the amplitudes along with the inversion can be carried out.

When we are inverting for dispersion we do not need to input the seismic amplitudes, only the balanced iso-frequency traces. The exact densities, P- and S-wave layer velocities are also input into the inversion. To calculate the angle of incidence we use a straight ray approximation rather than calculate the exact angles through ray-tracing. The small offsets are such that the differences between the exact answer and the approximation are small.

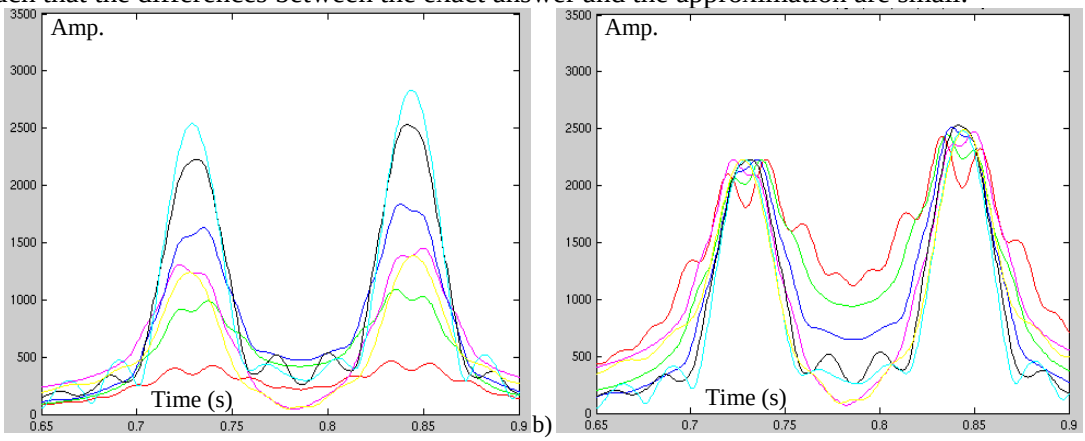

Figure 1: *a) The unbalanced iso-frequency first traces (red-10, green-20, magenta-25, blue-30, black-40, cyan-60 and yellow-80Hz) from the elastic, three-layer, synthetic. b) After balancing the first reflection, the deeper reflection has also been balanced.*

Example: 1D Synthetic Surface Seismic

We have created two, three-layer, synthetic gathers using a commercially available reflection code (Aniseis) that allows the use of fluid-sensitive frequency-dependent velocities in the model building. Each synthetic gather had traces at offsets 0, 150 and 300m, limiting the potential for NMO stretch in our spectra. The top-two layers are elastic and it is this top reflection that is used in the balancing described above. The bottom half-space was elastic in one synthetic and dispersive in the other; this is achieved by changing a time-scale parameter τ according to Chapman et al. (2006). In the dispersive half-space, the P-wave velocity increases with frequency within the seismic bandwidth. This results in lager reflection coefficients at increasing frequency as we go from a low to a high impedance medium (Class I). We see this effect on figure 2b). The unbalanced and balanced dispersive iso-frequency first-traces are shown in figure 2. The influence of dispersion is clearly visible in 2b) after balancing has been carried out. The low frequency (10Hz) red line in figure 2b) lies at approximately the same magnitude as in figure 1b) and the dispersion has increased the amplitudes of the reflection coefficient at higher frequencies.

We used a wavelet transform with a Gaussian wavelet to carry out the spectral decomposition. It offers a good balance between computing time and amplitude resolution but does unfortunately have relatively poor temporal resolution. There is significant 'false' energy, noise, introduced in figure 1 and 2 between the two reflections and is worst at the lower frequencies.

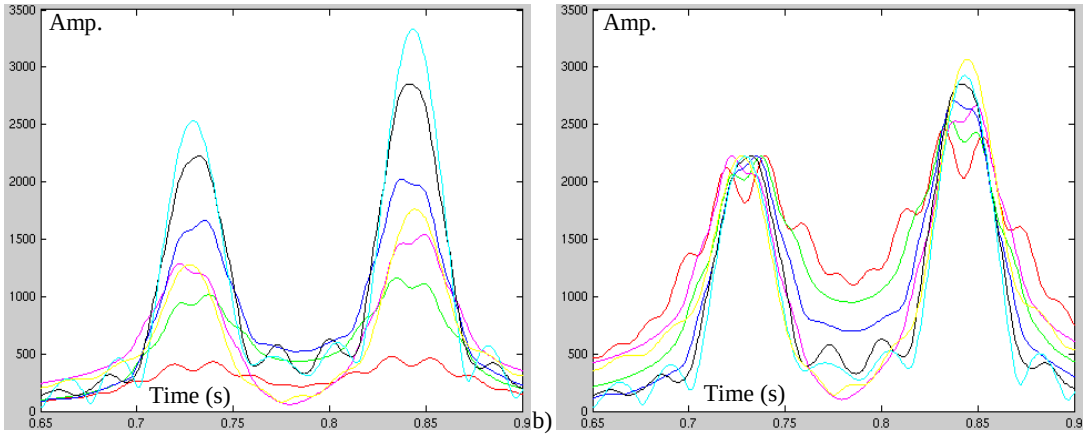

a) b)

Figure 2: *a) The unbalanced iso-frequency first traces (red-10, green-20, magenta-25, blue-30, black-40, cyan-60 and yellow-80Hz) from the dispersive synthetic. b) After balancing the first reflection has been balanced and the second reflection shows the dispersion with the higher frequencies having the highest amplitudes in agreement with theory.*

Results

We have calculated the spectral ratio for all offsets on both synthetics (figure 3 shows the first-trace ratios) as another interpretational step. For the elastic case, figure 3a), we obtain a flat, straight line over ~15-95Hz; in agreement with theory. For the dispersive case, figure 3b), we again have a straight line over the same bandwidth as before but with a positive gradient. This is due to the dispersive half-space at the reflecting boundary; the frequency-dependent reflection coefficient has boosted the amplitudes at higher frequencies affecting the spectral ratio. There is no attenuation in the dispersive case since the seismic wave doesn't propagate through the dispersive layer, this is an instantaneous effect related to the frequency-dependent AVO.

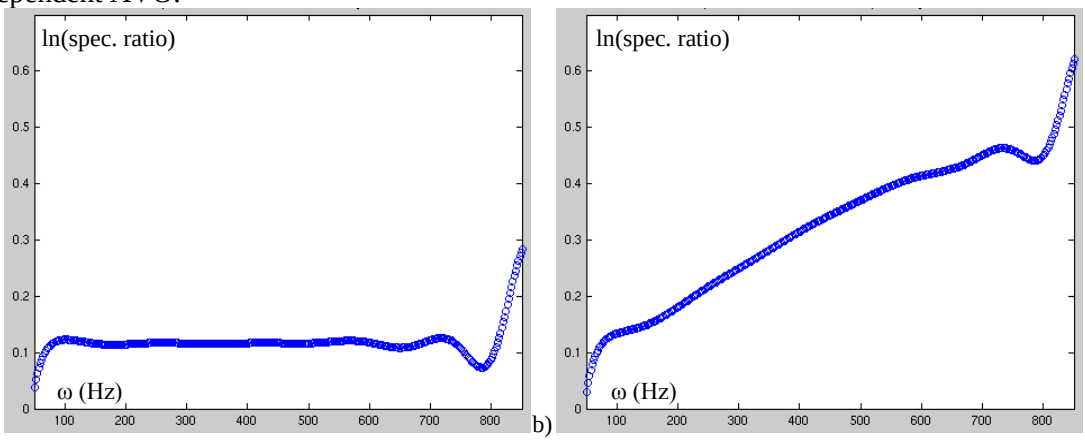

a) b)

Figure 3: *Spectral ratio of the first trace from the elastic (a) and dispersive (b) synthetic. In the elastic case the ratio is flat whilst in the dispersive case the gradient is positive (indicating a negative Q) that is a result of the increasing reflection coefficient with greater frequency.*

After examination of the balanced iso-frequency data (see figures 1 and 2) both synthetics were inverted using the frequencies 25, 30, 40, 60 and 80Hz. These two lowest frequencies (10 and 20Hz) were not included in the inversion because they were deemed to be under an acceptable threshold. This output from the elastic case is our null signature that we compare the dispersive output to. In figure 4b) the second peak at ~0.85s is larger than the peak at the elastic reflection at ~0.73s.

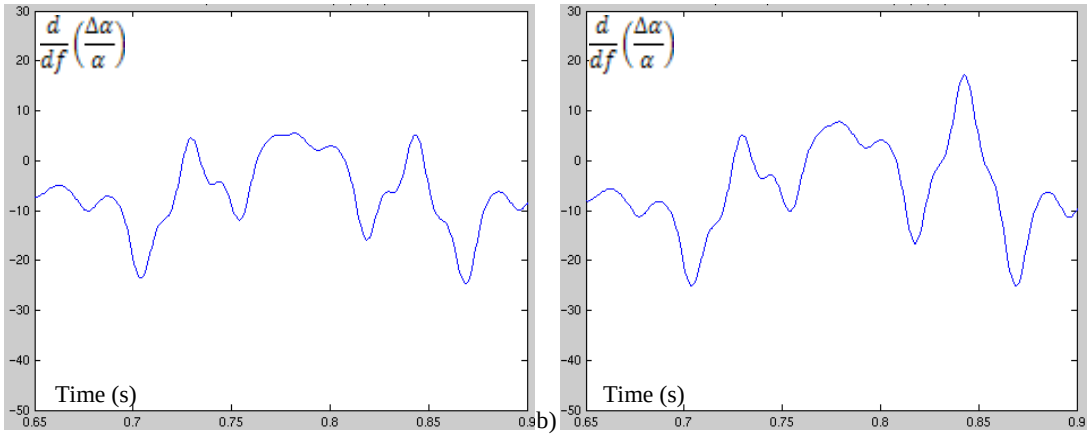

Figure 4: $\frac{d}{df}\left(\frac{\Delta\alpha}{\alpha}\right)$ *for the elastic (a) and the dispersive (b) synthetics using frequencies 25, 30, 40, 60 and 80Hz.*

Conclusions

We have developed an algorithm that extends Smith and Gidlow's (1987) two-term $\dot{P}\dot{P}$ approximation to the frequency-dependent case and have been able to invert for P-wave dispersion properties. Such dispersion anomalies can be due to hydrocarbon saturation. We have tested our algorithm and workflow on two synthetic data sets. The first dataset was created with elastic modelling whilst for the second dataset we included dispersion in the calculation. We have been able to detect a clear difference in signatures between the two cases. We believe this approach offers a novel approach to utilising spectrally decomposed data and can be incorporated in a fully frequency-dependent AVO analysis of seismic data. Whereas in standard AVO analysis multiple, and long, offsets are preferred we can invert for the frequency response, in principle with only one offset. Multiple offsets can stabilise the inversion but could introduce NMO stretch effects at longer offsets. We believe this approach can be a useful tool in hydrocarbon exploration as it can be used on seismic datasets to identify areas of dispersion that are commonly related to oil and gas deposits.

Acknowledgements

We are grateful to the EAP sponsors and the BUFI for supporting A. Wilson's PhD.

References

Castagna, J.P., Sun, S. and Siegfried, R.W., 2003. Instantaneous spectral analysis: Detection of low-frequency shadows associated with hydrocarbons. The Leading Edge, **22**, 120-127.

Chapman, M., Liu, E. and Li, X-Y., 2006. The influence of fluid-sensitive dispersion and attenuation on AVO analysis. Geophysical Journal International, **167**, 89-105.

Partyka, G., Gridley, J. and Lopez, J., 1999. Interpretational applications of spectral decomposition in reservoir characterization. The Leading Edge, **18**, 353-360.

Smith. G.C. and Gidlow, P.M., 1987. Weighted stacking for rock property estimation and detections of gas. Geophysical Prospecting, **35**, 993-1014.

Frequency-dependent AVO inversion

Adam Wilson, Mark Chapman and Xiang-Yang Li Edinburgh Anisotropy Project, British Geological Survey.*

Summary

It has been suggested that seismic velocities can be frequency-dependent, especially in hydrocarbon bearing rocks. Such velocity dispersion may prove useful as a fluid indicator if it can be measured directly. Following the assumptions of recent modeling studies, we consider reflections from a layer which exhibits velocity dispersion, so that the reflection coefficient can vary with frequency. We present a new technique which allows the frequency-dependence of the impedance contrasts to be determined from the reflection data. The method makes use of spectral decomposition and is essentially an extension of the Smith and Gidlow inversion technique to the multi-frequency case. Testing on synthetic data reveals that the method can be used to reliably infer dispersion properties. We hope that our developments may prove useful for the problem of fluid discrimination.

Introduction

Gassmann's formulae have provided a solid approach to the fluid-substitution problem. More recently, it has been realized that the Gassmann formulae are strictly valid only at very low frequency. For higher frequencies velocity dispersion can occur, and appears to be controlled by the fluid mobility (Batzle et al., 2006), defined as the ratio of permeability to fluid viscosity. It also appears possible that in some cases such dispersion may be an issue in the seismic frequency band.

The use of velocity dispersion as a fluid indicator is an attractive direction for research, but the robust detection of the effect has proven elusive.

In a modeling study, Chapman et al. (2005) considered the case of reflection from a layer with frequency-dependent properties overlain by a layer with frequency-independent velocities. It was shown that the most striking impact of the velocity dispersion came through the frequency-dependence of the reflection coefficient. The nature of the effect was strongly impacted by the AVO properties of the interface. For reflections from a class I interface the velocity dispersion gave rise to a reflection which was rich in high frequencies, while for a class III interface the low frequencies of the reflection were preferentially boosted. The analysis suggested that the frequency-dependence of AVO might be used to study the velocity dispersion.

In this paper we present a technique which allows the frequency-dependence of P- and S-wave impedance to be inferred from reflection data. The method extends the technique of Smith and Gidlow (1987) to the consideration of multiple frequencies, and relies on a spectral decomposition and balancing procedure. Numerical tests validate the method. We hope that the ability to detect the frequency-dependence of impedance may help us to discriminate fluids.

Theory

Following the approximations of Smith and Gidlow (1987), we consider that the reflection coefficient R can be written as:

$$R(\theta) = A(\theta)\frac{\Delta\alpha}{\alpha} + B(\theta)\frac{\Delta\beta}{\beta},$$

in which θ is the angle of incidence and the coefficients A and B can be given in terms of the velocities.

Following the arguments of Chapman et al. (2005), we now assume that due to the difference in dispersion properties on each side of the interface the reflection coefficient can vary with frequency. Specifically, we will allow the P- and S-wave impedances to vary with frequency:

$$R(\theta, f) = A(\theta)\frac{\Delta\alpha}{\alpha}(f) + B(\theta)\frac{\Delta\beta}{\beta}(f).$$

Since we expect to deal with rather narrow frequency-bands in our seismic data we will further assume that the frequency-variation of the impedance contrasts can be expanded as a Taylor series around a representative frequency f_0:

$$R(\theta, f) = A(\theta)\frac{\Delta\alpha}{\alpha}(f_0) + (f - f_0)A(\theta)I_a +$$

$$B(\theta)\frac{\Delta\beta}{\beta}(f_0) + (f - f_0)B(\theta)I_b$$

where we have introduced notation for the derivatives of impedance with respect to frequency evaluated at f_0:

Frequency-dependent AVO inversion

$$I_a = \frac{d}{df}(\frac{\Delta\alpha}{\alpha}); I_b = \frac{d}{df}(\frac{\Delta\beta}{\beta}) .$$

We now demonstrate how it is possible to obtain these derivatives of impedance from seismic reflection data.

Consider a typical AVO gather with n receivers denoted as a data matrix D(t, n). We assume that we have knowledge of the velocity model so that we can calculate the coefficients A and B through ray tracing and make the replacement:

$$A(\theta) = A_n(t); B(\theta) = B_n(t)$$

Following the techniques presented by Castagna et al. (2003) we can perform spectral decomposition on our data matrix, giving a representation:

$$D(t,n) \leftrightarrow S(t,n,f) .$$

In AVO analysis, we usually assume that the recorded amplitudes can be associated with the reflection coefficients through a simple transformation. The amplitudes in S, however, contain the overprint of the wavelet, so we must perform spectral balancing to remove this effect with a suitable weight function w:

$$B(t,n,f) = S(t,n,f)w(f) .$$

We now have the relation:

$$\begin{bmatrix} B(t,1,f_0) \\ \vdots \\ B(t,n,f_0) \end{bmatrix} = \begin{bmatrix} A_1(t) & B_1(t) \\ \vdots & \vdots \\ A_n(t) & B_n(t) \end{bmatrix} \begin{bmatrix} \frac{\Delta\alpha}{\alpha}(t,f_0) \\ \frac{\Delta\beta}{\beta}(t,f_0) \end{bmatrix}$$

and the P- and and S-wave impedances at f0 can be obtained at each time sample by least squares inversion.

Let us consider m+1 frequencies, and define the column vector a with (mn) rows as:

$$\begin{bmatrix} B(t,1,f_1) - A_1(t)\frac{\Delta\alpha}{\alpha}(f_0,t) - B_1(t)\frac{\Delta\beta}{\beta}(f_0,t) \\ \vdots \\ B(t,1,f_m) - A_1(t)\frac{\Delta\alpha}{\alpha}(f_0,t) - B_1(t)\frac{\Delta\beta}{\beta}(f_0,t) \\ \vdots \\ B(t,n,f_1) - A_n(t)\frac{\Delta\alpha}{\alpha}(f_0,t) - B_n(t)\frac{\Delta\beta}{\beta}(f_0,t) \\ \vdots \\ B(t,n,f_m) - A_n(t)\frac{\Delta\alpha}{\alpha}(f_0,t) - B_n(t)\frac{\Delta\beta}{\beta}(f_0,t) \end{bmatrix}$$

and further define the (mn) X 2 matrix e as:

$$\begin{bmatrix} (f_1 - f_0)A_1(t) & (f_1 - f_0)B_1(t) \\ \vdots & \vdots \\ (f_m - f_0)A_1(t) & (f_m - f_0)A_1(t) \\ \vdots & \vdots \\ (f_1 - f_0)A_n(t) & (f_1 - f_0)A_n(t) \\ \vdots & \vdots \\ (f_m - f_0)A_n(t) & (f_m - f_0)A_n(t) \end{bmatrix} .$$

We then have the relation:

$$a = e\begin{bmatrix} I_a \\ I_b \end{bmatrix},$$

and the terms Ia and Ib can be found by least squares inversion.

Numerical Example

We illustrate our method through application to the numerical example studied by Chapman et al. (2005). This was a high-to-low interface in which the top layer had P- and S-wave velocities of 2743m.s^{-1} and 1394m.s^{-1} respectively and a density of 2.06g.cm^{-3}. To generate a dispersive lower layer a frequency-dependent elastic

constant was generated by substituting gas of bulk modulus 200MPa and a suitable relaxation frequency into a medium that is defined under water saturation as having P- and S-wave velocities of 2835m.s^{-1} and 1472m.s^{-1}, density 2.08g.cm^{-3}, porosity 15% and crack density of 5%. For the Gassmann case the lower layer had P- and S-wave velocities of 2571m.s^{-1} and 1486m.s^{-1} and a density of 2.04g.cm^{-3}. The synthetic seismograms were calculated using the method of reflectivity with frequency-dependent materials.

Two 11 receiver gathers (0m – 1km) were acquired at a depth of 1km using a 40Hz ricker wavelet as our source. Figure 1a (Gassmann) and 1b (dispersive) show the resultant synthetic gathers.

(a) Gassman (b) Dispersive

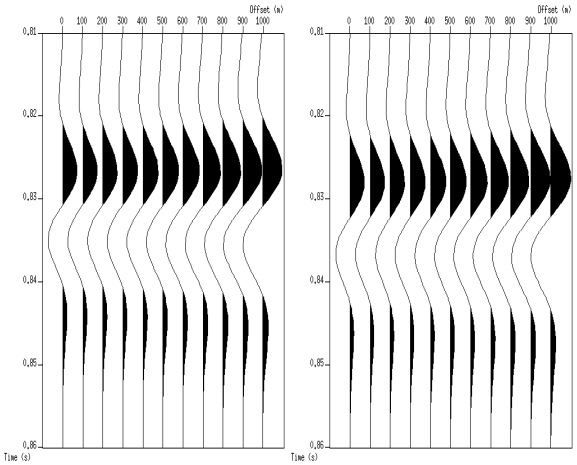

Figure 1: Synthetic gathers for a 1-layer model with a Gassman lower layer (a) and a dispersive lower layer (b) as described above.

Spectral decomposition was carried out using a continuous wavelet transform (CWT) algorithm at frequencies 40, 50, 60, 70 and 80Hz. Lower frequencies were not used due to ringing in the resultant iso-frequency traces. We derive a set of weights in the Gassman case by matching the peak amplitude of the iso-frequency trace to the 40Hz amplitude on an offset-by-offset approach. This maintains the AVO signature in the balanced data but removes the overprint of the wavelet as can be seen in figure 2a for the zero-offset trace. These same weights can be applied to the dispersive traces resulting in the frequency-dependent nature of the reflected amplitudes, figure 2b.

(a) Gassman (b) Dispersive

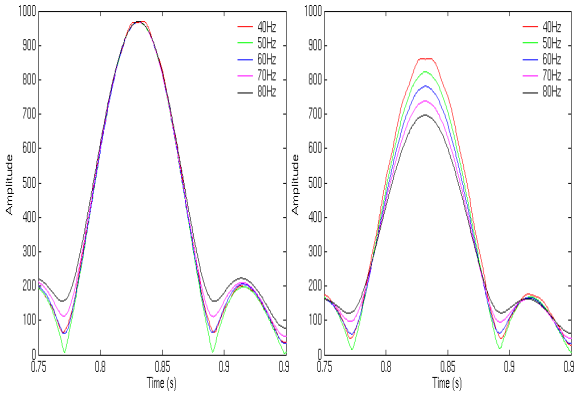

Figure 2: Balanced iso-frequency traces for the zero-offset trace at frequencies 40, 50, 60, 70 and 80Hz. In the Gassman case (a) the amplitudes are balanced and the source overprint has been removed but in the dispersive case (b) the frequency-dependent amplitude remains.

This frequency-dependent amplitude variation, figure 2b, is observed across all the offsets and all traces were used in the inversion. The addition of further offsets can help to stabilize the result whilst also introducing unwanted NMO stretch effects; however there is little difference in the result using offsets up to 200m (~6^{o}) and up to 1km (~27^{o}).

Figure 3 shows the inverted $\left|\frac{d}{df}\left(\frac{\Delta\alpha}{\alpha}\right)\right|$ traces for the Gassmann case (blue) and for the dispersive case (red). As is discernable from figure 2 the Gassmann case shows near-zero magnitudes, reflecting the elastic nature of the reflecting interface whilst the dispersive case shows a marked amplitude difference due to the dispersive nature of the lower layer.

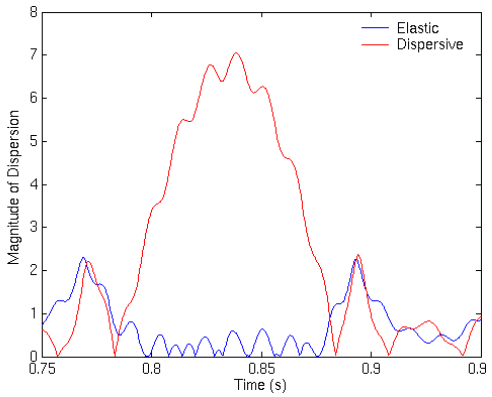

Figure 3: The inverted magnitude of dispersion for the reflected amplitudes. There is a clear difference between the Gassmann (blue) and dispersive case (red).

Conclusions

This paper has presented a technique which allows the frequency-dependence of P- and S-wave impedance to be estimated from reflection data. The algorithm is essentially an extension of the Smith and Gidlow (1987) inversion technique to the multi-frequency case, making use of a spectral decomposition technique.

Testing on synthetic data, calculated from the method of reflectivity with frequency-dependent materials, indicated that the method was robust. We were able to correctly determine dispersion properties from analysis of a single reflection.

It is important to note that the method can potentially be corrupted by a number of factors, notably the effects of tuning or NMO stretch, and much work is needed to establish the true utility of the technique. Nevertheless, we believe that the proposed method may prove useful in detecting fluid-related contrasts in dispersion properties.

Acknowledgements

This work was supported by the sponsors of the Edinburgh Anisotropy Project, and is presented with the permission of the Executive Director of the British Geological Survey (NERC). We are grateful to David Taylor for providing the code for reflectivity modeling with frequency-dependent properties (ANISEIS).

References

Batzle, M.L., Han, D.H., and R. Hofmann, 2006, Fluid mobility and frequency-dependent seismic velocity, direct measurements: Geophysics, **71**, N1-N9.

Castagna, J.P., Sun, S., and R.W. Siegfried, 2003, Instantaneous spectral analysis: detection of low-frequency shadows associated with hydrocarbons: The Leading Edge, **22**, 120-127.

Chapman, M., Liu, E., and X.Y. Li, 2005, The influence of fluid-sensitive dispersion and attenuation on the AVO signature: The Leading Edge, **24**, 1120-1125.

Smith, G.C., and P.M. Gidlow, 1987, Weighted stacking for rock property estimation and detection of gas: Geophysical Prospecting, **35**, 993-1014.

Frequency dependent AVO inversion using smoothed pseudo Wigner-Ville distribution

Xiaoyang Wu[1, 2], Adam Wilson[2,3], Mark Chapman[2,3] and Xiang-Yang Li[2,3]

[1]*Institute of Geophysics and Geomatics,China University of Geosciences, Wuhan, Hubei, P.R.China*
[2] *British Geological Survey, Murchison House, West Mains Road, Edinburgh EH9 3LA, UK, Email:xiaabc@bgs.ac.uk*
[3] *Geoscience School, University of Edinburgh, Grant Institute, West Mains Road, Edinburgh EH9 3JW*

Summary

Fluid-saturated rocks are generally expected to have frequency-dependent velocities, and it is attractive to try to use this property to discriminate different fluids with seismic data. Previous work has demonstrated how fluid-related dispersion results in a frequency-dependent AVO response. In this paper we show how to combine the smoothed pseudo Wigner-Ville distribution with a frequency-dependent AVO inversion scheme to obtain direct estimates of dispersion from pre-stack data. Numerical studies illustrate the application of the method to synthetic data, and we conclude that the work has the potential to be useful for fluid detection.

Introduction

Fluid substitution using Gassmann's theory lies at the heart of most seismic fluid-detection methods. While Gassmann has proven to provide an excellent approximation, the elastic behaviour of fluid-saturated rocks is often frequency-dependent, and this is not accounted for by the theory. Considerable effort has been expended on laboratory studies (Batzle et al. 2006) and theoretical investigations (Jakobsen and Chapman, 2009) with the goal of understanding this frequency-dependence. Being able to measure frequency-dependence of velocity from reflection data would greatly assist fluid discrimination efforts.

Chapman et al. (2005) performed a theoretical study of reflections from layers which exhibit fluid-related dispersion and attenuation, and showed that in such cases the AVO response was frequency-dependent. Application of spectral decomposition techniques allowed the behaviour to be detected on synthetic seismograms. Wilson et al. (2009) extended this analysis, introducing a frequency-dependent AVO inversion concept aimed at allowing a direct measure of dispersion to be derived from pre-stack data.

This paper represents a feasibility study for using the Wilson et al. (2009) technique for inferring dispersion properties from reflection data. We begin by introducing the Smoothed Pseudo Wigner-Ville distribution which we use for time-frequency analysis. We then outline the theory presented by Wilson et al. (2009), and perform a numerical study to demonstrate frequency-dependent AVO inversion on synthetic data. We conclude that the method is able to estimate dispersion properties from seismic data, and we hope that his may aid seismic fluid-detection efforts.

Smoothed Pseudo Wigner-Ville Distribution

We use Wigner-Ville Distribution (WVD) based method for spectral decomposition. WVD is well-recognized as an effective method for time-frequency analysis of nonstationary signals (Cohen, 1995). The WVD of signal $x(t)$ can be defined as:

$$WVD(t, f) = \int_{-\infty}^{\infty} X(t+\tau/2)\overline{X}(t-\tau/2)e^{-j2\pi f\tau}d\tau, \quad (1)$$

where τ is the time delay variable, X (t) is the analytical signal associated with the real signal x (t). Since the value is determined by all the values rather than part of the signal limited by a time window, WVD avoids a trade-off between time and frequency resolution. However, this improvement comes at the cost of suffering from cross-terms interference (CTI) due to bilinear feature. We use two smooth windows g(v) and $h(\tau)$ to reduce the effect of CTI, namely the Smoothed Pseudo Wigner-Ville Distribution (SPWVD, Claasen and Mecklenbräuker, 1980):

$$SW_{g,h,X}(t, f) = \int_{-\infty}^{\infty}\int_{-\infty}^{\infty} X(t+\frac{\tau}{2})\overline{X}(t-\frac{\tau}{2})g(v)h(\tau)e^{-j2\pi f\tau}dvd\tau, \quad (2)$$

where v is the time delay and τ is the frequency offset, $g(v)$ is the time smooth window, $h(\tau)$ is the frequency smooth window on condition that $g(v)$ and $h(\tau)$ are both real symmetric functions and $g(0)=h(0)$. SPWVD is a high "cost performance" method in resolution and calculating time which provides higher temporal resolution than STFT and CWT (Wu and Liu, 2009).

Frequency dependent AVO inversion

Smith and Gidlow's (1987) two-term AVO approximation of reflection coefficient R can be re-written as:

$$R(\theta) \approx A(\theta)\frac{\Delta V_p}{V_p} + B(\theta)\frac{\Delta V_s}{V_s}, \quad (3)$$

where θ is the angle of incidence and A and B can be derived in terms of the velocities. Following the arguments of Wilson et al. (2009), the reflection coefficient and the P- and S-wave impedances are considered to vary with frequency due to dispersion at the interface, then (3) can be written as:

$$R(\theta,\ f) \approx A(\theta)\frac{\Delta V_p}{V_p}(f) + B(\theta)\frac{\Delta V_s}{V_s}(f). \tag{4}$$

Expanding (4) as first-order Taylor series around a reference frequency f_0:

$$R(\theta, f) \approx A(\theta)\frac{\Delta V_p}{V_p}(f_0) + (f - f_0)A(\theta)I_a + B(\theta)\frac{\Delta V_s}{V_s}(f_0) + (f - f_0)B(\theta)I_b, \tag{5}$$

where I_a and I_b are the derivatives of impedance with respect to frequency evaluated at f_0:

$$I_a = \frac{d}{df}\left(\frac{\Delta V_p}{V_p}\right); I_b = \frac{d}{df}\left(\frac{\Delta V_s}{V_s}\right). \tag{6}$$

For a typical CMP gather with n receivers denoted as a data matrix $s(t, n)$. Coefficients A and B at each sampling point, denoted as $A_n(t)$ and $B_n(t)$, can be derived with the knowledge of velocity model through ray tracing. We perform SPWVD on $s(t, n)$ to derive the spectral amplitude $S(t, n, f)$ at a series of frequencies. However, S contains the overprint of seismic wavelet, so we perform spectral balance to remove this effect with a suitable weight function w:

$$D(t, n, f) = S(t, n, f)w(f). \tag{7}$$

In AVO analysis, we usually assume that the recorded amplitudes can be associated with the reflection coefficients through a simple transformation. According to (4), we can obtain $\Delta V_p/V_p$ and $\Delta V_s/V_s$ at the reference frequency f_0 by replacing R with D. Considering m frequencies $[f_1, f_2, \ldots f_m]$, equation (5) can be expressed as matrix form:

$$\begin{bmatrix} D(t,1, f_1) - A_1(t)\frac{\Delta V_p}{V_p}(f_0,t) - B_1(t)\frac{\Delta V_s}{V_s}(f_0,t) \\ \vdots \\ D(t,1, f_m) - A_1(t)\frac{\Delta V_p}{V_p}(f_0,t) - B_1(t)\frac{\Delta V_s}{V_s}(f_0,t) \\ \vdots \\ D(t,n, f_1) - A_n(t)\frac{\Delta V_p}{V_p}(f_0,t) - B_n(t)\frac{\Delta V_s}{V_s}(f_0,t) \\ \vdots \\ D(t,n, f_m) - A_n(t)\frac{\Delta V_p}{V_p}(f_0,t) - B_n(t)\frac{\Delta V_s}{V_s}(f_0,t) \end{bmatrix} \approx \begin{bmatrix} (f_1 - f_0)A_1(t) & (f_1 - f_0)B_1(t) \\ \vdots & \vdots \\ (f_m - f_0)A_1(t) & (f_m - f_0)B_1(t) \\ \vdots & \vdots \\ (f_1 - f_0)A_n(t) & (f_1 - f_0)B_n(t) \\ \vdots & \vdots \\ (f_m - f_0)A_n(t) & (f_m - f_0)B_n(t) \end{bmatrix} \begin{bmatrix} I_a \\ I_b \end{bmatrix}, \tag{8}$$

and I_a and I_b can be solved with least-squares-inversion.

Numerical Example

We consider a two-layer Class III AVO model presented by Chapman et al. (2005), where the top elastic layer had P- and S-wave velocities of 2743ms^{-1} and 1394ms^{-1}. For the dispersive model, the lower layer is defined as a material under water-saturation then substituted with gas by changing the fluid bulk modulus from 2GPa to 0.2GPa. For the elastic model, the P- and S-wave velocities of lower layer were calculated from elastic tensor for the dispersive model at low frequency. Eleven traces for each model are generated using 40Hz ricker wavelet as our source. The trace space is 100m.

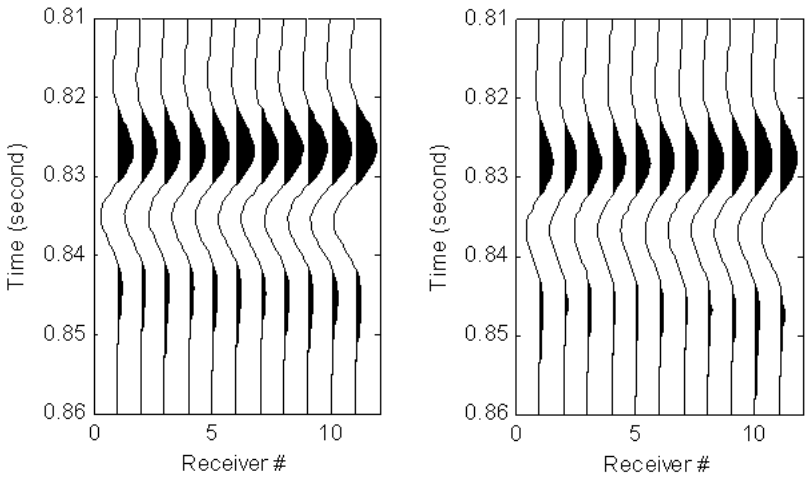

Figure 1 *Synthetic gathers for the two-layer model at the interface with (Left) elastic lower layer and (Right) dispersive lower layer.*

Figure 1 displays the synthetic gathers of the elastic and dispersive models at the interface respectively, both of which the amplitudes increase with the offset gradually. However, compared with the elastic model, the amplitudes for the dispersive model have decreased. Note that the event between 0.82s and 0.83s in the elastic gather arrives earlier than the corresponding event in the dispersive gather. This indicates the attenuation of energy and change of velocity in the dispersive model. SPWVD is performed to calculate the spectral amplitudes at 25, 30, 40, 50, 60, 70 and 80Hz. A set of weights are derived in the elastic model by matching the peak amplitude of the isofrequency trace to the 40Hz amplitude to remove the overprint of wavelet. These same weights are applied to the dispersive model. Figure 2 shows a comparison of isofrequency sections between the elastic and dispersive models at 25, 40, 60 and 80Hz. For the elastic model (upper), similar energy appears on each isofrequency section after spectral balance. In the dispersive case (lower), energy reduces at 25Hz compared with elastic model and decreases markedly with the increase of frequency.

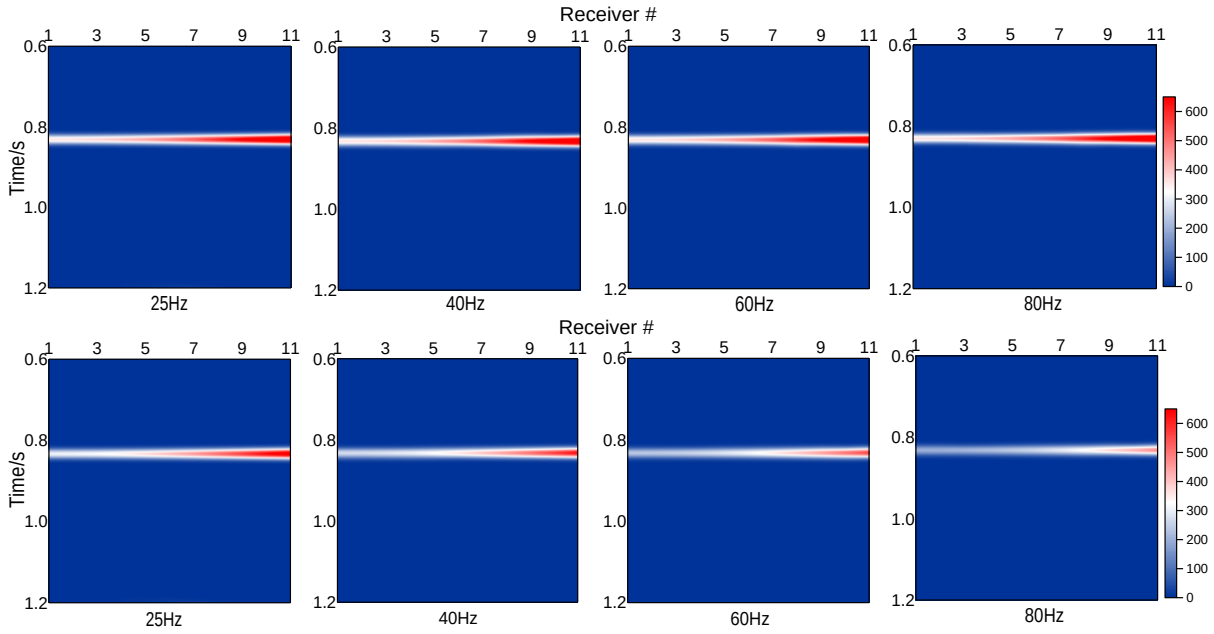

Figure 2 *Isofrequency sections of (upper) the elastic gather and (lower) dispersive gather at 25Hz, 40Hz, 60Hz and 80Hz. Spectral balance based on the input wavelet has been carried out with 40Hz as reference frequency.*

Figure 3 displays the inverted $\left|\frac{d}{df}(\frac{\Delta V_p}{V_p})\right|$ for the elastic and dispersive model. The magnitude of P wave dispersion for the dispersive model is more profound than the elastic model. We can also see the time delay between the dispersive and elastic arrivals due to the high temporal resolution of SPWVD.

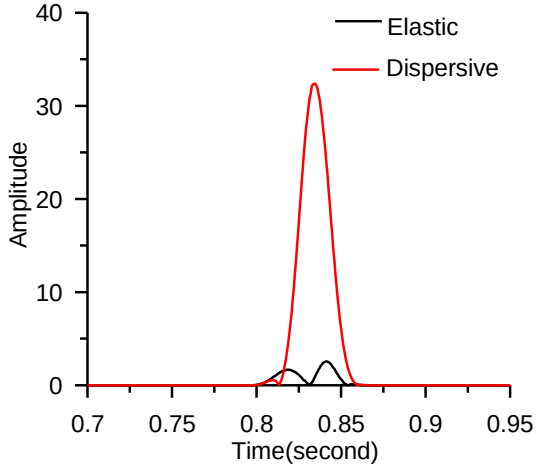

Figure 3 *The inverted magnitude of P wave dispersion for the elastic and dispersive models.*

Conclusions

Fluid-related dispersion and attenuation gives rise to a frequency-dependent reflection coefficient, and in many cases this can have a strong effect on reflection data. This paper combines a modern time-frequency analysis technique with a frequency-dependent AVO inversion scheme to demonstrate the possibility of inferring direct dispersion properties from pre-stack data. We believe that the technique has the potential to improve our ability to detect fluids with seismic data.

Acknowledgements

We are grateful to David Taylor for providing the code for reflectivity modelling with frequency-dependent properties (ANISEIS). This work was supported by the sponsors of the Edinburgh Anisotropy Project, and is presented with the permission of the Executive Director of British Geological Survey (NERC).

References

Batzle, M.L., Han, D-h, Hofmann, R. Fluid mobility and frequency-dependent seismic velocity, direct measurements. Geophysics, 71 (1): N1-N9.
Chapman, M., Liu, E. and Li X-Y., 2005. The influence of abnormally high reservoir attenuation on the AVO signature, The Leading Edge, 24(11): 1120-1125.
Claasen, T., Mecklenbräuker, W., 1980. The Wigner distribution: a tool for time–frequency signal analysis. Philips Journal of Research 35, 217-250.
Cohen, L., 1995. Time–Frequency Analysis. Prentice Hall Inc., New York, USA.
Jakobsen,M., and Chapman M., 2009, Unified theory of global flow and squirt flow in cracked porous media, Geophysics,74(2):WA65-WA76
Smith, G.C. and Gidlow, P.M., 1987. Weighted stacking for rock property estimation and detection of gas: Geophysical Prospecting, 35, 993-1014.
Wilson A., Chapman M., and Li X-Y., 2009. Frequency-dependent AVO inversion, 79th annual SEG meeting Expanded Abstracts, 28, 341-345.
Wu X. and Liu T., 2009, Spectral decomposition of seismic data with reassigned smoothed pseudo Wigner-Ville distribution, Journal of Applied Geophysics, 68(3): 386-393.

Appendix

Publications

1. **Wilson, A.,** Chapman, M. and Li, X.Y., 2009. *Use of frequency dependent AVO inversion to estimate P-wave dispersion properties from reflection data*, 71st Annual EAGE meeting.
2. **Wilson, A.,** Chapman, M. and Li, X.Y., 2009. *Frequency-dependent AVO inversion*, 79th Annual SEG meeting.
3. Wu, X., **Wilson, A.,** Chapman, M. and Li, X.Y., 2010. *Frequency-dependent AVO inversion using smoothed pseudo Wigner-Ville distribution*, 72nd Annual EAGE meeting.